



ISOTOPE REENTRY VEHICLE DESIGN STUDY CONCEPTUAL DESIGN -- PHASE IB -- TOPICAL REPORT

Prepared for

NATIONAL AERONAUTICS AND SPACE ADMINISTRATION

Contract NAS 3-10938

GPO PRICE \$ _____

CFSTI PRICE(S) \$ _____

Hard copy (HC) 3.00

Microfiche (MF) 1.65

ff 653 July 65

AVCO GOVERNMENT PRODUCTS GROUP
SPACE SYSTEMS DIVISION
201 Lowell Street
Wilmington, Massachusetts 01887

FACILITY FORM 602

N 68 3170	
(ACCESSION NUMBER)	(THRU)
324	
(PAGES)	(CATEGORY)
CR-72463	31
(NASA CR OR TMX OR AD NUMBER)	

NOTICE

This report was prepared as an account of Government sponsored work. Neither the United States, nor the National Aeronautics and Space Administration (NASA), nor any person acting on behalf of NASA:

- A.) Makes any warranty or representation, expressed or implied, with respect to the accuracy, completeness, or usefulness of the information contained in this report, or that the use of any information, apparatus, method, or process disclosed in this report may not infringe privately owned rights; or
- B.) Assumes any liabilities with respect to the use of, or for damages resulting from the use of any information, apparatus, method or process disclosed in this report.

As used above, "person acting on behalf of NASA" includes any employee or contractor of NASA, or employee of such contractor, to the extent that such employee or contractor of NASA, or employee of such contractor prepares, disseminates, or provides access to, any information pursuant to his employment or contract with NASA, or his employment with such contractor.

Requests for copies of this report should be referred to

National Aeronautics and Space Administration
Office of Scientific and Technical Information
Attention: AFSS-A
Washington, D.C. 20546

NASA CR-72463
AVSSD-0193-68-CR

ISOTOPE REENTRY VEHICLE DESIGN STUDY
CONCEPTUAL DESIGN -- PHASE IB^c -- TOPICAL REPORT

Prepared for
NATIONAL AERONAUTICS AND SPACE ADMINISTRATION

October 1968

Contract NAS 3-10938

TECHNICAL MANAGEMENT
NASA LEWIS RESEARCH CENTER
Cleveland, Ohio

BRAYTON CYCLE BRANCH
LLOYD I. SHURE

AVCO GOVERNMENT PRODUCTS GROUP
SPACE SYSTEMS DIVISION
201 Lowell Street
Wilmington, Massachusetts 01887

PRECEDING PAGE BLANK NOT FILMED.

ABSTRACT

This document summarizes the Task IB conceptual design effort on the Isotope Re-entry Vehicle (IRV) study. The major objective of the study is to develop a preliminary design of a 25 KW_t Pu 238 IRV. Major design emphasis is on system safety and developability. The IRV is configured to meet minimum practical diameter and weight limits. During Task IA various IRV, heat source, and heat-source heat exchanger concept combinations were developed and evaluated. Three IRV systems have been studied in a detailed conceptual design evaluation in Task IB.

These are all based on the use of a 60-degree blunted conical aeroshell entry vehicle. The concepts are:

1. A minimum diameter circular planar heat source (HS) array (with non-vented capsules),
2. A minimum diameter circular planar heat source (HS) array (with vented capsules),
3. A minimum diameter pin cushion HS array (with nonvented capsules).

The primary objective of Task IB has been to develop candidate designs to the level required for performance comparison and then to recommend one IRV for preliminary design.

EDITED BY:
EDITORIAL SERVICES
WILLIAM H. BARBER

CONTENTS

1.1	INTRODUCTION	1
1.1	Conceptual Design -- Phase IA	1
1.2	Conceptual Design -- Phase IB	7
1.3	Aerodynamic Test Program	8
1.4	Preliminary Design -- Phase II	8
1.5	Program Schedule	11
2.0	SUMMARY	13
2.1	Summary and Review -- Phase IA	13
2.2	Summary -- Phase IB	35
3.0	DESIGN APPROACH	55
4.0	FUEL CAPSULE	59
4.1	Ground Rules	59
4.2	Capsule Design	59
4.3	Fuel Capsule Spacing Analysis	59
5.0	HEAT SOURCE	67
5.1	Heat Source Design	67
5.2	Heat Sink Design and Requirements	81
5.3	Structural Load Environments	83
6.0	REENTRY VEHICLE	87
6.1	Heat Leak	87
6.2	Reentry Vehicle Design	92
7.0	TERMINAL SURVIVAL SYSTEMS	145
7.1	Drag Augmentation Devices	145
7.2	Impact Attenuation	149
7.3	Location Aids	163
8.0	IRV SYSTEM	167
8.1	IRV Design Description	167
8.2	HSHX Design	179
8.3	IRV/Brayton Cycle/Launch Vehicle Integration	251
Appendix	271

ILLUSTRATIONS

Figure 1.0-1	IRV/Brayton Cycle/Atlas-Centaur Integration	2
1.0-2	Fuel Capsules	3
1.2-1	Isotope Reentry Vehicle, 49-Inch Diameter Planar Array	9
1.2-2	Isotope Reentry Vehicle, 39-Inch Pin Cushion Array	10
1.5-1	Program Schedule	12
2.1-1	Deorbit and Recovery Profile	15
2.1-2	Separate Launch Sequence	16
2.1-3	System Design Requirements	17
2.1-4	Saturn IB Reentry Conditions	18
2.1-5	Aerodynamic Shape Concepts	21
2.1-6	Heat Source Configurations	23
2.1-7	HSHX Configuration	25
2.1-8	Support and Attachment Concepts	26
2.1-9	Impact Attenuation Concepts	28
2.1-10	Turnaround Concepts	29
2.1-11	Recovery Aids and Abort and Deorbit Rocket Integration Concepts	31
2.1-12	IRV Candidate Configuration Summary	33
2.1-13	Summary of Weight and Diameter Characteristics	34
2.2-1	Mechanical Details of Pin Cushion Array	40
2.2-2	Vented Capsule Retention, 46-Inch Diameter Planar Array	41
2.2-3	Rectangular Heat-Source Heat Exchanger Heat Dump Concept	43
2.2-4	Heat-Source Heat Exchanger Area Requirements	48
2.2-5	Cold Plate Concept with Recessed Corner	52

ILLUSTRATIONS (Cont'd)

Figure 2.2-6	Separate Abort Deorbit	53
3.0-1	Design Flow Chart	56
3.0-2	Vehicle Diameter Tradeoff, 47-Inch Circular Planar Heat Source	57
4.3-1	Model for Temperature Difference Calculations	61
4.3-2	Circular Planar Heat Source -- Effect of Capsule Spacing on Capsule Temperature Difference (Nonvented Capsule)	62
4.3-3	Circular Planar Heat Source -- Effects of Capsule Spacing on Capsule Temperature Difference (Vented Capsule)	64
4.3-4	Comparison of Nonvented Capsule and Vented Capsule Spacing on Capsule Temperature Difference	65
5.1-1	Circular Planar Array, 49-Inch-Diameter Heat Source ...	68
5.1-2	ACHX Header Modification	70
5.1-3	Circular Planar Array, 46-Inch-Diameter Heat Source (with Vented Capsules)	71
5.1-4	Pin Cushion Array, 39-Inch-Diameter Heat Source	72
5.1-5	Vertical Versus Stacked Log Array	73
5.1-6	Pin Cushion Heat Source Temperature Difference in a Vertical Pin Cushion Array	77
5.1-7	Circular Planar Heat Source Temperature Differences Around Nonvented Fuel Capsule	78
5.1-8	Circular Planar Heat Source Temperature Differences Around Vented Capsule	79
5.2-1	Capsule Heating Rate Versus BeO Weight	82
5.2-2	Pin Cushion Heat Source -- Vertical Array Capsule Temperature Rise (After 1 Hour of Heating from 1800 ^o F).....	84
6.1-1	Effect of Insulation Thickness on Heat-Source Heat Losses	88

ILLUSTRATIONS (Cont'd)

Figure 6.1-2	Thermal Losses Through Struts	89
6.1-3	Insulation System -- Heat Flow Model	90
6.1-4	Support Strut	91
6.2.1-1	Base Capsule Configuration	93
6.2.1-2	Capsule Heating Factor ($\alpha = 180^\circ$)	96
6.2.1-3	Maximum Heating Factor ($\alpha = 180^\circ$)	99
6.2.1-4	Flow Field Sketches	101
6.2.1-5	Base Heating, Recessed Base	105
6.2.1-6	Base Heating, Stacked Capsule Configuration	106
6.2.1-7	Capsule Base Heating Nominal Entry (High Spin Rate)	107
6.2.1-8	Capsule Base Heating Nominal Entry (Low Spin Rate)	108
6.2.1-9	Capsule Base Heating (180° Rearward)	109
6.2.1-10	Capsule Base Heating (Tumbling)	110
6.2.1-11	Capsule Base Heating (180° Rearward)	111
6.2.1-12	Capsule Base Heating (Tumbling)	112
6.2.1-13	Convective Heating Rate for Exposed Fuel Capsule Array	116
6.2.1-14	Circular Planar Heat Source -- Temperature Response of Fuel Capsules	117
6.2.2-1	Destabilizing Fence Characteristics	118
6.2.2-2	Pitch Rate History	120
6.2.2-3	Angle of Attack History	122
6.2.2-4	Angle of Attack Envelope	123
6.2.3-1	Schematic of IRV Blunt-Cone Shell	125
6.2.3-2	IRV Aeroshell Structure Effective Stress	126
6.2.3-3	Cone Pressure (Windward Meridian) and Angle of Attack Profiles	129

ILLUSTRATIONS (Cont'd)

Figure	6.2.3-4	Minimum Honeycomb Facesheet Thickness Versus Diameter	130
	6.2.3-5	Honeycomb Core Thickness Versus Vehicle Diameter	131
	6.2.3-6	Model 500 Data	132
	6.2.3-7	IRV -- Heat Shield Thickness Double Skip Entry Stagnation Point	136
	6.2.3-8	IRV -- Heat Shield Weight Double Skip Entry Stagnation Point	137
	7.1-1	Ring Sail Parachute (CD = 0.75)	146
	7.1-2	Tuck-Back Ballute (CD = 0.5)	147
	7.1-3	Aerodynamic Decelerator Comparison	148
	7.2-1	Cold Plate Concept	150
	7.2-2	IRV Geometry	151
	7.2-3	Stroke and Cold Plate Weight Requirements (Plate Thickness = f(H))	152
	7.2-4	Stroke and Cold Plate Weight Requirements (Plate Thickness = Constant)	153
	7.2-5	IRV Weight Versus Terminal Velocity	155
	7.2-6	Cold Plate Concept with Recessed Corner	156
	7.2-7	IRV Aeroshell Diameter (Heat Shield, Bond, and Aluminum Honeycomb) Versus Aeroshell Weight 60-Degree Blunt Cone, 15-Percent Cylinder	157
	7.2-8	IRV Weight Optimization Study (Capsule Mounting Options)	158
	7.2-9	IRV Weight, Diameter Tradeoff (Heat Source Weight Option)	159
	7.2-10	IRV Weight Versus Diameter (Corner Recess Effect)	160
	7.2-11	IRV Weight Versus Diameter (Cold Plate Thickness Option)	161
	7.2-12	IRV Weight Versus Diameter (Impact Velocity Effect)	162
	7.2-13	Reference Design Weight, Diameter Tradeoff Study	164
	7.3-1	Location Aids	165
	8.1-1	Isotope Reentry Vehicle, 49-Inch Diameter Planar Array	169

ILLUSTRATIONS (Cont'd)

Figure	8.1-2	Isotope Reentry Vehicle, 49-Inch Diameter Planar Array	170
	8.1-3	Detail of IRV Removable Door	171
	8.1-4	IRV Pin Cushion Array Reference Design	172
	8.1-5	IRV Circular Planar Array Reference Design (Vented Capsules)	173
	8.1-6	IRV Weight and Diameter Summary	174
	8.1-7	Detail of Truss Aeroshell Attachment Point	175
	8.1-8	Detail of Spin Motor Attachment	177
	8.1-9	Detail of Aft Cylindrical Ring Structure	178
	8.2.1-1	Brayton-Cycle Power Conversion Module	180
	8.2.1-2	Heat-Source Heat Exchanger System	180
	8.2-1	Temperature Gradient Around Nonvented Fuel Capsule (Circular Planar Heat Source)	183
	8.2-2	Layout of Heat Exchanger Involute -- 49-Inch Diameter	185
	8.2-3	Physical Model for Determination of Involute Tube Layout	186
	8.2-4	Thermal Model for Involute Heat-Source Heat Exchanger	191
	8.2-5	U-Flow Configuration for Equalizing Flow Distribution in the Heat-Source Heat Exchanger	193
	8.2-6	Fixed Insulation Concept	196
	8.2-7	Circular Planar Source -- Involute Tube Heat Exchanger (49-Inch Diameter)	197
	8.2-8	Circular Planar Source -- Involute Tube Heat Exchanger (49-Inch Diameter) (Heat Dump System)	199
	8.2-9	Thermal Conductivity Versus Temperature as a Function of Bearing Load	200
	8.2-10	Thermal Conductivity Comparison	202

ILLUSTRATIONS (Cont'd)

Figure	8.2-11	Assumptions for Heat Leak Estimates	203
	8.2-12	Heat Leaks -- Planar Circular Heat Source	204
	8.2-13	Involute Heat-Source Heat Exchanger Performance (Second Heat Exchanger in Operation) (49-Inch-Diameter)	205
	8.2-14	Involute Heat-Source Heat Exchanger Performance (First Heat Exchanger in Operation) (49-Inch-Diameter)	207
	8.2-15	Effect of Increasing Heat-Source Heat Exchanger Diameter (49-Inch-Diameter Heat Source)	208
	8.2-16	Heat-Source Heat Exchanger Area Requirements	209
	8.2-17	Heat-Source Heat Exchanger -- Weight Versus Reduction in Source Temperature (49-Inch- Diameter Source)	210
	8.2-18	Brayton Fluid Outlet Temperature Versus Effective Source Temperature (Circular Geometry)	211
	8.2-19	Turbine Inlet Temperature Versus Power Output	212
	8.2-20	Rectangular Heat-Source Heat Exchanger Circular Source (49-Inch-Diameter)	214
	8.2-21	Rectangular Heat-Source Heat Exchanger-Temperature Distributions (49-Inch-Diameter)	215
	8.2-22	Rectangular Heat-Source Heat Exchanger Circular Planar Source-Variation of Heat Flux Along Various Tubes	217
	8.2-23	Rectangular Heat-Source Heat Exchanger-Heat Dump Concept	220
	8.2-24	Circular Planar Source -- Rectangular Heat Exchanger (Heat Dump System)	221
	8.2-25	Heat Leaks	222
	8.2-26	Brayton Fluid Outlet Temperature Versus Effective Source Temperature (Rectangular Geometry)	223
	8.2-27	Heat-Source Temperature Reduction Versus Heat-Source Heat Exchanger Weight for Rectangular Geometry	224

ILLUSTRATIONS (Cont'd)

Figure	8.2-28	Fuel Capsule Temperature Gradient in a Vertical Pin Cushion Array	226
	8.2-29	Pin Cushion Heat-Source Heat Exchanger Approaches ...	227
	8.2-30	Pin Cushion Heat-Source Heat Exchanger (39-Inch-Diameter Source)	228
	8.2-31	Pin Cushion Heat-Source Heat Exchanger	229
	8.2-32	Layout -- Heat Exchanger, Vertical Pin Cushion	230
	8.2-33	Temperature Distributions in Pin Cushion Heat-Source Heat Exchanger	232
	8.2-34	Pin Cushion Source -- Tube-Fin Heat Exchanger	233
	8.2-35	Heat Leaks for Pin Cushion System	234
	8.2-36	Temperature Gradient Around Vented Capsule (Circular Planar Heat Source)	235
	8.2-37	Layout -- Heat Exchanger Involute (46-Inch-Diameter)	237
	8.2-38	Circular Planar Source -- Involute Tube Heat Exchanger (46-Inch-Diameter) (Heat Dump System)	238
	8.2-39	Heat Leaks -- Circular Planar Heat Source (Vented Capsules)	239
	8.2-40	Temperature and Heat Flux Distributions in HSHX No. 2 -- Planar Circular Source (Vented Capsule)	240
	8.2-41	Involute-Tube Circular Heat-Source Heat Exchanger (Vented Capsule) (46-Inch-Diameter)	241
	8.2-42	Heat-Source Heat Exchanger -- Area Requirements	242
	8.2-43	Typical Ideal Elastic-Plastic Load Cycles	246
	8.3-1	IRV/Brayton Cycle Launch Vehicle Integration	253
	8.3-2	Rectangular HSHX -- Heat Dump Concept	254
	8.3-3	Transverse Moment Effects	256
	8.3-4	Deorbit System Considerations	257

ILLUSTRATIONS (Concl'd)

Figure	8.3-5	Deorbit Considerations	261
	8.3-6	Separate Abort Deorbit	265
	8.3 7	Pin Cushion Heat Source -- Model for Radiation While in Deployed State	267
	8.3-8	Pin Cushion Heat Source -- Effect of Row Spacing on Peak Capsule Temperature	268
	8.3-9	IRV Integral Launch Study MORL/Min Diameter Vehicle	270

TABLES

Table 1.0-I	Program Ground Rules	4
1.0-II	IRV Design Criteria	5
1.0-III	Safety Criteria	6
1.2-I	Phase IB Ground Rules	7
2.1-I	Safety Mechanisms	20
2.2-I	Phase IB Study Areas	37
2.2-II	Heat Source Summary Comparison	38
2.2-III	Phase IB Heat-Source Geometries	39
2.2-IV	Phase IB Heat-Source Heat Exchanger Design Summary	45
2.2-V	Phase IB Heat-Source Heat Exchanger Performance Summary	46
2.2-VI	Reference Vehicle Performance Comparison Circular Planar Versus Pin Cushion Heat Source	49
2.2-VII	IRV Weight and Diameter Summary	50
5.1-I	Heat Source Mass and Moment Data	75
5.1-II	Thermal Performance Summary	80
5.3-I	IRV Structural Load Environment	85
6.2.1-I	Heat Transfer Distribution on Flat-Faced Cylinders	94
6.2.1-II	Aerodynamic Heating-Capsules	104
6.2.1-III	Aerodynamic Heating-Stagnation Point	114
6.2.2-I	Mass Characteristics	119
6.2.3-I	Summary of Structural Requirements for Major Structure Components	128
6.2.3-II	Insulation Characteristics of IRV Candidate Materials	135
6.2.3-III	Material Comparison for IRV Heat Shield at Stagnation Point	138
6.2.3-IV	Radiation Threshold Levels for Candidate Materials	143

TABLES (Concl'd)

Table 6.2.3-V	Properties of Typical Low-Density Ablators	144
8.1-I	IRV Reference Designs -- Mass Properties Comparison	168
8.2-I	HSHX -- System Requirements	181
8.2-II	Cb-1Zr Material Properties	248
8.2-III	Cb-1Zr Allowable Stresses	249
8.2-IV	Tube and Header Summary	250
8.2-V	Unwelded Tube Thermal Bending Moments	252
8.3-I	Spin-Rate Calculation Summary	259
8.3-II	Deorbit System Considerations	262

1.0 INTRODUCTION

This report summarizes the results of the Phase IB task of the Isotope Reentry Vehicle (IRV) Design Study. The study is being performed for the Lewis Research Center under Contract NAS3-10938. The major objective of this study is to develop a preliminary design of a 25 KW_t (end of life) Pu 238 Heat Source IRV. Required operational lifetime is 5 years, and major design emphasis has been placed on system safety and vehicle developability. In addition, the IRV has been configured for minimum diameter and weight. The design of the Heat Source Heat Exchanger (HSHX) is to be compatible with the characteristics of the Brayton Cycle Power Supply unit presently being investigated at Lewis Research Center.

Figure 1.0-1 shows an exploded view of an illustrative IRV Heat Source and Heat Source Heat Exchanger (HSHX) configuration mounted on an Atlas Centaur launch vehicle with the balance of the Brayton Cycle Power System. This is typical of a separately launched Isotope/Brayton system as specified by NASA. The isotope heat source consists of an array of isotope capsules containing PuO₂ fuel. Approximately 164 unvented capsules (Figure 1.0-2) are required to achieve a thermal power output of 25 KW at the end of the design lifetime goal. The heat source capsule array together with its BeO heat sink is mounted on a refractory metal support plate which in turn is attached to the reentry vehicle aeroshell via a truss network. Low-conductivity, high-temperature insulation is used to minimize heat leaks from the heat source to the reentry vehicle and its surroundings. Overall study ground rules are summarized in Table 1.0-I. Specific IRV design and safety criteria established at the outset of the study are listed in Tables 1.0-II and 1.0-III. Crushup material is provided between the heat source support plate and the aeroshell to attenuate the g-loading of the capsules during ground impact of the IRV occurring after reentry and terminal descent. The entire IRV is attached to the parent launch vehicle by a support ring which allows the IRV to be pivoted out of the launch vehicle for emergency cooling of the Heat Source (HS). Redundant and independently replaceable heat exchangers are provided to accept the thermal output of the heat source capsules which radiate with a maximum hot spot capsule temperature of less than 2000° F.

1.1 CONCEPTUAL DESIGN -- PHASE IA

During Phase IA of the study, a large number of isotope reentry vehicle (IRV)/heat source (HS)/heat source heat exchanger (HSHX) combinations were evaluated in terms of major design considerations, including aerodynamic shape, reentry performance, HS configuration, HSHX configuration, structural support and attachment, impact attenuation, recovery and location aid requirements, abort and deorbit rocket integration, and spacecraft (S/C) IRV integration. At the conclusion of Phase IA, three overall vehicle concepts were selected by NASA-LeRC for further evaluation in the Phase IB conceptual design effort. The concepts all employing 60-degree blunt cone IRV's were:

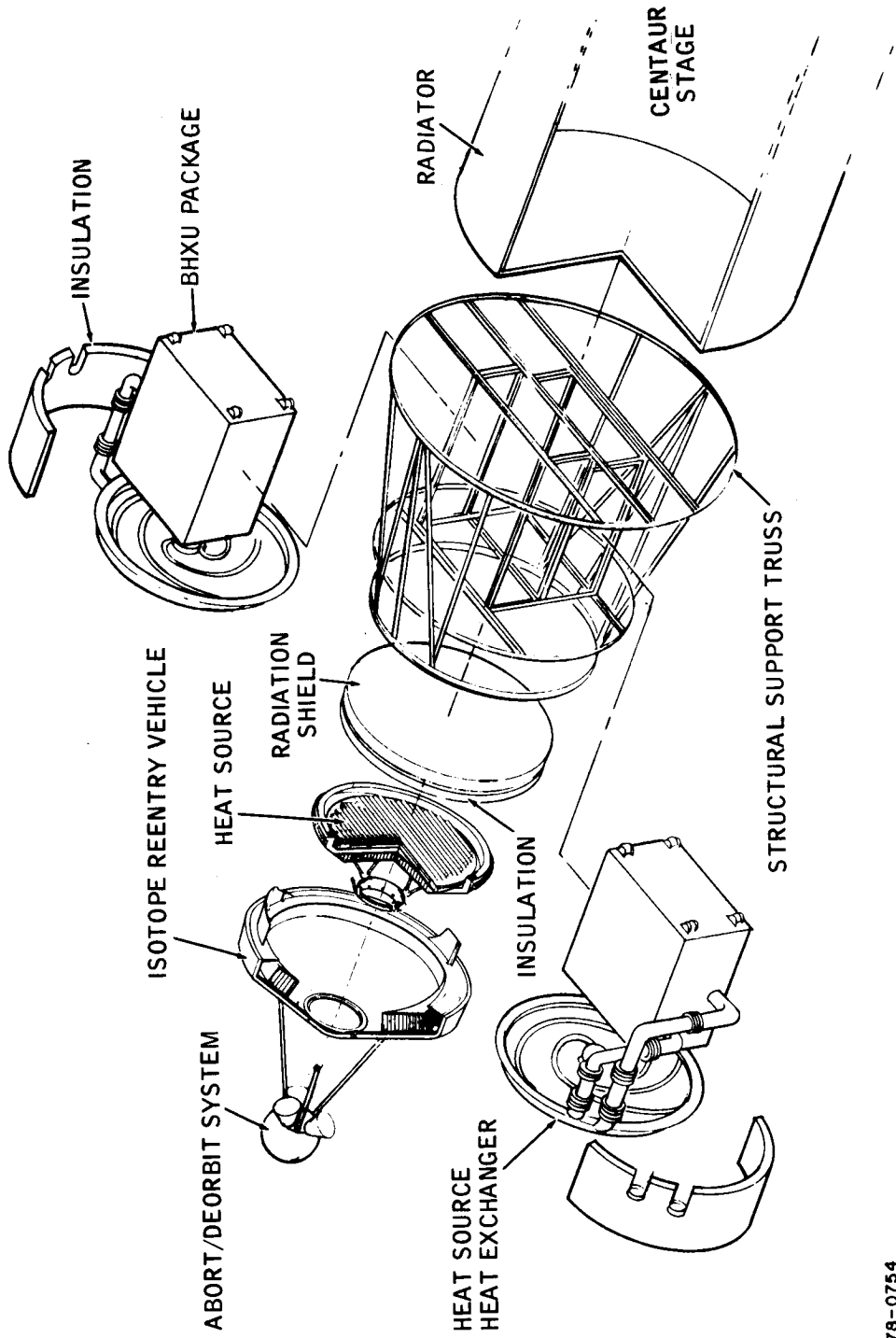
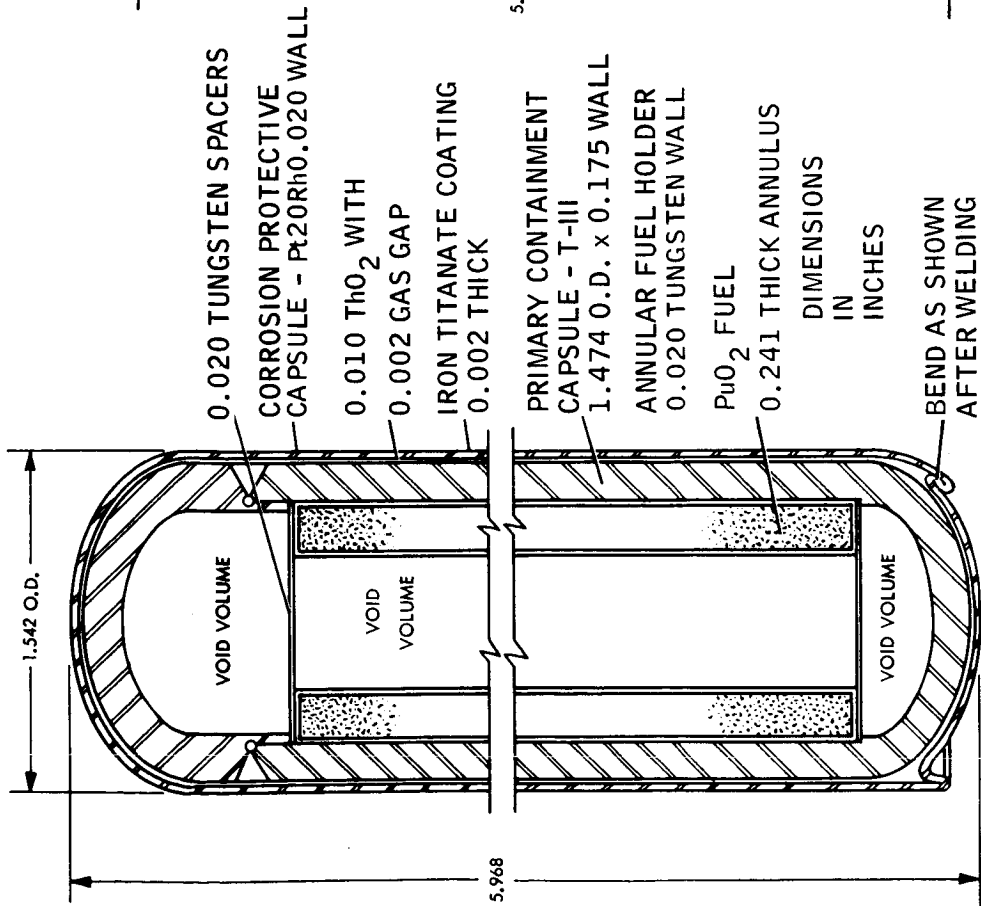


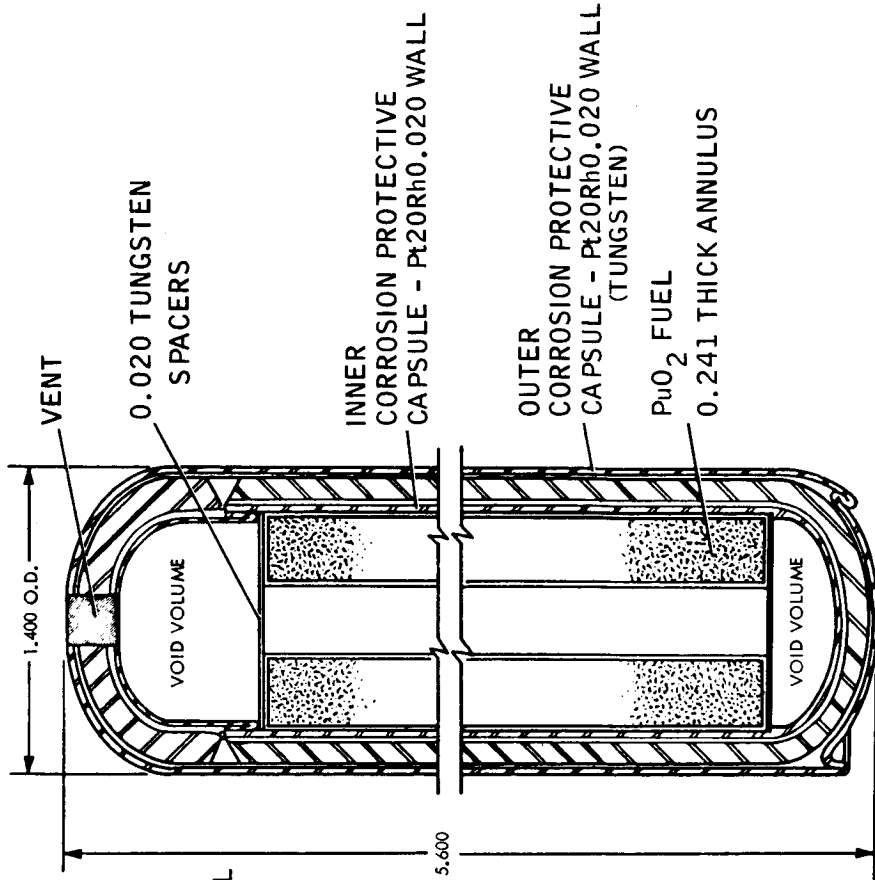
Figure 1.0-1 IRV/BRAYTON CYCLE/ATLAS-CENTAUR INTEGRATION

78-0754



POWER 157 WATTS (BOL)
 TOTAL SURFACE AREA 33.2 IN²
 WEIGHT = 4.6 LBS

NON-VENTED CAPSULE DESIGN



POWER 157 WATTS (BOL)
 TOTAL SURFACE AREA 28.4 IN²
 WEIGHT = 2.9 LBS

VENTED CAPSULE DESIGN

612385-6C

Figure 1.0-2 FUEL CAPSULES

TABLE 1.0-1

PROGRAM GROUND RULES

1. Use nonvented isotope heat source capsule characteristics
2. Consider both separate IRV launch (Atlas/Centaur) and integral launch (Saturn 1B-MORL)
3. Consider incorporation of recovery aids for the IRV
4. Aerodynamic configurations limited to 60° half-angle blunt cone and modified Apollo shape
5. HSHX to be in-place redundant and replaceable
6. Intact reentry capability during all mission phases
7. Design must provide for adequate heat rejection after impact

TABLE 1.0-II
IRV DESIGN CRITERIA

1)	Isotope Fuel	PuO ₂
2)	Capsule Design	See Figure 1.0-2
3)	Fuel Loading	25 KWt (EOL)
4)	IRV Ballistic Coefficient -- $\frac{W}{C_d A}$	$\leq 80 \text{ lb/ft}^2$ (Subsonic)
5)	Heat Leak -- IRV, HSHX, and ACHX	$\leq 1.5 \text{ KWt}^*$
6)	Heat Source Temperature:	
	Max Continuous, Surface	$\leq 2000^\circ\text{F}$
	Max Transient, Surface	$\leq 2500^\circ\text{F}^*$
	Max Launch Pad Equilibrium	$\leq 1400^\circ\text{F}$ (Operation with ACHX)
7)	Emergency Heat Rejection	Passive Radiation to Space by Body Deployment
8)	Thermal Storage:	
	Material	BeO
	Requirement	60 min (1800°F to 2500°F)
9)	Launch Abort	Rocket Ejection $\leq 10g$ Acceleration
10)	Orbital Emergency Separation	Redundant Pyrotechnic

*In the event of upside-down IRV earth impact, provision must be made to destroy or otherwise overcome the insulation and permit heat rejection without exceeding heat source temperature limits.

TABLE 1.0-III

SAFETY CRITERIA

- 1) Capsule design based on 10 half-life containment
- 2) No fuel release as a result of launch pad abort, fire, or entrapment of heat source in debris
- 3) Intact reentry of IRV from uncontrolled random reentry
- 4) Reentry vehicle ejection in the event of catastrophic launch abort
- 5) No burial of IRV after impact at terminal velocity
- 6) Radiation coupling between heat source and power conversion system - no physical connection
- 7) No credibility for assembly of critical mass

- a minimum diameter circular planar HS (ORNL fuel capsule).
- a pin cushion HS in a 60-degree blunt cone RV.
- a minimum diameter circular planar HS utilizing vented capsules.

Results of the Phase IA task are summarized in Reference 1.1-1.

1.2 CONCEPTUAL DESIGN -- PHASE IB

The three recommended concepts have been evaluated in terms of the following basic criteria during Phase IB:

- a. Safety
- b. Vehicle diameter
- c. Vehicle weight
- d. Reentry performance
- e. Overall reliability (simplicity) and developability
- f. Ability of the design to allow growth potential or changes in subsystem characteristics.

Phase IB ground rules are listed in Table 1.2-I below:

TABLE 1.2-I

PHASE IB GROUND RULES

- | |
|--|
| <ul style="list-style-type: none"> • Establish design characteristics of 3 IRV concepts (all 60° blunt cones) • Use truss support structure only • Impact attenuation system should be based on the use of peripheral crushup to insure heat source "flat" impact • Ballutes are to be considered for drag augmentation • Retro and abort rocket systems should be mounted on a tower in the A/C booster and on a minimum extension in the integral launch vehicle • Heat source and HSHX designs are to be based on maintaining a 1600° F turbine inlet temperature with the primary HSHX operating • HSHX designs shall be developed to meet in place redundancy and separate replaceability criteria |
|--|

In addition to the comparison of the three reference concepts, the major design area encompassed in the Phase IB scope are:

- Determination of minimum diameter reentry survival vehicles.
- Determination of impact survival system tradeoffs.
- Evaluation of fuel capsule cover plate utility for reentry heating protection.
- Consideration of ballutes for drag augmentation.
- Examination of HSHX design considerations in terms of reducing fuel capsule maximum hot spot operating temperatures.
- IRV/launch vehicle/spacecraft integration.

Figures 1.2-1 and 1.2-2 show perspective drawings of the circular planar HS IRV and the "pin cushion" IRV concepts, as developed during this phase of the study. The planar array vehicle, as shown in Figure 1.2-1, incorporates terminal impact survival subsystems, while the smaller diameter "pin cushion" concept provides no impact protection provision. Utilization of the vented capsule design, Figure 1.0-2, in the circular planar HS array does result in a significant reduction in IRV weight (~300 lbs).

1.3 AERODYNAMIC TEST PROGRAM

The major purpose of the test program is to define a passive aerodynamic device (such as a fence or fin) which ensures that the vehicle is not stable in a rearward attitude during reentry. Consequently, if the vehicle were to initially begin reentry in such an attitude (180-degree angle of attack) this device would guarantee vehicle "turn-around" at high altitudes prior to peak heating. Rearward (or high angle of attack) entry is undesirable because of the increased aerodynamic heating experienced by the heat source capsules which are located in the base region of the vehicle.

A number of different aerodynamic devices have been studied analytically and the most promising configurations are undergoing testing in the free flight shock tunnel and the arc wind tunnel test facilities by NASA/Ames. These facilities are capable of achieving the appropriate Reynolds Number ($10^4 - 10^5$) and Mach Number (>10) conditions. Sufficient data are being collected to provide a basis for making a preliminary selection of an effective turn-around device together with dimensional characteristics for use in the preliminary design phase.

1.4 PRELIMINARY DESIGN -- PHASE II

As a result of the Conceptual Design Phase IA and IB, a recommendation has been made to develop a more detailed preliminary design of the minimum diameter circular planar HS IRV. During the preliminary design phase the structural and thermal design of the IRV and the heat source heat exchanger will be completed. In addition, a detailed reentry performance analysis will be made to establish the performance limitations of the reference vehicle and its sensitivity to variations in the reentry trajectory, vehicle motions, and vehicle physical parameters.

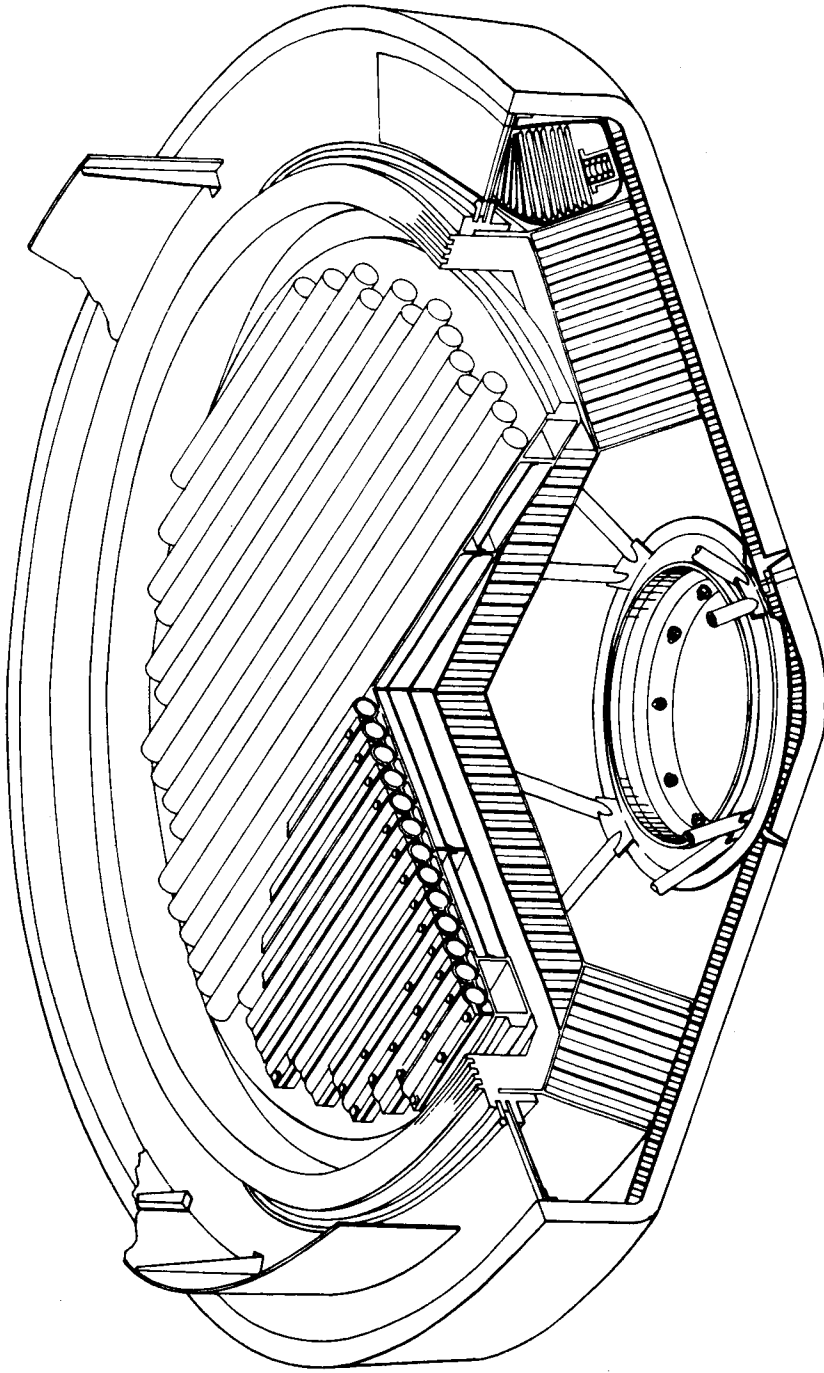


Figure 1.2-1 ISOTOPE REENTRY VEHICLE, 49-INCH DIAMETER PLANAR ARRAY

78-1610

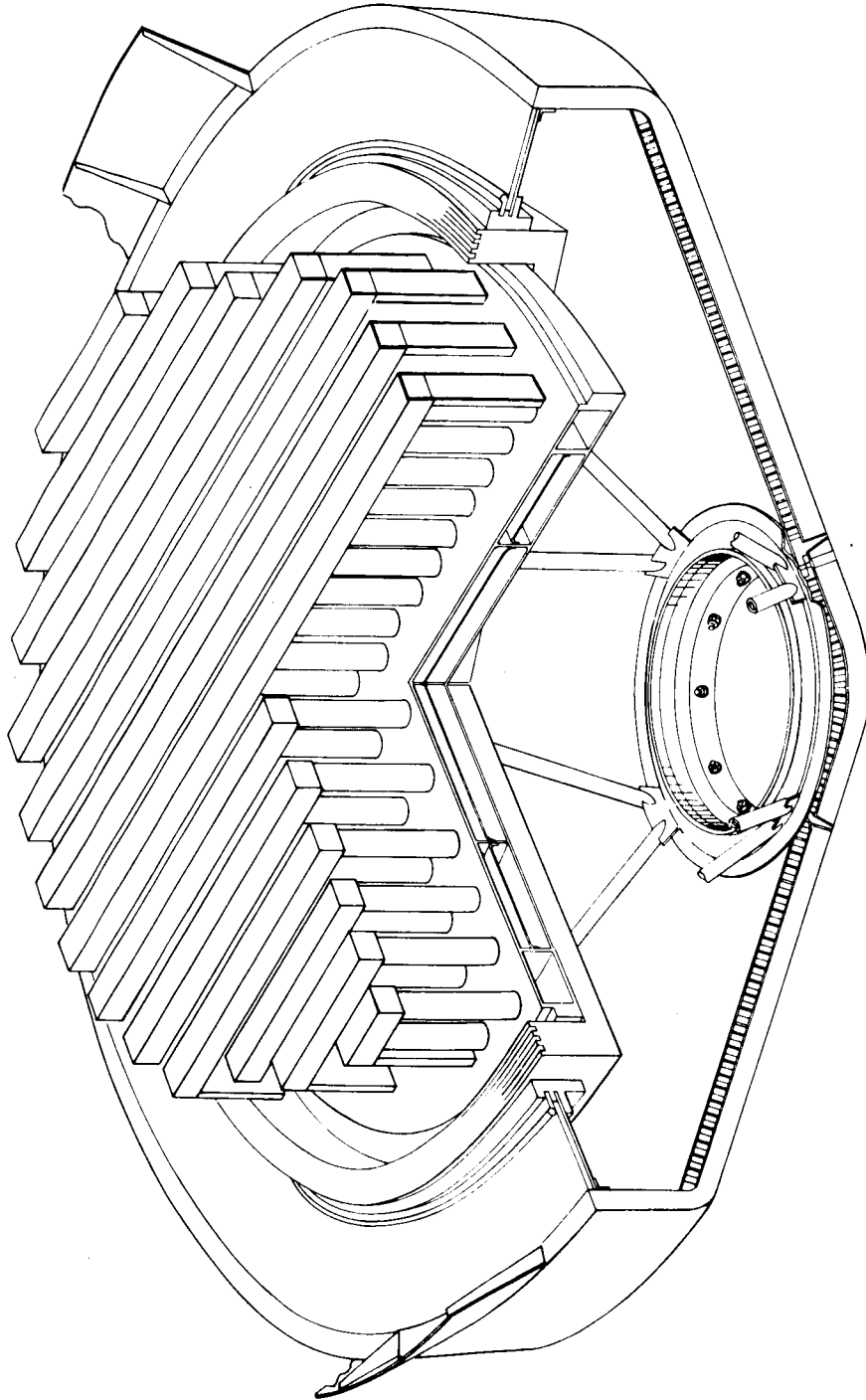


Figure 1.2-2 ISOTOPE REENTRY VEHICLE, 39-INCH PIN CUSHION ARRAY

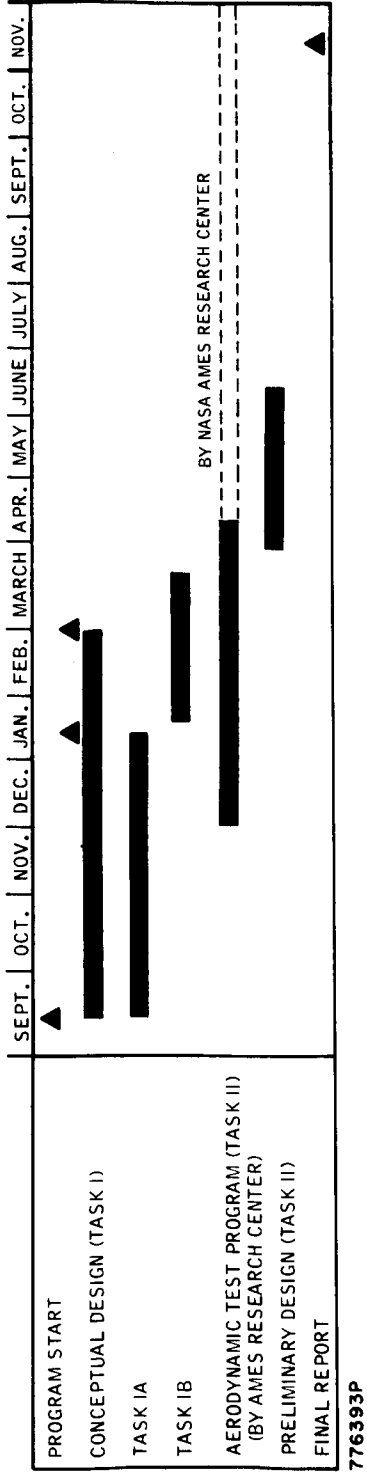
78-0611

1.5 PROGRAM SCHEDULE

Figure 1.5-1 shows the overall study schedule together with the time phasing of the three major tasks. The two milestones shown on Phase I (conceptual design) correspond to the two oral presentations which are given at the conclusion of Phase IA and Phase IB.

REFERENCES

- 1.1-1 Isotope Reentry Vehicle Design Study Conceptual Design -- Phase IA, Topical Report, AVSSD-0071-68-CR, NASA CR-72366.



776393P

Figure 1.5-1 PROGRAM SCHEDULE

2.0 SUMMARY

This section includes a brief review of the Phase IA effort, as well as a summary of the results of the Phase IB conceptual design study.

2.1 SUMMARY AND REVIEW--PHASE IA

During this period of the conceptual design phase, three major subtasks were completed leading to the selection of the three vehicle concepts which have been evaluated in detail during Phase IB.

First, a systems analysis was performed resulting in the definition of the critical system design requirements for the IRV (e.g., abort requirements, reentry conditions, impact attenuation requirements, etc.). Safety considerations and examination of various failure modes played a predominant role in the system analysis.

Second, a variety of conceptual designs were considered and evaluated for each of the critical IRV subsystems. Their relative advantages and disadvantages were examined and selections of preferred design alternatives were made wherever possible.

Third, a considerable number of total IRV conceptual designs were synthesized in order to examine the impact of different design alternatives on the total vehicle system. In addition, trade-off studies were performed to evaluate the effects of different design options on critical vehicle parameters (e.g., vehicle diameter). Using several selection criteria (i.e., vehicle weight, diameter, reentry performance, safety, developability, and growth potential), three vehicle concepts were recommended for further study.

The following sections briefly describe the results of these three subtasks.

2.1.1 Safety Systems Analysis

The purpose of the systems analysis was to establish IRV design requirements based on a detailed review of the basic mission and all associated failure modes. Reference launch vehicles were the Atlas/Centaur, for a separate launch mission, and the Saturn 1-B MORL, for an integral launch mission.

The major ground rules for the analysis were:

- a. For the separate launch case (Atlas/Centaur), a 260-nautical mile circular orbit with a 50-degree inclination was assumed. A yaw maneuver was included in the ascent trajectory to assure that the entire ascent trajectory (to orbital insertion) would take place over deep water.
- b. For the integral launch case (Saturn 1-B/MORL) a 164-nautical mile circular orbit with a 50-degree inclination was assumed.
- c. The nominal IRV return mode is controlled intact reentry, initiated by deorbiting the IRV from the space station.

d. The complete design envelope is defined by consideration of the maximum credible accident.

Figure 2.1-1 shows an illustrative launch, injection and docking sequence (for the separate launch case). Figure 2.1-2 shows a nominal deorbit and recovery sequence utilizing a parachute and flotation system. A thorough analysis of the total mission sequence was performed for both the separate and integral launches including abort condition envelopes for any point along the launch and injection trajectory, launch pad accidents, inorbit accidents, deorbit requirements, reentry trajectory perturbations, and ground and water impact conditions, etc. The resulting major system design requirements are shown in Figure 2.1-3. It should be pointed out that the worst heating rate conditions (i.e., the -10 degree trajectory, Figure 2.1-3) comes from the worst credible abort condition. It is possible to postulate even worse abort conditions by assuming that the launch vehicle destruct system fails, that the IRV abort system fails, and that the launch vehicle pitches over and expends all its remaining fuel by continuing to thrust at the pitch-over angle. This can result in entry velocities of about 25,000 to 26,000 fps and entry angles considerably in excess of 10 degrees as is illustrated in Figure 2.1-4. The probability of such a failure sequence, however, appears to be vanishingly small and therefore it has not been used as a design criterion.

The nuclear safety criteria to be met in the IRV system are as defined in Table 1.0-III. These ground rules have been followed in developing the systems safety requirement for the IRV. The items of most concern are potential criticality hazards and dispersion of fuel form fines in the biosphere. Fuel capsule burial in deep water has been assumed to be acceptable in the event of abort or eventual IRV disposal.

Nominal mission termination is designed to impact the IRV in a preselected recovery area in deep water. There is, however, as a result of some launch aborts for the integral launch concept or deorbit by natural decay and random entry, the possibility of land impact. Even for these extremely limited cases, the probability of water impact exceeds that of land impact. Land impact, however improbable, must be considered in the design of the IRV.

It is desirable in the design of the IRV to prevent significant deformation or physical damage to the fuel capsules at impact and to provide means for adequate post impact heat rejection. Three approaches are available to achieve this end:

a. Intact Impact -- The fuel capsules are retained in a cradle in the heat source plate which, in turn, is protected at impact by an impact attenuation system. The entire assembly is designed to survive impact with neither release of the capsules nor structural damage to the capsules.

b. Fracturable Plate -- The primary difference in this design approach is that the heat source plate is designed to fracture upon impact, spilling the capsules over the local surface. This approach provides an improved situation for post-impact heat rejection since the fuel capsules are spread out and can be treated singly or in small groups. However, the capsules may be damaged as the heat source plate fractures.

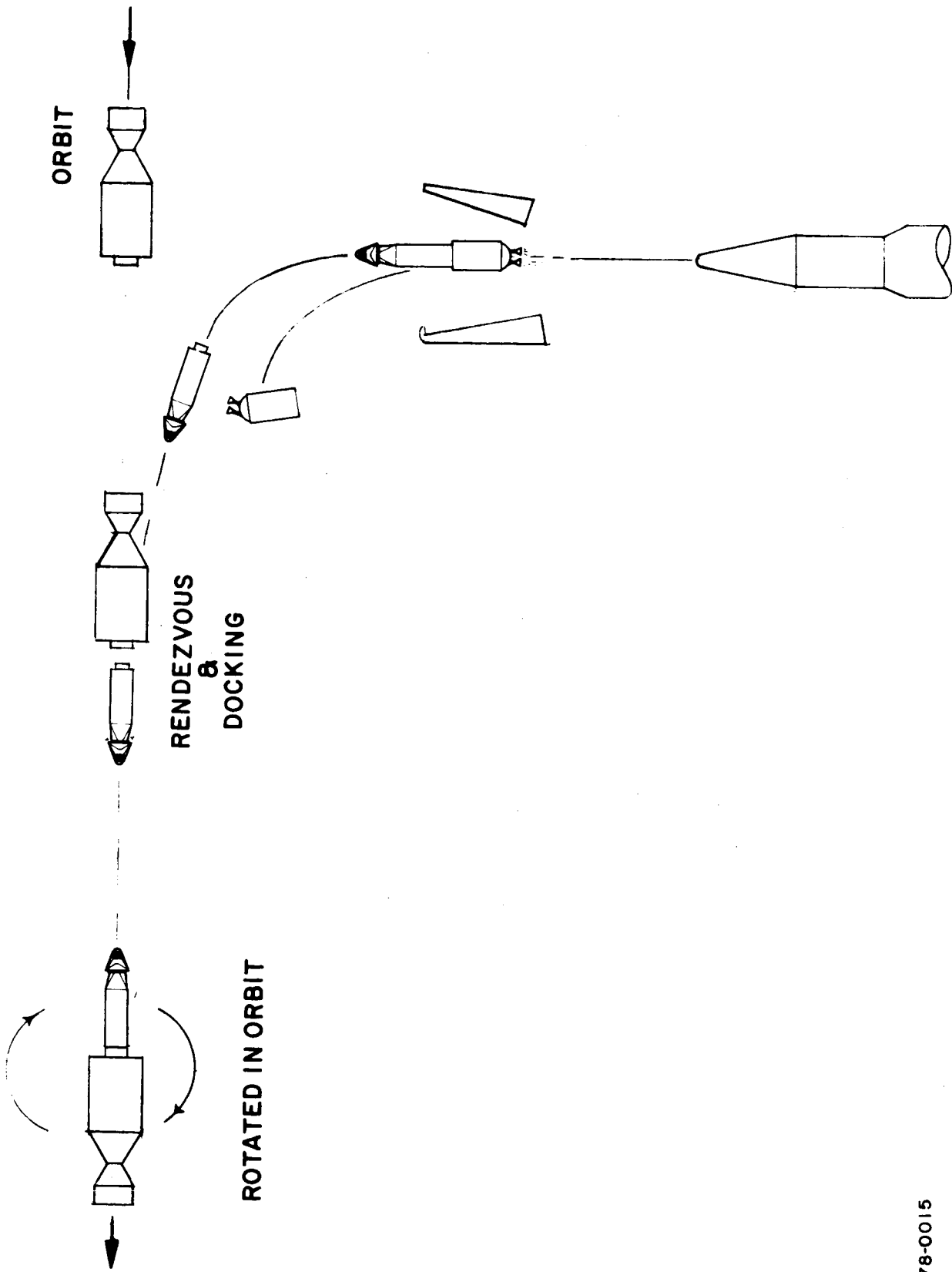
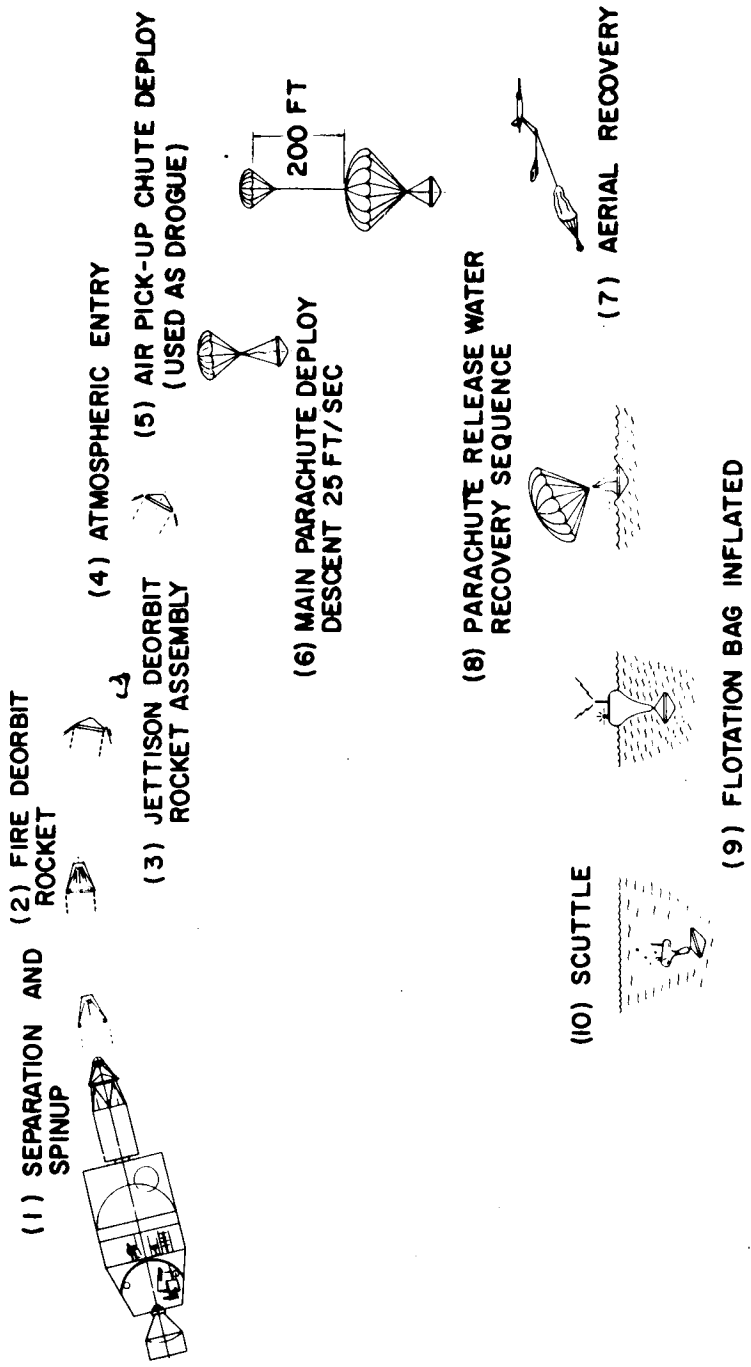


Figure 2.1.1-1 LAUNCH AND RENDEZVOUS DOCKING PROFILE

78-0015

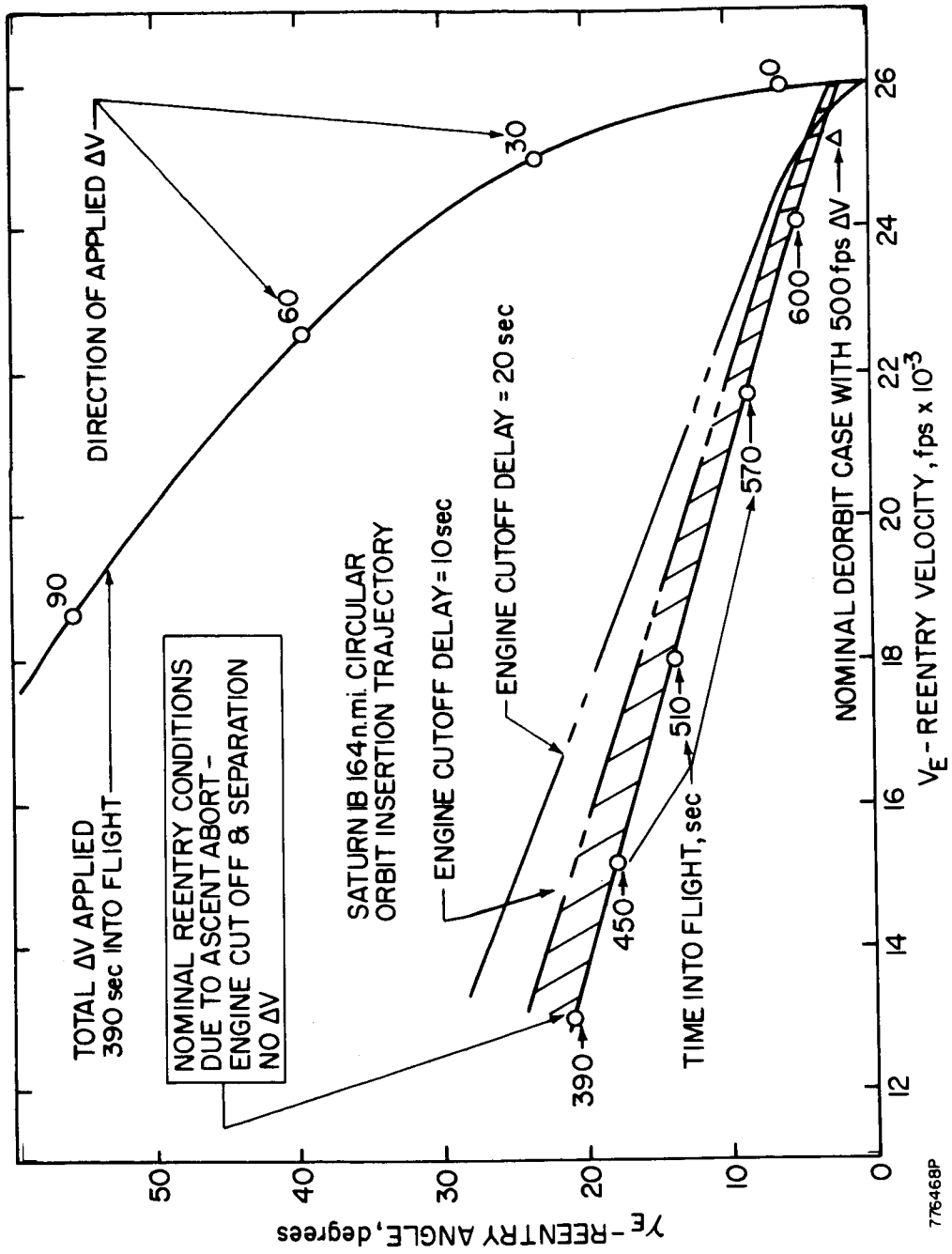


776327 F

Figure 2.1-2 DEORBIT AND RECOVERY PROFILE

AEROSHELL	ENTRY VELOCITY	26000 FPS
	ENTRY ANGLE	0 TO -10 DEG
	ENTRY BODY RATES	PITCH-YAW 5 RPM ROLL 20-40 RPM
	ANGLE OF ATTACK	70-120 DEGREES
	PEAK AXIAL LOADS	<+ 10, -31 G'S
	PEAK LATERAL LOADS	<+ 10 G'S
	PEAK INTEGRATED HEATING (2 SKIP ENTRY)	$Q = 50000 \text{ BTU/FT}^2 \text{ SEC}$ $\text{AT } \dot{q} = 210 \text{ BTU/FT}^2 \text{ SEC}$
	PEAK HEATING RATE (-10° ENTRY)	$\dot{q} = 330 \text{ BTU/FT}^2 \text{ SEC}$ $\text{AT } Q = 10,000 \text{ BTU/FT}^2$
IMPACT VELOCITY	160 - 240 FPS	
HEAT SOURCE	MAXIMUM CAPSULE TEMPERATURE (REENTRY)	2500°F
	MAXIMUM CAPSULE TEMPERATURE (NORMAL OPERATING)	2000°F
	REQUIRED IMPACT ATTENUATION	ROTATION SYSTEM WITH COLD PLATE
ABORT AND DEORBIT ROCKETS	THRUST	2800 LB
	VELOCITY DECREMENT	500 FPS
	G. G. OFFSET	<1 INCH
	SPIN RATE	20-40 RPM
	LAUNCH PAD ABORT RANGE	50-200 FT.

Figure 2.1-3 SYSTEM DESIGN REQUIREMENTS



776468P

Figure 2.1-4 SATURN IB REENTRY CONDITIONS

c. Pre-impact Capsule Dispersion -- This design approach disperses the capsules before impact and allows them to impact individually. This approach appears to overcome the problems of the previous two approaches; however, realistic mechanization of the dispersal subsystem is a major problem for the application.

Selection between these three approaches to impact protection is not clearcut; however, preliminary analysis indicates that the intact impact concept provides the most predictable design.

One conclusion that can be drawn from the IRV safety analysis is that during each mission phase, there are several orders of safety mechanisms which act to prevent the occurrence of a nuclear hazard. Table 2.1-I shows these safety mechanisms. It is important to note that there are always at least 5 orders of safety mechanisms, with 6 orders of safety mechanisms acting during the critical pre-launch, ascent, and orbital phases.

2.1.2 Major IRV Subsystem Design Alternatives

The critical IRV design areas where different approaches must be evaluated are listed below:

- a. Aerodynamic shape selection
- b. Heat source configuration
- c. Heat source heat exchanger configuration
- d. Heat source attachment and support
- e. Impact attenuation
- f. Turn-around devices
- g. Recovery aid integration
- h. Deorbit and abort rocket integration.

Various design concepts have been considered and evaluated for each of these areas. These concepts and the results for each area are summarized in the following sections.

2.1.2.1 Aerodynamic Shape Concepts

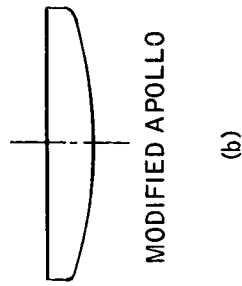
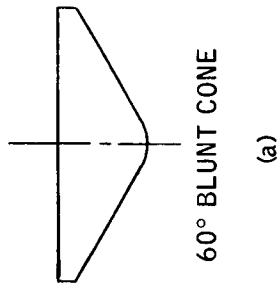
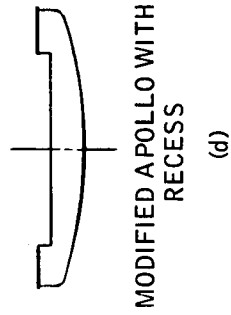
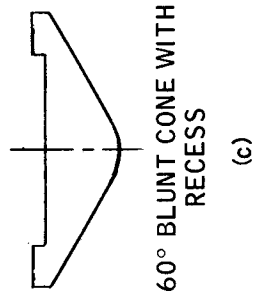
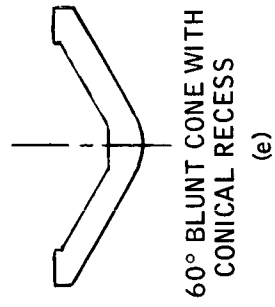
To reduce aerodynamic heating and ground impact velocities, it is desirable to achieve low vehicle ballistic coefficients ($W/C_D A$). Consequently, blunt, high-drag configurations are most desirable. Such configurations also provide generally good packaging characteristics and can be employed efficiently over the total range of achievable reentry conditions. Figure 2.1-5 presents the aerodynamic shape concepts which have been considered. Basically, they consist of two configurations, a 60-degree half-angle blunt cone (Figure 2.1-5(a)) and a modified Apollo shape (Figure 2.1-5(b)) where the normal afterbody has been replaced by a short cylindrical section. The drag and stability characteristics

TABLE 2.1-1

SAFETY MECHANISMS

	GROUND HANDLING	ON THE PAD	ASCENT	ORBITAL	REENTRY	DESCENT	IMPACT
1ST ORDER SAFETY MECHANISM	SHIPPING CONTAINER	REDUNDANT AUXILIARY COOLANT SYSTEM	HEAT SINK (BeO)	ALTERNATE HEAT REJECTION SYSTEM	AEROSHELL	DRAG AUGMENTATION	DRAG AUGMENTATION
2ND ORDER SAFETY MECHANISM	BeO	ABORT & RECOVERY SYSTEM	ABORT, REENTRY AEROSHELL & RECOVERY SYSTEM	ABORT, REENTRY AEROSHELL & RECOVERY SYSTEM	BeO	KENOSHELL	WATER IMPACT
3RD ORDER SAFETY MECHANISM	FUEL PLATE	BeO	IMPACT ATTENUATION SYSTEM	IMPACT ATTENUATION SYSTEM	FUEL PLATE	FUEL PLATE	FUEL PLATE
4TH ORDER SAFETY MECHANISM	FUEL CAPSULE	FUEL PLATE	FUEL PLATE	FUEL PLATE	FUEL CAPSULE	FUEL CAPSULE	FUEL CAPSULE
5TH ORDER SAFETY MECHANISM	FUEL FORM	FUEL CAPSULE	FUEL CAPSULES	FUEL CAPSULES	FUEL FORM	FUEL FORM	FUEL FORM
6TH ORDER SAFETY MECHANISM		FUEL FORM	FUEL FORM	FUEL FORM			

78-0003



776459P

Figure 2.1-5 AERODYNAMIC SHAPE CONCEPTS

of both configurations are quite similar. The modified Apollo shape appeared to possess superior packaging characteristics for planar heat source configurations and was included for that reason. The configuration of primary interest was the blunt cone. To reduce the heating to the heat source capsules (located in the rear of the vehicle), recessing of the heat source into the vehicle was examined and the resultant configurations are shown in Figure 2.1-5(c) and (d). In addition, in the case of conical heat source configurations, the heat source can be recessed into the conical cavity of the blunt cone as shown in Figure 2.1-5(e). Investigation has shown that when impact attenuation (requiring crushup stroke), heat source recession and recovery aid integration are considered, the Apollo configuration is inferior in packaging (i.e., requires larger vehicle diameters). Consequently, the blunt cone has been recommended as the reference aerodynamic configuration for the IRV.

2.1.2.2 Heat Source Configurations

The heat source configuration can have a major influence on vehicle diameter and weight, as well as seriously influencing vehicle stability (through the center of gravity location and inertias and the capsule heating environment). Furthermore, different heat source configurations will react differently to the g-loading associated with ground impact. Several generically different capsule array configurations have been examined in order to evaluate their advantages and disadvantages.

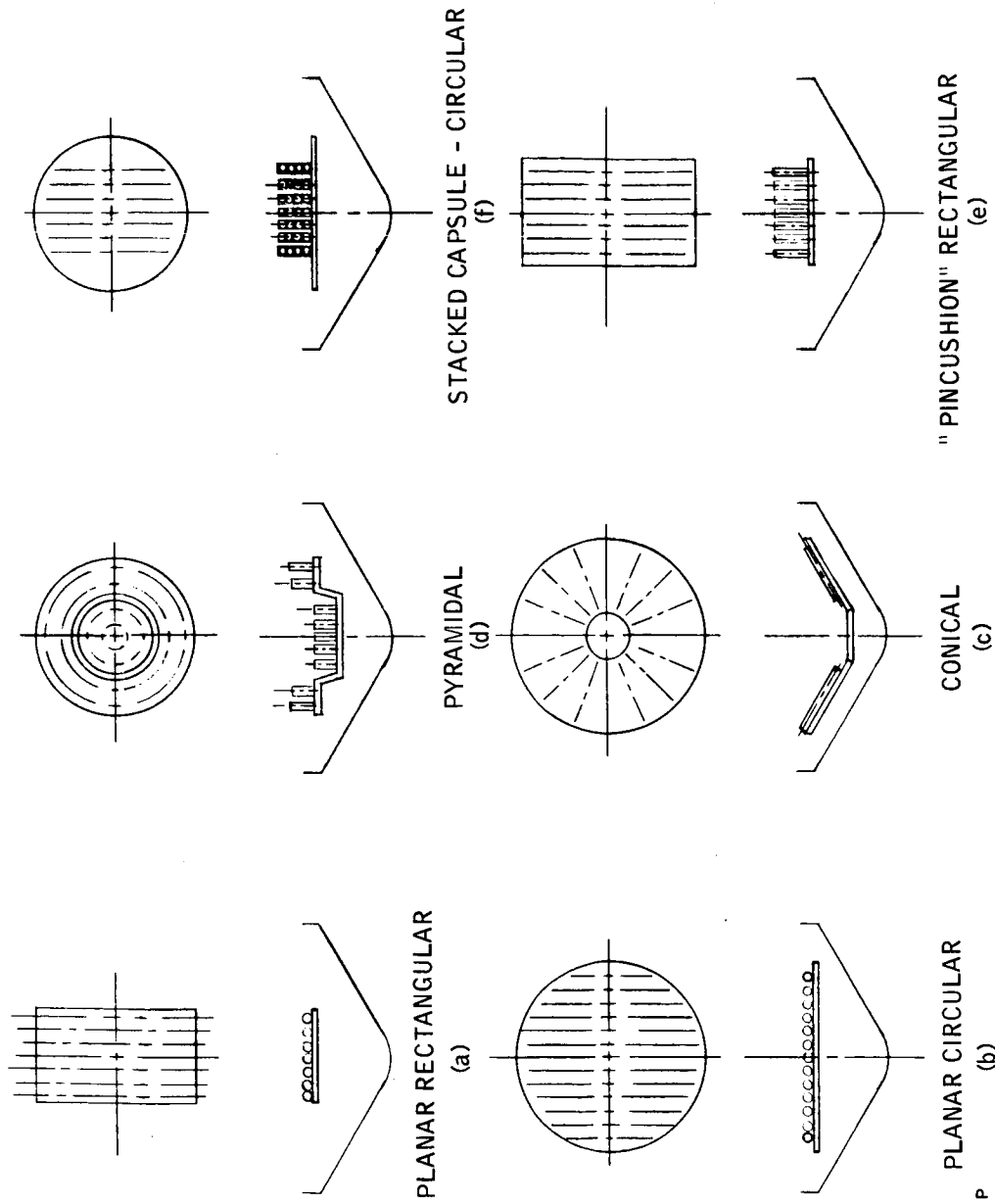
The simplest configuration is the planar array (Figure 2.1-6(a) and (b)). In the two concepts the circular array results in the smallest diameter heat source, while the rectangular array facilitates incorporations of recovery and location aids within a circular vehicle configuration.

The conical and pyramidal configurations (Figure 2.1-6(c) and (d)) represent an attempt to take full advantage of the aeroshell conical shape thereby improving the center of gravity location.

The "pin cushion" and stacked capsules arrays (Figure 2.1-6(e) and (f)) represent an attempt to arrive at the smallest possible heat source diameter so as to aid in minimizing total vehicle diameter.

Capsule retention schemes can be used which support the capsules uniformly (i.e., in a "cradle") thereby improving the impact resistance of the heat source. (A review of the heat source failure modes during ground impact has indicated that maintaining heat source plate integrity after impact is a desirable goal.) For 164 capsules the minimum circular heat source diameter appears to be about 49 inches (based on allowable maximum capsule temperature). Recessing the array provides heat protection during reentry and, if necessary, a cover plate can be used to provide additional heating protection as well as additional impact retention protection. The disadvantage of the planar array lies in the fact that all capsules are relatively far aft in the vehicle so that favorable center of gravity locations are hard to achieve.

The conical and pyramidal arrays provide better center of gravity location, and the conical array results in advantageous capsule recession and somewhat better vehicle aerodynamic turn-around capability. However, the array requires significantly larger heat source diameters (and consequently larger heat source weights),



776471P

Figure 2.1-6 HEAT SOURCE CONFIGURATIONS

and the impact loadings at oblique angles can cause heat source breakup more readily than for the planar array. Capsule retention schemes for the pyramidal array are more complicated; auxiliary cooling on the launch pad is more difficult, and aerodynamic heating on the capsules which protrude beyond the vehicle base is greater.

The pincushion array is quite similar to the pyramidal array and suffers from the same limitations. The stacked capsule array with rows of capsules stacked on top of each other in principle provides the smallest heat source diameter (of about 40 inches) but creates considerable difficulty in launch pad cooling, heat exchanger design, capsule reentry temperatures and capsule retention and impact performance. It is also very difficult to achieve reasonable center of gravity locations in a minimum diameter vehicle since so many of the capsules are located at the extreme aft end of the vehicle.

The planar configuration appears most attractive when all factors are considered.

2.1.2.3 Heat Source Heat Exchanger Configurations

To accommodate the different heat source configurations a number of HSHX configurations have been considered. Both tube fin and plate fin heat exchangers have been evaluated in both single and two-pass configurations.

The various HSHX concepts are shown in Figure 2.1-7. The tube fin devices appear easier to fabricate and are lighter than the plate fin devices. The use of a two-pass flow system minimizes the temperature gradients across the heat source and thereby result in lower maximum capsule operating temperatures. Consequently, it appears that two-pass, tube fin HSHX configurations are most attractive.

2.1.2.4 Heat Source Support and Attachment Concepts

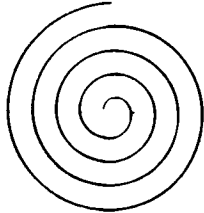
The heat source plate must be attached to the aeroshell and supported to withstand the launch and reentry loads. In addition, heat leaks from the heat source through the attachments and supports should be minimized and the loading distribution acting on the heat source during ground impact should be as uniform as possible.

The various support and attachment concepts which have been examined are shown in Figure 2.1-8. Four basic schemes have been evaluated. One is peripheral attachment of the heat source to the aeroshell at a few distinct points with bending of the heat source plate constrained by crushup material located beneath the HS plate (Figure 2.1-8(a)). It is also possible to attach the plate at several points directly to the crushup material without peripheral attachments (Figure 2.1-8(c)), or the plate can be attached peripherally to a ring structure without requiring the support by crushup material (Figure 2.1-8(d)). All of these attachment schemes result in fairly high heat leak values. Thermally, the most attractive support scheme is a refractory metal truss support which penetrates the superinsulation to attach to the heat source plate.

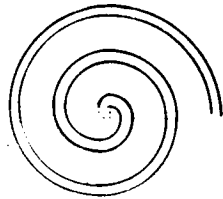
2.1.2.5 Impact Attenuation Concepts

As a design goal it is desirable for the isotope fuel capsules to remain intact at all times. To meet this design goal, care must be taken to assure that if the IRV impacts on land the resulting g-loads do not rupture the capsules. The

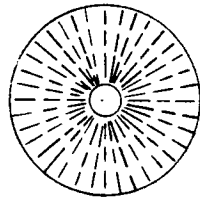
CIRCULAR PLANAR



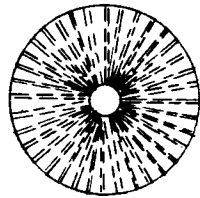
SINGLE PASS - SPIRAL TUBE FIN



TWO PASS - SPIRAL TUBE FIN

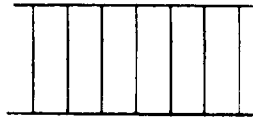


SINGLE PASS - RADIAL PLATE FIN

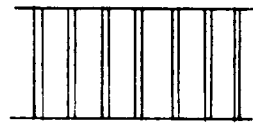


TWO PASS - RADIAL PLATE FIN

RECTANGULAR PLANAR



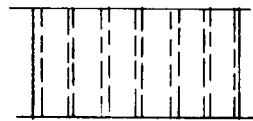
SINGLE PASS - TUBE FIN



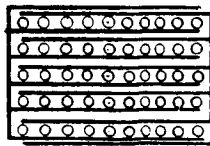
TWO PASS - TUBE FIN



SINGLE PASS - PLATE FIN



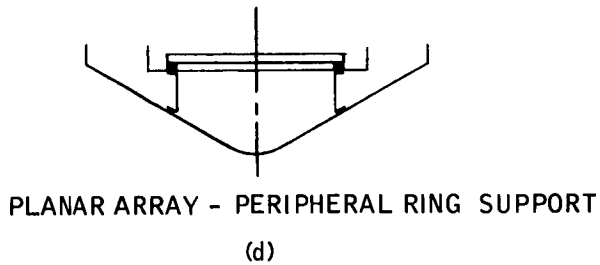
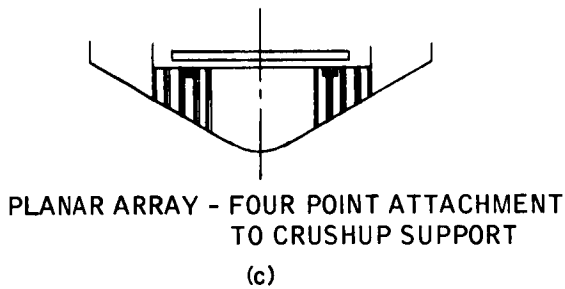
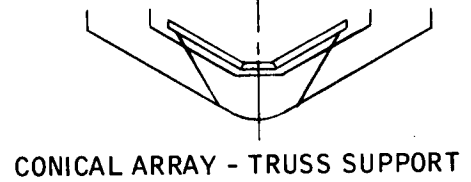
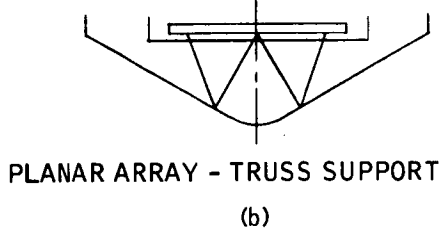
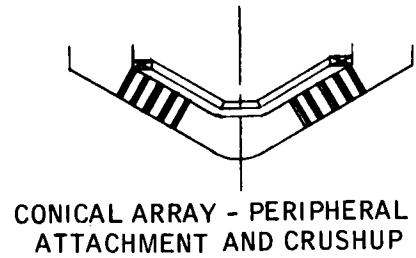
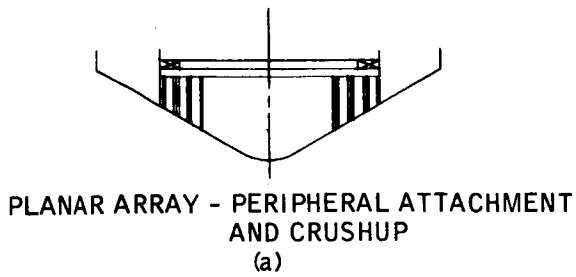
TWO PASS - PLATE FIN



PINCUSHION - TWO PASS TUBE FIN

776473P

Figure 2.1-7 HSHX CONFIGURATION



776460P

Figure 2.1-8 SUPPORT AND ATTACHMENT CONCEPTS

impact loading tolerance of the capsules depends strongly on how the loading is applied. It is expected that for a uniform distribution of loads (i.e., in a "cradle") the capsules could survive g-loads as high as 100,000 to 200,000 g's. Therefore, one of the design goals is to furnish a capsule retention scheme which supports the capsules very well during impact. Cradle type retention schemes are therefore most desirable. The actual impact g-loading is of course dependent on a complex interaction between the IRV terminal velocity, the terrain, the efficacy of the retention scheme for different impact geometries and the amount and rate of impact energy absorption by the IRV. Crushup materials can be designed to be useful in attenuating the impact loading. However, further analysis (and probably testing) will be required to specify an optimum impact attenuation concept.

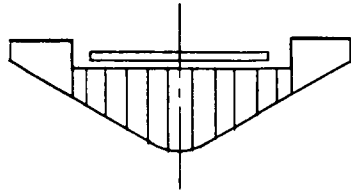
Figure 2.1-9 illustrates various impact attenuation concepts. The simplest concept is to fill the aeroshell with isotropic crushup material (Figure 2.1-9(a)). For non-zero angles of impact (i.e., away from vertical impact) anisotropic crushup material and the variation in crushup stroke can combine to greatly decrease impact attenuation material utility. Even for vertical impact the loads are not distributed uniformly over the heat source plate because the most forward portion of the crushup transmits high loads to the center of the plate before the material outboard of the nose region begins to crush.

The situation can be somewhat alleviated by using different crushup materials for different portions of the vehicle and by orienting the crushup material so that it performs better at non-zero impact angles. This is illustrated in Figure 2.1-9(b). However, to prevent destruction of the heat source plate and the capsule retention mechanism, it is necessary to use long crushup strokes to reduce the g-loadings, and this necessitates large vehicle diameters. Furthermore, the large amount of crushup material needed imposes a severe vehicle weight penalty. Consequently, an effort has been made to find an impact attenuation scheme which results in less severe vehicle design penalties. Figure 2.1-9 (c) illustrates such a potentially attractive method. It consists of a ring of crushup material which supports a strengthened heat source plate. At impact angles of up to ± 30 degrees this crushup ring causes the plate to rotate so that it impacts flat on the ground and absorbs the impact energy by plastic deformation. This impact geometry is most favorable for the distribution of loading on the capsules in their cradle retention. The heat source plate must be designed with sufficient strength so as not to fail due to the loads acting on it while it is rotating. This appears to be the lightest attenuation system and requires only modest crushup stroke lengths of several inches.

2.1.2.6 High Altitude Turn-around Devices

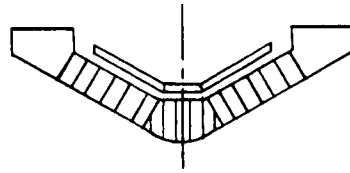
If the vehicle starts to reenter in a backward attitude, it is desirable to cause it to right itself at high altitudes so as to minimize the aerodynamic heating to the fuel capsules.

A variety of different approaches can be used to assure that the vehicle will be unstable in rearward attitudes. Most of these are illustrated in Figure 2.1-10. The center of gravity offset is conceptually the simplest and most reliable method, but it greatly complicates the vehicle design and the deorbit system and results in trim angles of attack after turn-around. A large afterbody can be used to effect turn-around but it interferes seriously with the HSHX and heat source design

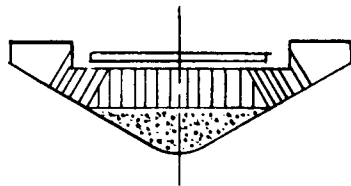


PLANAR ARRAY - NON-ORIENTATED
AND NON-LOAD DISTRIBUTING

(a)

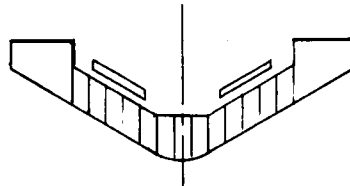


CONICAL ARRAY - ORIENTATED
AND NON-LOAD DISTRIBUTING

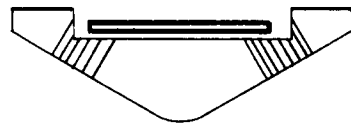


PLANAR ARRAY - ORIENTED
PLUS LOAD DISTRIBUTING

(b)

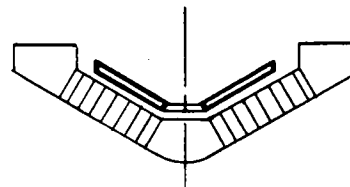


CONICAL ARRAY - NON-ORIENTATED
AND NON LOAD DISTRIBUTING



PLANAR ARRAY - ORIENTED CRUSHUP
RING PLUS "BEEFED UP" PLATE

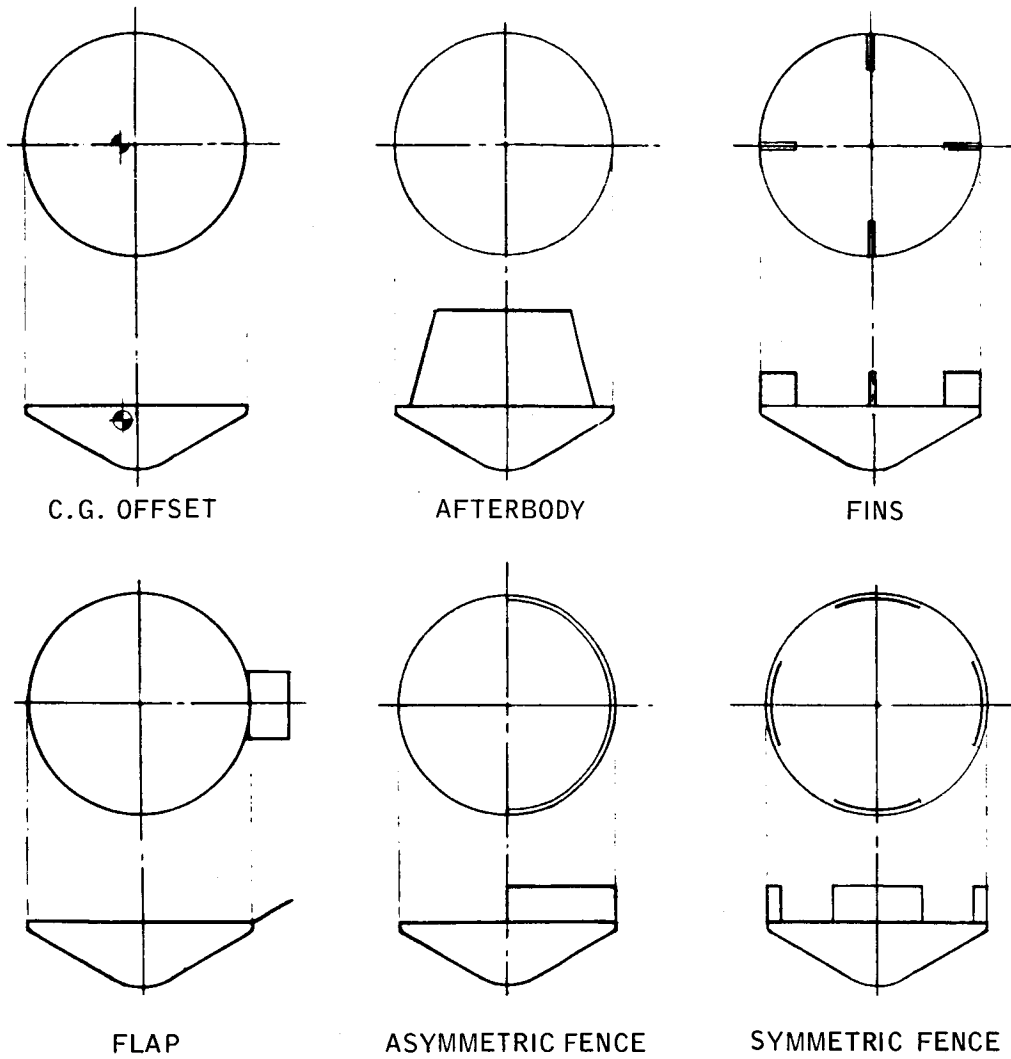
(c)



CONICAL ARRAY - ORIENTATED
PLUS "BEEFED UP" PLATE

776472P

Figure 2.1-9 IMPACT ATTENUATION CONCEPTS



78-0017

Figure 2.1-10 TURNAROUND CONCEPTS

and greatly degrades the transonic and subsonic vehicle stability. Fins can be used but rather large fin sizes are required for high-altitude turn-around. Flaps are effective devices, but generally must be actively deployed and also result in non-zero flight trim angles. Fences appear to be the most promising devices. An aerodynamic test program is being conducted by the Ames Research Center to assist in selection of a fence configuration.

2.1.2.7 Recovery Aid and Deorbit and Abort System Integration Concepts

The incorporation of decelerators (e.g. parachutes, ballutes) and location aids (beacons, etc.) has been considered as an aid in the recovery of the IRV. These devices can be packaged either around the periphery of the IRV or they can be located in the center if a cavity is provided in the heat source. The top part of Figure 2.1-11 illustrates this schematically. The peripheral location is preferable since it eases the thermal insulation problems and imposes fewer constraints on the heat source configuration design.

Several different options are also available for the integration of the abort and deorbit rocket system as illustrated in the lower portion of Figure 2.1-11. Several rockets can be located peripherally or a single rocket can be located in the center of the rear of the vehicle. The peripheral arrangement has the disadvantage that if one of the rockets fails large tumble rates are produced, while the single central rocket is very difficult to integrate within the heat source, interferes with the HSHX integration, and poses a difficult thermal insulation problem. The major advantage of the central mounting is that the potentially catastrophic failure mode of the peripherally mounted deorbit rockets is eliminated. However, as shown in Figure 2.1-11 there are other ways of achieving this goal by mounting the rockets on short tower systems which are attached to the IRV.

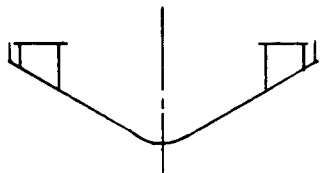
2.1.3 IRV Conceptual Design Synthesis and Evaluation

In addition to the various design alternatives associated with the IRV subsystems, several overall vehicle performance requirements were considered in the synthesis of the different conceptual designs. The most critical requirements influencing the overall IRV design were:

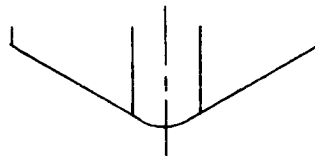
- a. Heat source reentry heating protection
- b. Vehicle aerodynamic stability
- c. Ground impact attenuation
- d. Incorporation of recovery and location aids.

These factors are interrelated and often impose conflicting requirements on the vehicle design thereby necessitating trade-off studies to select the best design.

An analysis of the interaction between the various performance requirements indicated that accommodation of all in a single design resulted in a substantial increase in vehicle size and weight. To better understand the trade-offs, the approach was to evolve four basic IRV configurations which are "bare" (i.e., do

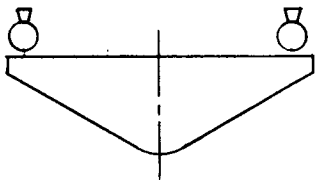


PERIPHERAL LOCATION

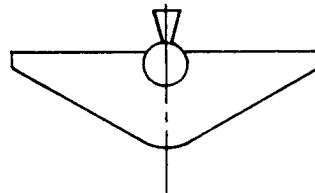


CENTRAL LOCATION

**DEORBIT AND ABORT ROCKET
INTEGRATION CONCEPTS**

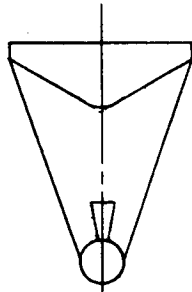


FOUR ROCKET PERIPHERAL
LOCATION



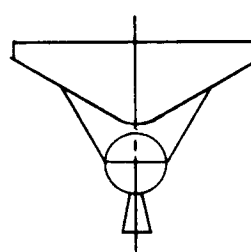
SINGLE ROCKET
CENTRAL INTERNAL
LOCATION

CONCEPT 3



SINGLE ROCKET
TOWER SYSTEM

CONCEPT 4



SINGLE ROCKET
HEAT SHIELD MOUNTING

77-6470P

Figure 2.1-11 RECOVERY AIDS AND ABORT AND DEORBIT ROCKET INTEGRATION CONCEPTS

not contain recovery aids or impact attenuation) and then to examine the effect on the vehicle design of adding impact attenuation and recovery aids.

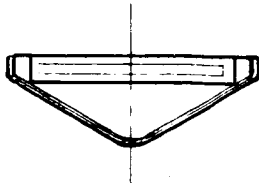
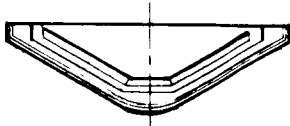
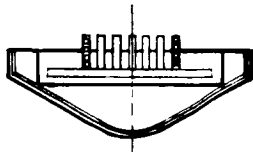

Figure 2.1-12 shows the four basic "bare" IRV vehicle concepts corresponding to the three different heat source configurations housed within the blunt cone aeroshell plus the planar heat source housed in the modified Apollo aeroshell configuration. The corresponding vehicle diameters and weights are also indicated on the figure. It should also be pointed out that the planar heat source vehicle design is derived for a heat source plate recession of one capsule diameter. This means that the top of the isotope capsules are flush with the rear plane of the vehicle.

Figure 2.1-13 shows what the effects are on vehicle diameter and weight for additional recessing, crushup provisions, and the incorporation of recovery aids. The extreme left hand column indicates the generic heat source configurations used. The next column lists the dimensions and configuration of the heat sources. The third column shows the diameters and weights for the "bare" vehicles and corresponds to Figure 2.1-12. The fourth column indicates the effects of recessing the heat source plate three-capsule diameters below the base. The fifth column shows the effect of adding crushup while maintaining a recess of only one capsule diameter. The sixth column shows the effect of incorporating only recovery aids (parachutes) along the periphery of the vehicle without adding impact attenuation and still keeping the recess at one capsule diameter. The seventh column is the same as the sixth but with a three-capsule diameter recess. The eighth column shows the combination of a three-capsule diameter recess, crushup, and recovery aids. The last column shows the effect of locating the rocket and the recovery aids in a central cavity within the IRV.

2.1.4 Conclusion--Phase IA

The major conclusions reached were:

- a. The blunt cone aeroshell configuration is preferable to the modified Apollo configuration.
- b. A graphite encapsulated "pin cushion" heat source offers potential for lowest vehicle diameter and weight. Further analysis is required to evaluate this. This design is quite complicated and should be considered further only if the analysis indicates substantial diameter and weight savings.
- c. The recommended HSHX concept is a two-pass, tube fin heat exchanger design.
- d. The truss support for the heat source minimizes heat leakage and appears to be the best concept for the heat source attachment to the aeroshell.
- e. Impact attenuation imposes large vehicle size and weight penalties.
- f. Parachute recovery aid inclusion imposes significant vehicle penalties.
- g. Pending further study the tower concept for abort and deorbit rocket integration is most attractive.

1	CIRCULAR PLANAR		DIA 64.00	WT 1500
2	CONICAL		DIA: 77.00	WT 1660
3	CIRCULAR PLANAR PIN CUSHION		DIA: 62.00	WT: 1320
4	APOLLO CIRCULAR PLANAR		DIA: 66.30	WT 1500

78-0054

Figure 2.1-12 IRV CANDIDATE CONFIGURATION SUMMARY

CONFIGURATION	VEHICLE	FLUSH		RECESSED (3 CAPSULE DIAMETER)		CRUSH-UP		FLUSH RECOVERY AIDS		RECESSED RECOVERY AIDS		RECESSED CRUSH-UP RECOVERY AIDS		CRUSH-UP RECOVERY AIDS			
		DIA.	WT.	DIA.	WT.	DIA.	WT.	DIA.	WT.	DIA.	WT.	DIA.	WT.	DIA.	WT.		
	CIRCULAR 47" DIA.	64"	1500	73"	1530	89"	1900	98"	1950	84"	1690	84"	1690	98"	2080	113"	3210
		89"	1690	92"	1710	107"	2080	116"	2140	89"	1800	92"	1830	116"	2290	-----	-----
	CONICAL 57" DIA.	77"	1660	77"	1660	91"	2030	101"	2040	94"	1860	94"	1860	101"	2190	103"	3160
		62"	1320	-----	-----	-----	-----	-----	-----	85"	1520	-----	-----	-----	-----	-----	-----
	39" DIA. 4" PROTRUSION 20% CYL. 32x56 RECT. 4" PROTRUSION 20% CYL.	81"	1435	-----	-----	-----	-----	-----	-----	81"	1535	-----	-----	-----	-----	-----	-----
		66"	1500	80"	1550	102"	1950	119"	2040	92"	1710	92"	1710	119"	2180	-----	-----
	CIRCULAR 47" DIA. APOLLO	66"	1500	80"	1550	102"	1950	119"	2040	92"	1710	92"	1710	119"	2180	-----	-----
		-----	-----	-----	-----	-----	-----	-----	-----	-----	-----	-----	-----	-----	-----	-----	-----

78-0018

Figure 2.1-13 SUMMARY OF WEIGHT DIAMETER CHARACTERISTICS

The following recommendations were made on the basis of the Phase IA Study:

- a. The vehicle concepts to be studied further include a circular planar heat source array, a conical array, and a "pin cushion" array. The aeroshell configuration is a blunt cone.
- b. Both circular and rectangular tube fin HSHX should be evaluated.
- c. Evaluate potential gains in system performance which can be achieved if the ground rule for full power output from the secondary HSHX with primary HSHX in place is modified to allow reduced power operation.
- d. Evaluate cover plates for heat source capsule retention and reentry heat protection.
- e. Determine minimum impact attenuation system for the various vehicle concepts.
- f. Evaluate both low-density and graphitic ablative aeroshell heat shields.

2.2 Summary--Phase IB

The Phase IB conceptual design ground rules are:

- Establish design characteristics of 3 IRV concepts (all 60-degree blunt cones)
 - - a minimum diameter circular planar HS array (nonvented capsules)
 - - a minimum diameter circular planar HS array (vented capsules)
 - - a minimum diameter pin cushion array (nonvented capsules)
- Use truss support structure only
- Impact attenuation system should be based on the use of peripheral crush-up to insure heat source "flat" impact
- Ballutes are to be considered for drag augmentation
- Retro and abort rocket systems should be mounted on a tower in the A/C booster and on a minimum extension in the integral launch vehicle
- Heat source and HSHX designs are to be based on maintaining a 1600°F turbine inlet temperature with the primary HSHX operating
- HSHX designs shall be developed to meet in place redundancy and separate replaceability criteria

The only significant change from the approach recommended at the conclusion of Phase IA is the substitution of a circular planar vented capsule design in place of the conical array as the third reference concept. This revision in approach, by direction of NASA-LeRC, was occasioned by the desire to provide a preliminary

evaluation of the impact of vented fuel capsule HS arrays on the basic IRV concepts as part of the Phase IB task.

The approach followed in the development of the IRV conceptual designs is outlined in Section 3.0. Figure 3-1 illustrates in flow diagram form the overall study logic. The format of the Phase IB Topical Report follows the flow of logic shown in Figure 3-1 to the extent practicable.

This subsection summarizes the results of the Phase IB technical effort, the significant differences between the three designs, and the study conclusions and recommendations to date. The technical effort summary treats the three major study areas, i.e., the HS, the HSHX and the IRV system, including S/C and launch vehicle integration.

2.2.1 Heat Source (HS)

Study areas treated in Phase IB are listed in Table 2.2-I. The prime objective in Phase IB was to perform a comparative study of the three reference HS configurations to select a candidate design for the Phase II Preliminary Design Study. Prime emphasis was therefore placed on the development of feasible retention systems for both the nonvented and vented fuel capsules designs; the development of minimum diameter heat sources for both the circular planar and the pin cushion or stacked log class arrays; better characterization of the thermal performance of all three types of heat sources in all required operating (or survival) modes; better definition of aeroshell/HS interface constraints; and development of ACHX and BeO location and sizing details.

Mechanical and thermal performance characteristics developed are summarized in Table 2.2-II. From a weight consideration, the circular planar design with vented capsules offers a substantial advantage over the other two designs. The larger weight for the pin cushion design is primarily due to the increased weight requirement of the BeO heat sink (220 pounds versus 140 pounds for the circular planar design). On the other hand, the pin cushion design offers the smallest heat source diameter. Reduction in diameter for the circular planar design with vented capsules compared to the nonvented capsule heat source design is not as much as the reduction in capsule size may indicate (1.40 inch diameter x 5.6 inch long compared to 1.542 inch diameter x 5.968 inch long for nonvented capsule). This is primarily due to the fact that the required 164 capsules, arranged with 8 capsules in a row at the center, determine the heat source diameter. It should also be noted that the radiation heat transfer area facing the HSHX cannot be reduced much without a penalty in the peak capsule temperature. A radiation heat transfer area of approximately 11.5 ft² appears to be the minimum permissible.

The peak capsule temperature of the pin cushion design is not affected by the mode of HSHX operation, either primary or secondary heat exchanger. A relatively low temperature of 1790°F is achieved compared to the other two circular designs. It is estimated that with the circular planar designs the peak capsule temperature is 200°F higher with the secondary HSHX operating if 1600°F turbine inlet temperature was required for this operating mode.

The development of an attachment and support scheme for the pin cushion HS that met thermal and spacing constraints as set by the HSHX and fuel capsule operation temperature limits, while allowing incorporation of required ACHX channels and

TABLE 2.2-1

PHASE I-B STUDY AREAS

Circular Planar		Pin Cushion
Nonvented Capsule	Vented Capsule	Nonvented Capsule
Fuel Capsule Retention System	Retention	Graphite Versus Refractory Metal
HSHX Thermal Interface Constraints	Capsule Spacing	Log Versus Vertical Configuration
Heat Source Attachment	HSHX Thermal Interface	Temperatures in Deployed Condition
Crushup Distance		Mechanical Details
Truss Thermal Optimization		BeO Location
		HSHX Thermal Interface

TABLE 2.2-II

HEAT SOURCE SUMMARY COMPARISON

	CONFIGURATION		
	PLANAR	PLANAR VENTED	PIN CUSHION
WEIGHT	1288 LB	983 LB	1365 LB
HEAT SOURCE DIAMETER	49.0 IN	46.0 IN	39.0 IN
NUMBER OF CAPSULES	164	164	165
CENTER-OF-GRAVITY FROM NOSE	27.8 IN	27.5 IN	26.8 IN
PEAK CAPSULE TEMP. GRADIENT	120°F	155°F	70°F
HEAT SOURCE RADIATION AREA	13.1 FT ²	11.5 FT ²	17.5 FT ²
PEAK CAPSULE TEMP.			
A. PRIMARY HSHX OPERATING	1870°F	1925°F	1790°F
B. SECONDARY HSHX OPERATING (1600° F Turbine Inlet)	2060°F	2115°F	1790°F

BeO heat sink material was a complex design problem. Figure 2.2-1 shows a detail of the pin cushion attachment system. It should be noted that while this system does meet basic operational requirements, its utility in limiting fuel capsule damage during terminal impact situations is not as good as the cradle retention system developed for the circular planar arrays (Figure 2.2-2 shows the cradle retention system with a vented capsule). This is the only basic deficiency in any of the three heat source designs considered during Phase IB.

It has been concluded that the circular planar design with nonvented capsules is a preferred design for the preliminary IRV design effort during Task II. The circular planar heat source is lighter and much simpler to design and fabricate. Its mechanical performance is also more predictable and better understood for ground impact condition.

Feasibility of using vented capsules in a circular planar heat source without any unsurmountable difficulty has been shown. Although the vented capsule development is still in the early state compared to the nonvented capsules, it offers an attractive potential in weight reduction and some size reduction.

2.2.2 Heat Source Heat Exchanger (HSHX)

As noted previously, three heat sources were identified that would receive detailed analysis during the Phase IB study. These three heat sources are listed in Table 2.2-III.

TABLE 2.2-III

PHASE I-B HEAT-SOURCE GEOMETRIES

Source	Dimensions
Circular Planar	49-inch diameter
Pin cushion	39-inch diameter
Circular planar (vented capsules)	46-inch diameter

From the Phase IA studies, the most attractive approach in the HSHX's design was found to be the tube-fin, two-pass type of heat exchanger. As a result, this was the only approach considered in Phase IB of the study for each of the three heat sources listed above. While previous studies indicated that the tube-fin heat exchanger offered the lowest weight design, elimination of the fins between the tubes and utilization of an all-tubular heat exchanger would make fabrication easier. All-tubular heat exchangers were therefore employed, where possible, throughout the Phase IB studies.

Circular Planar

For this heat-source geometry, two HSHX designs were developed. The first was a two-pass, tubular, circular involute heat exchanger, and the second was a two-pass, tubular, rectangular heat exchanger.

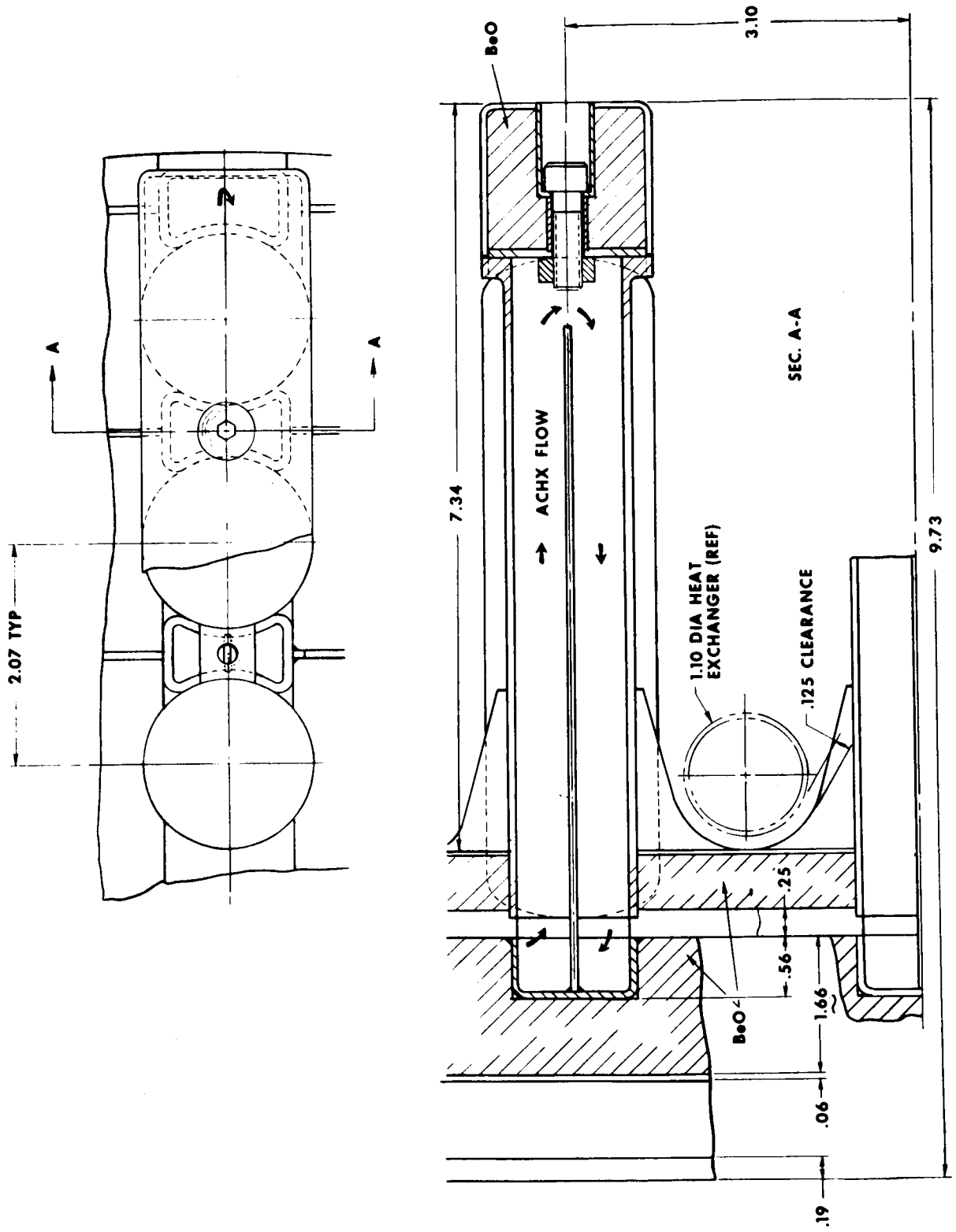


Figure 2.2-1 MECHANICAL DETAILS OF PIN CUSHION ARRAY

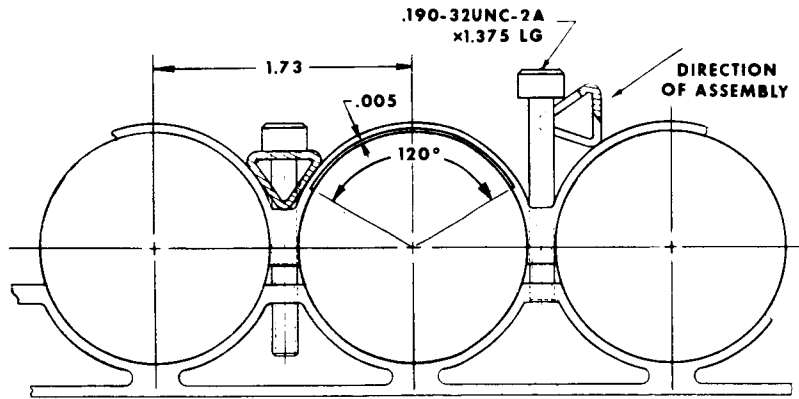
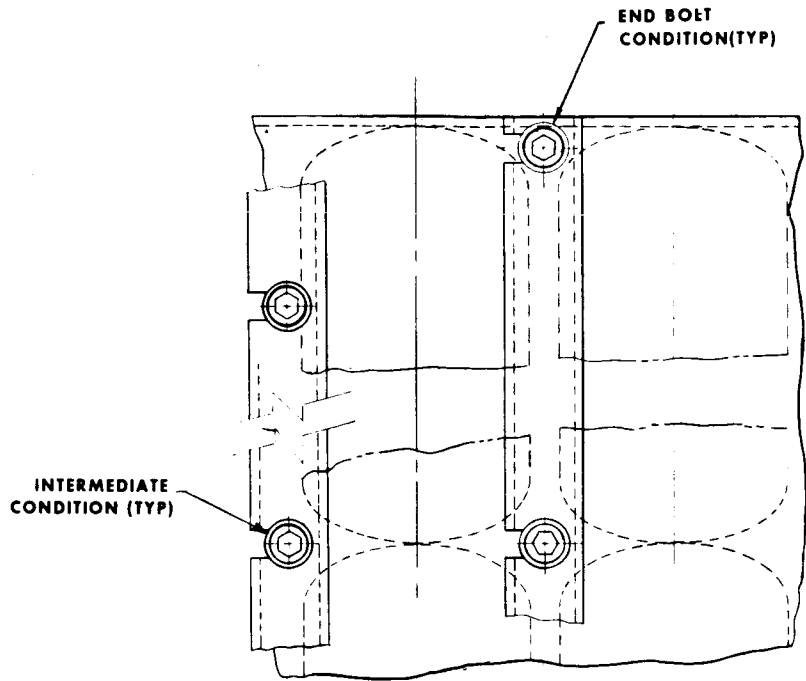


Figure 2.2-2 VENTED CAPSULE RETENTION, 46-INCH DIAMETER PLANAR ARRAY

The core of the circular involute HSHX consists of 18 1.34-inch-diameter tubes, each 72 inches long. This array of tubes completely fills the projected area opposite the heat source with the exception of a small central reversing plenum. The flow is distributed to nine inlet tubes by a large, circular manifold. The gas flows through the nine tubes in an involute path across the heat source to the central plenum where the flow is reversed and distributed to a second set of nine tubes; these nine tubes duct the flow on a second pass across the heat source to the periphery where it enters a large circular exit manifold. Thus the core is composed of a circular planar array of two sets of involute tubes with the flow in adjacent tubes alternately in and out. The two sets of tubes are welded together at their tangent point with a large weld bead to enhance conduction between the adjacent hot and cold tubes. The heat exchanger is Cb-1% Zr throughout; and minimum gage material, 30 mils in thickness, is used for the tubes and inlet manifold while 42-mil material is required for the outlet manifold.

The rectangular HSHX that is designed for the 49-inch-diameter heat source consists of a planar array of 48 1.0-inch-diameter tubes. The tubes are welded together and connected on one end to a common reversing manifold and on the other to large inlet and exit manifolds. Twenty-four tubes duct the flow from the inlet manifold across the source to the reversing manifold, and 24 tubes provide the return pass and terminate at the exit manifold. As before, adjacent tubes contain alternately hot and cold gas. The inlet and outlet manifolds are slightly curved to more closely conform to the shape of the heat source. In this heat exchanger configuration, the flow to each set of tubes is distributed in proportion to the power radiated to the individual tubes. This provides a uniform gas exit temperature from all tubes. Proper flow distribution is accomplished by providing an orifice for each individual tube. The primary purpose in designing a rectangular HSHX for a circular heat source was to locate the large inlet and exit manifolds at one end of the heat exchanger rather than have them completely surround the heat exchanger as they do in the involute design. This approach suggested itself when consideration was given to a heat dump system which involved removal of a portion of the superinsulation from around the heat exchanger-heat source cavity as shown in Figure 2.2-3.

Locating the large manifolds as shown permits radiation from the heat source as well as secondary radiation from the HSHX surfaces directly to space. While this type of heat dump system can be applied to the circular involute design, it requires a larger cavity than the rectangular heat exchanger because of the blockage introduced by the large circular manifolds surrounding the heat exchangers.

The heat dump system shown in Figure 2.2-3 obviates the necessity of rotating the heat-source assembly to reject heat in the event of failure, or prior to startup, of the Brayton-cycle systems. In some installations, it may be more convenient to remove the lightweight insulation panels than to rotate the complete IRV system. Alternatively, both heat dump approaches can be incorporated to provide an additional measure of safety.

Pin Cushion

The pin cushion heat source consists of 13 parallel rows of fuel capsules with the rows (which contain varying numbers of capsules) axially mounted on

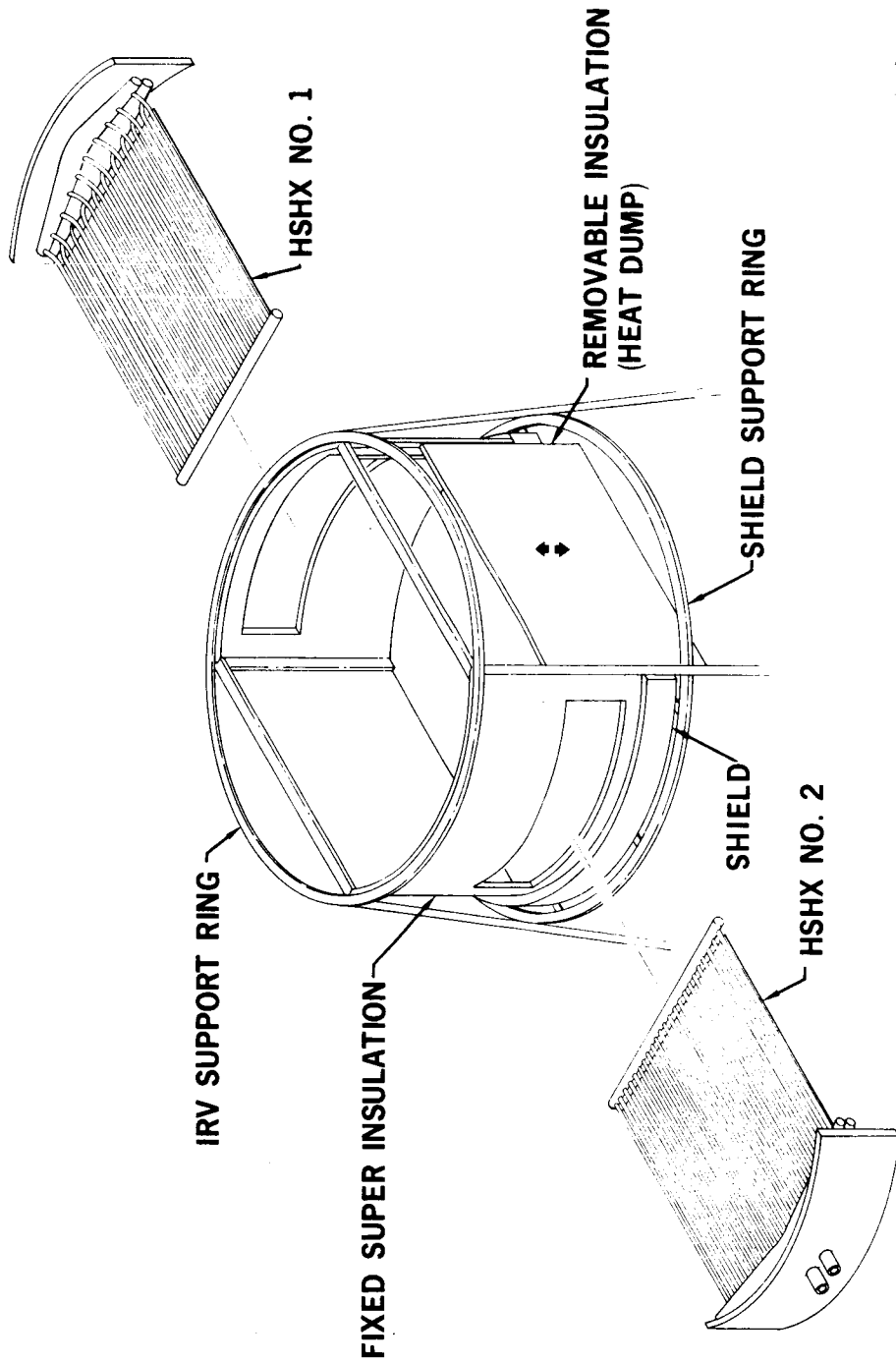


Figure 2.2-3 RECTANGULAR HEAT-SOURCE HEAT EXCHANGER HEAT DUMP CONCEPT

a 39-inch-diameter source plate. The HSHX that was designed for this source consists of seven legs whose length corresponds to the length of the individual rows of fuel capsules. Each leg of the HSHX consists of a two-pass, rectangular array of tubes (or tubes and fins) which is inserted between alternate rows of fuel capsules.

For this configuration, the heat from two adjacent rows of fuel capsules is radiated to a single bank of tubes. The spacing between the rows of fuel capsules is taken as the OD of the HSHX tubes plus 0.5 inch. Since the rows are comprised of varying numbers of fuel capsules, the flow to each of the seven legs must be proportioned to the total number of capsules traversed by each heat exchanger segment. This is done by varying the tube diameters and the number of tubes within each leg and by providing orifices for the different inlet manifolds. With this system, the performance of HSHX No. 1 is identical to that of HSHX No. 2 because both heat exchangers are directly adjacent to the fuel capsules. Only the direction of heat flow changes when operation is switched from system 1 to system 2. Each of the seven legs of the heat exchanger has its own inlet and outlet manifold on one end and a reversing manifold on the other end. The individual inlet and outlet manifolds are fed by a common inlet and outlet distribution manifold which ties the seven legs together.

Circular Planar (Vented Capsules)

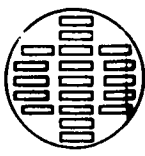


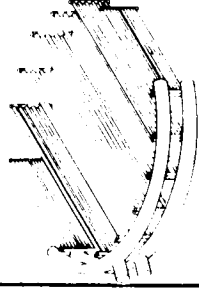
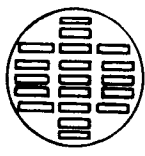

For the circular planar vented capsule design, an involute tubular HSHX was developed which was similar to the one described for the 49-inch circular planar source. The number of tubes and the tube diameter were the same, but the length of the tubes was reduced to 62 inches, and the core diameter was reduced to 46 inches to match the projected area of this smaller source.

The physical characteristics of the four HSHX's are summarized in Table 2.2-IV.

The performance characteristics of the three heat sources and four HSHX designs that were developed in this phase of the study are summarized in Table 2.2-V. The first item is the minimum weight HSHX design (i.e., minimum material thickness), and the second item is the maximum fuel capsule temperatures associated with full power output on HSHX No. 2. Only the pin cushion design falls below the 2000°F temperature level. The third item is the increase in the HSHX weight required to reduce the capsule operating temperature to 2000°F under the condition of HSHX No. 2 delivering full power. The fourth item is the maximum source temperature associated with the minimum-weight heat exchangers for HSHX No. 1 in operation. If the temperatures of line 4 are set as a new maximum, the Brayton fluid outlet temperatures of the HSHX No. 2 are calculated, and this result is translated into a power output of PCS No. 2, the values listed in line 5 emerge. For example, with an 1870°F maximum source temperature, 100-percent power can be achieved from the first system, and 74.5-percent power can be achieved from the second system. The sixth line gives an estimate of the heat leaks associated with the installation of each of the systems examined, with and without heat dump capability. These heat leak estimates are necessarily approximate because the details of the supporting structure and the mechanical interfaces with the IRV have not been worked out in detail. The major problems of each HSHX are listed as comments (item seven). The circular involute HSHX represents a more

TABLE 2.2-IV

PHASE I-B HEAT-SOURCE HEAT EXCHANGER DESIGN SUMMARY

Heat Source		Heat-Source Heat Exchanger							
Geometry	Size	Geometry	Type	Dimensions, in.	Tube OD, in.	No. of Tubes	Core weight, lb	Manifold weight, lb	Total weight, lb
Circular planar 	49-in. OD		Circular involute 2-pass tubular	Core 49 OD Overall 53.5 OD	1.34	18	54	35	89
			Rectangular 2-pass tubular	Overall 50 by 57	1.0	48	71	14	85
Pincushion 	39-in. OD		7-parallel rectangular legs 2-pass tube-fin	Overall 45.5 by 42.3	0.297 0.594 1.06 1.123 1.08 0.871 0.491	16 8 4 4 4 6 10	24	15	39
			Circular involute 2-pass tubular	Core 46 OD overall 50.5 OD	1.34	18	47	32	79
Circular planar (vented capsules) 	46-in. OD		Circular involute 2-pass tubular	Core 46 OD overall 50.5 OD	1.34	18	47	32	79

A-34850

TABLE 2.2-V

PHASE I-B HEAT-SOURCE HEAT EXCHANGER PERFORMANCE SUMMARY

	49-in.-dia Source		46-in.-dia Source,	39-in.-dia Source,
	Circular	Rectangular	Vented Capsule	Pincushion
1. HSHX weight, lb	89	85	79	39
2. Maximum source temperature (2nd HSHX in operation)	2060°F	2020°F	2115°F	1790°F
3. ΔWT to meet 2000°F max. source temperature (HSHX No. 2 in operation)	100	25	--	0
4. Maximum source temperature (HSHX No. 1 in operation)	1870°F	1845°F	1925°F	1790°F
5. Power output of HSHX No. 2 with maximum source temperature of (4)	74.5%	76%	74%	100%
6. Heat leaks, w No heat dump With heat dump	922 991	887 945	907 971	823 --
7. Comments	1. Complex fabrication 2. Large volume with heat dump	1. Difficult flow distribution problems 2. Simple fabrication	1. Highest temperatures 2. Complex fabrication 3. Large volume with heat dump	1. Requires movement of source to replace HSHX 2. No heat dump capability 3. Simple fabrication 4. Lowest temperatures

complicated fabrication problem than the rectangular HSHX; large cavity volumes are required to accommodate the large circular headers. Distributing the required flow to each of the tubes appears to be the most difficult design problem for the rectangular HSHX, but this heat exchanger will still be the easiest to fabricate. For the pin cushion configuration, the source must be rotated before the HSHX can be removed; the heat dump must be accomplished by rotating the IRV. The pin cushion configuration has the lowest source temperature and HSHX weights, and it provides 100-percent power output from both PCS units.

For the circular planar heat-source arrays, the maximum fuel capsule operating temperatures with PCS No. 2 in operation at full power (Item 2, Table 2.2-V) are considerably higher than reported in the Phase IA studies. The circular planar heat source of Phase IA had a diameter of 53 inches. The two circular planar heat sources considered in this phase of the study had diameters of 49 and 46 inches which represent a 17- and 32-percent decrease, respectively, in radiating heat transfer area. This decrease in radiating areas plus a more accurate determination of the temperature levels associated with this geometry resulted in the higher source temperatures indicated.

The HSHX area requirements as a function of maximum effective source temperature and source size for full power output are shown in Figure 2.2-4 for both HSHX No. 1 and HSHX No. 2. The temperature drop around the fuel capsule which is typically 120°F for the 49-inch-diameter source and 155°F for the 46-inch-diameter source, must be added to the temperatures given in the figure to arrive at the maximum fuel capsule temperature.

Integration Studies

Conceptual designs of integrated HSHX-Power Conversion Module (PCM) with the Atlas/Centaur and MORL vehicles were developed for each of the four HSHX's and the three heat sources. In addition, conceptual installation designs were developed for both the rectangular and the circular HSHX's employing a movable insulation heat dump system.

2.2.3 Isotope Reentry Vehicle (IRV)

Primary emphasis during Phase IB has been placed on the development of IRV systems incorporating the three reference HS configurations. Aerodynamic performance of the three vehicles is comparatively similar in that they are all 60-degree blunt cones with the same general weight, diameter, and aerodynamic coefficient characteristics.

Table 2.2-VI lists the comparative characteristics of the three reference IRV concepts developed during Phase IB. The two circular planar arrays incorporate an impact attenuation system based on the "Rotating Plate Concept", introduced in Phase IA and described in Subsection 7.2 of this document. Therefore, the weight and size advantage of the Pin Cushion concept over the 49-inch-diameter circular Planar Array is illusory, in that it includes no provision for impact attenuation. (As is shown in Table 2.2-VII, a comparison on the same basis, for

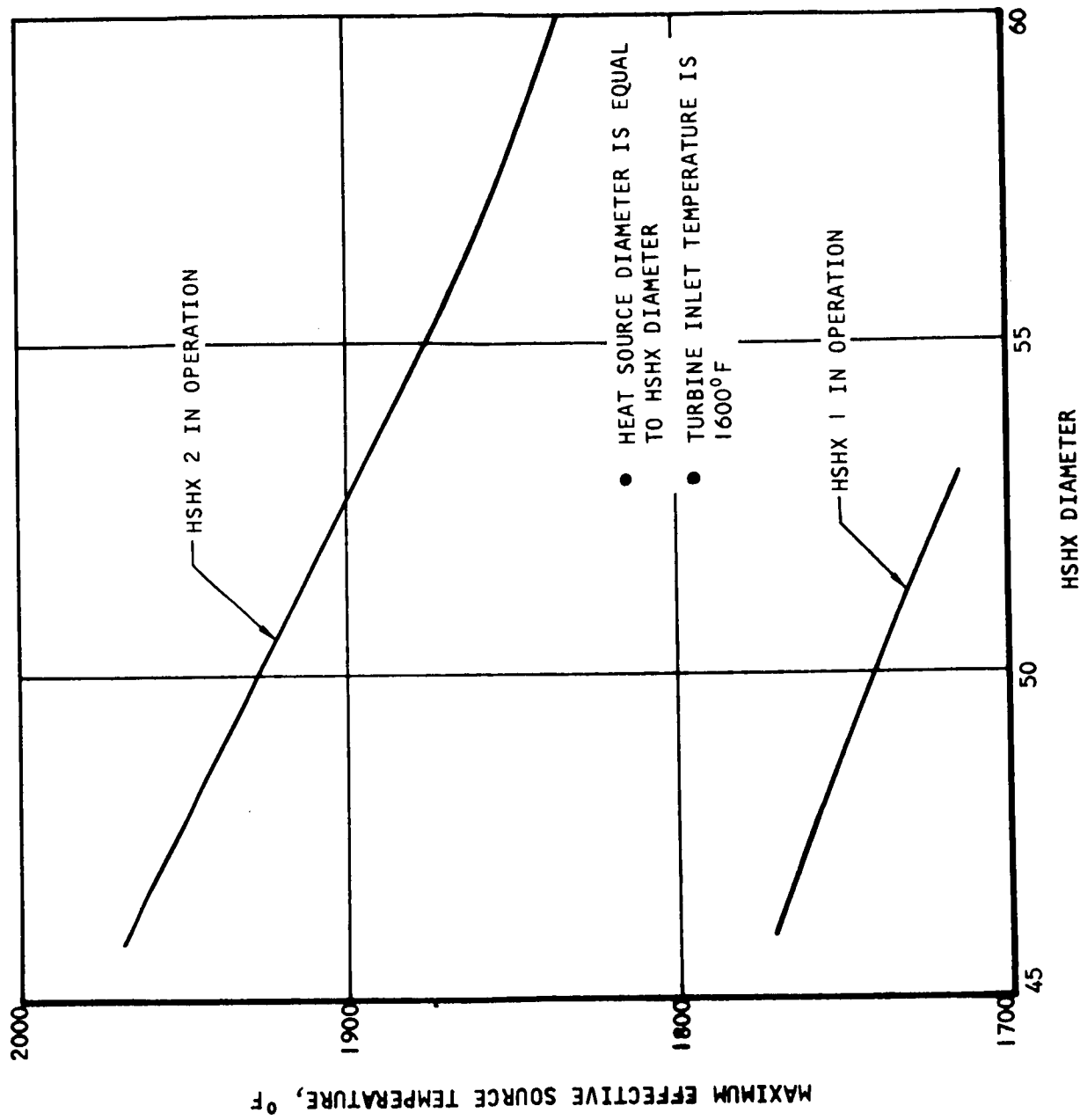


Figure 2.2-4 HEAT-SOURCE HEAT EXCHANGER AREA REQUIREMENTS

TABLE 2.2-VI

REFERENCE VEHICLE PERFORMANCE COMPARISON
CIRCULAR PLANAR VERSUS PIN CUSHION HEAT SOURCES




	CIRCULAR PLANAR H. S. ARRAY (49 IN. DIAM.)	CIRCULAR PLANAR H. S. ARRAY (46 IN. DIAM. VENTED CAPSULE)	PINCHSHION H. S. ARRAY (39 IN. DIAM.)
VEHICLE DIAMETER (IN.)	85	75	70.5
XCG/D (IN.)**	0.31	0.33	0.34
W/C _{PA} (LBS/FT ²)	29	30	38
HEAT SOURCE WEIGHT (LBS.)	1288	985	1365
IRV AEROSHELL WEIGHT (LBS.)	553	480	281
IRV ENTRY WEIGHT (LBS.)	1841	1465	1646*
HSHX WEIGHT (LBS.)	166	148	70
NUMBER OF FUEL CAPSULES	164	164	164
THERMAL POWER EOL (KW)	25	25	25
MAXIMUM CAPSULE TEMPERATURE (°F) (NORMAL OPERATION)	1870	1920	1790
INPLACE REDUNDANCY AND SEPARATE REPLACEABILITY	OK	OK	REQUIRES ROTATION OF HSHX OR IRV
IMPACT ATTENUATION	INTACT PLATE CONCEPT	INTACT PLATE CONCEPT	INTACT PLATE CONCEPT NOT FEASIBLE WITHOUT LARGE WEIGHT PENALTY (>1000 LBS)
DEVELOPABILITY	G	G	P
ATTACHMENT AND SUPPORT	G	G	P
AERODYNAMIC HEATING	G	G	P

* NO IMPACT ATTENUATION SYSTEM

** X_{CG} MEASURED FROM NOSE STATION

TABLE 2.2-VII

IRV WEIGHT AND DIAMETER SUMMARY

PERTURBATION (1) HEAT SOURCE CONFIGURATION	REF. DESIGN	A MIN. DIA. (BARE)		B ISOTROPIC CRUSH-UP	C CRUSH-UP		D CRUSH-UP WITH RECESS	
		DIA. IN.	WT. LB.		MIN. DIA.	MIN. WT.	MIN. DIA.	MIN. WT.
A 49.0 CIRC. PL 	85 1841	66.0 1551	66.0 2151		90.0 1826	75.0 1986	75.0 2083	
B 46.0 CIRC. PL - VENTED 	75.0 1464	62.3 1232	62.3 1772		75.0 1464	70 1540	71.1 1585	
C 39.0 PIN CUSHION 	70.5 (2) 1646 (2)	70.5 (2) 1646 (2)	70.5 (2) 1916 (2) 82.5 (3) 1893 (3)					

(1) ALL CONFIGURATIONS HAVE BALLUTE & FLUSH HEAT SOURCE UNLESS OTHERWISE SPECIFIED

(2) PROTRUDING (4.0") HEAT SOURCE

(3) WITH TOP OF FUEL CAPSULES FLUSH WITH REAR SURFACE OF IRV

"bare" vehicles, shows a significant weight and diameter margin for the circular planar array.) This diameter and weight margin is increased substantially when the pin cushion array is mounted in a flush position, to reduce reentry heating effects on the fuel capsules.

Referring again to Table 2.2-VI, the potential weight and diameter savings possible with a vented capsule HS is indicated in the IRV entry weight totals and vehicle diameters. Again, it should be noted that the diameter and weight totals reflect the inclusion of the impact attenuation system. The "bare" vehicle comparison is shown in Table 2.2-VII.

As noted previously, the normal operating temperature of the fuel capsule with the Pin Cushion HSHX is approximately 80° lower than the ORNL 49-inch HS array, and 130° lower than the Vented Capsule HS. The differences are due to the more efficient usage of heat transfer area in the case of the Pin Cushion HS, and less conductive area availability in the case of the Vented Capsule HS.

This comparison only attempts to evaluate the relative developability and fabricability of the two classes of systems in qualitative terms. However, the fabrication of the Pin Cushion system is certainly more complex than is that of the circular planar arrays. In addition, provision of a system to ensure similar impact performance with the Pin Cushion system to the circular planar arrays could only be achieved with large weight penalties.

Finally, the comparative heating on the capsules during the various classes of entry situation is much higher in the case of the complex, protruding, Pin Cushion array, than it is for the flush mounted circular planar arrays.

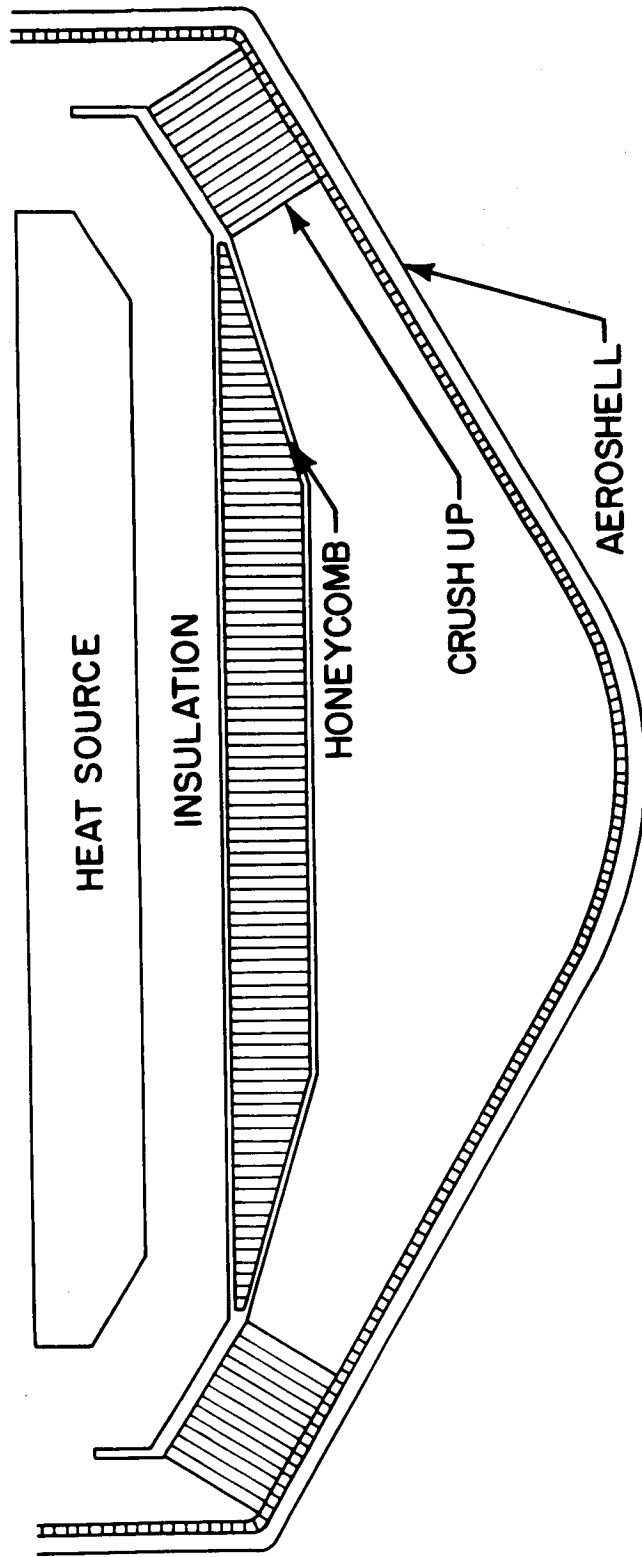
An optimization study of the intact plate, impact attenuation system has been completed during Phase IB. Figure 2.2-5 shows a section view of the conceptual scheme, incorporating a "cold plate" support structure to provide support for the HS during rotation during impact, and HS edge geometry modification to allow inclusion of rotational crushup at minimal cost in IRV diameter. The results of the optimization study are reported in Subsection 7.2. Table 2.2-VII shows IRV weights and diameters for minimum weight, minimum diameter, and optimum combination (Reference Designs) for Circular Planar HS IRV's using this intact impact concept. For comparison IRV weights are also shown for a crude attenuation system which employs isotropic crushup in the void volume below the HS.

Integration studies were also performed to develop separation, and abort/deorbit system requirements for Saturn IB-MORL, and Atlas-Centaur mountings of the reference concepts. There proved to be no significant differences between the three vehicles in terms of integration requirements.

An analysis of the spinup requirements for deorbit showed that the IRV inertia ratios are consistent with the deorbit rocket mounting illustrated in Figure 2.2-6. This mounting, however, then requires a separate set of abort rockets for pad aborts.

2.2.4 Conclusion and Recommendations

The following major conclusions and recommendations are made on the basis of the Phase I Conceptual Design Study:



78-0627

Figure 2.2-5 COLD PLATE CONCEPT WITH RECESSED CORNER

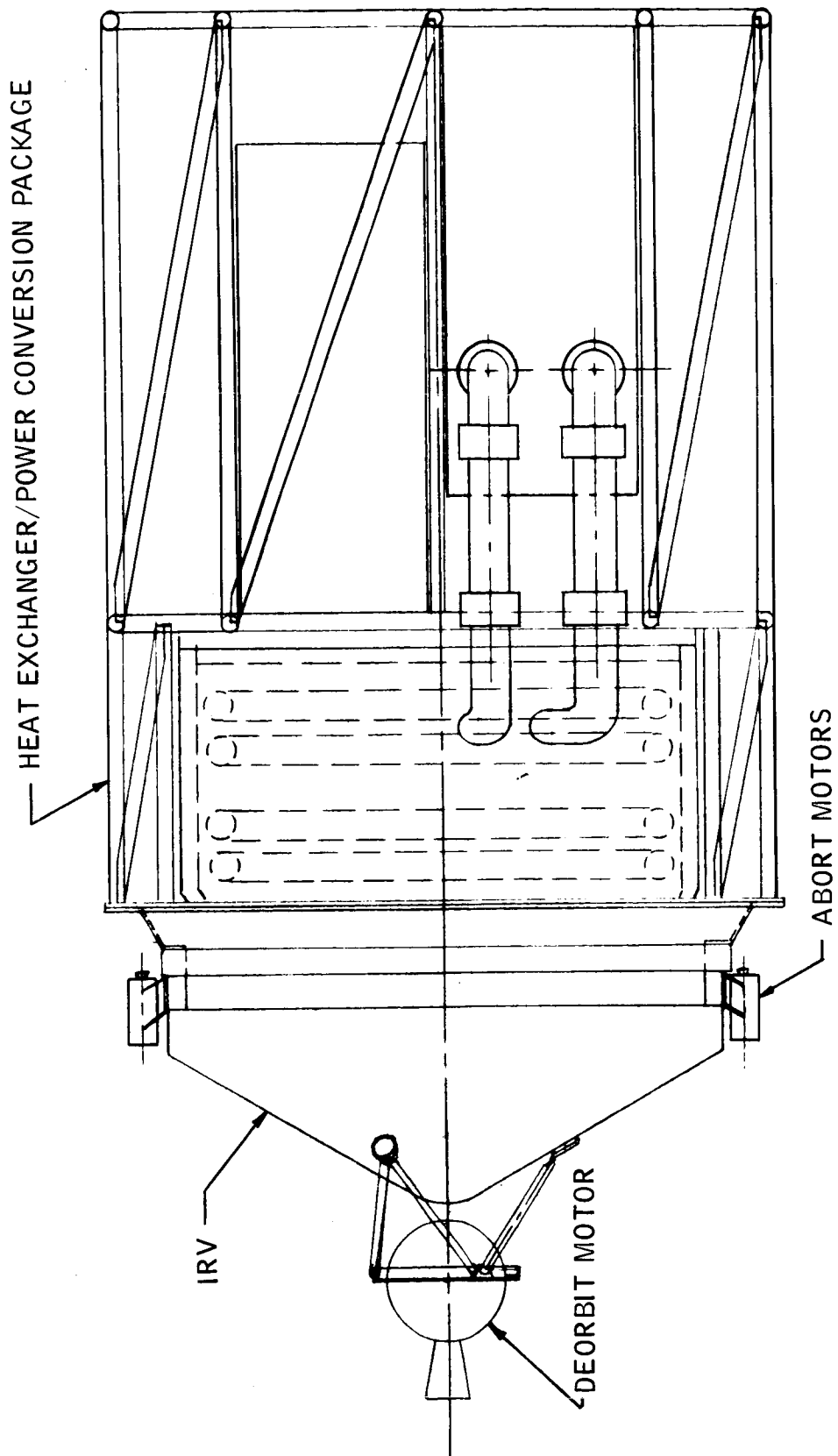


Figure 2.2-6 SEPARATE ABORT DEORBIT

78-0615

1. The circular planar HS array is recommended for preliminary design. The only significant "pin cushion" advantage is somewhat lower capsule operating temperatures. Developability and fabricability, reentry heating, impact protection, structural support, heat source weight, and HSHX replaceability are all more favorable for the circular planar array.
2. For comparable aerodynamic vehicle performance the "pin cushion" results in only slightly smaller vehicle diameters. The vented capsule circular planar HS array yields significantly lower vehicle weights and diameters (since impact attenuation can be provided for smaller diameter penalties).
3. The HS cover plate can be used to reduce reentry peak capsule temperatures.
4. Two-pass, tube fin HSHX are recommended for preliminary design.
5. Circular planar HS maximum capsule operating temperature can be reduced to less than 1850°F by adding tube wall weight (~100 lbs) to the HSHX.
6. A tower mounted deorbit system is recommended. Further work is needed on spin stabilization and reentry performance trade-offs.
7. An intact HS concept for impact attenuation can be used with reasonably small weight and diameter penalties.
8. A practical minimum vehicle diameter with impact attenuation is about 75 inches (nonvented capsules).

3.0 DESIGN APPROACH

The general Phase IB design approach has consisted of an examination of the various design alternatives available for each of the IRV subsystems, followed by a synthesis of a number of vehicle concepts which have then been compared and evaluated on the basis of the criteria noted earlier.

To facilitate understanding of the relationship between the factors which affect the total system design, Figure 3.0-1 is provided to show the design synthesis process in flow diagram form. Knowledge of the isotope heat source characteristics (e.g., materials, dimension, allowable temperature, etc.) allows a determination of the minimum spacing between capsules which can be achieved without exceeding the maximum allowable capsule operating temperature. Spacing together with the heat source (HS) total power level (i.e., number of capsules required) establishes a HS diameter. Capsule constraints are based on the nonvented and vented designs (Figure 1.0-2) furnished by NASA-Lewis.

In theory, the HSHX temperature area requirements should also be a factor in the establishment of the HS diameter; however, in this study the HSHX designs have been able to accommodate all achievable HS designs without affecting HS diameter.

Consideration of the heat sink requirements (i.e., volume and location) and the structural load environment during launch and reentry is required to establish an adequate HS and HS support structure design. These two factors combine to define overall HS depth (or thickness). With the basic size of the HS now determined, i.e., depth and diameter, it is now possible to develop the basic reentry vehicle design characteristics.

The allowable heat leak specification determines the required superinsulation packaging requirement around the heat source. The aerodynamic heating and structural loadings resulting from the worst case reentry and abort condition combinations, together with the associated hypersonic, transonic, and subsonic stability requirements, determine the design of the aeroshell which houses and protects the heat source during reentry. At this stage of the design then, one has a minimum diameter IRV which will survive reentry intact over the entire range of reentry conditions (including all abort modes). This is termed a "bare" reentry vehicle design.

The factors controlling the design of the basic or "bare" reentry vehicle are shown in the "Reentry Design" column of Figure 3.0-1. (Again, for the power level of interest in this study the HSHX does not have an appreciable impact on the basic IRV design.) It should be noted that all of these factors directly affect reentry vehicle diameter. It is readily apparent that overall IRV diameter is a direct function of HS diameter. In addition, the total height or depth of the HS and its insulation system strongly influences IRV diameter due to the subsonic stability limitation on the length dimension of the cylindrical portion of the aeroshell. Vehicle diameter is also influenced by aerothermal heating effects both in terms of basic aeroshell design requirements and possible HS recessing to alleviate "backside" heating on fuel capsules during reentry. The combined effect of the foregoing factors on IRV diameter is illustrated in Figure 3.0-2 for a typical circular planar HS.

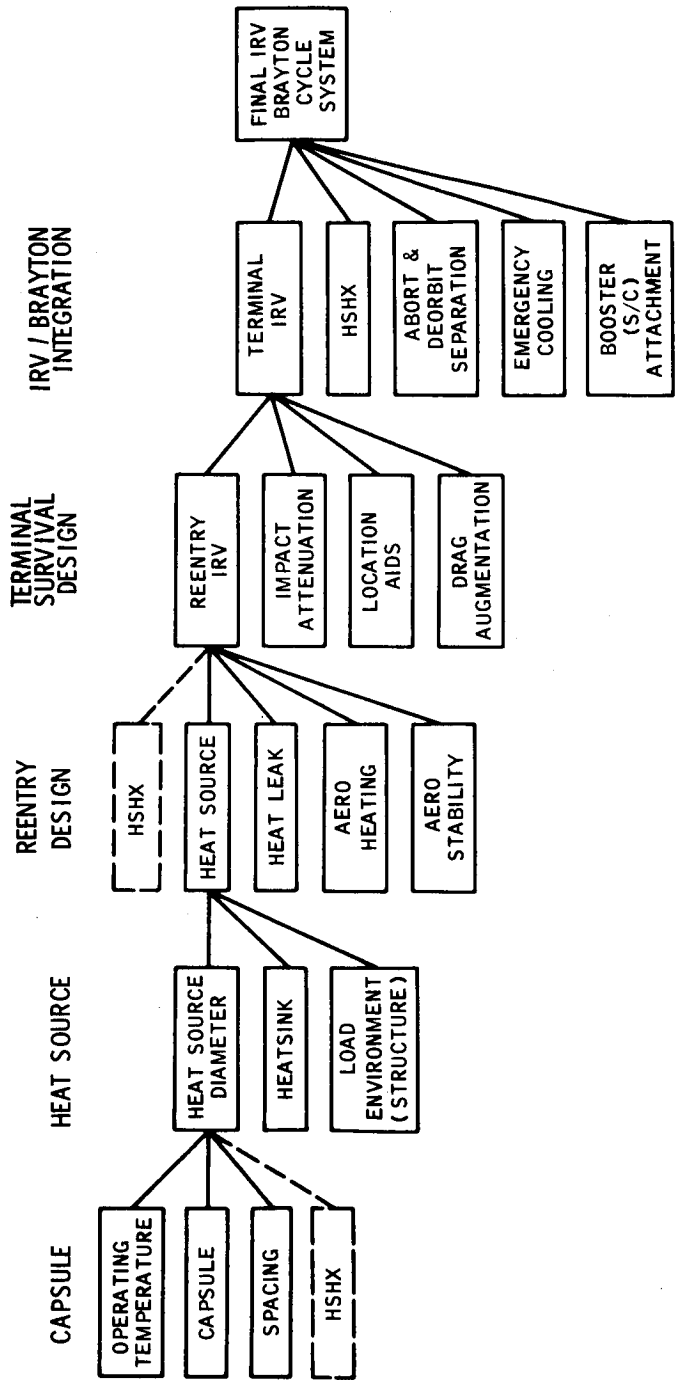
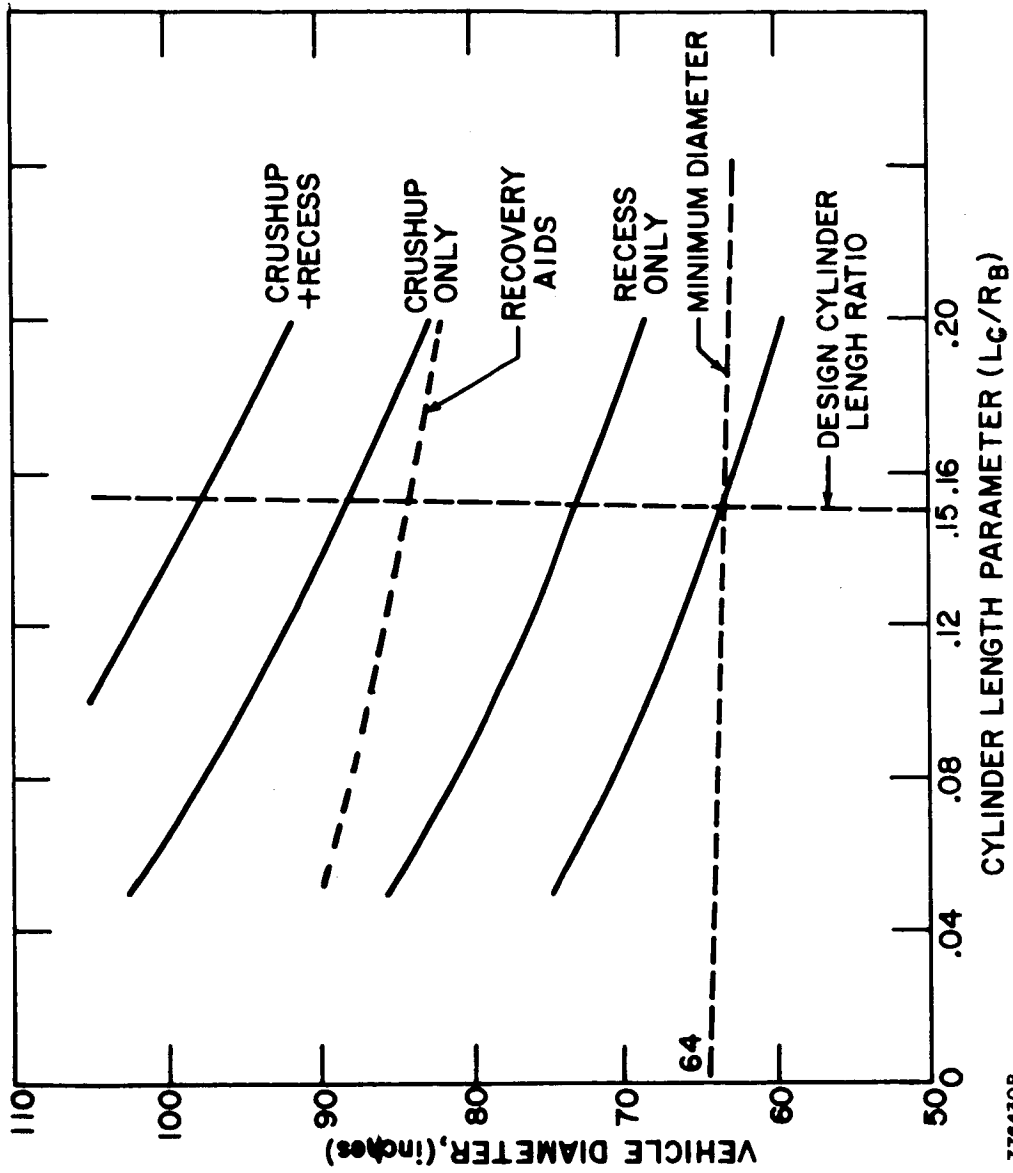


Figure 3.0-1 DESIGN FLOW CHART



776430P

Figure 3.0-2 VEHICLE DIAMETER TRADEOFF, 47-INCH CIRCULAR PLANAR HEAT SOURCE

As has been noted previously, an evaluation of intact impact and recovery and/or terminal velocity retardation systems has been completed during Phases IA and IB of the study. If it is desired to provide further protection for the isotope capsules during ground impact, it is necessary to incorporate an impact attenuation system into the IRV. Similarly, if lower descent velocities are desirable (so as to reduce ground impact loading on the capsules), drag augmentation devices such as parachutes or ballutes are necessary. Parachute recovery aids (i.e., parachutes) study has not been continued beyond Phase IA. However, designs of retardation device ballutes have been developed during Phase IB. Finally, location aids (such as pingers or beacons) may be incorporated in the IRV to aid in the tracking and possible physical recovery of the IRV. The incorporation of all of these factors into the IRV results in what is termed in Figure 3.0-1 as a terminal survival design.

The addition of any of these subsystems (other than a minimal complement of location aids) to the "bare" IRV can further enlarge total vehicle diameter. In particular, the inclusion of an impact attenuation system drastically affects vehicle diameter. For example, the HS rotational system which imposes a minimal stroke allowance requirement on the IRV adds almost 20 inches to the basic vehicle diameter for a near optimum total weight IRV system. The effect of location aids and ballutes on vehicle diameter and weight is comparatively slight.

Once the total range of IRV designs has been defined, the interaction of the IRV with the balance of the system, the Brayton Cycle components, and the spacecraft (S/C) must be considered.

At this point the design of the HSHX, particularly in terms of packaging, insulation, redundancy, replaceability, and support requirements, strongly enters into the definition of IRV/Brayton integration constraints. Consideration now must also be given to the requirements for abort and/or deorbit rocket inclusion in the IRV system, along with ancillary separation and spin-up subsystems. In addition to the immediate impact of these subsystems on the IRV design per se, their effect on the S/C (and/or launch vehicle) structure and operational sequence must also be considered. The abort/separation subsystem requirements must be evaluated in the context of the emergency cooling mode to properly determine optional placement of equipments, hinge points, and IRV/Brayton system associated hatches and payload shroud penetration. Finally, consideration must be given to the launch vehicle (or S/C) payload shroud (or compartment) constraints as they affect IRV/Brayton system packaging, support, and attachment schemes.

The preceding paragraphs have briefly outlined the logic of the design approach followed in the development of the comparative IRV design during Phase IB. The following sections are keyed to this design logic and generally follow the flow sequence illustrated in Figure 3.0-1.

4.0 FUEL CAPSULE

Fuel capsule applications work performed during Task 1-B consisted of evaluating the feasibility of a circular planar heat source design utilizing a reference vented capsule and a capsule spacing analysis. This section includes the ground rules on which this study was based, the design of the capsule, and the results of the optimization study of the effects of capsule spacing on capsule temperature gradient.

4.1 GROUND RULES

The vented capsule design used in this study was specified by NASA/Lewis Research Laboratory in consultation with Sandia Corp. The selection of materials and geometry where they were not specified by NASA were based on the nonvented capsule design used in the main IRV study effort. This study was based on substitution of the vented capsule for the nonvented capsule used in Task 1-A. (It should be noted that the nonvented capsule design has not been optimized in terms of material choice fuel loading, size or geometry. Therefore the potential weight and size savings with vented capsules are even greater than indicated in this brief study.)

The circular planar heat source configuration was the configuration considered. The fuel capsule arrangements were studied to minimize the heat source diameter. A minimum capsule spacing was determined from a thermal optimization study. The capsule retention scheme used in the analysis was the coverplate system. The balance of the study ground rules remained as stated in Tables 1.0-I, II, and III in Section 1.0.

4.2 CAPSULE DESIGN

The nonvented fuel capsule design used in Task 1-A of the program has been documented in Reference 1.1-1. It utilizes a thick refractory metal shell as a pressure vessel to contain helium generated by the PuO_2 fuel over ten half-lives. A 20-mil Pt-20% Rh clad is provided at the outside to protect the refractory shell from oxidation damage.

The vented capsule design is based on a totally different design concept. A vent is built into the capsule, which allows the helium generated by the fuel to leak out, while containing the fuel particles. The advantages of this design are that a heavy pressure vessel is no longer required to contain the helium nor does the void volume need to be as large; consequently, a volume and weight saving is achievable. Figure 1.0-2 illustrates both the nonvented capsule and the vented capsule supplied by NASA-LeRC.

4.3 FUEL CAPSULE SPACING ANALYSIS

During Task 1-A thermal analysis of the fuel capsules during steady state operation indicated that the centerline spacing between adjacent capsules strongly influences the difference between the peak capsule temperature and that of the cover plate facing the HSHX. Since the HSHX temperature is fixed by Brayton cycle performance requirements, the peak capsule temperature difference must be

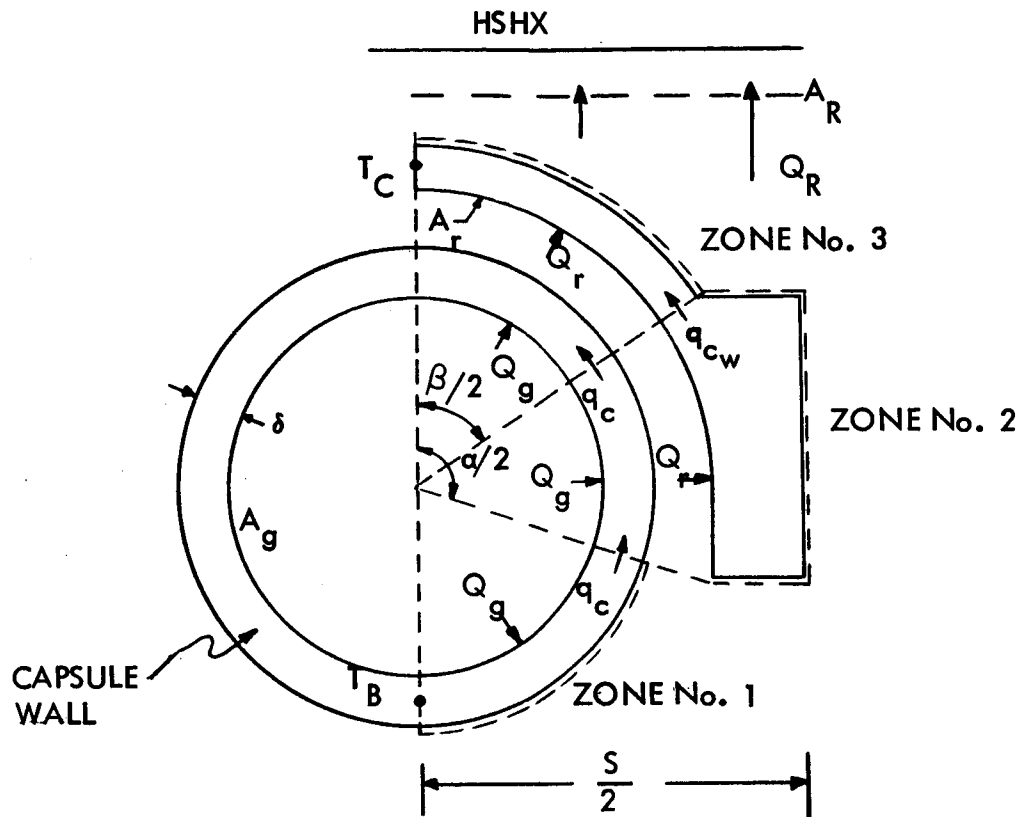
minimized to maintain a peak temperature of 2000^oF (or less) for steady state operation. A reduction in the capsule temperature difference can be achieved by increasing the capsule spacing which, of course, is in opposition to the objective of minimizing the heat source diameter.

The effect of spacing on the steady-state temperature profile around a capsule was, therefore, analyzed for covered capsules in a planar array to determine the optimum capsule spacing to provide a minimum heat source diameter with a minimum sacrifice in thermal performance. The analysis was based on a model shown schematically in Figure 4.3-1. As shown in this figure, the capsule was divided into three zones for calculation purposes. Model assumptions include:

- a. Thermal energy conducted radially from the PuO₂ to the capsule wall
- b. In Zone No. 1 (Figure 4.3-1), all heat is conducted circumferentially through the capsule wall
- c. No axial conduction
- d. No radiation gap internal to the surface of the capsule
- e. All heat radiated from capsule to the cover uniformly
- f. Heat is conducted circumferentially in the cover plate and radiated uniformly across the projected area of the cover plate to the heat exchanger
- g. Cover plate thickness is 0.060 inch
- h. Calculations are based on a 2000^oF peak capsule surface temperature.

The assumption made that there were no radiation gaps internal to the surface of the capsule is optimistic. The probability and effect of a radiation gap existing between the T-111 capsule wall and the platinum shell is discussed in Section 5.1.2.

Figure 4.3-2 is a plot of the capsule temperature gradients around the nonvented capsule as a function of capsule spacing. The bottom line represents the radiation temperature drop from the mean cover temperature to the heat exchanger temperature (assuming a uniform heat exchanger temperature). This curve reflects the effect of decreasing the cover heat transfer area and thus increasing the heat flux and associated radiation temperature drop. The second and third lines from the bottom represents the peak capsule surface temperature drop from the base of the capsule to the top of the cover adjacent to the top of the capsule. The third line from the bottom was based on a calculation performed in Task 1-A with the assumptions of a maximum cover-plate angle () of 210 degrees and circumferential conduction through the T-111 capsule wall only. The second line from the bottom was calculated in Task 1-B for a maximum radiation gap angle of 240 degrees and included circumferential conduction through the platinum clad as well as the T-111 wall. This was performed to provide a consistent basis for comparison to the vented capsule design and represents a reasonable temperature profile without undue optimism.



ASSUME:

1. $Q_g/A_g = \text{CONSTANT}$
2. $Q_r/A_r = \text{CONSTANT}$
3. $Q_R/A_R = \text{CONSTANT}$

where:

$$A_r = \pi DL \frac{\alpha}{360}$$

$$A_R = SL$$

$$A_g = (d - \delta) L$$

Figure 4.3-1 MODEL FOR TEMPERATURE DIFFERENCE CALCULATIONS

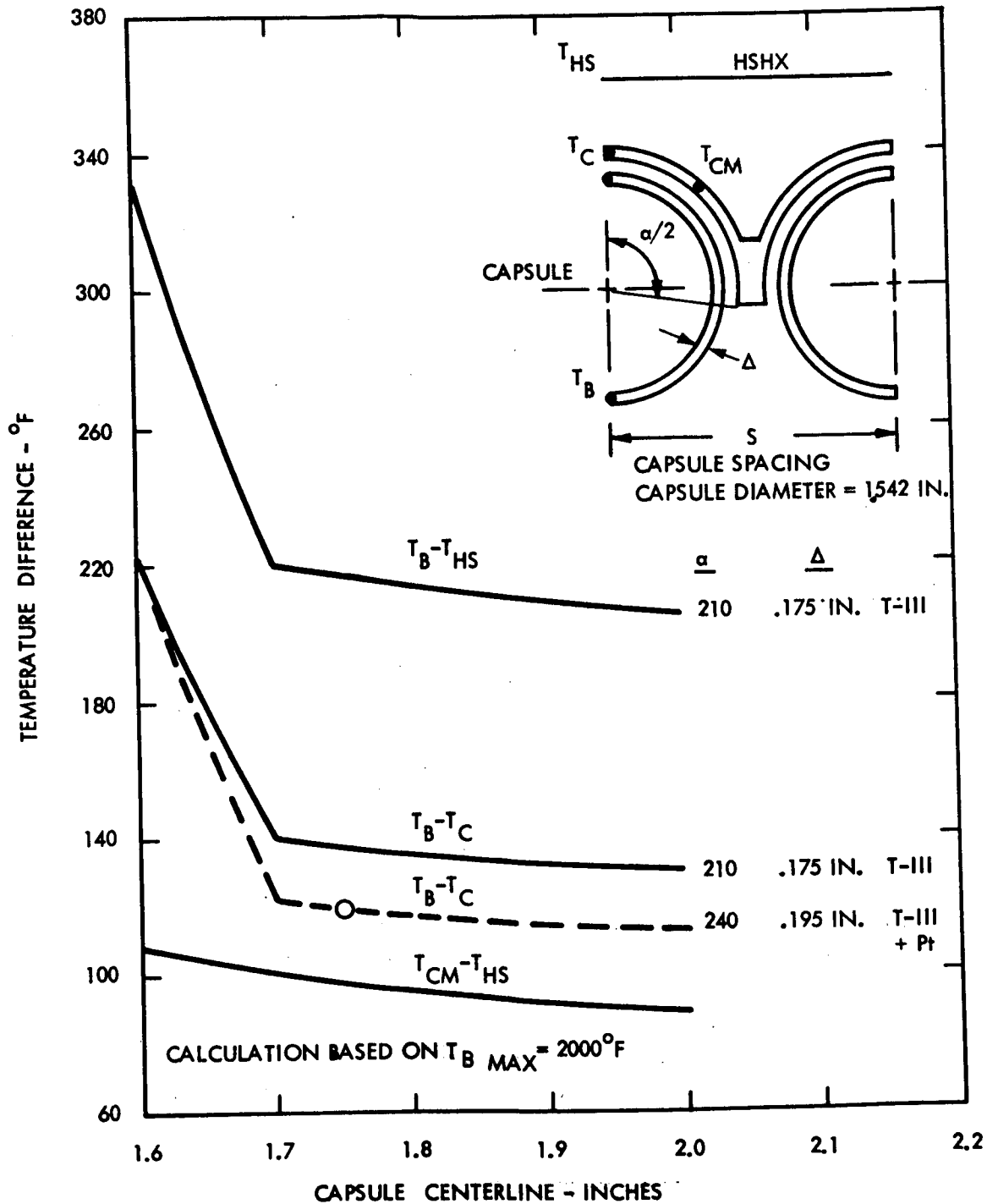


Figure 4.3-2 CIRCULAR PLANAR HEAT SOURCE -- EFFECT OF CAPSULE SPACING ON CAPSULE TEMPERATURE DIFFERENCE (ORNL CAPSULE)

For tight spacings, the angle over which a coverplate can be placed adjacent to the capsule varies from approximately 120 degrees at a spacing of 1.6 inches to the maximum coverplate angle (210 degrees or 240 degrees dependent upon the cradle design) at approximately 1.7 inches. This change in angle reflects a change in the radiation area between the capsule and the cover and thus the radiation gap temperature drop. The radiation gap temperature drop is a large percentage of the total capsule temperature drop; therefore, an alteration in radiation area resulted in a large temperature drop change. For spacings greater than 1.7 inches, the gradual decrease in capsule temperature difference is caused by a slight reduction in the amount of heat conducted around the cover. The top line in this figure represents the total temperature drop from the peak capsule surface temperature to the heat exchanger temperature for $\alpha = 210^\circ$, and conduction in the T-111 wall only. From a thermal standpoint, the minimum desirable spacing is that spacing in which the cover can be fully extended between the capsules thus eliminating the steep temperature gradient region. For the nonvented capsule, this spacing corresponds to 1.7 inches. Mechanical packaging of the capsules results in the same overall diameter for a 1.7-inch spacing and a 1.73-inch spacing. Since the 1.73-inch spacing results in a small performance gain and more freedom for the mechanical design without an increase in the heat source diameter, the 1.73-inch capsule spacing was selected as the optimum design point.

Figure 4.3-3 is a similar curve for the vented capsule. The four curves presented here represent the temperature drop from the peak capsule surface temperature (T_B) at the bottom of the capsule to the minimum cover temperature (T_C). The top two curves were calculated for maximum coverplate angles of 210 degrees and 240 degrees respectively and for circumferential conduction in a 0.060-inch thick T-111 capsule wall only. For this thin structure, the effect of the platinum clad (two clads of 0.020-inch thickness each) is much greater on the conduction path temperature drop than the one layer of platinum in the nonvented design and cannot be neglected in the analysis. The third line represents the capsule temperature drop for $\alpha = 240^\circ$ with circumferential conduction through the T-111 and platinum. The bottom line represents the same geometry assumptions as for the third line with an allowance for radiation internally from the bottom of the capsule to the top surface. The effect of increasing the coverplate angle to a maximum (limited by the cradle structural requirements) on capsule temperature drop is again clearly shown. For this capsule design (O.D. = 1.4 inches), the minimum desirable spacing thermally is 1.55 inches. From a capsule packaging standpoint, there is no change in overall heat source diameter for a 1.55-inch to a 1.60-inch spacing; therefore, the 1.60-inch spacing represents an optimum spacing for this capsule design.

Figure 4.3-4 is a comparison of the peak capsule temperature drops ($T_B - T_C$) for the two capsule designs as a function of the distance between adjacent capsule surfaces. These two lines are presented for a maximum coverplate angle of 240 degrees and for circumferential conduction in the T-111 and platinum rings. The circles represent the optimum distances used in establishing the design. The resulting capsule spacings are 1.73 inches and 1.60 inches for the nonvented and vented capsule designs. For the nonvented capsule, a peak surface temperature difference of 120°F is predicted; whereas, for the vented capsule a corresponding difference of 155°F is predicted. A 35°F penalty in performance for the vented capsule design is counterbalanced by a 3-inch reduction in overall heat source diameter from 49 to 46 inches.

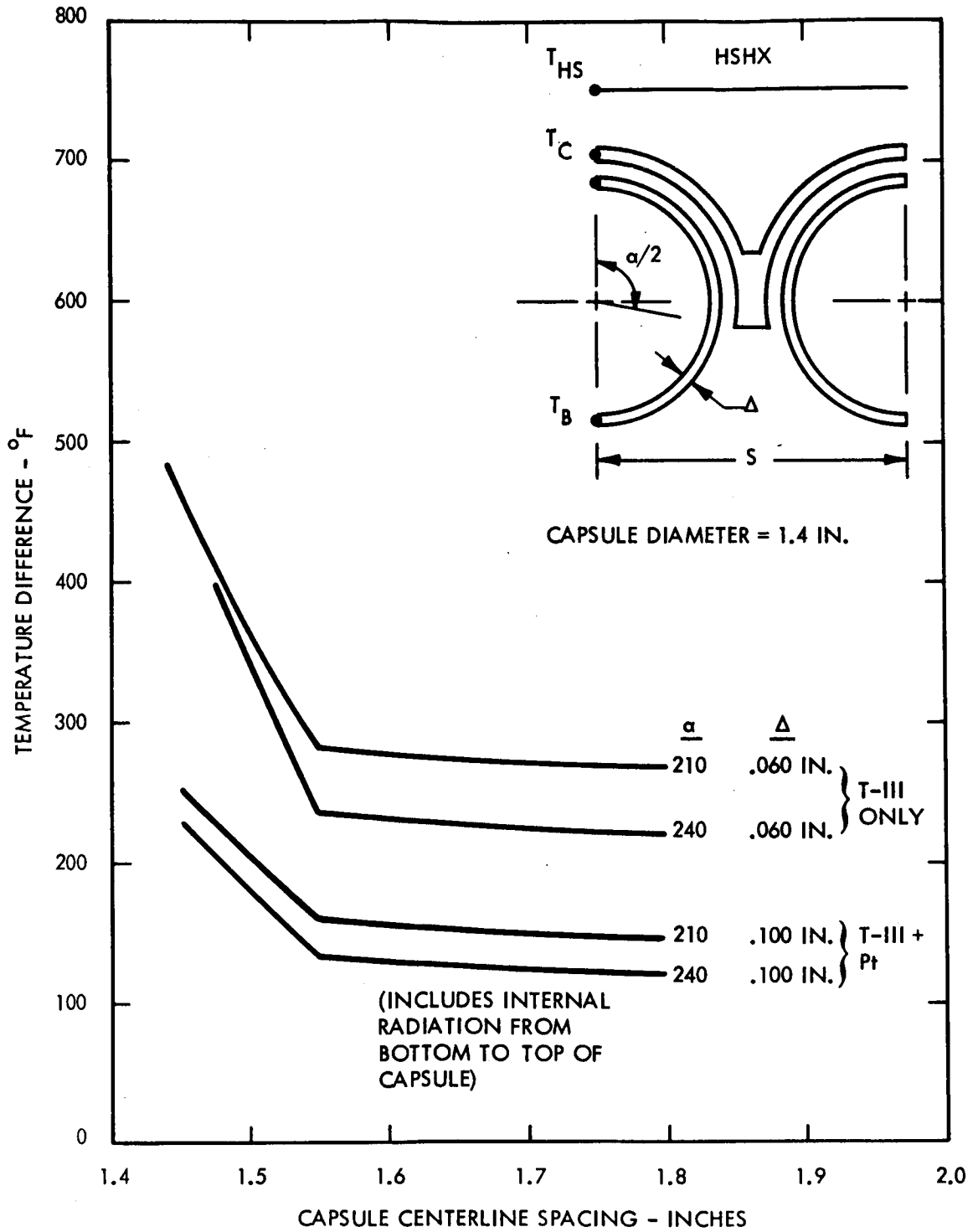


Figure 4.3-3 CIRCULAR PLANAR HEAT SOURCE -- EFFECT OF CAPSULE SPACING ON CAPSULE TEMPERATURE DIFFERENCE (VENTED CAPSULE)

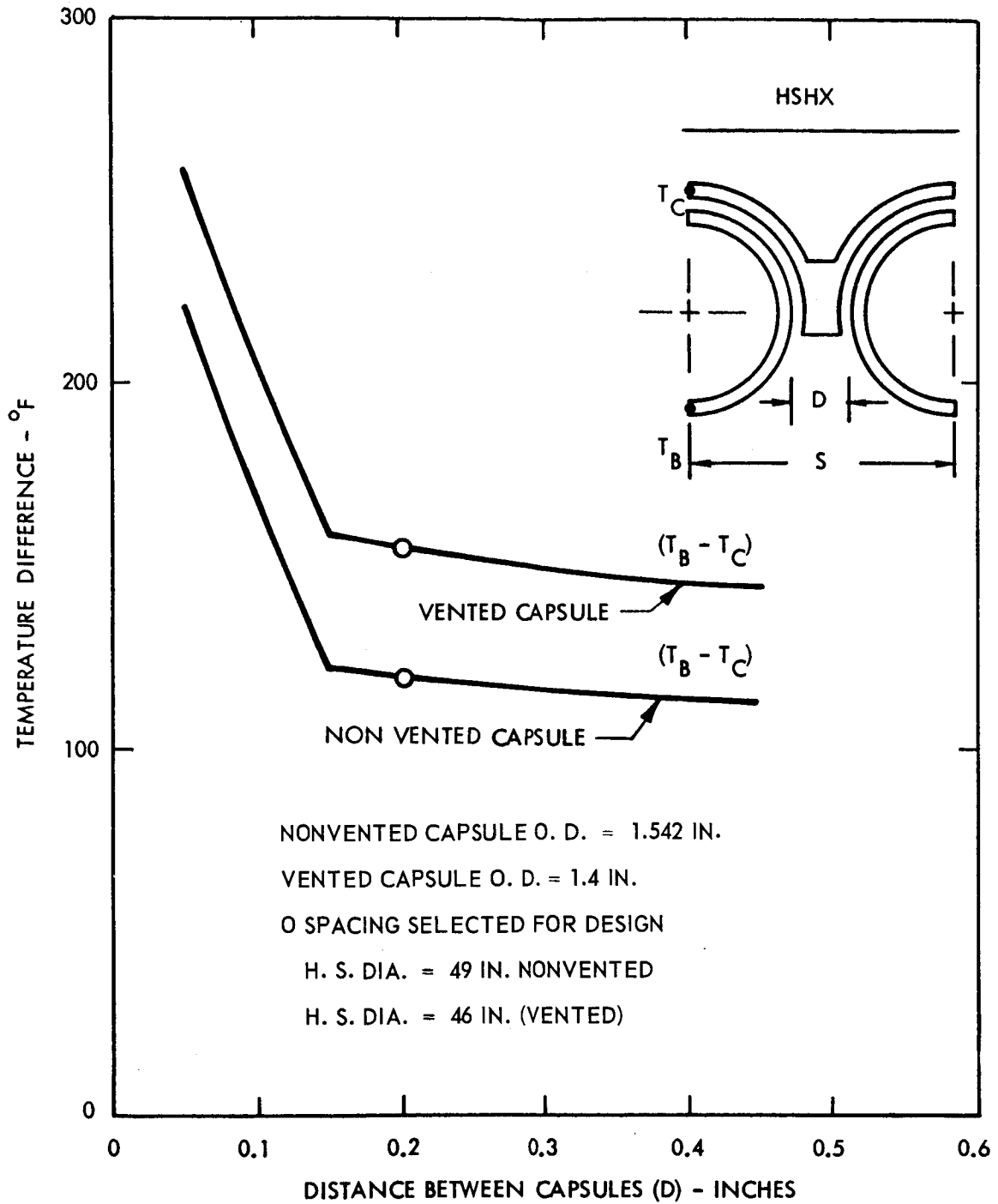


Figure 4.3-4 COMPARISON OF NONVENTED CAPSULE AND VENTED CAPSULE SPACING ON CAPSULE TEMPERATURE DIFFERENCE

A centerline spacing of 2.07 inches between adjacent capsules in a row of a pin cushion array is obtained from ACHX coolant channel requirements, support structure thickness required for structural strength and axial thermal conduction requirements for transient operation. The row spacing is discussed in Section 5.5.

In summary, optimum capsule spacings of 1.73 and 1.6 inches are recommended for the nonvented and vented capsule design respectively. These two spacings result in a 49-inch-diameter circular planar heat source with a 120°F capsule temperature difference for the nonvented capsule and a 46-inch-diameter heat circular planar source with a 155°F capsule temperature difference for the vented capsule. The cover-plate thickness of 0.060 inch was selected for this analysis as an acceptable thickness on the basis of preliminary thermal and structural calculations and was not considered as a parameter of the analysis. The steady-state coverplate temperature profiles for the two selected spacings are reported in Section 5.1.2 for the planar arrays along with similar temperature profiles for the pin cushion array.

5.0 HEAT SOURCE

Considering the three reference concepts, the circular planar and pin cushion concepts represented extensions of studies carried on during Task I-A. The third concept was an alternate to the circular planar based on the substitution of vented fuel capsule for the reference nonvented capsule.

The isotope heat source assembly consists of fuel capsules, capsule retention hardware, heat source plate assembly, heat sink material, thermal insulation system, auxiliary cooling heat exchanger (ACHX), and support structure.

During this phase, the designs for the circular planar and the pin cushion heat source with the nonvented capsule were refined and the design for the circular planar heat source with a vented capsule was established. For the three modified designs, weights, structural performance, and thermal performance during steady-state operation and ACHX cooling were determined. The heat sink requirements for the circular planar arrays were estimated, and a parametric study of heat sink weight and location requirements for the pin cushion design was performed.

5.1 HEAT SOURCE DESIGN

Mechanical designs for the three heat source arrangements are presented below with a summary of the weight, dynamic performance during impact, and steady-state thermal performance in space and on the launch pad.

5.1.1 Mechanical Design

5.1.1.1 Description of Configurations

- a. The 49-inch-diameter circular planar array which evolved from the optimum capsule spacing study carried out in Task I-A included 164 (nonvented) fuel capsules.
- b. The minimum diameter circular planar array with 164 vented capsules was optimized at the 46-inch diameter and is similar to the 49-inch planar array.
- c. The pin cushion array minimum diameter was achieved after a comprehensive study of log versus vertical capsules was performed. Capsule spacing was primarily the governing factor in setting the heat plate diameter at 39 inches to accommodate the 165 (nonvented) capsules which are located in vertical rows.

Configuration No. 1 (Figure 5.1-1)

To optimize the conceptual design of the 49-inch planar array, thermal and mechanical designs were reviewed. Capsule spacing and thermal analysis of the nonvented capsule were evaluated. Effects of radiation gaps between the T-111 refractory shell and the Pt-Rh noble metal clad, internal radiation of fuel, and Pt-Rh clad thickness were considered. The capsule spacing of 1.73 inches was selected as an optimum as noted earlier.

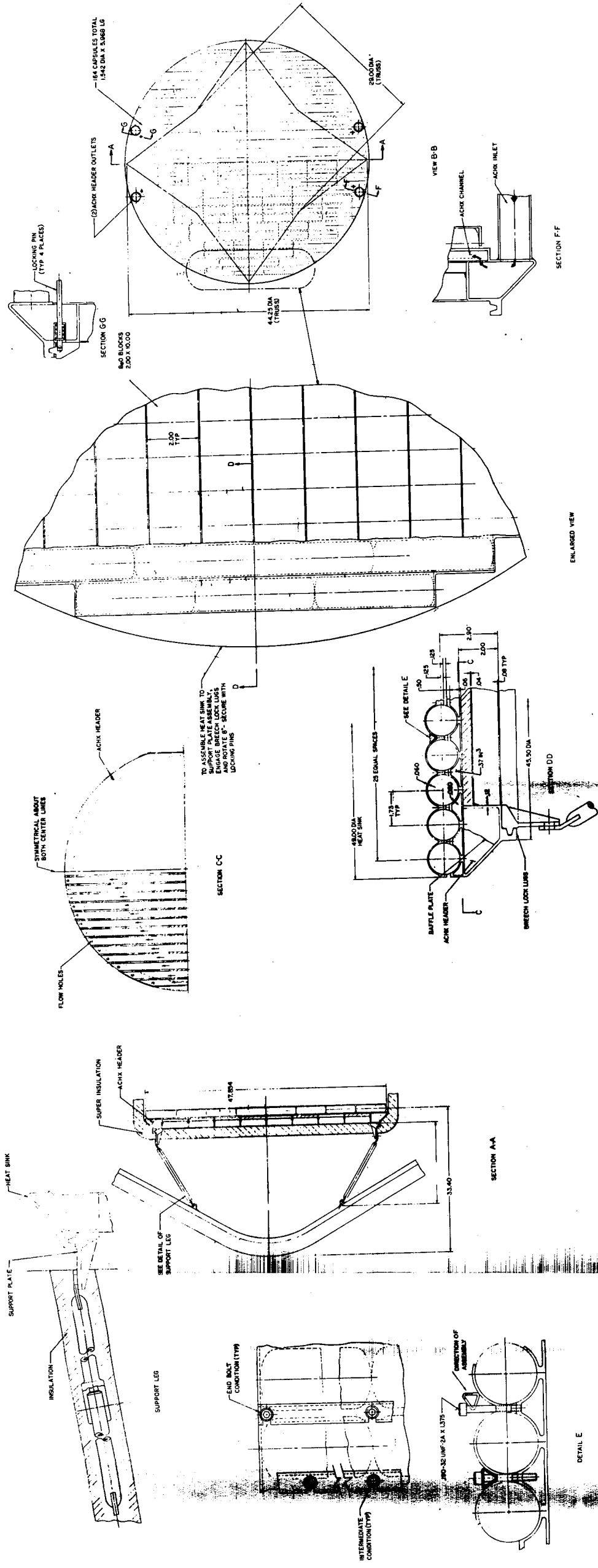


Figure 5.1-1. CIRCULAR PLANAR ARRAY, 49-INCH-DIAMETER HEAT SOURCE

The refractory metal support plate and retention hardware were reviewed for structural integrity during reentry and plate sections were reduced to afford the lightest weight structure.

The coverplate retention method is used since the reentry heating analysis showed a distinct advantage over the bare capsule retention in terms of the capsule peak temperature (Figure 2.2-2). It also offers added assurance of being able to maintain intact reentry in case of retention bolt failures.

The truss support was also reviewed and redesigned to reduce the heat loss and minimize the temperatures at the connection to the aeroshell. To accomplish this the tensile yield strength of the lower section of the strut (Rene' 41 treated at 1950°F and aged at 1400°F) was based on an allowable value of 100 ksi. This enabled the strut to be redesigned to work at 1400°F rather than the 1000°F considered under Task I-A. It also allowed a reduction in the cross sectional area from 0.29 to 0.093 in.²

An additional review was also made of the capsule support plate where the plate periphery was redesigned to add additional stroke to the crushup structure on impact. Approximately two inches of stroke was gained by chamfering the edge of the plate into the ACHX header (Figure 5.1-2). This results in a reduction of vehicle diameter.

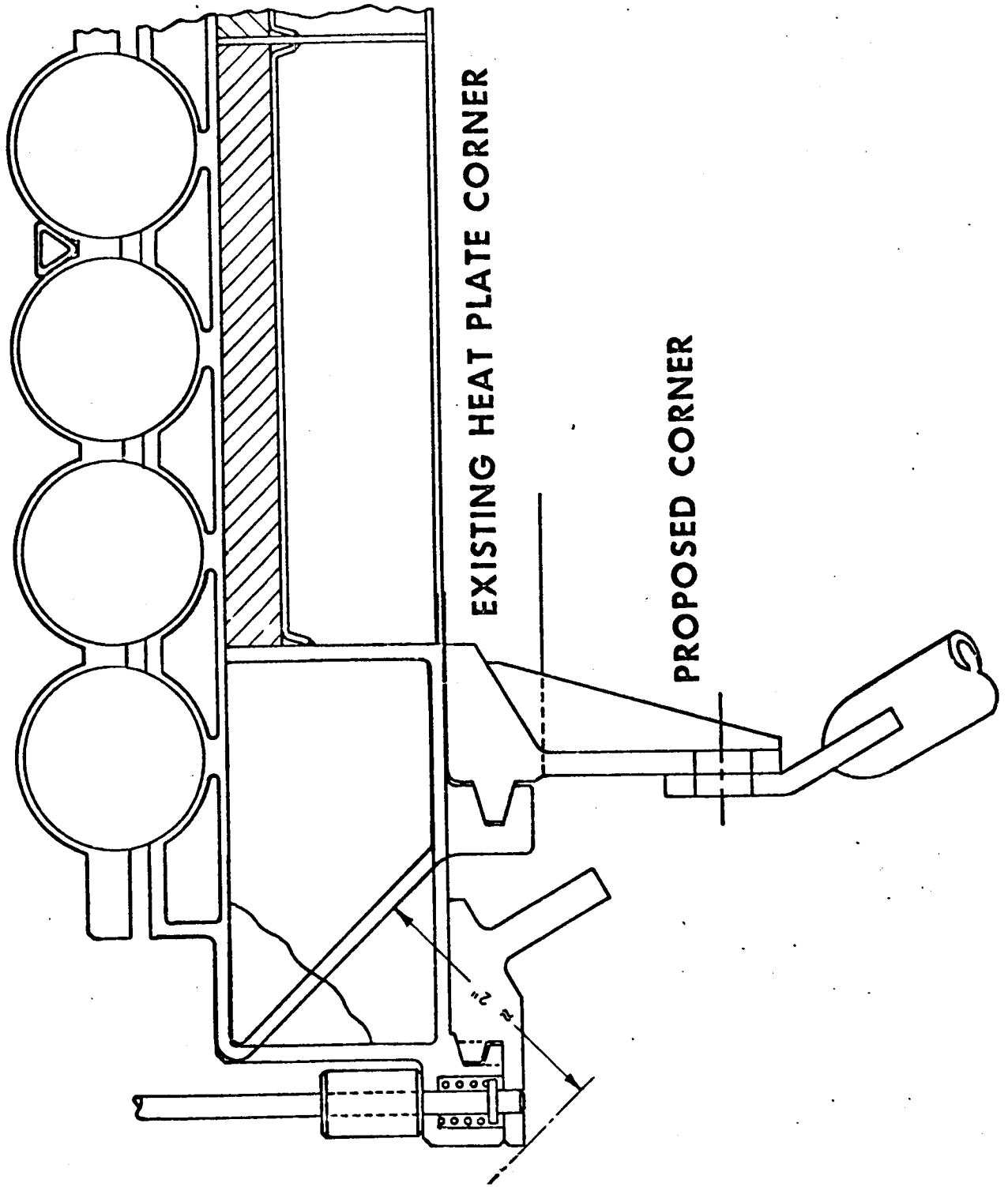
Configuration No. 2 (Figure 5.1-3)

The thermal and mechanical design of a circular planar array with a vented capsule established that a reduction in the capsule size did not greatly reduce the overall diameter of the heat source. This is basically because the length of the capsule (5.6 inches versus 6.0 inches) is the governing criteria. The capsule center line spacing of 1.6 inches was selected to maintain approximately the same distance between capsules (Figure 2.3-1) for both circular planar arrays. This resulted in an overall support plate diameter of 46 inches.

The vented capsule design configuration realizes a total weight saving of approximately 300 pounds; however, of this, 280 pounds can be attributed to the capsules themselves. A further 80-pound reduction realized from the reduced diameter support plate is offset by the addition of 60 pounds of beryllium oxide included to maintain the heat capacitance required in the heat source. The additional capacitance is required because of the significant reduction in fuel capsule wall thickness in this concept.

Configuration No. 3 (Figure 5.1-4)

The pin cushion array discussed under Task I-A of the IRV design study program was initially a rectangular heat source configuration; however, during Task I-B, a circular configuration evolved with both vertical and log capsule arrays (Figure 5.1-5). Two comparisons were made. The first indicated that although the stacked log array theoretically (based on an equal row spacing) reduced the heat source support plate diameter, deployed cooling requirements dictated that a greater distance was required between the stacked log rows than the vertical rows. Consequently heat source support plate diameters for both stacked log and vertical pin cushion configurations were identical at 39 inches. The vertical



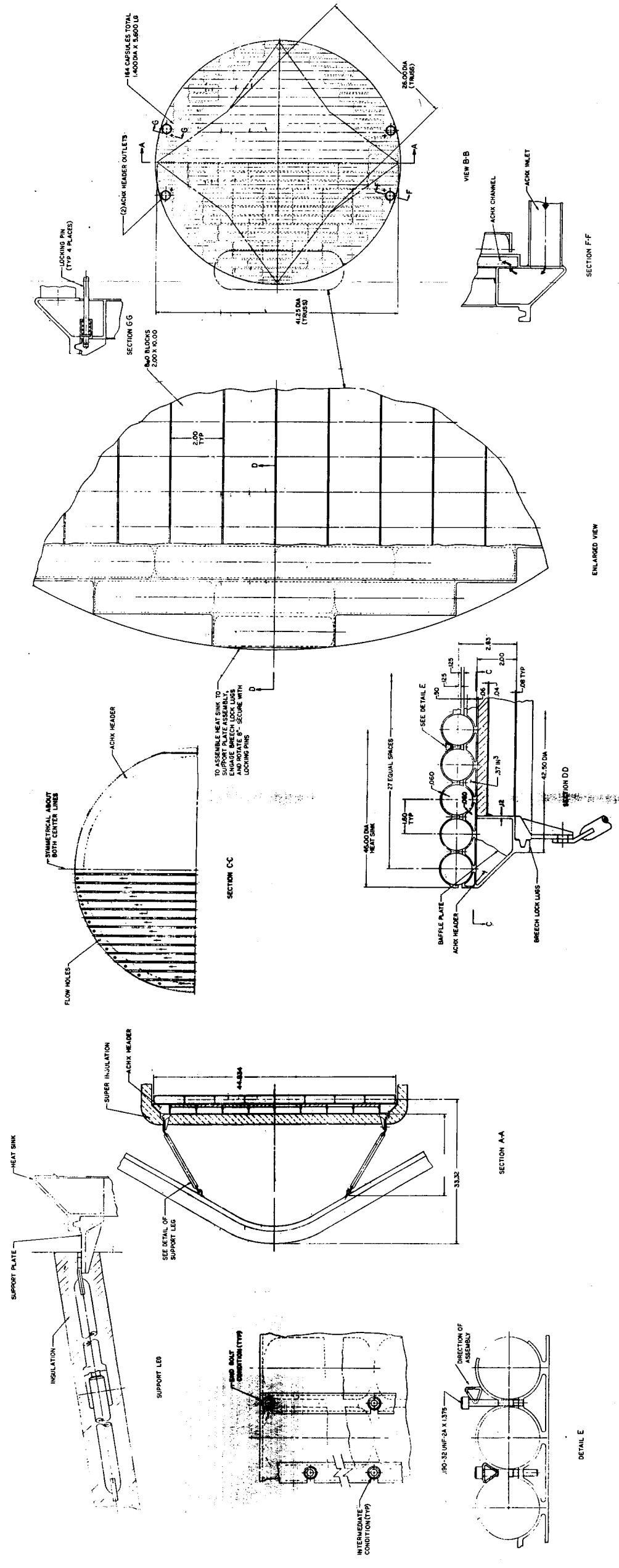


Figure 5.1-3 CIRCULAR PLANAR ARRAY, 46-INCH-DIAMETER HEAT SOURCE (WITH VENTED CAPSULES)

FOLDOUT FRAME /

FOLDOUT FRAME 2

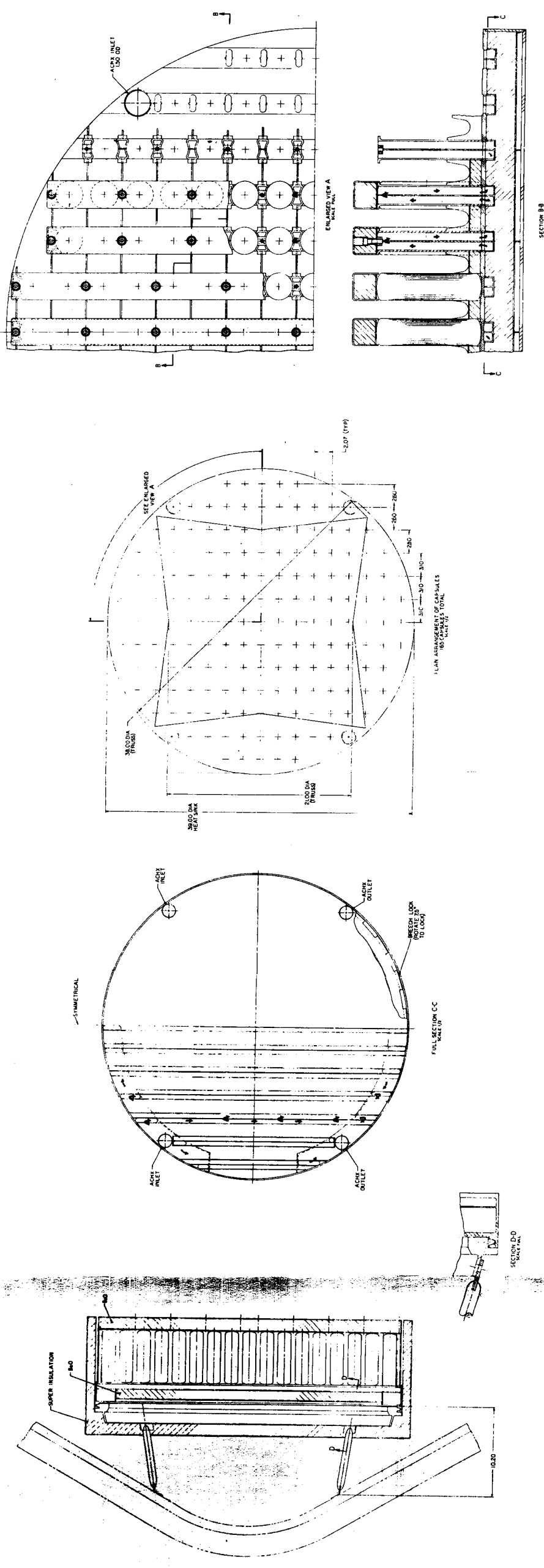
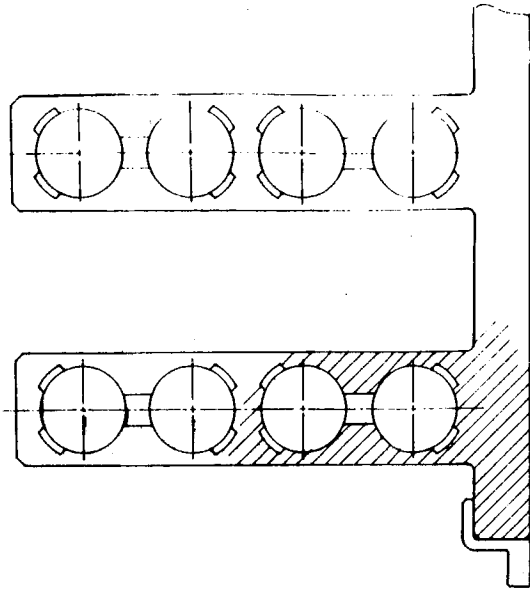
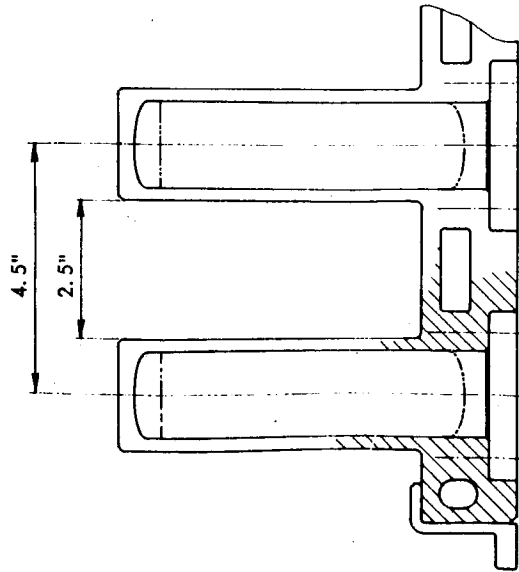


Figure 5.1-4 PIN CUSHION ARRAY, 39-INCH-DIAMETER HEAT SOURCE



PIN CUSHION
HORIZONTAL

612221-4B



PIN CUSHION
VERTICAL

Figure 5.1-5 VERTICAL VERSUS STACKED LOG ARRAY

configuration was finally selected because of simpler fabrication and less complex ACHX requirements. The bases for these selections is discussed in the following paragraphs.

Although graphite eliminated the requirement of the beryllium oxide heat sink, its structural performance is unpredictable during reentry loading and on impact. It is also incompatible with the refractory metal and iron titanate emissivity coating. The desired arrangement of ACHX flow channels was more readily obtained with a refractory metal structure and was in fact integrated into the refractory metal support pillars and retention mechanism. As shown in Figure 5.1-4, capsule row spacing was varied from 3.10 inches for the center rows to 2.60 inches for the outermost rows. This matches the thermal loading and hydraulic performance of the HSHX coolant tubes. Spacing between capsules within a row was kept constant at 2.07 inches. Although the optimum diameter of 39 inches represents a considerable reduction in heat source size, the overall weight of the pin cushion configuration increased. This was due mainly to the additional beryllium oxide which was required. Sixty pounds of the 220 pounds required was located in the retention plate positioned on top of the vertical capsule rows.

Heat source mass and moments of inertia data were calculated and are summarized in Table 5.1-I.

5.1.1.2 Structural Design

The circular planar and pin cushion structural plate designs were found to be adequate for reentry conditions (31 g's) (a condition encountered during a -10° , 26,000 fps reentry - Table 5.3-I) including the tumbling reentry loads. The collapse load of the circular plate (limit analysis), assuming the plate is homogeneous, uniformly loaded, and simply-supported to failure, is over 140 g's. The pin cushion design was analyzed only for the capability of the projections from the plate which contain the fuel capsules. With the 1/16-inch-thick gusset plates at the base of the projections, the lateral load capability is approximately 100 g's. This assumes one capsule per projection and the beryllium oxide weight of 0.38 lb on the apex of the projection is accounted for. Containment of the fuel capsules upon impact would probably be difficult to achieve with the pin cushion design however. Both the circular planar and the pin cushion plate design configurations are anisotropic, but the internal rib structures are designed to minimize the induced anisotropy of the fuel capsule support systems. Containment of the beryllium oxide heat sink in the heat source plate presents no problem since a full weld about the BeO retainer plate will result in over 2600 g's capability for an allowable weld shear stress of 5000 psi. The beryllium oxide will not fracture at g-loads less than a thousand. Plate panels and ribs were found to be independently adequate for reentry g-loads.

The heat source support struts were further sized to reduce heat losses through the ends of the struts where they attach to the aeroshell support ring. The use of Rene' 41 for a partial length of the strut, where temperatures permitted, allowed a reduction in the conductivity value and the cross-sectional area. Since Rene' 41 has higher strength than T-111, the load carrying integrity of the struts was maintained while reducing the Rene' 41 cross-sectional area from 0.29 to 0.093 in.² assuming a 75 percent fixed end condition which results in approximately 60 g's load integrity. An allowable stress of 100 ksi was used for Rene' 41 at 1400°F.

TABLE 5.1-1

HEAT SOURCE MASS AND MOMENT DATA

	39-inch Pin Cushion Array (lbs)	46-inch Planar Array (lbs)	49-inch Planar Array (lbs)
Capsules	760.0(165)	475.0*(164)	755.0(164)
Support Plate	278.0	194.0	263.0
BeO and Retainer Plate	238.0	218.0	160.0
Truss Support	51.0	56.0	68.0
Insulation	38.0	40.0	42.0
	<hr/>	<hr/>	<hr/>
Total Weight	1365.0	983.0	1288.0
Moments of Inertia			
I_P (Slugs/ft ²)	54.7	54.1	86.3
I_T (Slugs/ft ²)	30.6	28.5	43.4

*vented capsules

5.1.2 Thermal Design

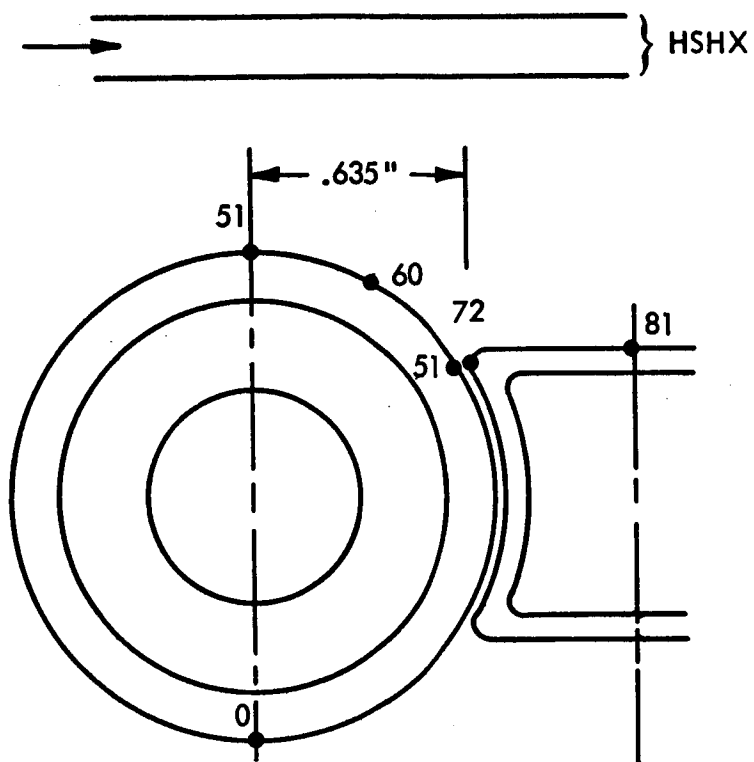
As described in Section 4.3, a capsule temperature difference exists across the capsule from a peak temperature located at a point farthest removed from the HSHX to the capsule or capsule cover side facing the HSHX. Minimization of this capsule difference is an important design criterion due to the requirements of maintaining a peak capsule temperature below 2000°F without reducing the HSHX coolant temperature below 1600°F specified by the Brayton cycle design requirements.

Based on the optimization of capsule centerline spacing for the circular planar arrays and based on the design of the pin cushion array, steady-state temperature differences across the capsule and cover were calculated for the three designs with peak temperatures of 2000°F. Figures 5.1-6, 5.1-7, and 5.1-8 present the temperature profiles for the nonvented capsule in a pin cushion array, the nonvented capsule in the circular planar array, and the vented capsule in a circular planar array, respectively.

The fuel capsule in a pin cushion array has an axial temperature drop of 70°F. The peak capsule to cover ΔT 's for the two circular planar designs are 120° and 155°F for the nonvented and vented capsule designs.

Table 5.1-II summarizes the thermal performance of the three heat source designs, while on the launch pad and in space, and the hydraulic performance of the ACHX. All three designs have considerable temperature margin for operation with the primary HSHX in use. Temperatures above the 2000°F fuel capsule temperature limit are calculated for the circular planar design when the secondary HSHX must be used, if 1600°F is still required at turbine inlet, namely 2060°F for the nonvented capsule design and 2115°F for the vented capsule design. Either a reduction in Brayton cycle gas inlet temperature or a small increase in heat source diameter would bring these temperatures down to the 2000°F limit or lower. The design approach taken was to minimize heat source size at the expense of possible reduction in performance in the event of primary HSHX failure. All three designs can be readily cooled to peak capsule temperature less than 350°F with the ACHX using 90 psi air or nitrogen.

In the analysis of the capsule steady-state temperature gradient, the peak capsule temperature has been assumed as the temperature of the T-111 shell since it is the metal which maintains the encapsulation of the PuO₂ and must maintain good structural properties. In the analysis performed in Task I-A and Task I-B, the platinum layer externally adjacent to the T-111 shell has been assumed to be in good thermal contact with the T-111. Since platinum's coefficient of thermal expansion is considerably greater than the coefficient of expansion for T-111, a gap will occur at high operating temperatures in space which implies that the heat will need to traverse an additional gap to be transferred to the HSHX. If the T-111 and platinum surfaces are coated with a high-emissivity coating ($\epsilon = 0.85$) and a vacuum exists in the gap, then the gap temperature drop will be approximately 70°F. Without coatings, the gap temperature drop will be considerably larger due to the low emissivity of platinum (0.05 to 0.3). In the latter case, the temperature drop with a vacuum could be sufficiently large to hinder a practical heat source design. A necessary capsule design criterion is, therefore, the maintenance of thermal contact between the T-111 and the exterior layer of platinum or provision of a conducting gas such as helium in the gap.



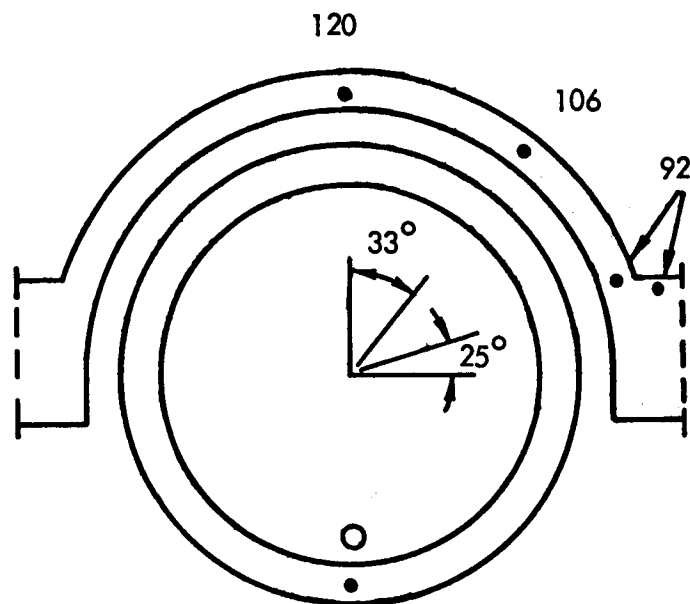
CAPSULE DIAMETER = 1.55 IN.

CAPSULE CENTERLINE
SPACING = 2.07 IN. (IN SAME ROW)

CALCULATION BASED ON $T_{MAX} = 2000^{\circ}F$

612385-21B

Figure 5.1-6 PIN CUSHION HEAT SOURCE TEMPERATURE DIFFERENCE IN A VERTICAL PIN CUSHION ARRAY

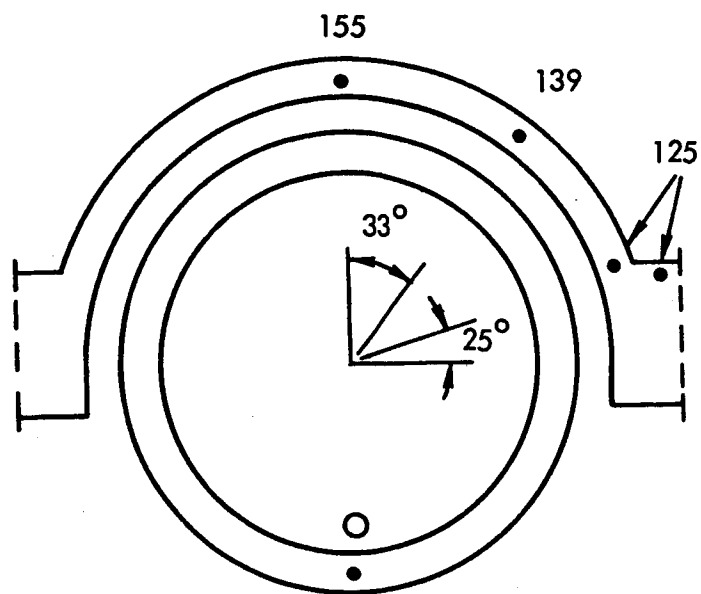


CAPSULE DIAMETER = 1.55 IN.
 COVER THICKNESS = 0.060 IN.
 CAPSULE CENTERLINE
 SPACING = 1.73 IN.

CALCULATION BASED ON $T_{MAX} = 2000^{\circ}F$

612385-11B

Figure 5.1-7 CIRCULAR PLANAR HEAT SOURCE TEMPERATURE DIFFERENCES
 AROUND NONVENTED FUEL CAPSULE



CAPSULE DIAMETER = 1.4 IN.
 COVER THICKNESS = .060 IN.
 CAPSULE CENTERLINE
 SPACING = 1.6

612385-15B

CALCULATION BASED ON $T_{MAX} = 2000^{\circ}F$

Figure 5.1-8 CIRCULAR PLANAR HEAT SOURCE TEMPERATURE DIFFERENCES
AROUND VENTED CAPSULE

TABLE 5.1-11

THERMAL PERFORMANCE SUMMARY

	CONFIGURATION	
	PLANAR	PIN CUSHION
<u>STEADY STATE</u>		
PEAK CAPSULE TEMPERATURE GRADIENT	120°F	155°F
HEAT SOURCE RADIATION AREA	13.1 FT ²	11.5 FT ²
PEAK CAPSULE TEMPERATURE		70°F
A. PRIMARY HSHX OPERATING	1870°F	1925°F
B. SECONDARY HSHX OPERATING *	2060°F	2115°F
<u>ACHX OPERATION</u>		
MASS FLOW RATE	3.14 LB/SEC	3.44 LB/SEC
VELOCITY	105 FT/SEC	115 FT/SEC
PRESSURE	6 ATM	6 ATM
PEAK CAPSULE TEMPERATURE	350°F	350°F
		1790°F
		1790°F
		2.54 LB/SEC
		70 FT/SEC
		3 ATM
		340°F

*with Brayton cycle power system operating at rated power

In summary, all three heat source designs are acceptable thermally during steady-state cycle operation and while the heat source is being cooled on the ground.

5.2 HEAT SINK DESIGN AND REQUIREMENTS

One of the design requirements for the Isotope Reentry Vehicle System specified in the program outline is the inclusion of sufficient thermal capacitance in the heat source to prevent the fuel capsules from heating from 1800° to 2500°F in less than one hour to maintain capsule temperature below 2500°F during launch and startup. To meet this requirement, the heat source is designed to absorb the entire amount of heat generated. (The heat sink is also provided to maintain fuel capsule temperature below 2500°F in the event of a launch pad abort and subsequent entrapment of the HS in the after-fire; and to allow reaction time for minor repairs during orbital operations.) For a metallic structural design, the structure and capsules do not provide sufficient thermal capacitance; therefore, a material with a high thermal capacity must be included in the design. The primary material considered for this application has been beryllium oxide.

During the Task I-A study, BeO weight requirements were determined for the five preliminary designs based on the parametric curve of capsule heating rate versus BeO weight for initial temperatures of 300°F and 1800°F as shown in Figure 5.2-1. This curve was developed for a total capsule weight of 700 pounds with a thermal capacity corresponding to T-111 and a total structural weight of 450 pounds with the thermal capacity of Cb-1%-Zr. Furthermore, this curve was developed for the assumption of no temperature lag between the capsule and the BeO. For the planar fuel capsule arrays, the BeO could be placed sufficiently close to the capsule such that a conduction ΔT between the capsule and BeO of no more than 50°F would be required to transfer all of the heat to the BeO. This ΔT was not considered detrimental to the performance of the thermal capacitance material. Referring to Figure 5.2-1, it is noted that a total weight of 110 pounds is required to maintain a maximum heating rate of 700°F/hr from an initial temperature of 1800°F. For the five designs considered in Task I-A, 140 pounds of BeO were included which provided a maximum heating rate of 630°F. This heating rate provided allowance for a 70°F conduction ΔT lag between the fuel capsules and the BeO.

Minimization of the heat source diameter with a nonvented capsule and the use of the lighter weight vented capsule has resulted in smaller structural and capsule weights for the two circular planar arrays considered in the Task I-B studies. To compensate for the loss in the thermal capacitance of the heat source, the weight of the BeO has been increased to 200 pounds for the planar array with the vented capsule design. The weight of the BeO used in the nonvented capsule heat source was maintained at 140 pounds.

Two fuel capsule arrangements were considered for the pin cushion fuel capsule array designated as the third heat source design. One arrangement consisted of vertically mounted fuel capsules. The other arrangement consisted of capsules stacked four high in a horizontal "log-type" arrangement. Based on a detailed analysis of the fuel capsule array in a deployed state, described in Section 5.5, the vertical pin cushion array was selected as a more favorable design. This was because the row spacing requirements for deployed cooling coupled with row spacing requirements for the HSHX resulted in no substantial heat source diameter differences between the two designs; whereas, the vertical pin cushion

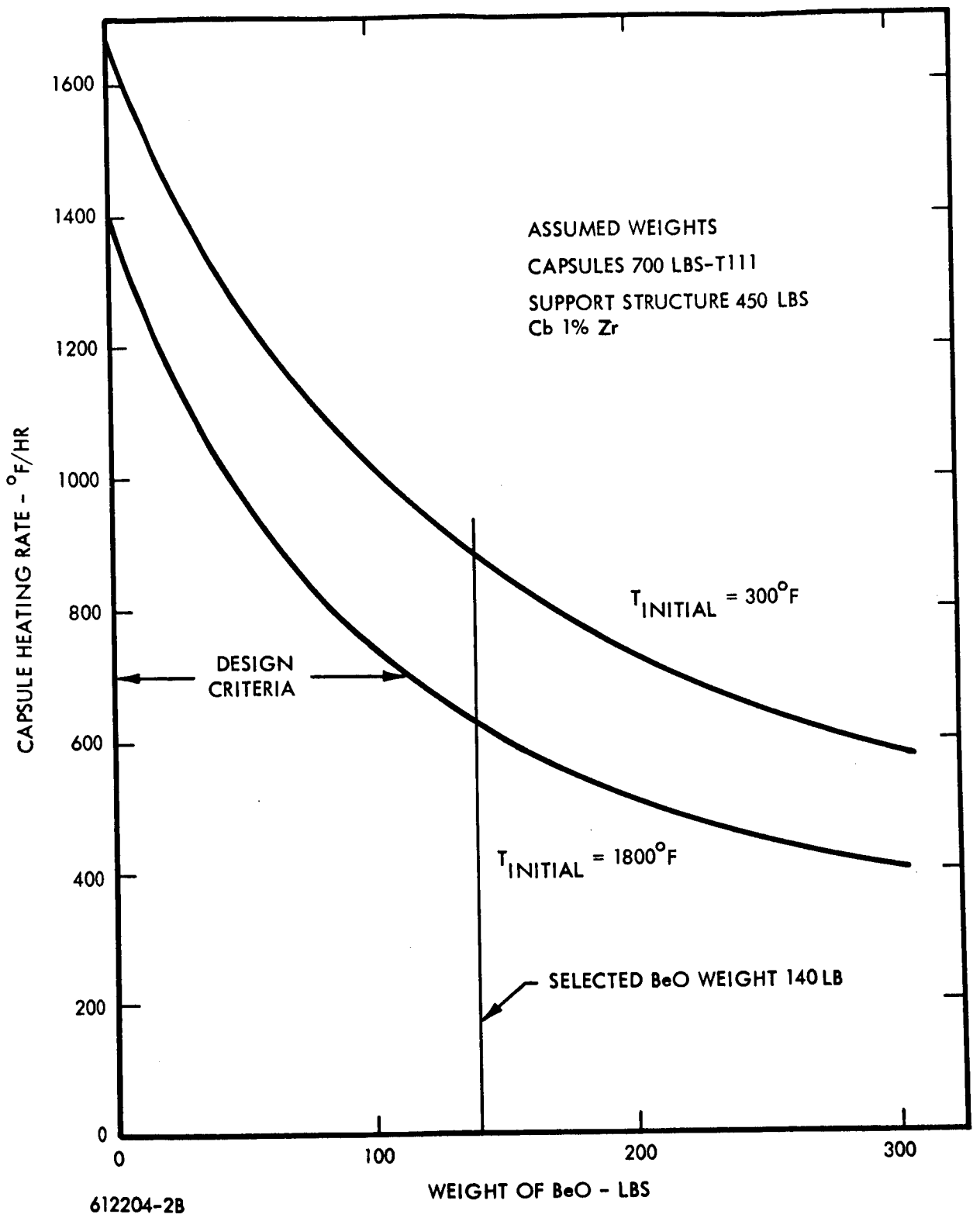


Figure 5.2-1 CAPSULE HEATING RATE VERSUS BeO WEIGHT

heat source was mechanically simpler in terms of BeO placement and ACHX design. Preliminary scoping calculations of the thermal capacitance requirements for the two arrays indicated that very large temperature differences between the capsules and the BeO would exist in the log-type capsule array, and moderate temperature gradients would exist in a vertical fuel capsule array. A detailed analysis was, therefore, performed for the vertical pin cushion array. BeO was placed at the top and at the base of the fuel capsules to reduce the temperature difference from the peak capsule temperature point to the BeO by distributing the heat flow and reducing the heat flow path. Figure 5.2-2 presents a curve of the capsule temperature difference as a function of the total BeO weight and the weight of the BeO at the top of the fuel capsule. The bottom curve in this figure represents the thermally ideal case of no temperature lag between the fuel capsule and the BeO. Based on spacing limitations, a maximum of 60 pounds could be placed at the top of the fuel capsules. The total BeO weight requirement was 220 pounds with 60 pounds at the top to limit the capsule temperature rise to 700°F after one hour of elapsed time from an initial uniform temperature of 1800°F.

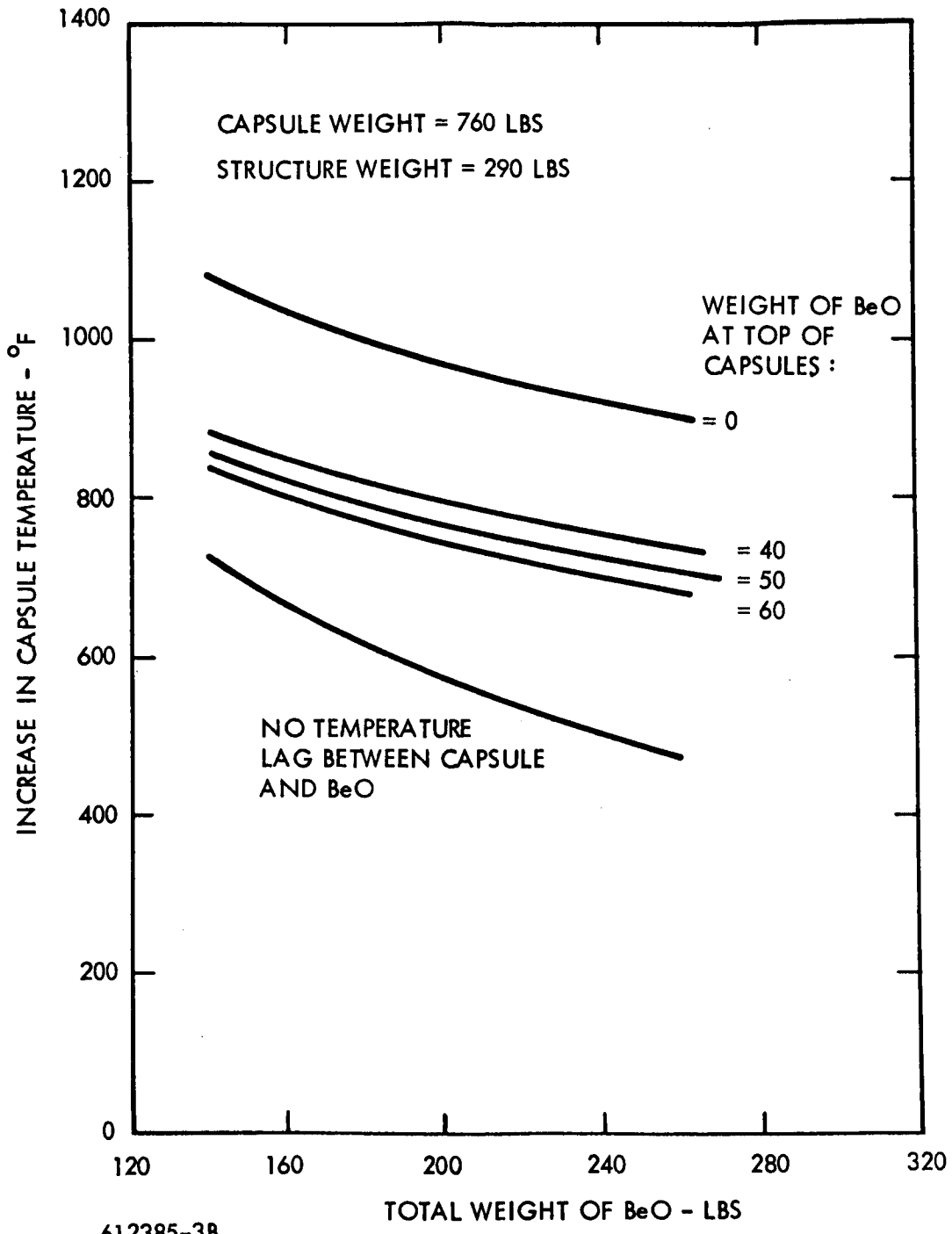
In summary, therefore, the BeO requirements for meeting the restriction of a one-hour minimum time for the capsule to heat from 1800°F to 2500°F are 140, 200, and 220 (60 at the top) pounds for the planar nonvented capsule heat source, the planar vented capsule heat source, and the pin cushion heat source respectively.

5.3 STRUCTURAL LOAD ENVIRONMENTS

The significant structural load environments considered for the Phase IB IRV design study include launch, abort, reentry, and parachute opening and air snatch. The load factors which represent the maximum expected load conditions are summarized in Table 5.3-I for the above environments. For design, these limit load factors are multiplied by a safety factor of 1.25 except for the Saturn I-B launch and abort conditions where an adequate safety factor has already been considered.

Launch acceleration loads for both launch vehicles considered in the IRV design study, the Atlas-Centaur and Saturn I-B, are given in terms of the launch vehicle axis. For the Saturn I-B configuration, the IRV vehicle axis is normal to the launch vehicle axis and hence the longitudinal (A_x) and lateral (A_n) accelerations of 10 and 2 g's, respectively, are transposed into longitudinal and lateral accelerations of 2 and 10 g's, respectively, for the IRV. For the Atlas-Centaur launch configuration, the IRV and launch vehicle axis are parallel and hence the loads factors can be applied directly as shown to the IRV.

The load factors for reentry are the most severe. In addition to the reentry inertia loads, the aeroshell will experience a maximum aerodynamic pressure load of 15.6 psi (including a factor of safety of 1.25).



612385-3B

Figure 5.2-2 PIN CUSHION HEAT SOURCE -- VERTICAL ARRAY CAPSULE TEMPERATURE RISE (AFTER 1 HOUR OF HEATING FROM 1800°F)

IRV STRUCTURAL LOAD ENVIRONMENT

LAUNCH	AX	AN	G'S
1. ATLAS-CENTAUR			
(a) MAXIMUM AXIAL LOAD CONDITION (INCLUDES VIBRATION COMPONENT)	6.4	0.5	
(b) MAXIMUM LATERAL LOAD CONDITION (INCLUDES VIBRATION COMPONENT)	2.3	2.0	
2. SATURN I-B			
NOMINAL (DOES NOT INCLUDE VIBRATION COMPONENTS)	4.7	1.0	
DESIGN LOADS (INCLUDING VIBRATION SAFETY FACTOR)	10.0	2.0	
ABORT A _X (WITH RESPECT TO IRV)	10.0	2.0	
REENTRY ($\gamma = -10$ DEGREES TUMBLING)	31.0	2.8	
CHUTE DEPLOYMENT AND AIR SNATCH	8.0	2.0	

6.0 REENTRY VEHICLE

This section summarizes the technical efforts in the areas of heat leak analysis, and aerodynamic performance requirements. As described in Section 3.0, these factors combine with the heat source design as established in the previous section to define the basic requirement for a "bare" reentry vehicle design. As is also noted in Section 3.0, the HSHX design is not a constraint on the IRV design, and therefore discussion of the HSHX design effort is included in Section 8.0 IRV/Brayton System.

6.1 HEAT LEAK

During Task I-B, the thermal losses through the struts were evaluated for a re-designed composite strut consisting of T-111 and Rene' 41 materials with a peak Rene' 41 temperature of 1400°F. The total thermal losses for the circular planar array were updated for the reduced strut losses and the changes in heat source geometry affected in Task I-B.

6.1.1 Insulation

With the minimization of the circular planar heat source diameter to 49 inches for an array of nonvented capsules, some reduction in thermal losses through the superinsulation was obtained on the basis of a reduction in insulation surface area. Further reduction in the total thermal losses was obtained through a reduction in strut losses described below. Figure 6.1-1 is a plot of the total heat loss and the heat loss through the seal and superinsulation area as a function of insulation thickness. This curve is presented for a heat source to aeroshell temperature drop of 1700°F (2000° to 300°F). For the 2-inch layer of superinsulation which has been used in the designs to date, the total thermal losses from the heat source can be maintained under 400 watts.

6.1.2 Strut Heat Leak Analysis

One strut design was used for the five heat source designs which were evaluated in the Task I-A studies. This design consisted of eight composite struts of 22-inch length containing T-111 in the hot region and Rene' 41 (a superalloy with a considerably lower thermal conductivity than T-111, (15 Btu/hr-ft °F versus 40 Btu/hr-ft °F) in the colder section of the strut. The length of the T-111 section of the strut was designed to maintain a maximum Rene' 41 temperature of 1000°F for the nominal hot side to cold side temperature. For the Task I-B studies, the strut was redesigned to minimize heat losses. Maximum use of low conductivity Rene' 41 with a low cross-sectional area was achieved by designing to a maximum Rene' 41 temperature of 1400°F. This temperature limit was selected because of material degradation problems that occur with Rene' 41 in a vacuum at temperatures in excess of 1400°F.

Figure 6.1-2 presents the heat loss through eight 22-inch struts as a function of the cold end temperature of the strut for a heat source temperature of 2000°F and a maximum Rene' 41 temperature of 1400°F. The model is shown in Figure 6.1-3. Cross-sectional areas of T-111 and Rene' 41 are enumerated in Figure 6.1-4. Superinsulation surrounding the struts is 0.25-inch thick.

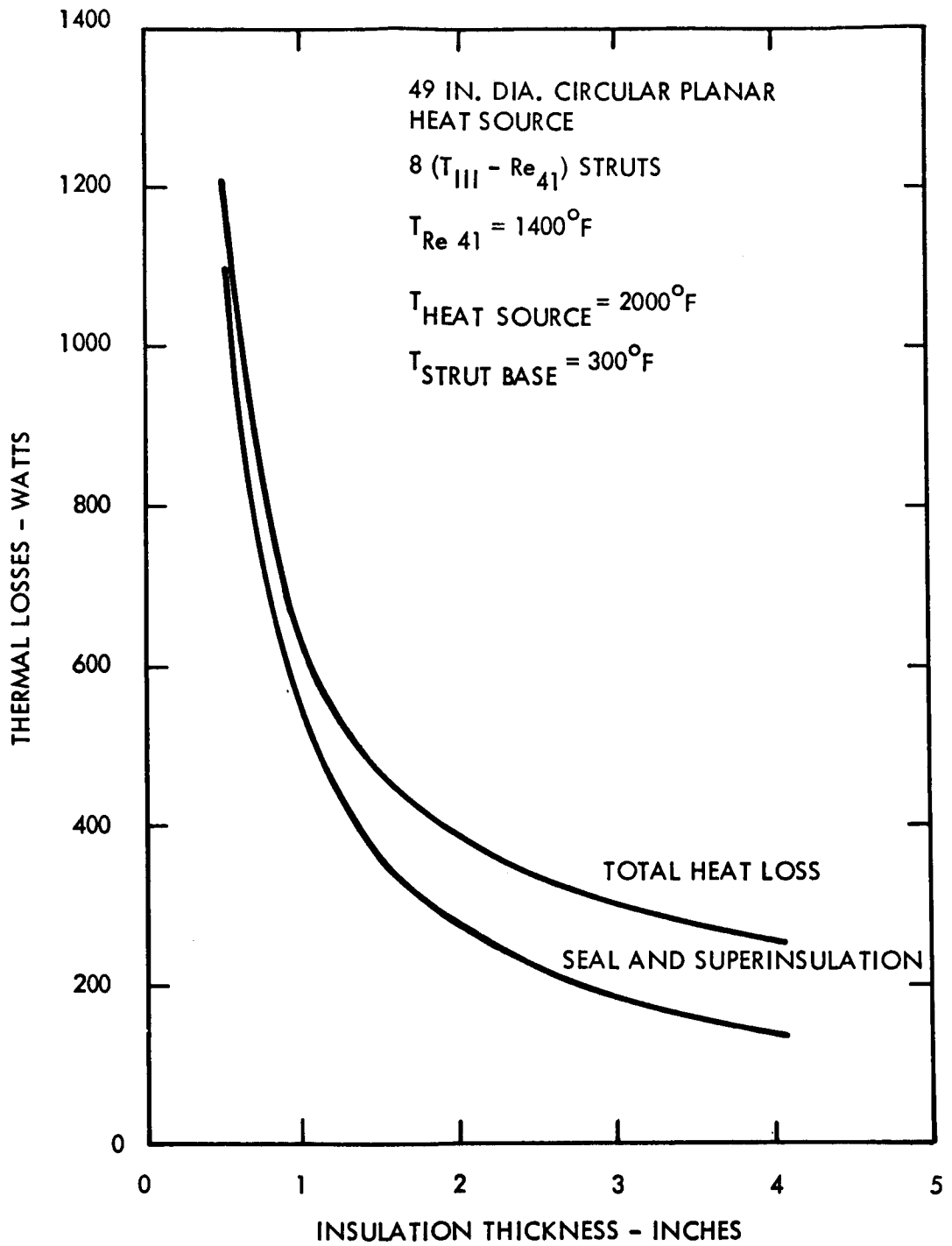


Figure 6.1-1 EFFECT OF INSULATION THICKNESS ON HEAT-SOURCE HEAT LOSSES

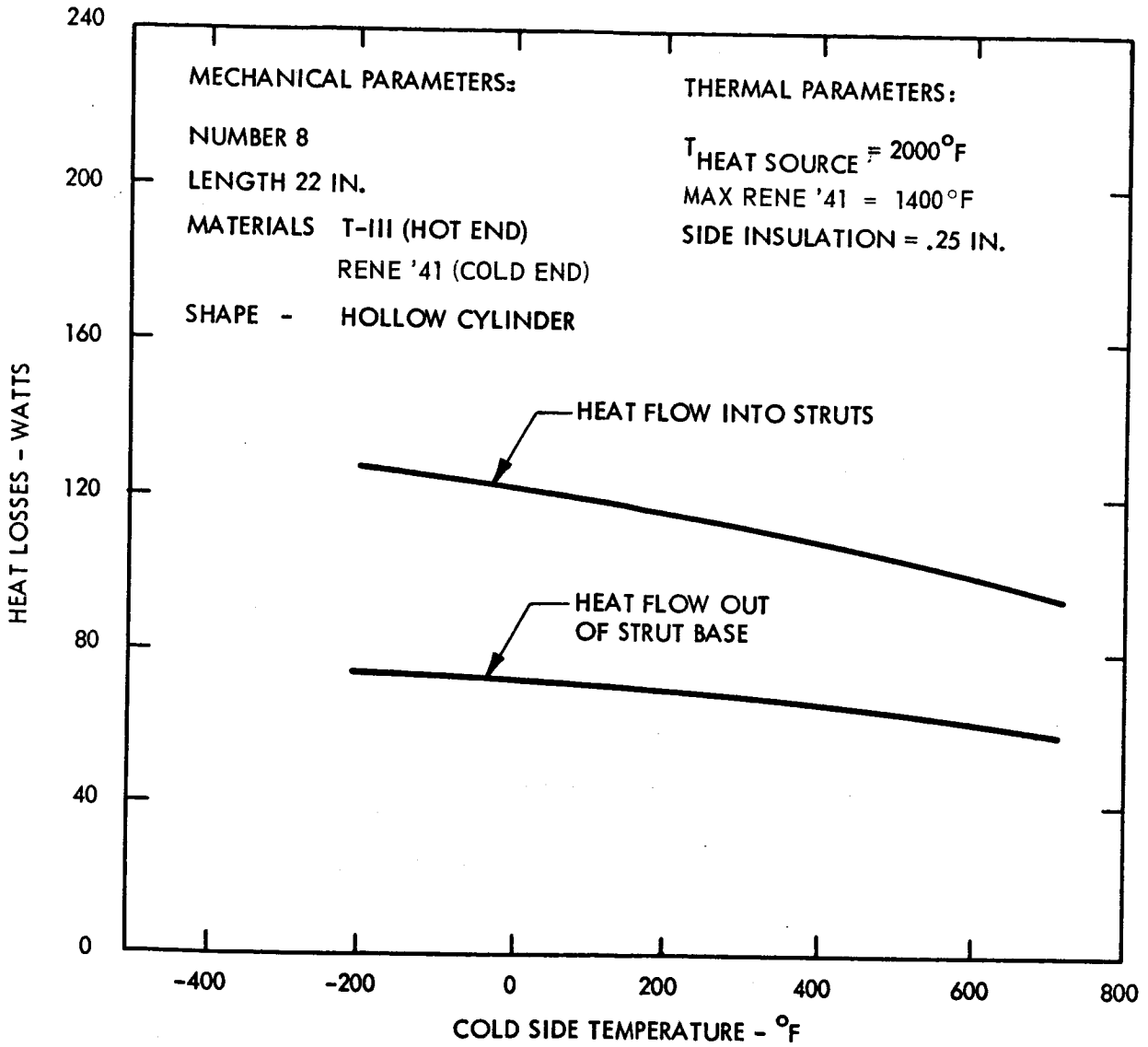
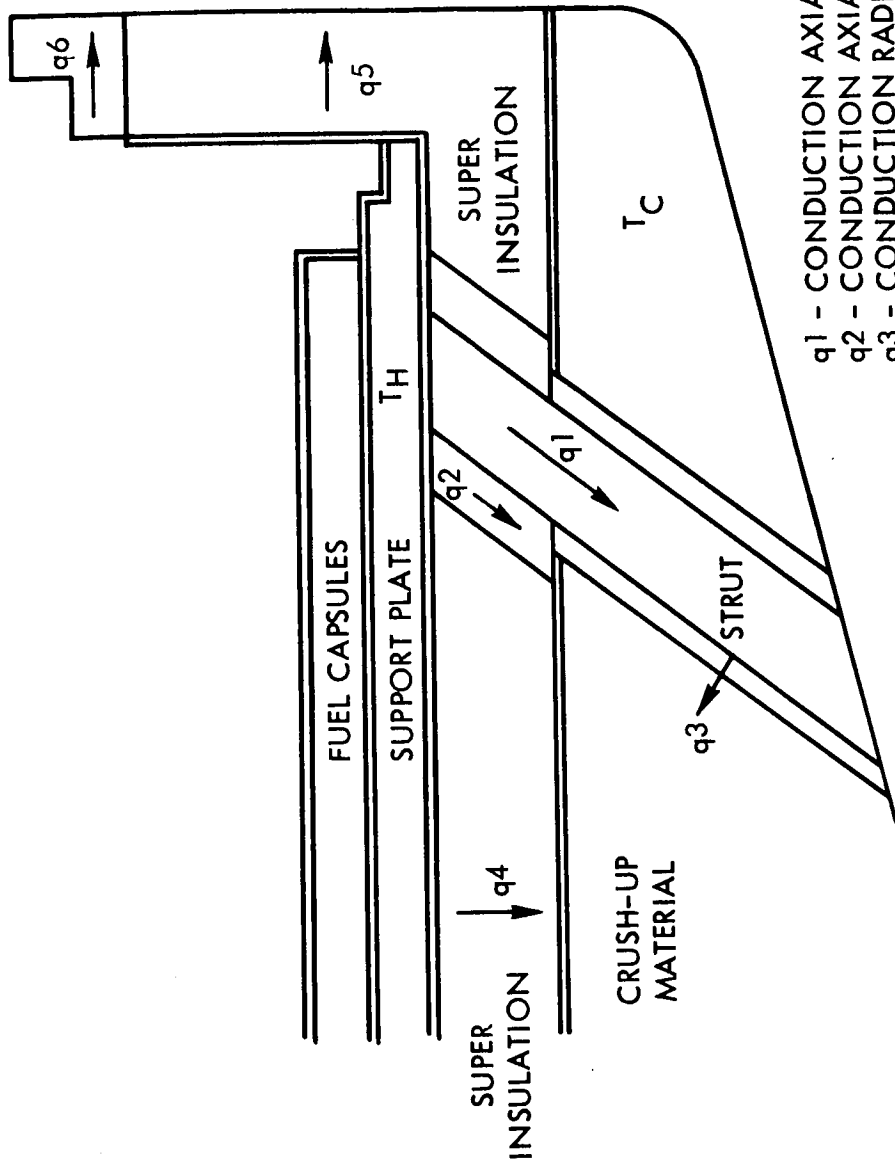
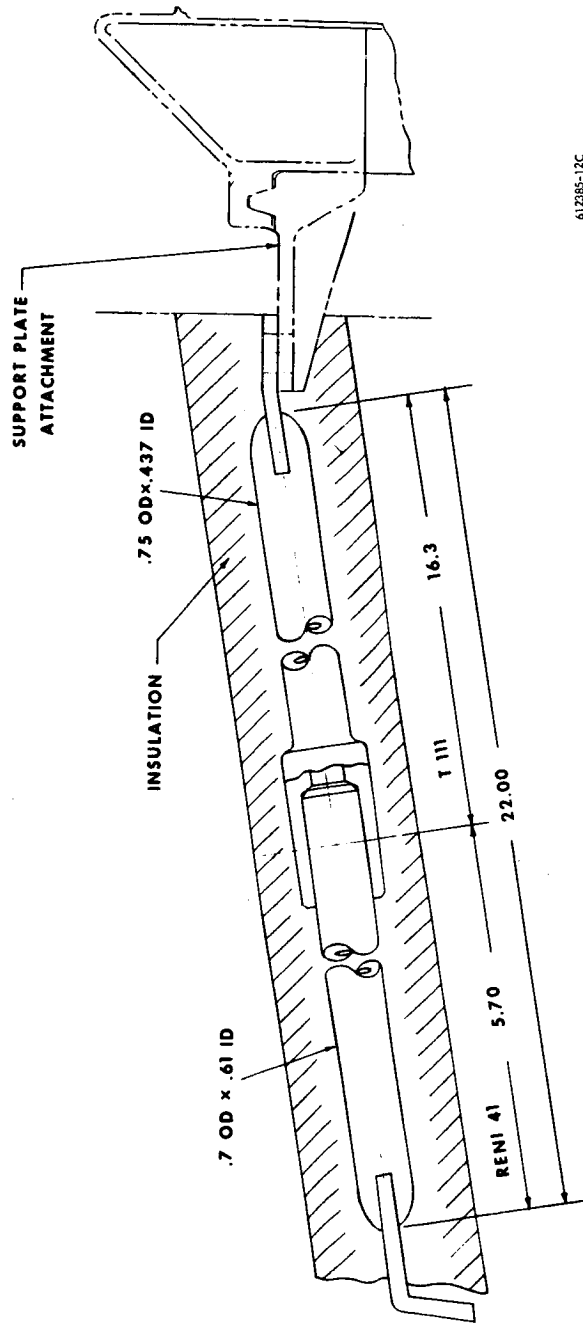


Figure 6.1-2 THERMAL LOSSES THROUGH STRUTS



- q1 - CONDUCTION AXIALLY ALONG STRUT
- q2 - CONDUCTION AXIALLY ALONG MIN-K RING
- q3 - CONDUCTION RADIALLY THRU STRUT INSULATION
- q4, q5 - CONDUCTION THRU SUPER INSULATION (SIDE AND BOTTOM)
- q6 - CONDUCTION THRU MIN-K CONNECTION RING

Figure 6.1-3 INSULATION SYSTEM -- HEAT FLOW MODEL



612285-12C

Figure 6.1-4 SUPPORT STRUT

The top line on Figure 6.1-2 shows the total heat loss through the struts and is the sum of the losses which are conducted out the base of the strut plus the losses conducted radially through the insulation and radiated to the crushup material. The bottom line represents heat loss conducted through the base of the strut. For a 300°F cold side temperature, the total heat losses through eight struts are 112 watts of which 68 are conducted through the base of the strut (14 watts per strut total and 8.5 watts per strut base respectively). Increasing the superinsulation thickness decreased the side losses from the strut and linearizes the temperature profile in each of the two sections of the strut. The net result is a reduction in the total heat losses through the struts and an increase in heat losses through the base of the struts. Referring to Figure 6.1-2, this can be visualized as the compression of the two curves to one curve at an intermediate position. For 300°F cold side temperature, elimination of the side losses by increasing the insulation thickness results in the reduction of total heat loss to 80 watts (10 watts per strut), all conducted at the strut base.

Figure 6.1-4 is a sketch of the support strut for nominal operation with hot and cold end temperatures of 2000° and 300°F and with a maximum T-111 to Rene' 41 junction temperature of 1400°F. The overall length of the strut was maintained at 22 inches with the length of the T-111 member at 16.3 inches. The strut is enclosed with superinsulation with a minimum thickness of 0.25 inch. The heat loss for this nominal temperature difference is 14 watts per strut of which 8.5 watts are coming out of the base of the strut and 5.5 watts are lost radially to the crushup material.

6.2 REENTRY VEHICLE DESIGN

The basic characteristics that have been analyzed in the comparative evaluation of the reentry vehicle design are described in this subsection. These analyses are grouped under the headings of aerodynamic heating, aerodynamic stability, and aeroshell design. The vehicle performance characteristics as defined in this section also hold true for both "bare" and "terminal" survival-class vehicles.

6.2.1 Aerodynamic Heating

6.2.1.1 Aerodynamic Heating Environment

6.2.1.1.1 General -- The heating analysis was performed for two heat source configurations using the 60-degree blunt cone shape which were the 1) circular planar shape flush mounted and 2) the pin cushion capsule arrangement with the capsules extending aft of the forebody base plane. The two shapes schematically drawn for the heating analysis are shown in Figure 6.2.1-1. The ratio of the vehicle nose radius to base radius was defined as 0.25 and the ratio of shoulder radius to base radius was set at 0.05. The shoulder cylinder length was limited to a maximum value of 15 percent of the base radius. The capsule heating factors were determined for the two design configurations for tumbling and spinning entry modes. The analysis was performed in two parts: a parametric analysis showing the effects of the capsule recession and protruding parameters at 180-degree angle of attack, and the effect of angle of attack for the specific shapes.

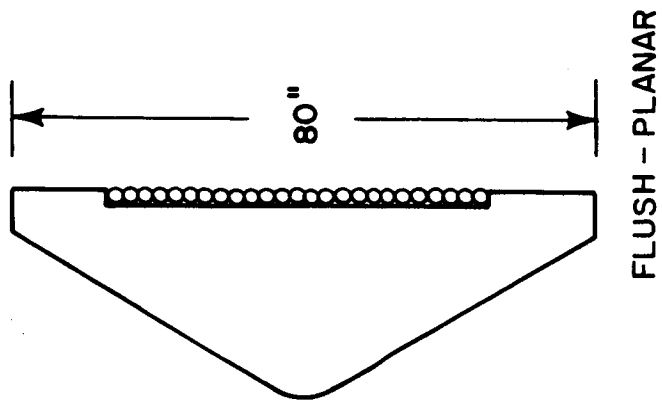
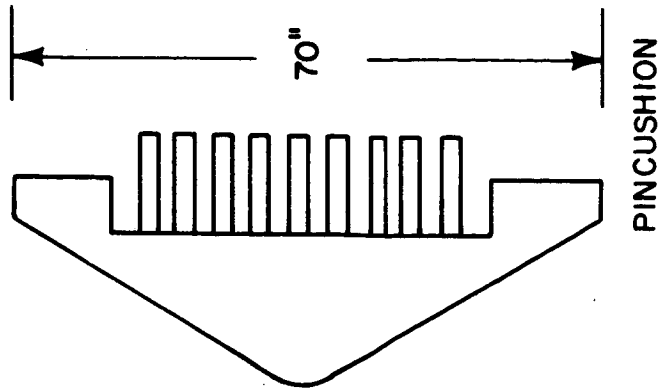


Figure 6.2.1-1 BASE CAPSULE CONFIGURATION

78-2912

Presented are aerodynamic heating factors for a general set of isotope capsule vehicle base configurations. Both recessed and protruding configurations were considered, with the restriction that the capsule, or plate on which the capsules lie, is solid. Thus, for the protruding system, the capsules sit on a solid cylindrical protrusion above the base plane of the vehicle. Although the geometry is generalized the heating factors obtained are applicable to the configurations considered. Because the analyses differ for recessed and protruding configurations, each is discussed separately below.

Although 180-degree angle of attack does not represent the maximum absolute heating attitude, it does represent the maximum heating in a possible stable attitude in case of a fence malfunction. The 180-degree case therefore must be considered in the design of the capsule configuration.

6.2.1.1.2 Flush and Recessed Capsule Analysis -- Forming the basis for both analyses is the data published by Nestler and Masser in Reference 6.2.1-2. This reference presents data for the laminar heat flux distribution over a flat-faced cylinder for Mach numbers between 1.5 and 13. Since no clear Mach number dependence is shown by the data, the authors use a single curve to represent all the data. This curve is summarized in the following table.

TABLE 6.2.1-1

HEAT TRANSFER DISTRIBUTION ON FLAT-FACED CYLINDERS

Local Radius Ratio (R/R_B)	0	0.2	0.4	0.6	0.8	0.9	1.0
Local Heating Ratio (\dot{q}/\dot{q}_{SF})	1.0	1.025	1.05	1.13	1.25	1.41	1.75
$R_B =$ Body Radius							
$\dot{q}_{SF} =$ Stagnation point heating rate on a flat-faced cylinder							

It is assumed here that if the tops of the capsules lie in the base plane of the vehicle, and no protrusions exist, then the resulting surface will be sufficiently flat for the curve of Table 6.2.1-1 to be applicable. The standard of reference for heating factors is, however, the nose stagnation point heating with vehicle at zero angle of attack ($\alpha = 0$). Therefore a relationship must be developed between the flat-faced cylinder stagnation heating rate and the hemisphere stagnation heating rate. Turning again to Reference 6.2.1-2, the authors present data for the ratio of flat-faced to hemisphere-stagnation velocity gradient (G_F/G_S). This at Mach 8. Therefore, since

$$\dot{q}_{SF}/\dot{q}_s = \sqrt{G_F/G_S} \quad (6-1)$$

then the ratio of flat-faced cylinder stagnation point heating to hemispherical stagnation heating is roughly one-half, if the cylinder radius is equal to the spherical radius. Since the heating rate is also proportional to the square

root of the nose radius, the desired stagnation heating factor for a 25-percent nose radius is

$$\dot{q}_{SF}/\dot{q} = \sqrt{\left(\frac{G_F}{G_S}\right) \left(\frac{R_n}{R_B}\right)} = 0.25 \quad (6-2)$$

Applying this factor to the values in Table 6.2.1-I produces the curve labelled $\Delta/D_c = 1.0$ in Figure 6.2.1-2.

The heating factor for the exposed capsules (see Reference 6.2.1-3), i.e., $\Delta D_c = 0$, is obtained from Reference 6.2.1-4, wherein potential flow theory is used to show that the velocity gradient is increased over the flat-faced value by a factor of 2, and that heating on the exposed capsules is, therefore, increased by $\sqrt{2}$.

To obtain the heating on recessed capsules, the local stagnation point heating variation with depression distance Δ/R_B is obtained from Reference 6.2.1-2, where it is presented as a function of varying concave nose radius (R_c/R_B). Omitting the details of the simple geometric derivation, the relationship between concave radius and depression length is

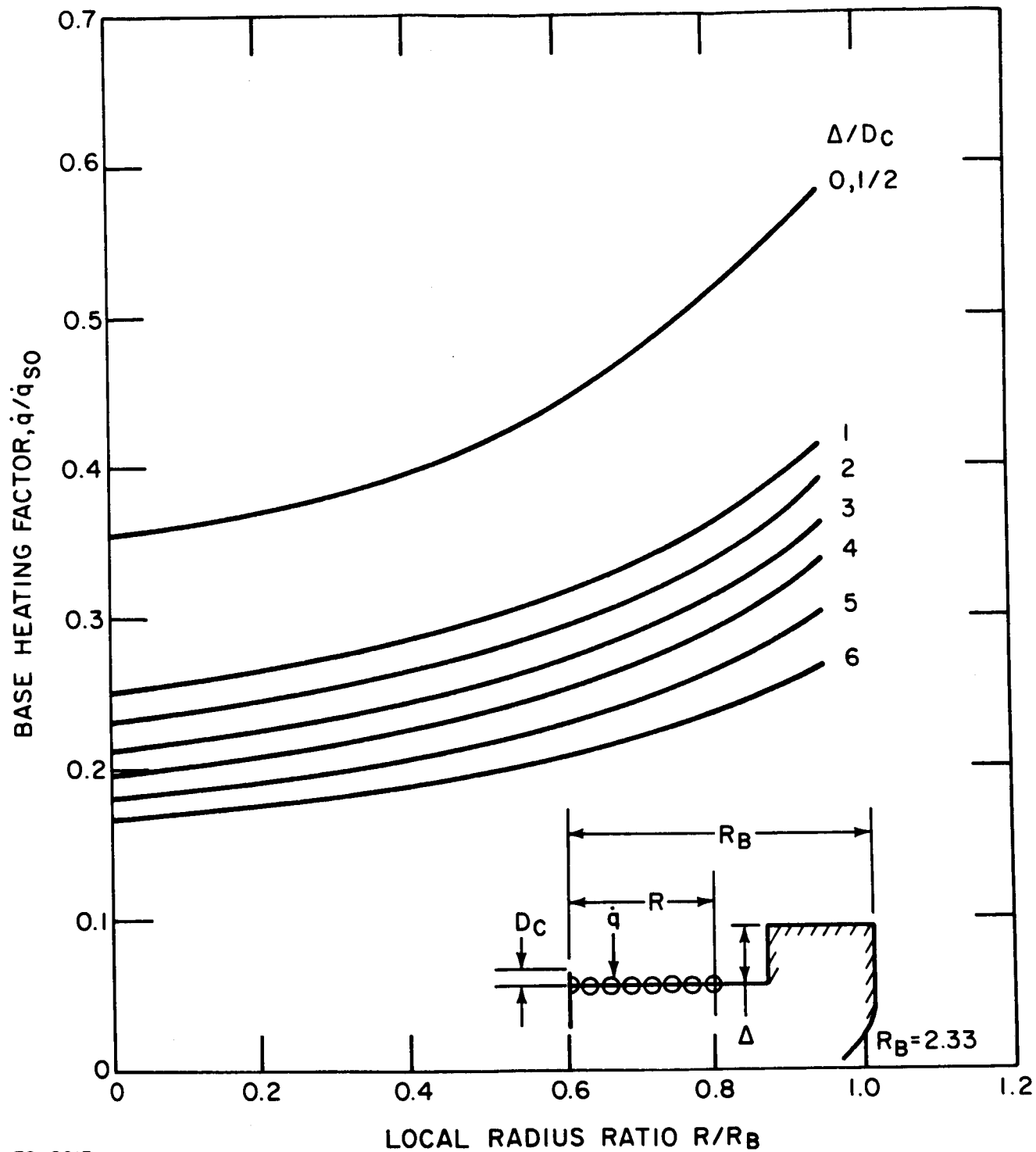
$$\frac{R_c}{R_B} = \operatorname{cosec}(\pi - \operatorname{arccot} \Delta/R_B) \quad (6-3)$$

Inherent in this equation is the assumption that the depression extends to the edge of the body, i.e., to R_B . It should be noted here that curves similar to Figure 6.2.1-2 were published previously (Reference 6.2.1-5) under the assumption that the depression did not extend to R_B . This would imply that the character of the shock is determined by the depression width. Reference 6.2.1-2 shows that the shock stand-off distance, at least, is essentially unaffected by the concavity geometry. The Reference 6.2.1-5 assumption leads to a more rapid decrease of heating factor with Δ/D_c than does the current assumption. Although the accuracy of both assumptions is open to argument, Figure 6.2.1-2 is preferred for its conservatism and because it does not violate the shock structure data.

To the above stagnation heating factor values, the flat-faced heating distribution is applied, with due consideration given to the increased surface length of the depression sides. This effective length increase is, however, relatively unimportant.

The resulting curves represent heating distributions for various depression depths regardless of the radial extent of the depression. The maximum capsule heating factor always occurs on the most outboard capsules. Each curve applies, however, only to the capsules and the capsule tray, and does not apply to the depression sides or base plane. Base plane heating factors are obtained from the curve $\Delta/D_c = 1$.

6.2.1.1.3 Protruding Capsule Analysis -- Unlike surface depressions, protrusions from the base plane will definitely alter flow and the heating distribution. Consider two flat-faced cylinders of radii R_1 and R_B , with R_1 less than R_B . The ratios of stand-off distance to body radius are equal.



78-2913

Figure 6.2.1-2 CAPSULE HEATING FACTOR ($\alpha = 180^\circ$)

$$\delta_I/R_I = \delta_B/R_B = k \quad (6-4)$$

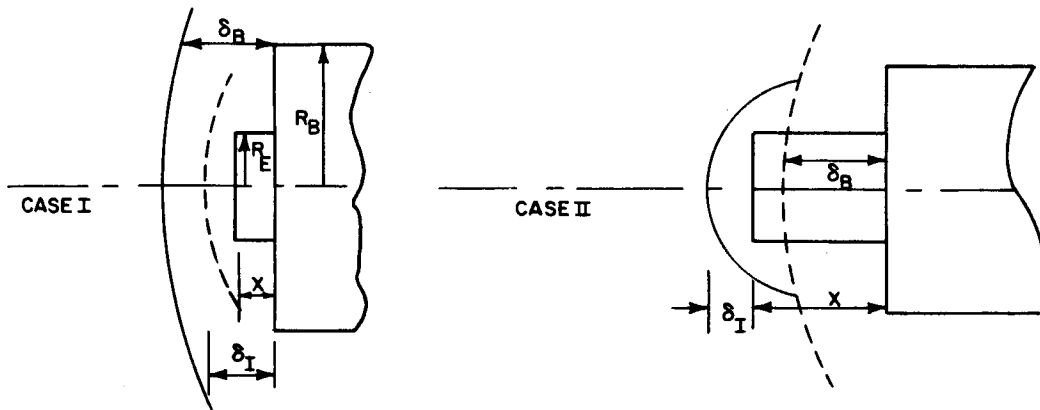
If the smaller cylinder is placed such that it protrudes a length, x , from the larger cylinder, two distinct conditions emerge. Namely,

$$\text{Case I: } \delta_I + x \leq \delta_B \quad (6-5)$$

and

$$\text{Case II: } \delta_I + x \geq \delta_B \quad (6-6)$$

These cases are represented graphically in the sketches below. In Case I, the sonic point lies on the outer radius of the composite body, at R_B , and the flow over the frontal surfaces is subsonic. In Case II, sonic points occur on the shoulders of both cylinders, at R_I and R_B the flow is mixed, and the flow over the face of the inner (smaller) cylinder is unaffected by the presence of the downstream shock.



In the general symmetrical blunt body flow field, the velocity gradient normal to the free stream direction varies along the stagnation streamline from a maximum immediately behind the normal shock to the stagnation value G_s at the body. The variation is small, and is here assumed to be linear with x . Returning to Case I, it is assumed that the presence of the smaller cylinder will truncate the G -profile, so that the velocity gradient at the stagnation point (on the small cylinder) will vary linearly with x between the limits of the case. The velocity gradient for any x may therefore be written:

$$G_s(x) = G_{sB} + x \left(\frac{G_{sI} - G_{sB}}{\delta_B - \delta_I} \right) \quad (6-7)$$

it can also be shown that

$$G = K'/R \quad (6-8)$$

where K' is a proportionality constant and the subscripts B and I refer to conditions associated with the flat-faced cylinders of radius R_B and R_I , respectively.

By combining Equations (6-4), (6-7), and (6-8), there results the simple expression:

$$G_s(x) = G_{sB} \left[1 + \frac{1}{K} \frac{(X/R_B)}{(R_I/R_B)} \right] \quad (6-9)$$

subject to the restriction of Equation (6-5).

In Case II,

$$G_s(x) = G_{sI} = \text{constant} \quad (6-10)$$

for all x of Equation (6-6).

Since the dependence of stagnation point heating on velocity gradient is known, the variation of stagnation heating factor $\dot{q}_s(x)/\dot{q}_{so}$ can be calculated. (The factor $\sqrt{2}$ must be included in all protrusion calculations to account for the velocity increase due to capsules.)

By using the conversion

$$X = n\Delta \quad (6-11)$$

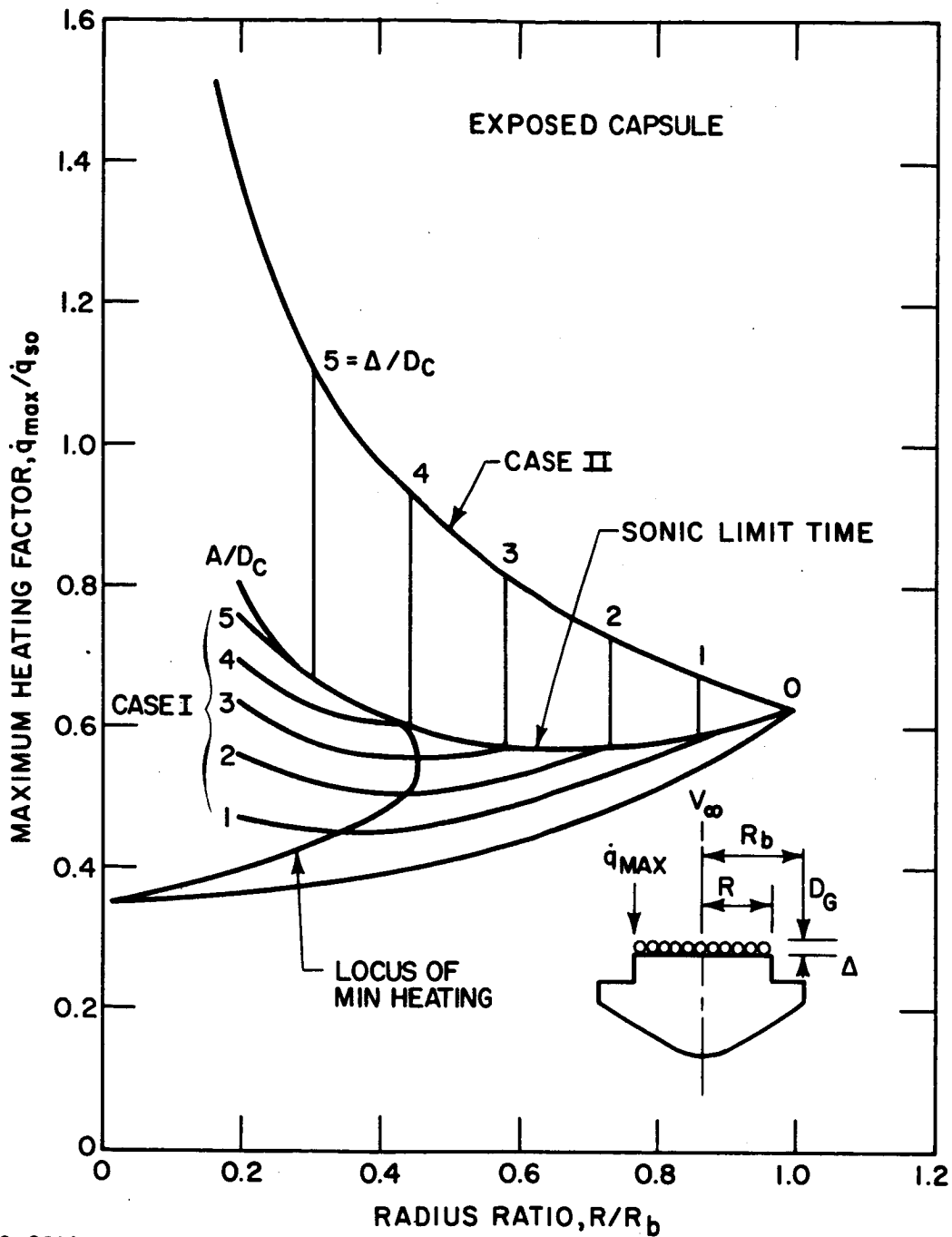
in Equation (6-9) and assuming the distribution of Table 6.2.1-I, the curves of Figure 6.2.1-3 were generated. It is to be noted that Equation (6-9) represents a two parameter family of curves. The variation in Figure 6.2.1-3 of $\dot{q}_{max}/\dot{q}_{so}$ with R_I/R_B for any fixed Δ/D_c represents discrete values of \dot{q}_{max} on the outboard capsule at radius R_I ; it does not represent a distribution over the surface of the smaller cylinder. Thus, for all $\Delta/D_c > 0$, $\dot{q}_{max}/\dot{q}_{sc}$ approaches infinity as R_I/R_B approaches zero because the stagnation point heating approaches infinity. The resulting curves corresponding to Case I, shown below the sonic limit line in Figure 6.2.1-3 exhibit a minimum point, the locus of which is also drawn in. This locus indicates a preferred radius for any required protrusion length to obtain minimum heating.

The sonic limit line defines the transition point from the Case I conditions to the Case II condition of sonic flow at the shoulder of the smaller cylinders (and on the outboard capsule). The transition is, of course, discontinuous and the maximum heating factor jumps to a much higher level for all greater values of R_I/R_B , then decreases along the maximum sonic heating line as

$$\dot{q}_{max}/\dot{q}_{so} \sim \sqrt{\frac{R_B}{R_I}} \quad (6-12)$$

due to the decrease in stagnation heating rate.

6.2.1.1.4 Results -- The curves presented in Figure 6.2.1-2 and 6.2.1-3 define the variation in heating factors on the IRV isotope capsules at an angle of attack of 180 degrees, that is, for rearward reentry and rearward descent. As might



78-2914

Figure 6.2.1-3 MAXIMUM HEATING FACTOR ($\alpha = 180^\circ$)

have been expected, the curves indicate that protrusions are undesirable, and that depressed arrays are advantageous in terms of heat load. The decrease in heating factor is monotonic from maximum protrusion to maximum depression. Depression depths beyond $\Delta/D_c = 5$, however, produce continuously lesser decreases in heating.

The variation with radius ratio is not as simple. For depressed capsules, it is evident that the capsules should be placed as close to the central axis as is possible, if heating factors are to be minimized. Where a protruding capsule tray is required, however, an optimum radius exists for any protrusion height. The preferred radii generally fall around $0.4 R_B$ for current designs. Radii smaller than $0.2 R_B$ produces heating factors approaching "infinity" and excessively large radii incur the penalty associated with sonic point heating.

Although the trend and relative levels of heating factors presented in Figures 6.2.1-2 and 6.2.1-3 are felt to be reasonably accurate, it should be stressed here that the calculations are based on ideal gas data of limited accuracy. To correct the data for real gas effects would reduce the stagnation point heating values by 25 percent. However, the flat-faced stagnation point heating data shows a variation of ± 30 percent about the value used. In addition, the distributions given in Table 6.2.4-I are based on data which show deviations up to 20 percent. A reasonable upper bound of the data with the real gas correction included closely approximates the values given here. Again it must be stressed that there is no entirely adequate theoretical analysis for the complex shapes considered here and that shock tunnel tests of the actual configurations are highly desirable.

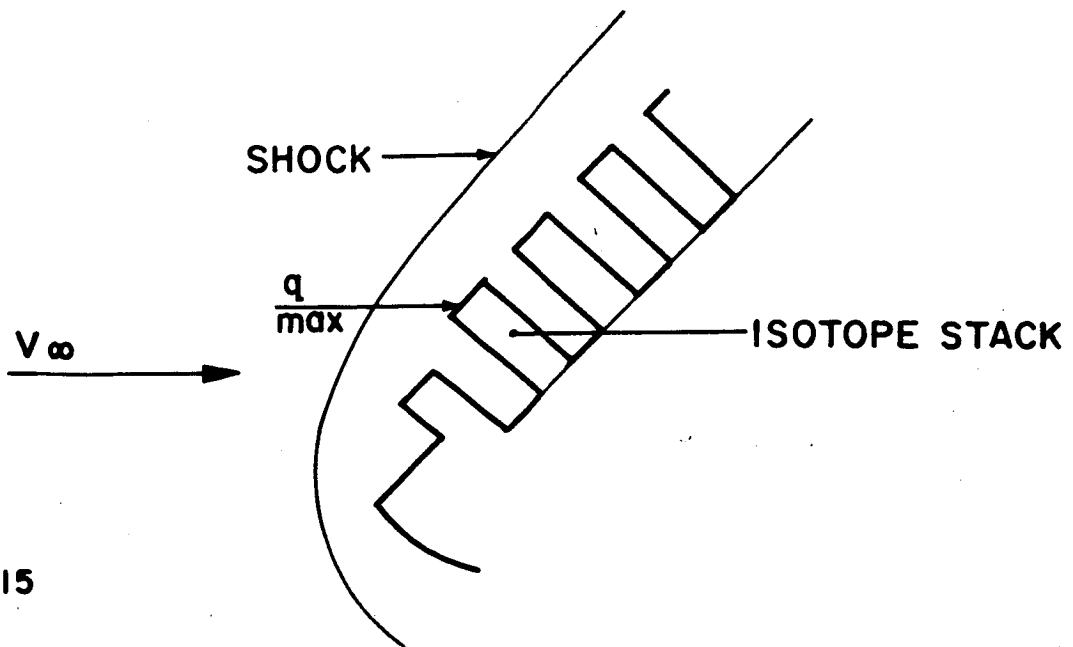
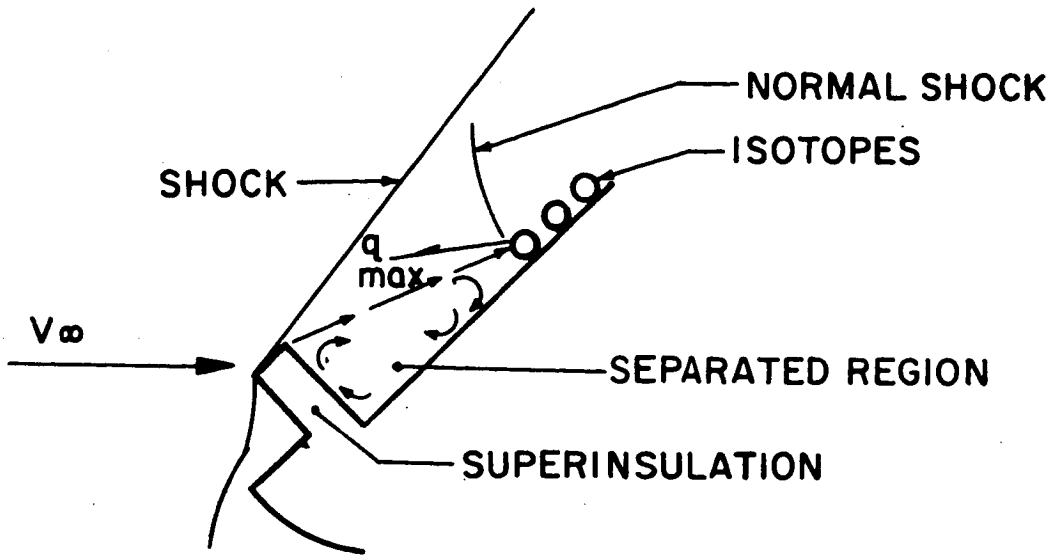
Angle of Attack Effects

The complex geometry of each configuration makes exact analysis of the flow geometry impossible without test data. The geometry must be simplified and some rather gross assumptions must be made before a reasonably simple analysis can be formulated. The results must also be considered somewhat tenuous under these circumstances, and shock tube tests of the several configurations are clearly indicated.

The first case chosen for this study was a tumbling entry trajectory for which the entry conditions were $V_e = 26,000$ fps, $\gamma_e = -10^\circ$ at $Z_e = 400$ kft. Free stream conditions were a velocity (V_∞) of 26,000 fps, a Mach number of $M_\infty = 30$, and a Reynolds number of $Re_D = 10^4$. These conditions correspond to a maximum heating point for the tumbling portion of a trajectory. General assumptions for all configurations are a) that the flow across the maximum diameter can be treated as two-dimensional, and b) that a steady state flow field exists.

Analysis

Flow field sketches for the two configurations are shown in Figure 6.2.1-4. Employed on Configuration 1 is an attached shock emanating from the superinsulation (using the super insulation produces the most aggravated heating rates). From this point the flow separates, to re-attach to the nearest isotope capsule while passing through a normal shock (though not necessarily stagnating).



78-2915

Figure 6.2.1-4 FLOW FIELD SKETCHES

These models are simplified, but do provide a reasonably accurate picture with which to define the heating rates. The inviscid flow is defined numerically by simple oblique shock relations while the separated region does not require detailed analysis. An analysis along the lines of Brower's work (Reference 6.2.1-6) showed that the flow cannot re-attach upstream of the isotope capsule position. The presence of the protruding capsule, however, implies the existence of a strong shock in this region. The assumption of reattachment at the "leading edge" of the isotope capsule produces conservatism in the results which is not unrealistic. Laminar similarity theory (Reference 6.2.1-7) is used to define the maximum heating. It can be shown that the heating ratio may be written as

$$\frac{\dot{q}_{\max}}{\dot{q}_{\text{so}}} = k \sqrt{\left(\frac{\rho}{\rho_{\infty}}\right) \left(\frac{\phi}{\phi_{\infty}}\right) \left(\frac{T}{T_{\infty}}\right) \left(\frac{R_n}{X}\right)}$$

where

ρ = density

ϕ = velocity

T = temperature

R_n = vehicle nose radius

X = length from stagnation point

k = constant dependent upon free stream and stagnation conditions

subscript ∞ = free stream condition.

In this development, viscosity is assumed to be linearly dependent upon temperature. Since the length parameters are fixed for each configuration, it remains only to maximize the ρUT -product to maximize the heating.

For Configuration 2 a strong shock is assumed to envelop the stacked region of isotope capsules. The maximum heating orientation is taken to be that at which the shock lies closest to the stack corners. The heating on a corner stack must be defined with respect to an effective flat-faced radius. The effective flat-faced radius at this point can be defined as

$$R_{\text{eff}} = \frac{1}{\pi} \int_0^{\pi} k(\phi) d\phi$$

where R is measured from a point equidistant from the three nearest edges of one stack, and ϕ is measured from the centerline on the face of the stack. The heating factor at this point may be characterized by

$$\frac{\dot{q}_{\max}}{\dot{q}_{\text{so}}} = \left(\frac{\dot{q}_{\text{comer}}}{\dot{q}_{\text{sflat}}}\right) \left(\frac{\dot{q}_{\text{sflat}}}{\dot{q}_{\text{ssemi}}}\right) \sqrt{\frac{R_n}{R_{\text{eff}}}}$$

Here $\dot{q}_{\text{comer}} / \dot{q}_{\text{sflat}}$ is obtained from extrapolation of the data of Reference 6.2.1- , and $\dot{q}_{\text{s flat}} / \dot{q}_{\text{s hemi}}$ is the conversion factor from flat face stagnation point heating to hemispherical stagnation heating obtained from Nestler's work (Reference 6.2.1-2). This procedure yields a value of 2.02 at the corner of the stack. It should be stressed, however, that the corner of the stack does not actually represent the isotope capsule, since the capsule is submerged an unknown increment in the graphite stack.

The capsule heating factors are applied as follows: For the fixed angle of attack entry the capsule heating factors are as shown in Figures 6.2.1-5 and 6.2.1-6. For tumbling entry the average values for the over the full 360 degrees are used. For the vehicle spinning, with a specific angle of attack envelope value, α , the capsule heating factor has been taken to be the average of the $\pm \alpha$ values.

Capsule Heating

The capsule heating is shown in Figures 6.2.1-7 through 6.2.1-12 and the heating comparison in Table 6.2.1-II. The comparison of the two design shapes shows that for all cases the capsule heating is higher for the pin cushion shape than for the planar. The two dominant factors effecting the heating are the $W/C_D A$ and the influence of the capsule configuration on the capsule heating factors. Both factors tend to increase the capsule heating for the pin cushion due to a higher $W/C_D A$ (41.4 compared to 33.1 for the planar) and higher base heating factors (see Figures 6.2.1-5 and 6.2.1-6). A comparison of the two failure modes, tumbling and rearward, shows higher integrated heating for the rearward case because of the lower effective $W/C_D A$ for each shape.

A comparison of the nominal entry mode with the failure modes cannot determine the most severe condition because the capsule temperature which is a function of both the integrated heating and the heat rate is the criterion to be analyzed. A comparison does show that for a spin rate of 0.785 rad/sec on the nominal trajectory failure mode cases will produce higher temperatures because both integrated and heat rate values are higher. The spin rate of 2.09 rad/sec will produce lower temperatures than the failure modes for the pin cushion shape but some reentry angle dependency is noted for the circular planar configuration and a thermal analysis would be required to determine the controlling trajectory. This same effect occurs when comparing entry angles within the failure mode analysis where the $\gamma_E = -10$ trajectory produces higher heat rates but lower integrated heating than the $\gamma_E = 0$ condition.

A comparison of the entry conditions for various spin rates indicates that the higher spin rate will produce higher capsule heating. This difference in heating includes not only the effect of spin rate but also a change in angle of attack which resulted when the retro rocket orientation was changed from the doughnut mounted concept to a nose mounted concept. This higher entry angle of attack, 121 degrees compared to 78 degrees, resulted in a higher angle of attack throughout the trajectory and the subsequent higher heating factors (Figure 6.2.1-4). This comparison is valid if it is remembered that two different retrorocket concepts are being compared, not one concept at different spin rates, the changes in the resulting moments of inertia required the spin rate change for vehicle stability.

TABLE 6.2.1-II
AERODYNAMIC HEATING CAPSULES

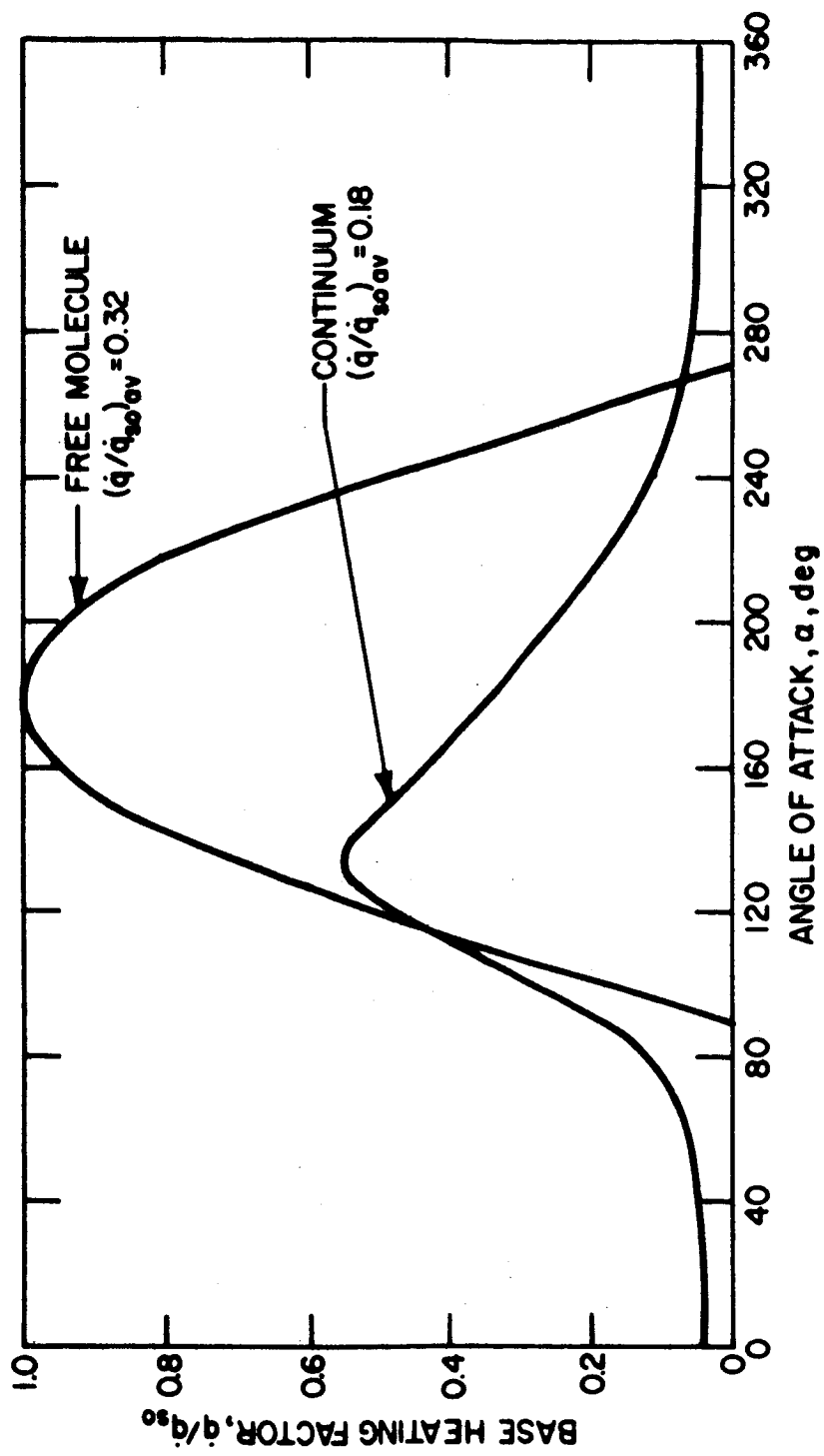
Degree	Circular Planar (Flush)				Pin Cushion			
	Tumbling		Rearward		Tumbling		Rearward	
	(Btu/ft ²)	(Btu/ft ² - sec)	(Btu/ft ²)	(Btu/ft ² - sec)	(Btu/ft ²)	(Btu/ft ² - sec)	(Btu/ft ²)	(Btu/ft ² - sec)
0	9900	43	23950	50	43870	185	51200	178
-10	3600	130	4100	136	13260	505	14000	493

Nominal Trajectory

$\gamma_E = - 2.25$ Deg

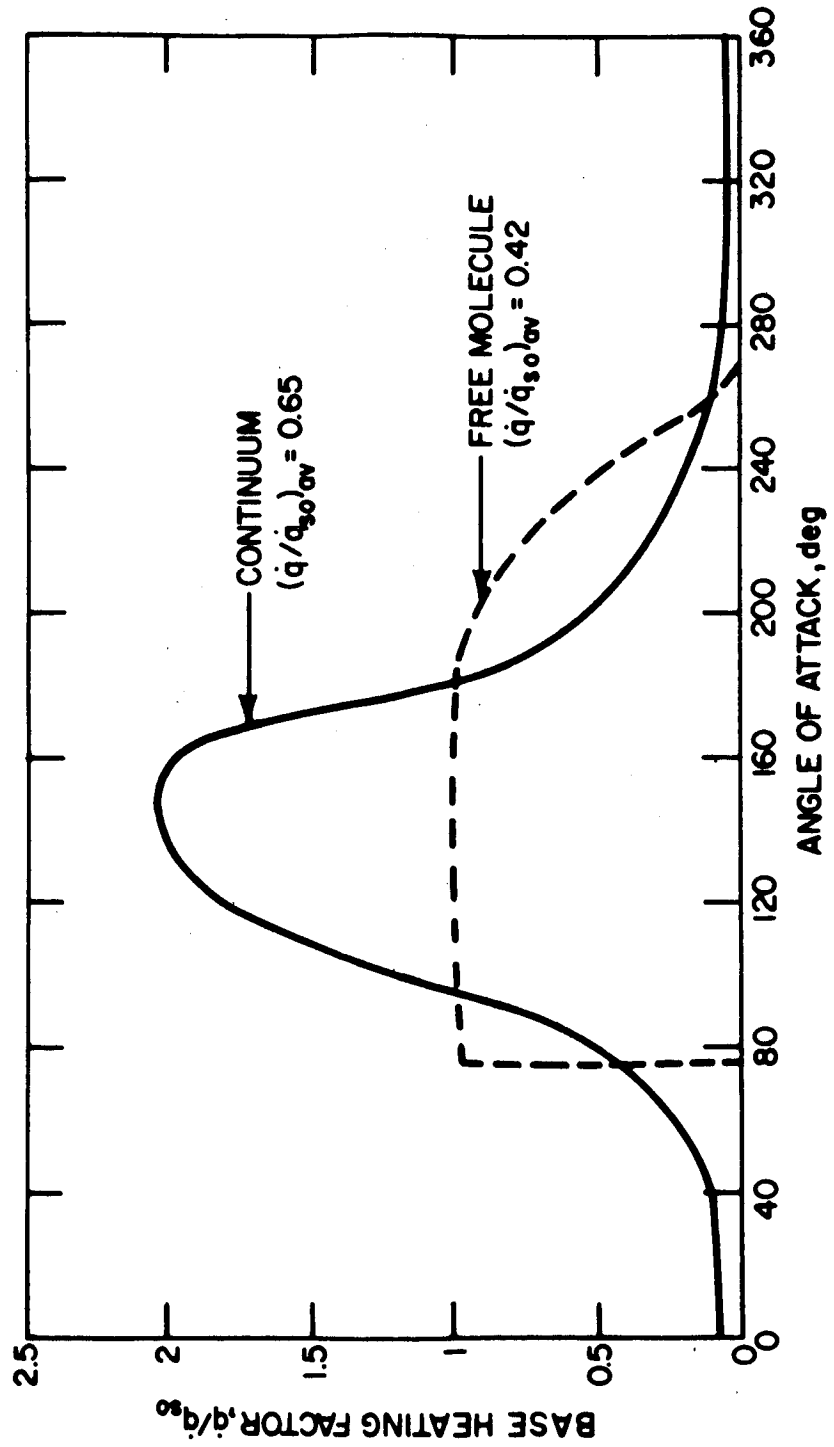
Capsule Heating

P_E (Rad/sec)	Circular Plan (Flush)		Pin Cushion	
	\dot{Q}_c (Btu/ft ²)	$\dot{Q}_{c_{max}}$ (Btu/ft ² -sec)	$\dot{Q}_c dt$ (Btu/ft ²)	$\dot{Q}_{c_{max}}$ (Btu/ft ² -sec)
0.785	1430	13	3350	29
2.09	4325	54	12320	160



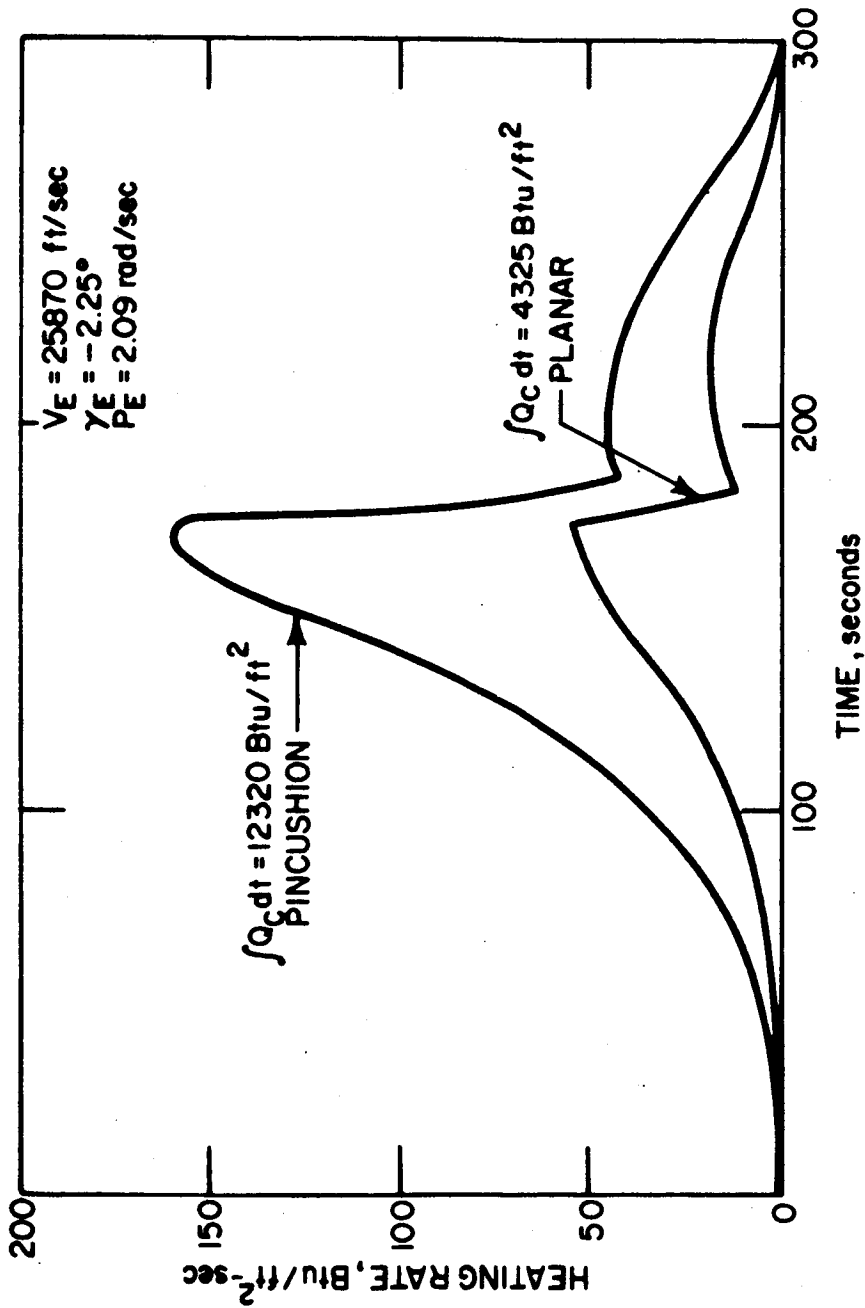
78-2916

Figure 6.2.1-5 BASE HEATING, RECESSED BASE



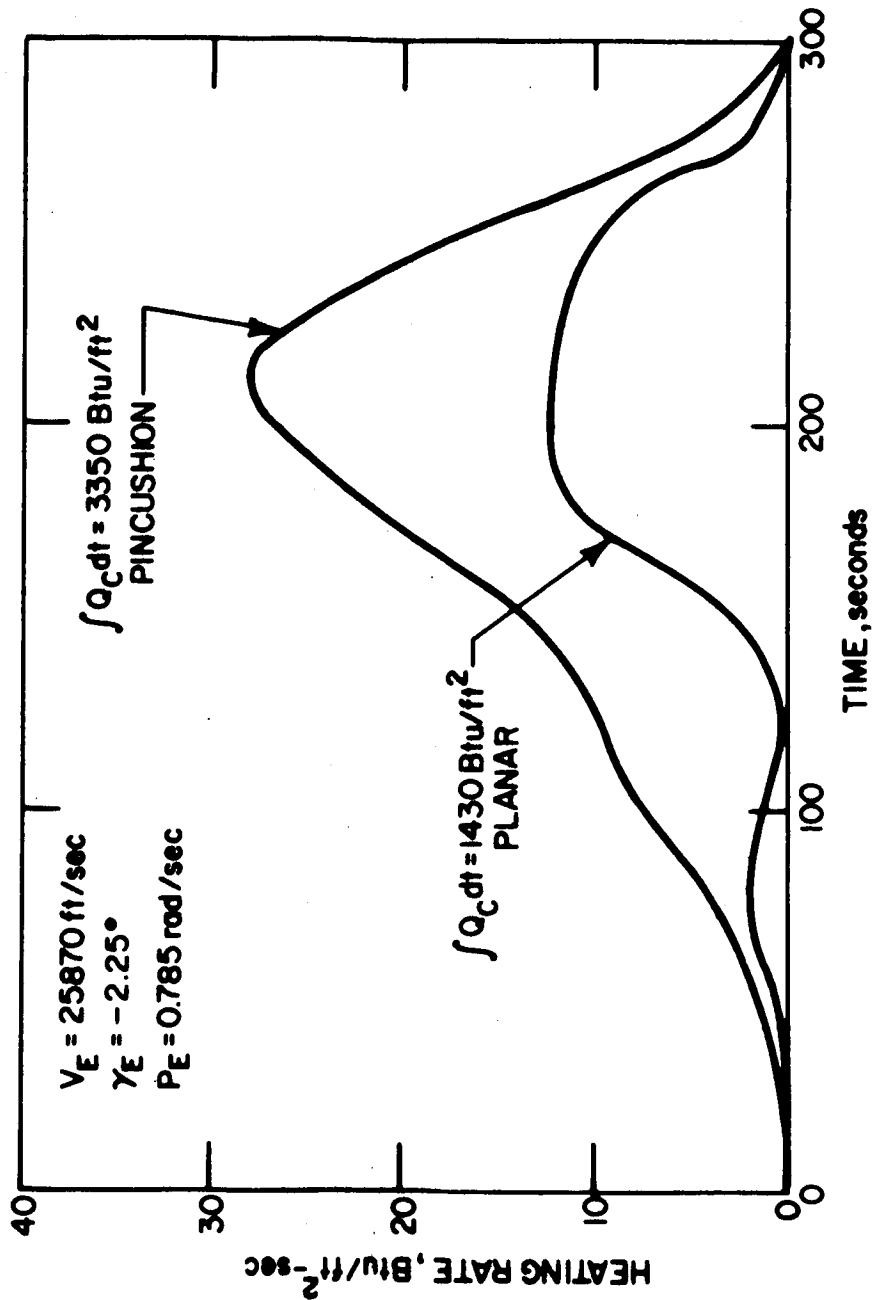
78-2917

Figure 6.2.1-6 BASE HEATING, STACKED CAPSULE CONFIGURATION



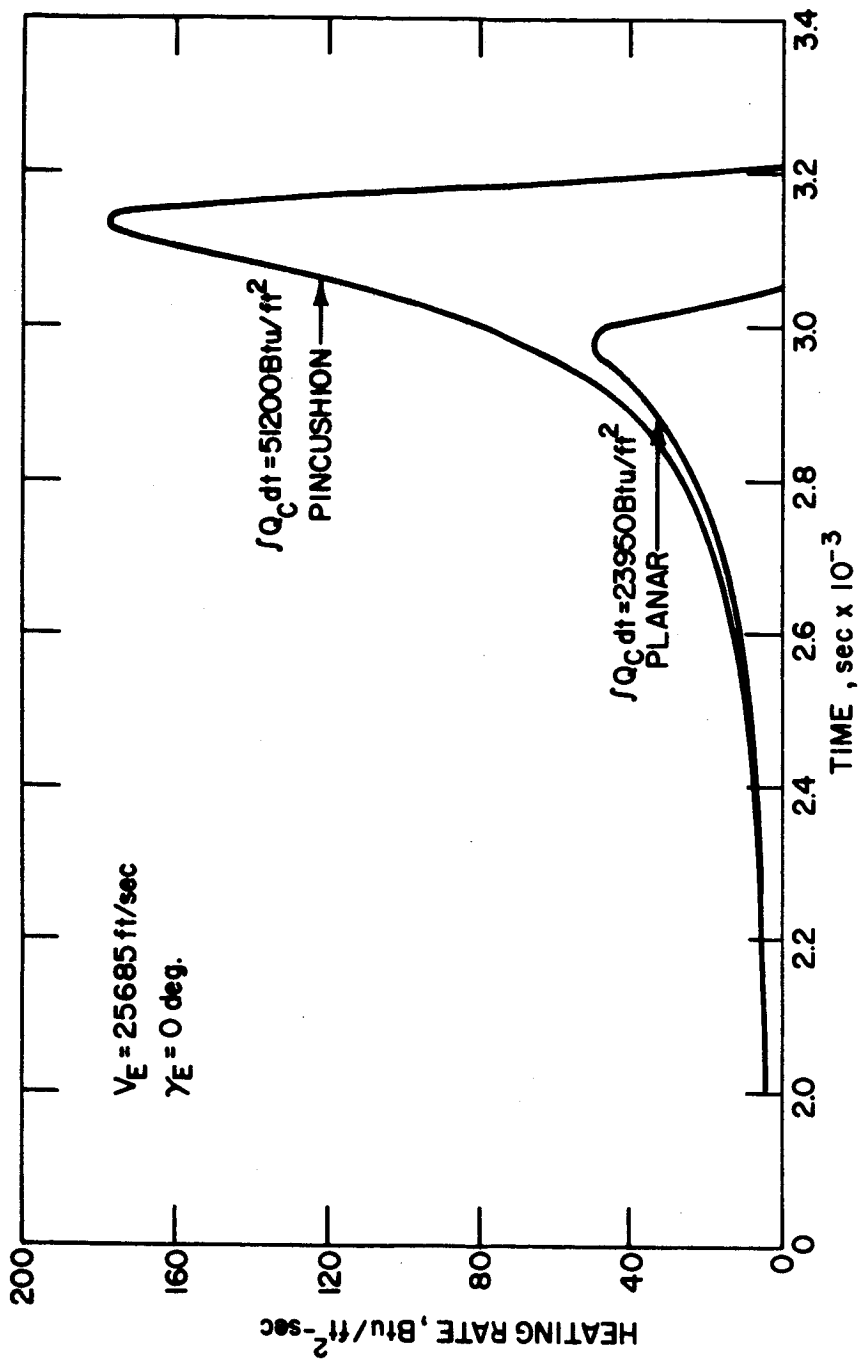
78-2918

Figure 6.2.1-7 CAPSULE BASE HEATING NOMINAL ENTRY (HIGH SPIN RATE)



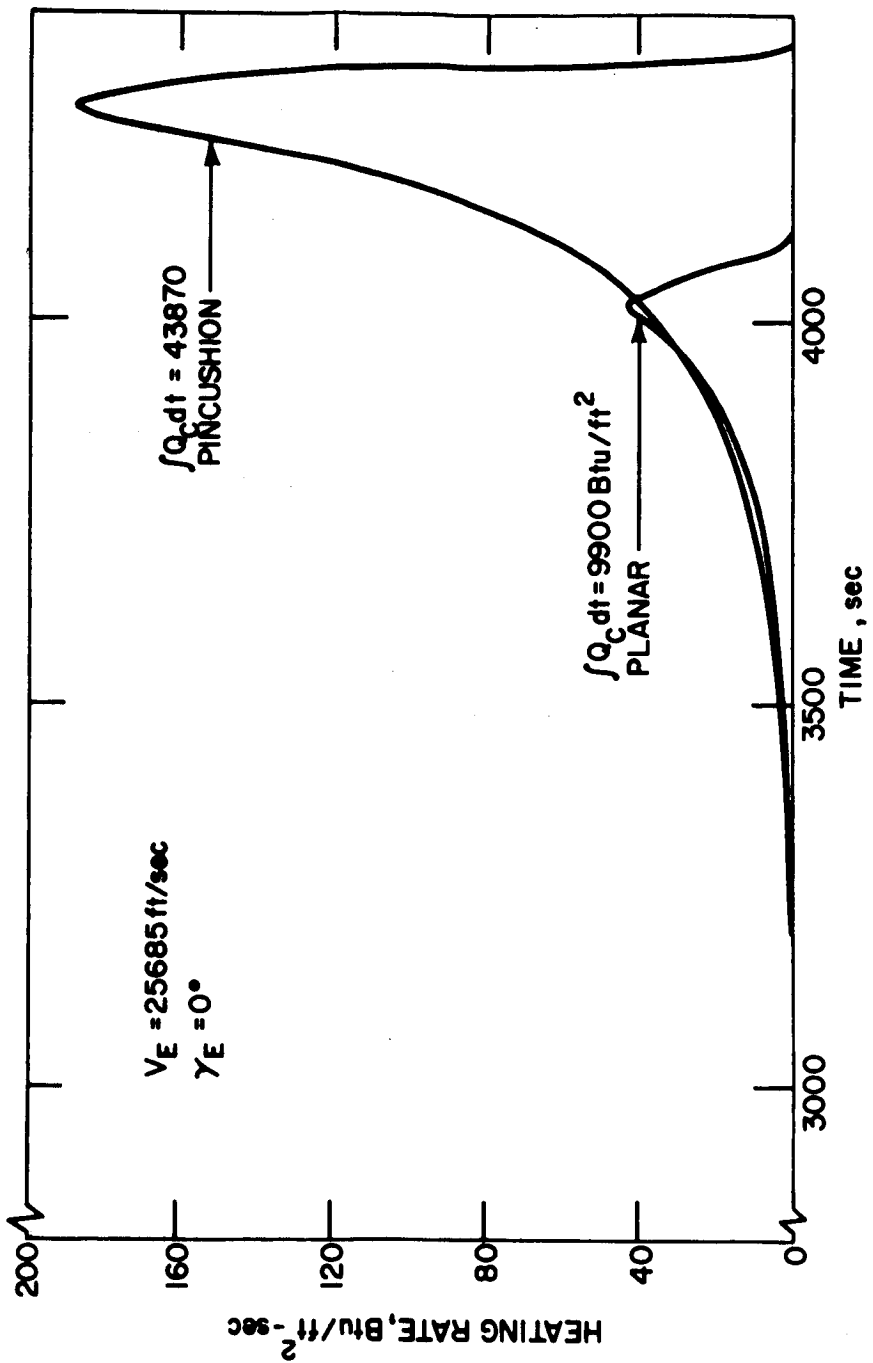
78-2919

Figure 6.2.1-8 CAPSULE BASE HEATING NOMINAL ENTRY (LOW SPIN RATE)



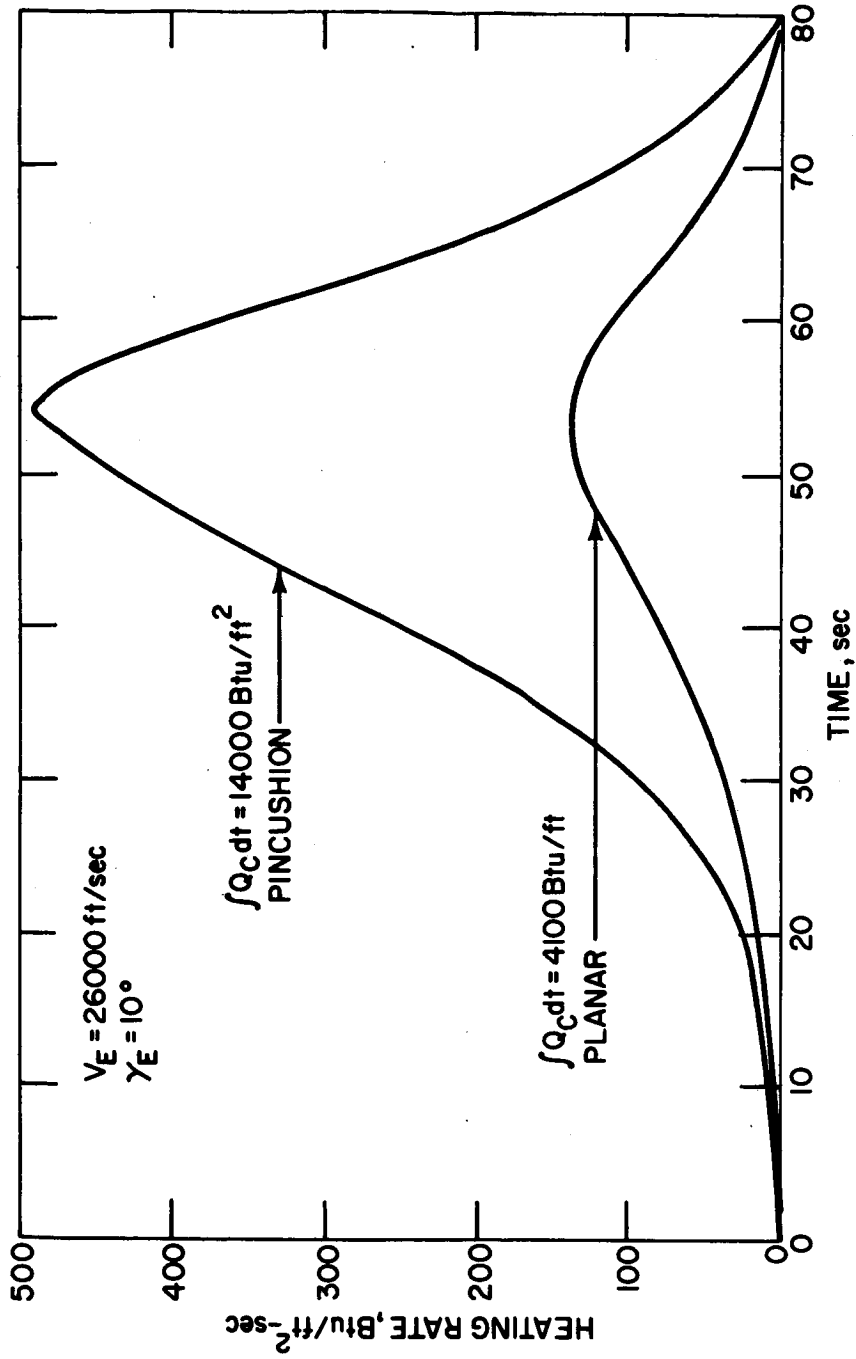
78-2920

Figure 6.2.1-9 CAPSULE BASE HEATING (1.80° REARWARD)



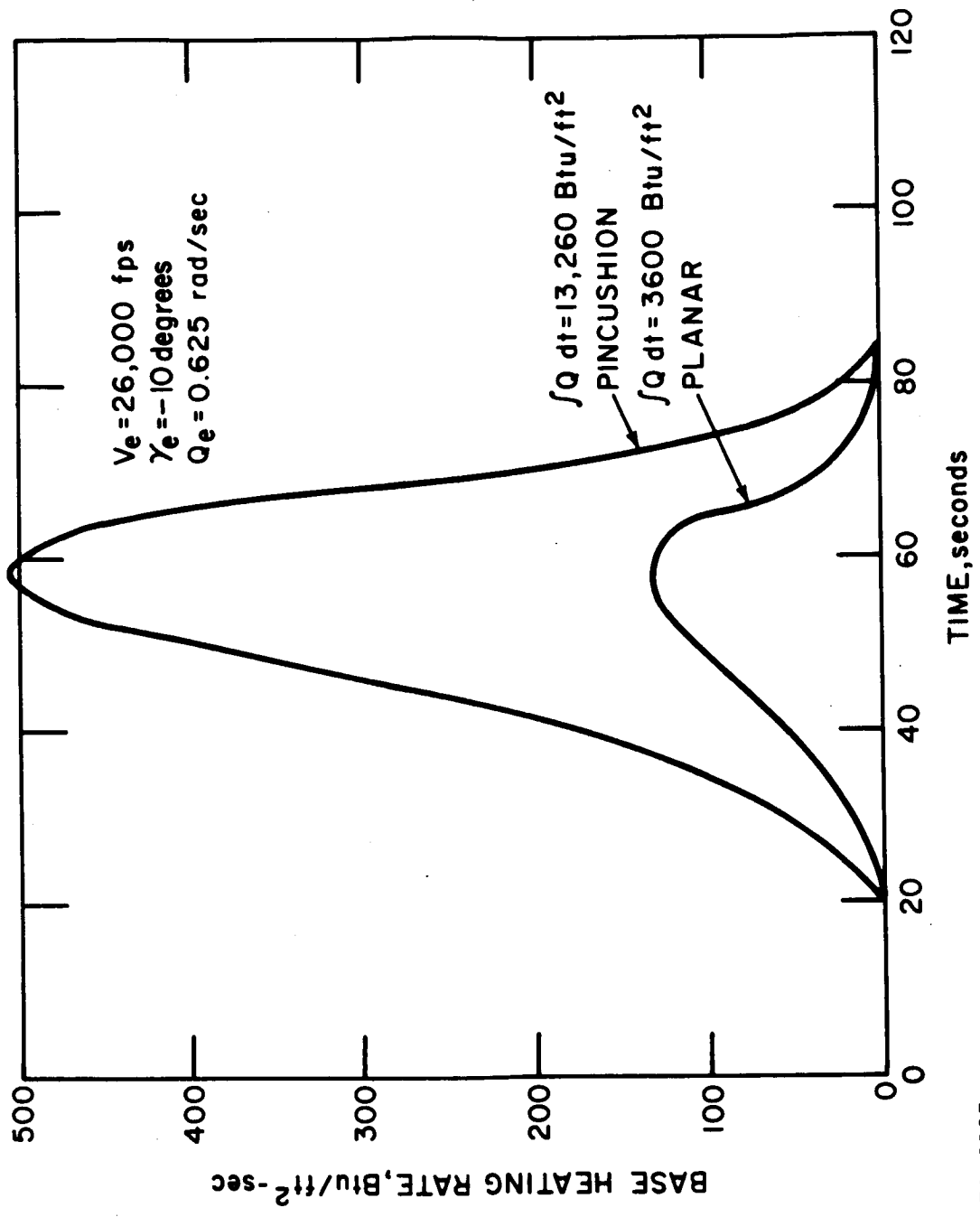
78-2921

Figure 6.2.1.1.0 CAPSULE BASE HEATING (TUMBLING)



78-2922

Figure 6.2.1-11 CAPSULE BASE HEATING (180° REARWARD)



78-2923

Figure 6.2.1-12 CAPSULE BASE HEATING (TUMBLING)

Aeroshell Heating -- The aeroshell heating analysis was performed by the same methods as shown in the previous Topical Report (Reference 6.2.1-10). Updated entry conditions and vehicle mass properties were used for Phase I-B for the planar and pin cushion configurations. The maximum rate and maximum integrated heating are shown in Table 6.2.1-III for the two shapes in the tumbling mode, rearward entry mode and nominal entry at spin rates, the pin cushion having higher values because of its higher $W/C_D A$ value.

The heating on the cover plate is the same as the heating for the capsule in the flush mounted planar configuration.

REFERENCES

- 6.2.1-1 Phase I -- IRV Topical Report
- 6.2.1-2 Nestler, D., and I. Musser, "Correlations for Convective Heat Transfer, Pressure Distribution and Shock Detachment Distance for Blunt, Axisymmetric Forebodies," Aerophysics Engineering Technical Memorandum No. 149, General Electric MSD (January 1960).
- 6.2.1-3 Ryan, R. L., "IRV Flushing the Exposed Recess" (sic), Interoffice Memorandum, Avco Space Systems Division (February 26, 1968).
- 6.2.1-4 Zappa, O., to be published.
- 6.2.1-5 Georgiev, S., letter to Mr. Lloyd I. Shure of NASA/Lewis Research Center; Avco Space Systems Division (February 9, 1968).
- 6.2.1-6 Brower, W., Jr., "Leading Edge Separation of Laminar Boundary Layers in Supersonic Flow," Avco/RAD, Aerodynamics Section Memo No. 189 (March 17, 1959).
- 6.2.1-7 Schurmann, E., "Engineering Methods for the Analysis of Aerodynamic Heating," Avco/RAD, Technical Memorandum RAD TR-63-68 (November 11, 1963).
- 6.2.1-8 Marvin, J., and A. Sinclair, "Convective Heating in Regions of Large Favorable Pressure Gradient," AIAA Journal, pp. 1940-9 (November 1967).
- 6.2.1-9 Nestler, D., and I. Musser, "Correlations for Convective Heat Transfer, Pressure Distribution, and Shock Detachment Distance for Blunt Axisymmetric Forebodies," Aerophysics Engineering Technical Memorandum No. 149, General Electric-MSD (January 1960).
- 6.2.1-10 IRV Design Study Conceptual Design -- Phase IA, Topical Report NASA CR-72366 (May 1968).

TABLE 6.2.1-III

AERODYNAMIC HEATING STAGNATION POINT

γ_c	Circular Planar (Flush)				Pin Cushion			
	Tumbling		Rearward		Tumbling		Rearward	
	$\int \dot{Q}_{Sdt}$	\dot{Q}_{Smax}	$\int \dot{Q}_{Sdt}$	\dot{Q}_{Smax}	$\int \dot{Q}_{Sdt}$	\dot{Q}_{Smax}	$\int \dot{Q}_{Sdt}$	\dot{Q}_{Smax}
0	57600	243	44200	154	67500	290	52680	184
-10	17800	672	11750	413	20400	780	13900	490

Nominal Trajectory Stagnation Point

$\gamma_e = -2.25$ Degrees

P_E	Circular Planar (Flush)		Pin Cushion	
	$\int \dot{Q}_{Sdt}$	\dot{Q}_{Smax}	$\int \dot{Q}_{SL}$	\dot{Q}_{Smax}
0.785	27400	250	29400	268
2.09	30831	290	33200	312

6.2.1.2 Fuel Capsule Thermal Response (Reentry Heating)

The effect of reentry heating on the capsule surface temperature was analyzed for updated heating rate data (Figure 6.2.1-13). The purpose of this analysis was to determine if rearward reentry without turn-around (righting) was tolerable and for this assumed worst case to compare two retention schemes to determine their effect on the temperature history of the capsule. The type of retention designs considered were bare and covered capsules. Exposed, flush, and recessed heat source mounting arrangements were studied.

Figure 6.2.1-13 is a curve of the heating rate for the exposed fuel capsule array for an entry angle of -5 degrees and an orientation of 180 degrees (rearward reentry). The heating rates for the flush and recessed arrays were 36 and 22 percent of the exposed heating rates. Figure 6.2.1-14 presents the temperature histories of the bare and covered capsules for three heat source mounting arrangements based on the calculation model described in detail in Task I-A topical report. This figure shows the reduction in overheating that is obtained by recessing the capsule array into the surface of the heat source. Also, the effect of a cover-plate on the peak capsule temperature is shown to result in a 300°F reduction for the flush and recessed arrays.

Of the six cases considered only the recessed array with covered capsules prevented the fuel capsule from exceeding 2600°F for the possible worst case of stable rearward reentry. Positioning the heat source in a flush or recessed arrangement provided significant increases in the allowable time for vehicle orientation correction. Covering of the fuel capsules was also very beneficial in reducing reentry heating problems.

6.2.2 Aerodynamic Stability

6.2.2.1 Destabilizing Device

a. Configuration -- The two configurations are shown in Figure 6.2.1-1, the planar capsule configuration and the pin cushion shape. The mass characteristics used in the analysis are as shown in Table 6.2.2-1.

b. Turnaround Requirements -- The turnaround requirements are as stated in the Phase IA Topical Report; the two requirements being that the vehicle have a single trim point at zero angle of attack and that the vehicle turn around sufficiently soon that the base heating does not exceed critical design values. The criterion used for this comparison is that the fence design would provide the same characteristics as the nominal configuration for Phase IA. The fence configurations required to accomplish this are shown in Figure 6.2.2-1. The designs were based on the $\gamma_E = -10$ degree abort trajectory in the tumbling mode and provided aerodynamic characteristics such that the temperatures on the capsules did not exceed the design value of 2500°F . The analysis used the techniques of Reference 6.2.2-1, -2, and -3 for the fence design and was intended to determine both an asymmetric and a symmetric fence for each shape the advantages of a symmetric being symmetrical stability characteristics. The asymmetric fence for the flush planar configuration is the same size nondimensionally as the nominal configuration in Reference 6.2.1-1.

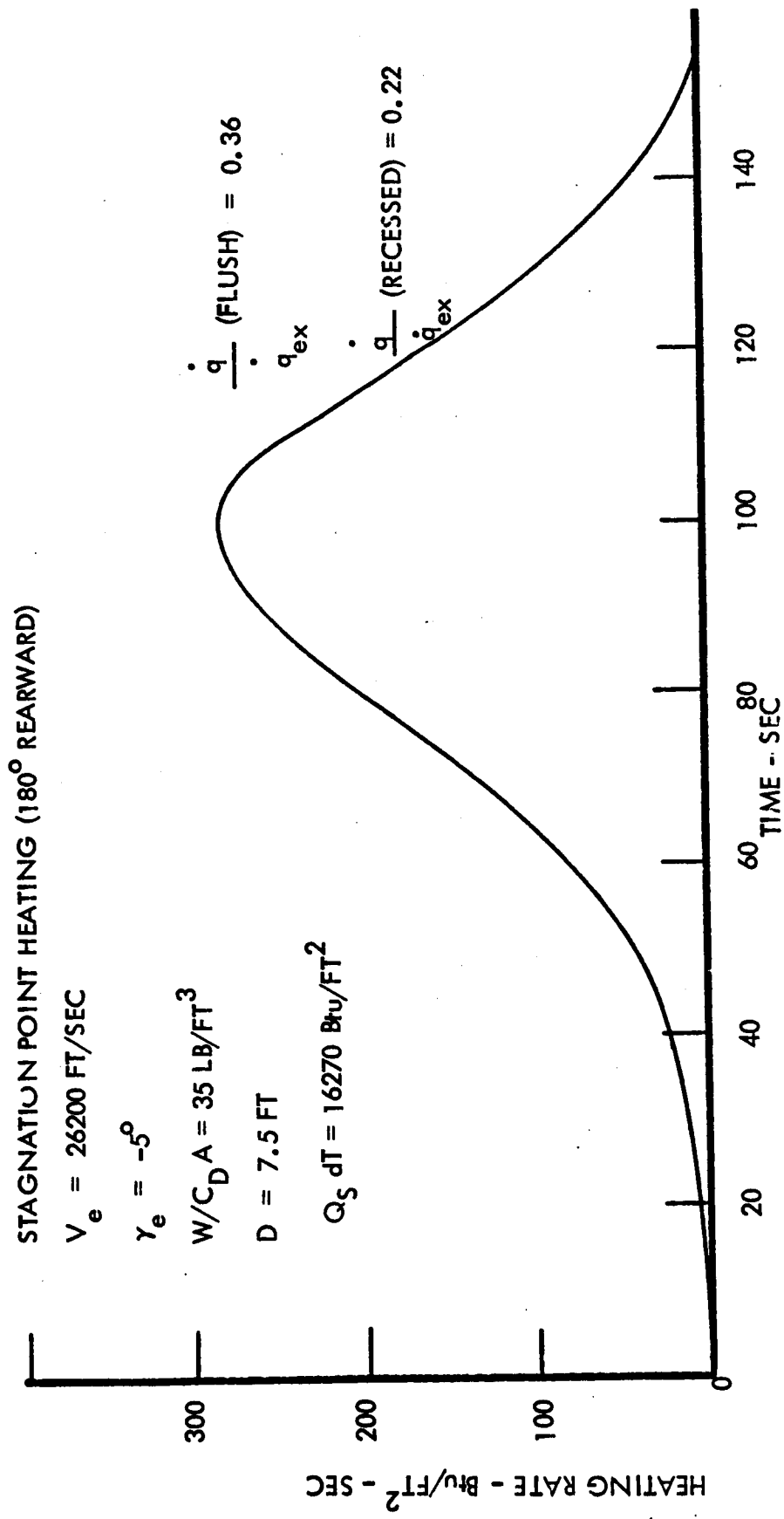


Figure 6.2.1-13 CONVECTIVE HEATING RATE FOR EXPOSED FUEL CAPSULE ARRAY

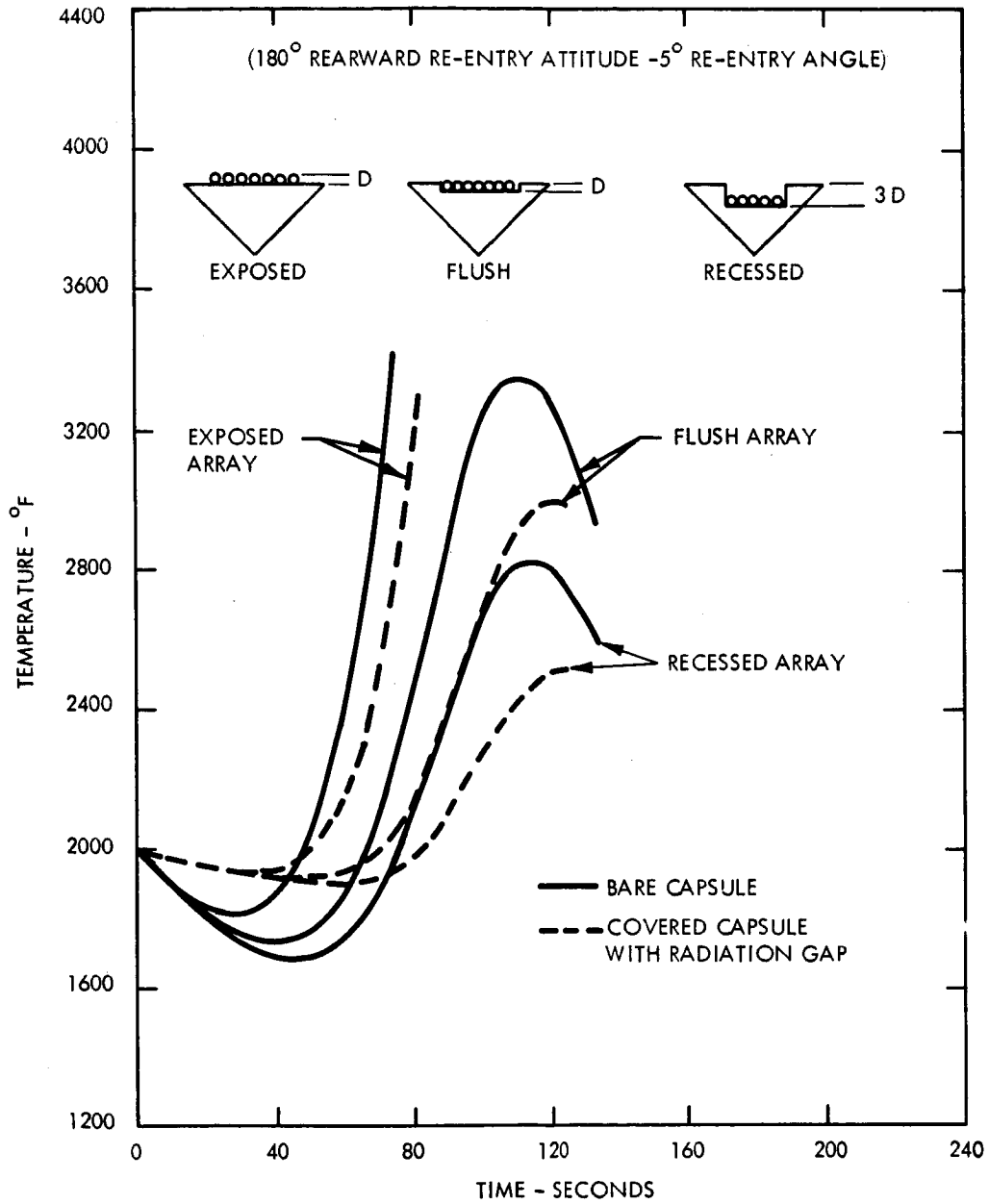
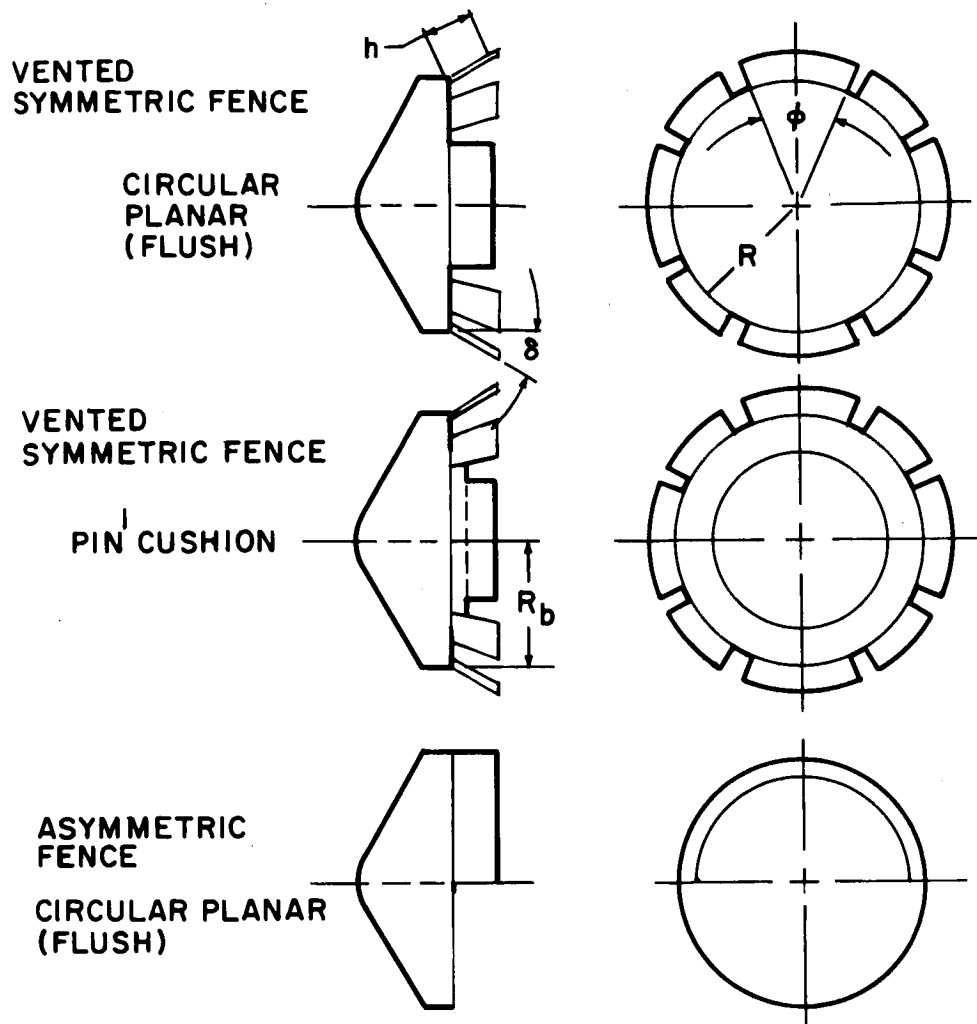


Figure 6.2.1-14 CIRCULAR PLANAR HEAT SOURCE -- TEMPERATURE RESPONSE OF FUEL CAPSULES



FENCE CONFIGURATION		δ (DEG)	h/R_b	ϕ (DEG)	R/R_b
SYMMETRIC	CIRCULAR PLANAR	30	0.2	45	1.0
	PIN CUSHION	30	0.35	45	1.0
ASYMMETRIC	CIRCULAR PLANAR	0	0.2	180	1.0

78-2924

Figure 6.2.2-1 DESTABILIZING FENCE CHARACTERISTICS

As shown in Reference 6.2.2-3, the asymmetric fence at $\delta = 0$ deg will provide insufficient pitching moment to produce the same turnaround characteristics for the pin cushion shape.

TABLE 6.2.2-1
MASS CHARACTERISTICS

	Planar (Flush)	Pin Cushion
Weight (lb)	1842	1760.7
X_{CG}/D	0.324	0.334
I_{ROLL} (sl-ft ²)	178.9	115.6
I_{PITCH} (sl-ft ²)	97.7	66.2
I_{YAW} (sl-ft ²)	97.7	66.2
Diam (ft)	6.66	5.83
$W/C_D A$ (lb/ft ²)	33.1	41.4

This is caused by the adverse effects of the pin cushion capsule configuration on the flow. Reduced turnaround capabilities may be allowable but further studies are required to determine the limiting conditions.

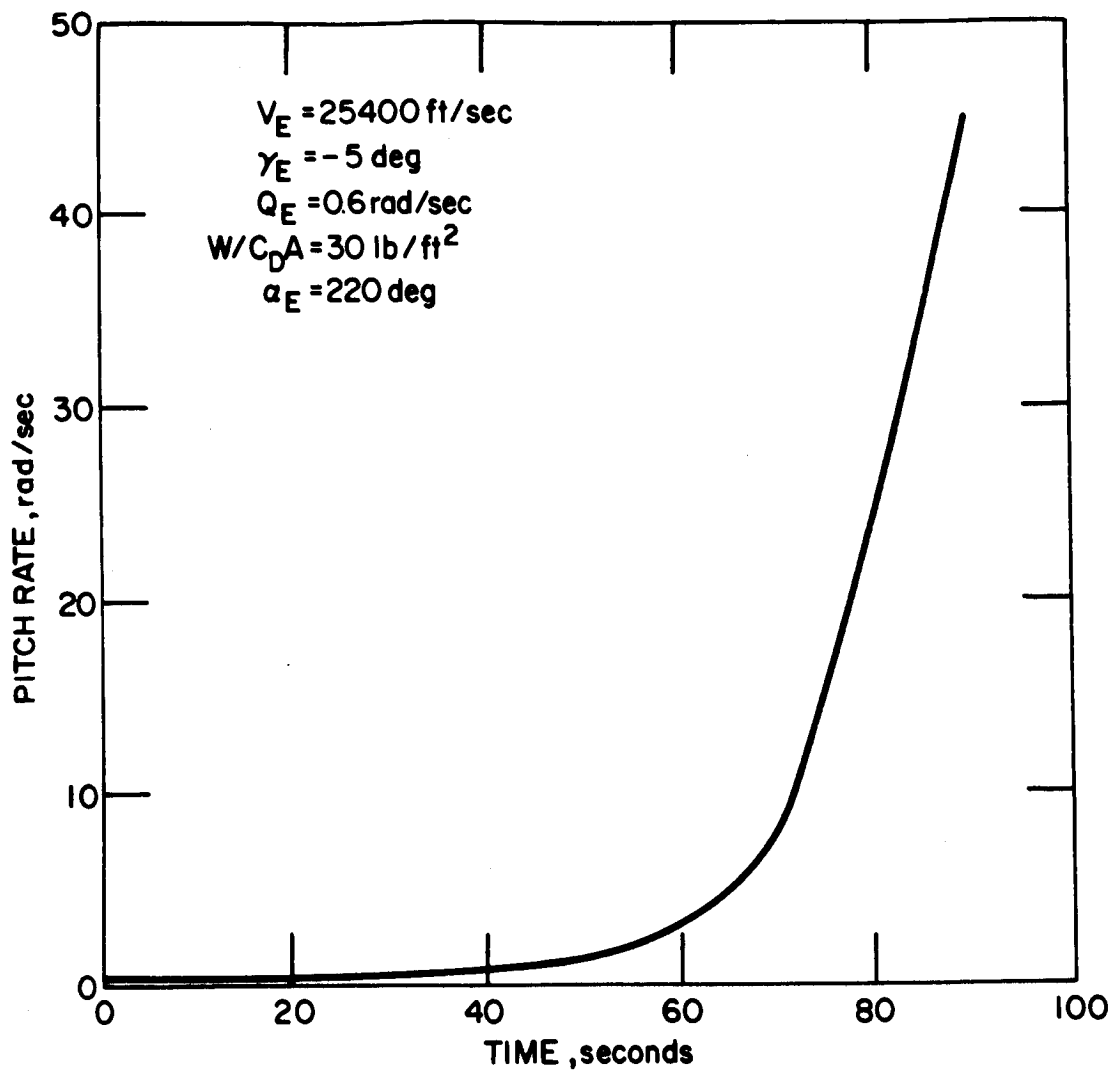
The adverse effects of the pin cushion are also shown for the symmetric fence where a larger fence is required for the pin cushion than for the flush planar. A disadvantage of the symmetric fence is that, in order to obtain sufficient pitching moment, the fence must be canted 30 degrees as shown in the figure. This obviously increases the diameter envelope with possible packaging problems.

An additional study of the asymmetric fence indicates that it will be unacceptable as a turnaround device in the tumbling mode. The asymmetric stability causes a tumbling rate divergence with the rate increasing (Figure 6.2.2-2) instead of damping out. The divergence is caused by the reinforcing pitching moment due to the asymmetry which adds to the tumbling inertia and overcomes the damping tendencies which you normally expect. This becomes more pronounced as the tumbling inertia and asymmetry is increased.

6.2.2.2 Vehicle Stability

6.2.2.2.1 Turnaround Performance

a. Tumble -- The vehicle stability for the tumbling and rearward entry modes will be the same as that for the Phase IA study since the fences are designed to provide the same turnaround capability. These proved satisfactory in producing sufficiently low capsule temperatures.



78-2925

Figure 6.2.2-2 PITCH RATE HISTORY

b. Spinning -- The spinning mode stability is shown in Figures 6.2.2-3 and 6.2.2-4 for the angle of attack envelopes. The envelopes converge for each condition.

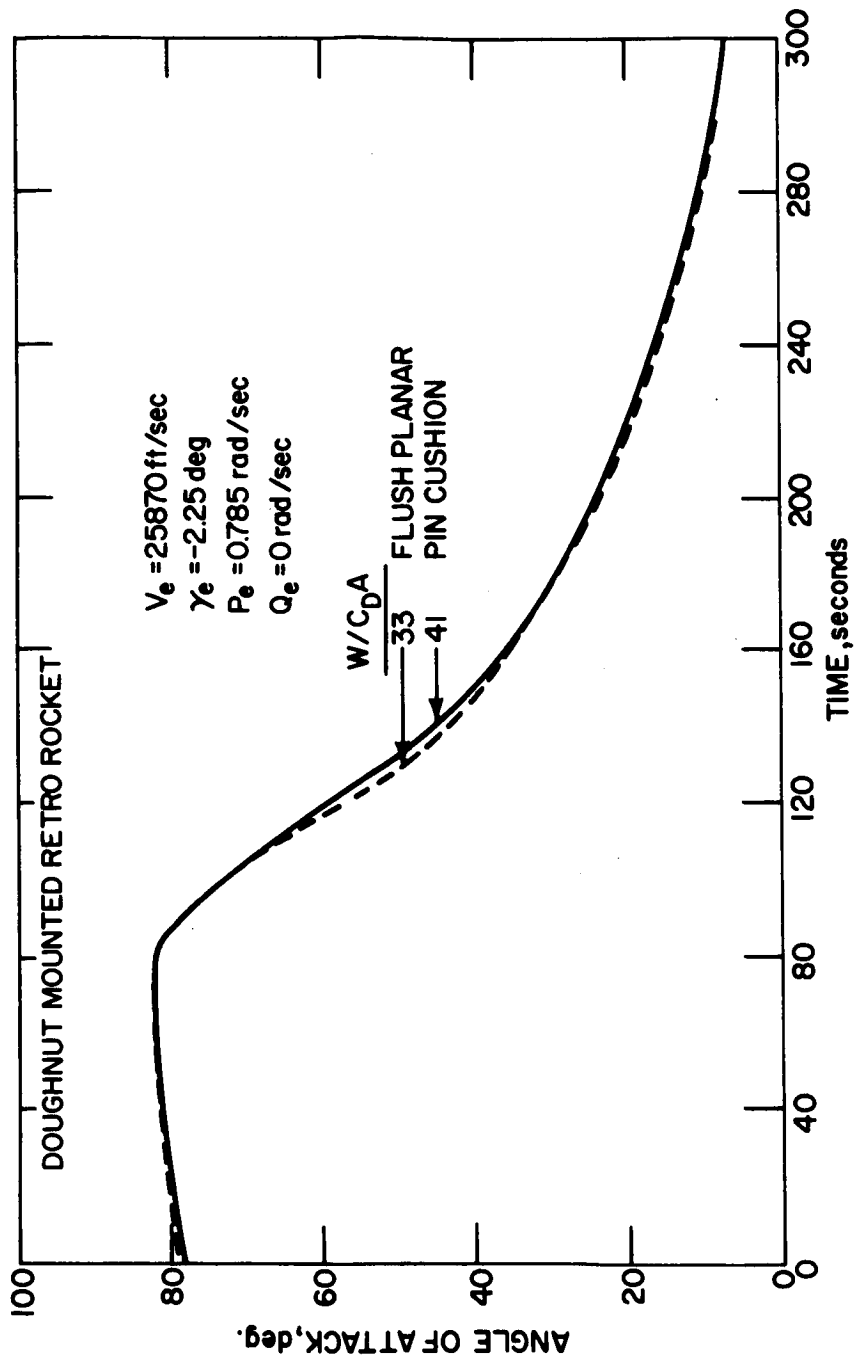
The comparison of the two shapes, Figure 6.2.2-3, shows small changes in angle of attack profile for the two shapes entering at the same angle of attack with the variation only due to mass characteristics of the two shapes. By changing the retrorocket mounting concept, however, the entry angle of attack also changes as does the required spin rate for stability. The difference in the angle of attack profile for these entry conditions is shown in Figure 6.2.2-4. The higher spin rate for the nose mounted retrorocket produces higher angles of attack with the increased capsule heating factors stated in the previous Section 6.2.1.

Conclusions

1. A vented segmented symmetric fence recommended by Ames Research Center will be used for the Task II Study. This is necessitated by the inability of the asymmetric fence to stabilize the vehicle at $\alpha = 0$ degree when entering in the tumbling mode.
2. The vented symmetric fence will provide a turnaround capability equivalent to Configuration 1 of Task IA for either the planar or pin cushion configuration.
3. Additional studies are required to determine whether reduced turnaround capability is allowable.

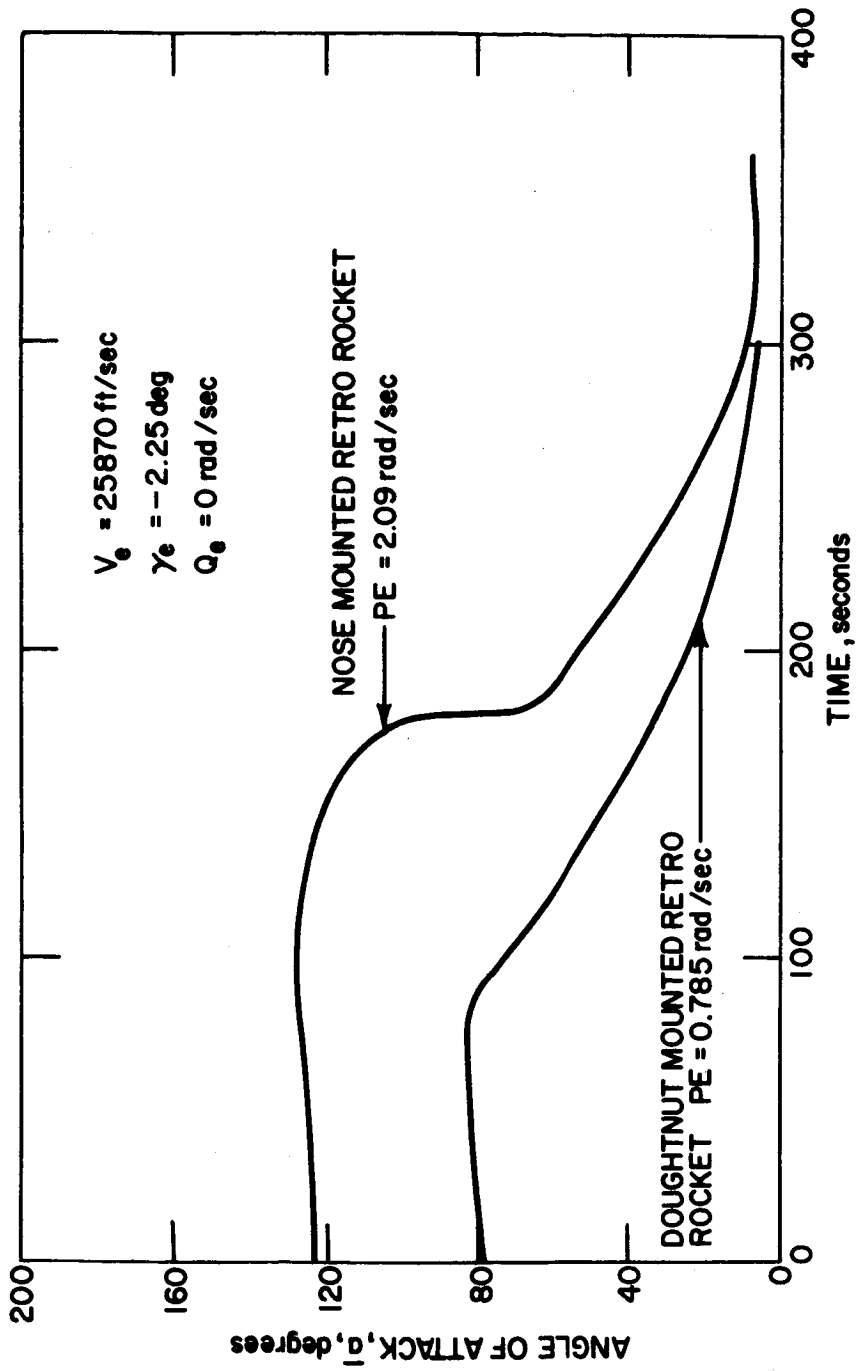
REFERENCES

- 6.2.2-1 Wagner, R. E., "Comparison of Five Design Configurations for Turnaround Capability," TR/VE/REW/87 (January 23, 1968).
- 6.2.2-2 Morgan, B., "Righting Moment Contribution of Four Symmetrically Located Fences at 150 Degree Angle of Attack," TR/VE/BM/88 (January 23, 1968).
- 6.2.2-3 Morgan, B., "Fence Effectiveness on a Protruding Capsule Vehicle Configuration," TR/VE/BM/95 (March 15, 1968).
- 6.2.2-4 Morgan, B., "Isotope Heating Factors in Tumbling Flight For Three Configurations," TR/R550/VE/BM/90 (January 25, 1968).



78-2926

Figure 6.2.2-3 ANGLE OF ATTACK HISTORY



78-2927

Figure 6.2.2-4 ANGLE OF ATTACK ENVELOPE

6.2.3 Aeroshell Design

6.2.3.1 Structural Design

A detailed stress analysis of the IRV aeroshell was performed using Avco Computer Program 1322D. This program solves for the total stresses and strains of a thin-elastic, multi-layered, multi-region orthotropic shell of revolution under axisymmetric pressure loads and temperature distributions. A schematic of the honeycomb shell, honeycomb dimensions and the symmetrical pressure distribution considered is shown in Figure 6.2.3-1. The pressure shown represents the condition for the most severe load environment based on preliminary particle trajectory studies (i.e., $V_e = 23,000$ fps, $\gamma_e = -10$ degrees, $W/C_{DA} = 40$ lb/ft²). The pressure on the cone is 75 percent of the stagnation pressure since a Newtonian pressure distribution was assumed. Environmental limit loads were multiplied by 1.25 for the analysis. A uniform core depth of 0.38 inch was used based on general buckling stability of the aeroshell. The Von Mises yield criteria for biaxial stress was used to compare the computed shell stresses to the allowable stress of aluminum. An allowable yield stress of 52,000 psi used for aluminum was obtained from Reference 6.2.3-1. It is based on 2024-T81 aluminum at 350°F subsequent to a 5-year exposure at 200°F. Since high bending and shear stresses were anticipated at the payload support ring due to the concentrated application of the heat-source inertia loads, the face sheets were tapered over a 6-inch length from a nominal thickness of 0.016 to 0.08 inch at the truss support ring.

The computed effective stress distributions for the inner and outer face-sheet surfaces are plotted as a function of vehicle location and compared to the allowable yield stress in Figure 6.2.3-2. The results show that the assumed taper of the shell region adjoining the payload support ring was sufficient to keep the local substructure bending stresses well below the allowable yield limit. However, the assumed local face-sheet taper increases the shell weight by approximately 8 pounds and since resulting local stress levels are low, a thinner taper should be considered to conserve weight.

A maximum effective stress of approximately 40,000 psi was computed in the inner face sheet for a segment of the cone where the face-sheet thickness is 0.016 inch. This maximum stress is well below the allowable yield strength of 52,000 psi. For a 5-year exposure temperature of 300°F, the allowable yield stress of 2024-T81 aluminum is only 41,000 psi at 350°F and the 0.016-inch face-sheet thickness, although adequate, is almost marginal. One other major consideration in sizing the shell particularly at the truss support ring is the effect of asymmetrical loads. It is anticipated that the stresses at the windward meridian in the local region of the heat-source truss-support ring would be most affected by an asymmetrical pressure distribution due to the unsymmetrical moment and shear reaction forces resulting from the heat source normal and angular accelerations.

Dynamic trajectory studies indicate that for certain entry cases such as rearward entry the angle-of-attack profiles, particularly at peak load, are significant and will affect the maximum pressure levels on the aeroshell. From the standpoint of peak loads, these studies indicated that the following entry condition is most critical: $V_e = 26,000$ fps, $\gamma_e = -10$ degrees, $W/C_{DA} = 31.6$ lb/ft², Q_e (pitch rate) = 0.628 rad/sec, $a_c = 179^\circ$ (rearward entry). The maximum conical pressure and angle-of-attack profiles for this condition are shown in Figure

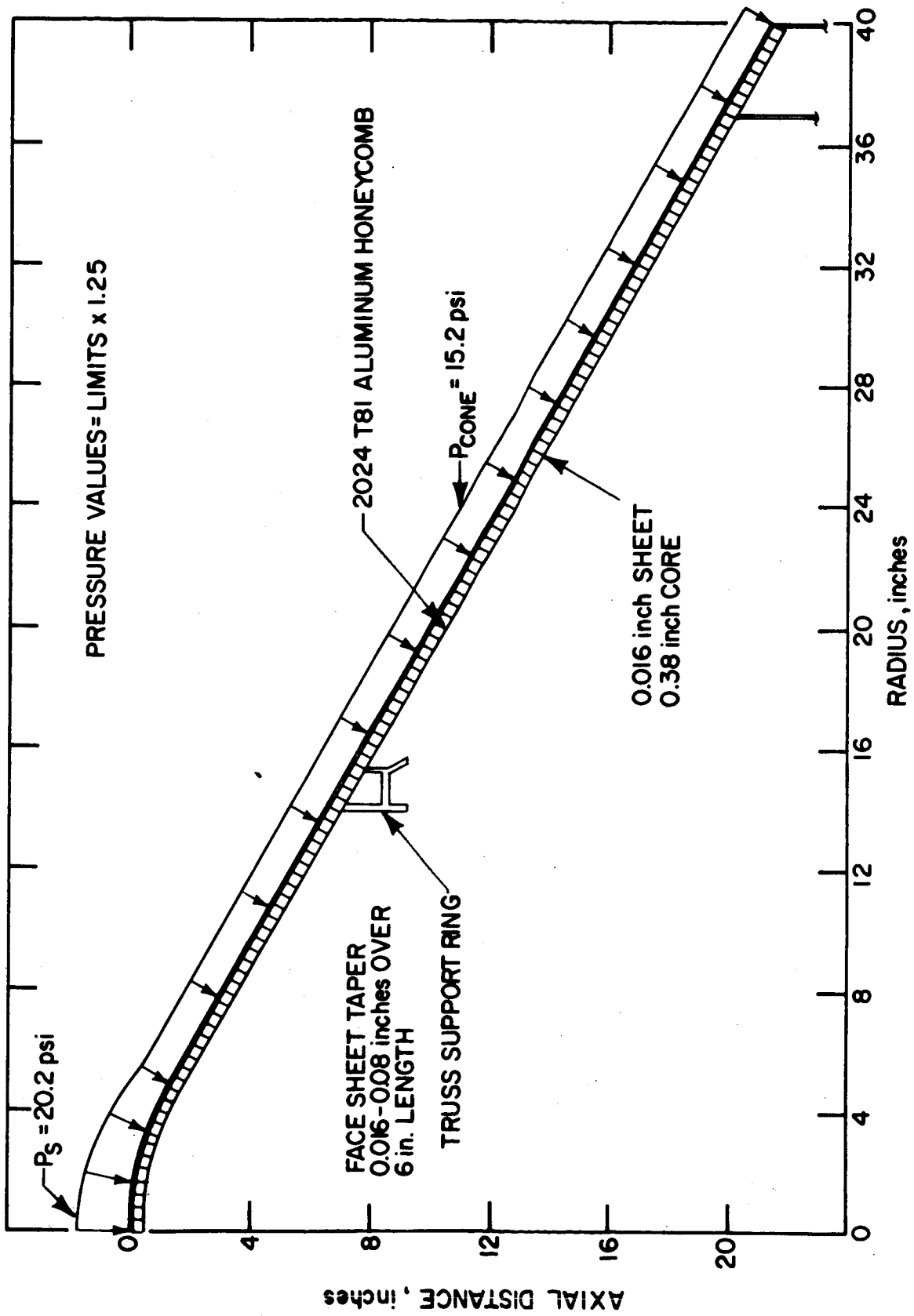
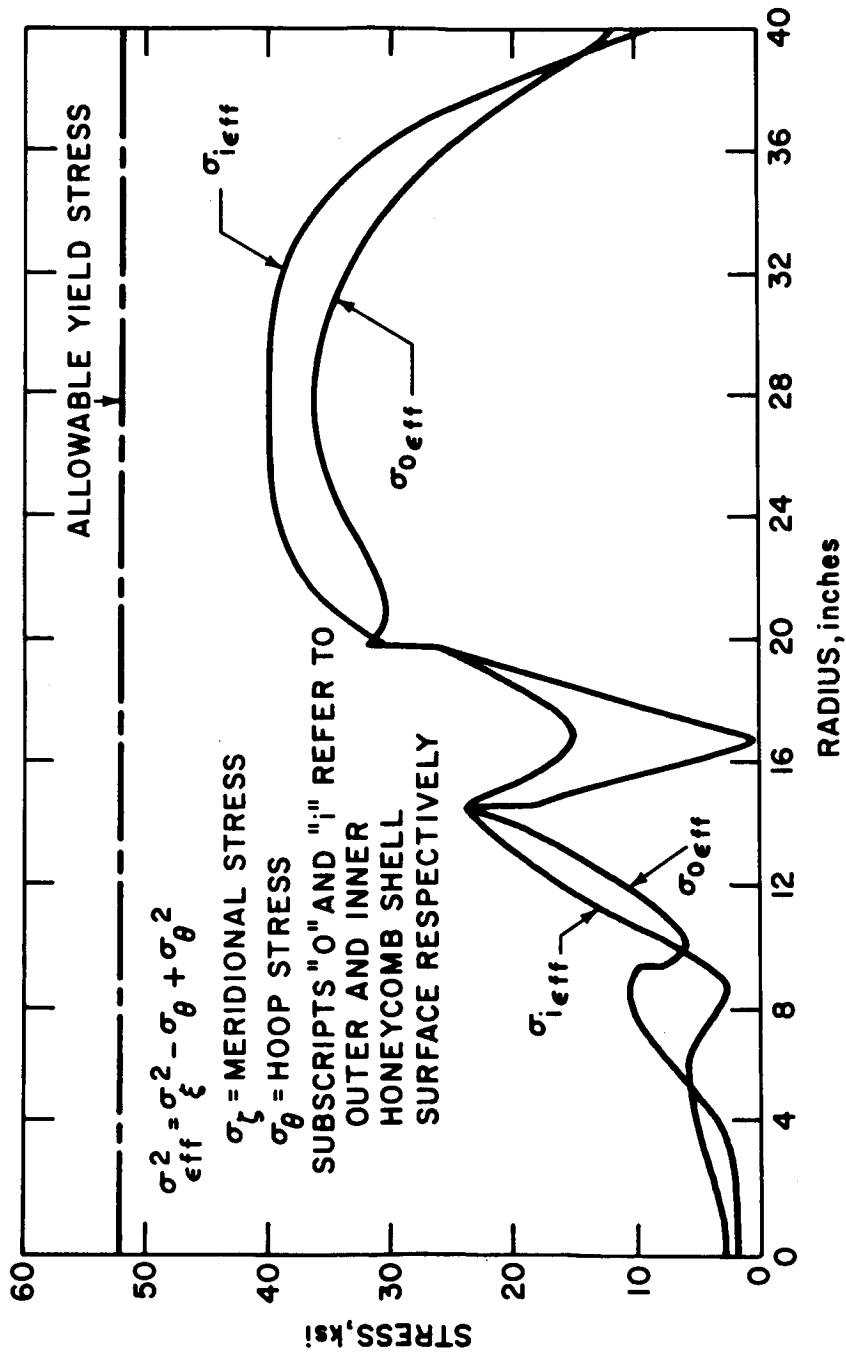


Figure 6.2.3-1 SCHEMATIC OF IRV BLUNT-CONE SHELL

78-2928



78-2929

Figure 6.2.3-2 IRV AEROSHELL SUBSTRUCTURE EFFECTIVE STRESS

6.2.3-3. The maximum cone pressure of 15.6 psi occurs at the windward meridian. The comparable cone pressure profile for the zero angle-of-attack case is also shown. The peak stagnation pressure for the critical dynamic trajectory mentioned is actually lower than the design level established previously by preliminary particle trajectory studies. Although a higher entry velocity of 26,000 fps was considered for the critical dynamic trajectory versus approximately 23,000 fps for the critical particle trajectory, the lower $W/C_D A$ more than compensated for the increase in velocity and resulted in a peak stagnation pressure of 1960 psf as compared to 2320 psf for the particle trajectory. Because of the relatively large angle of attack, however, the maximum cone pressure of 15.6 psi (including a factor of safety of 1.25) for the dynamic case just slightly exceeds the previously used value of 15.2 psi.

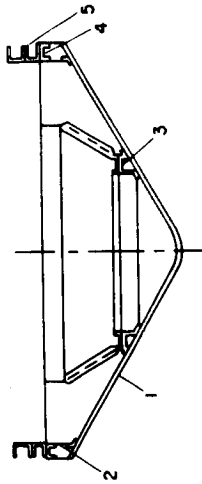
The honeycomb face sheet and core requirements were reevaluated based on the increased pressure and an 85-inch diameter aeroshell. Using membrane theory, a symmetrical pressure load equal to the maximum windward pressure of 15.6 psi and the Von Mises yield criteria for the biaxial stress condition, the face-sheet thickness requirements for the conical portion of the aluminum aeroshell were computed and plotted in Figure 6.2.3-4 as a function of diameter with yield strength, which is affected by the space environment, as a parameter. The results which do not include bending indicate that a nominal aluminum face-sheet thickness of 0.017 inch is adequate for the major portion of the aeroshell even if the 5-year operating temperature of the shell is 300°F and the temperature rises to 350°F at peak loads during entry. The membrane stress analysis indicated that increased face-sheet thicknesses are necessary closer to the heat-source support ring; however, the aeroshell would normally be beefed-up in this region anyway due to local bending and shear forces. Local requirements at mounting and base rings and joints will be established through more detailed analysis. For a lower 5-year operating temperature of 200°F, the higher yield strength would allow the use of thinner face sheets and hence final sizing will depend on the results of a comprehensive thermal control analysis. Honeycomb core thickness requirements based on resistance to general buckling instability are plotted in Figure 6.2.3-5 as a function of capsule base diameter. The core requirements are based on a face-sheet thickness of 0.017 inch and a maximum cone pressure of 15.6 psi. For the 85-inch diameter reference capsule design, the core thickness required is 0.52 inch. It may be observed that the core thickness requirements of Figure 6.2.3-5 are larger than previous results reported in the Phase IA Topical Report. The current results, however, include the additional design factor of 0.80 applied to the theoretical critical pressure for cylindrical and conical shells subjected to external surface pressure as recommended in Reference 6.2.3-2.

The increase in core thickness from 0.38 to 0.47 inch for the 80-inch capsule would affect the stress distributions presented in Figure 6.2.3-2 particularly in the support-ring region where high bending loads exist. However, an increase in core thickness will reduce face-sheet stresses due to bending loads. The increase in core would have little effect on face-sheet stress in that portion of the shell away from junctions and concentrated loads where stresses are principally membrane.

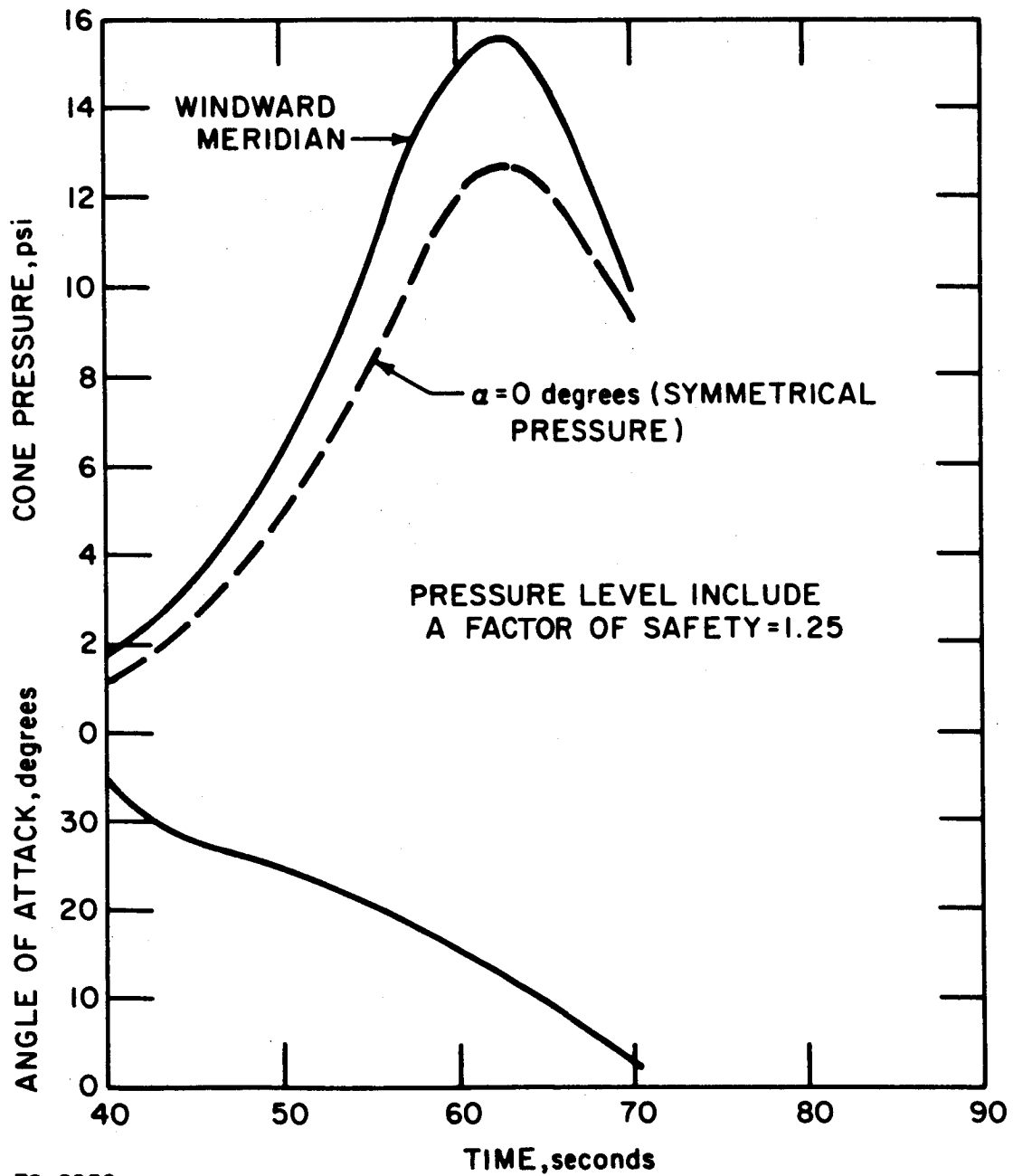
A structural evaluation of the other major aeroshell components and interface rings has been performed to establish approximate structural dimensions. The results are summarized in Table 6.2.3-I. The critical design load environments

TABLE 6.2.3-1

SUMMARY OF STRUCTURAL REQUIREMENTS FOR MAJOR STRUCTURE COMPONENTS

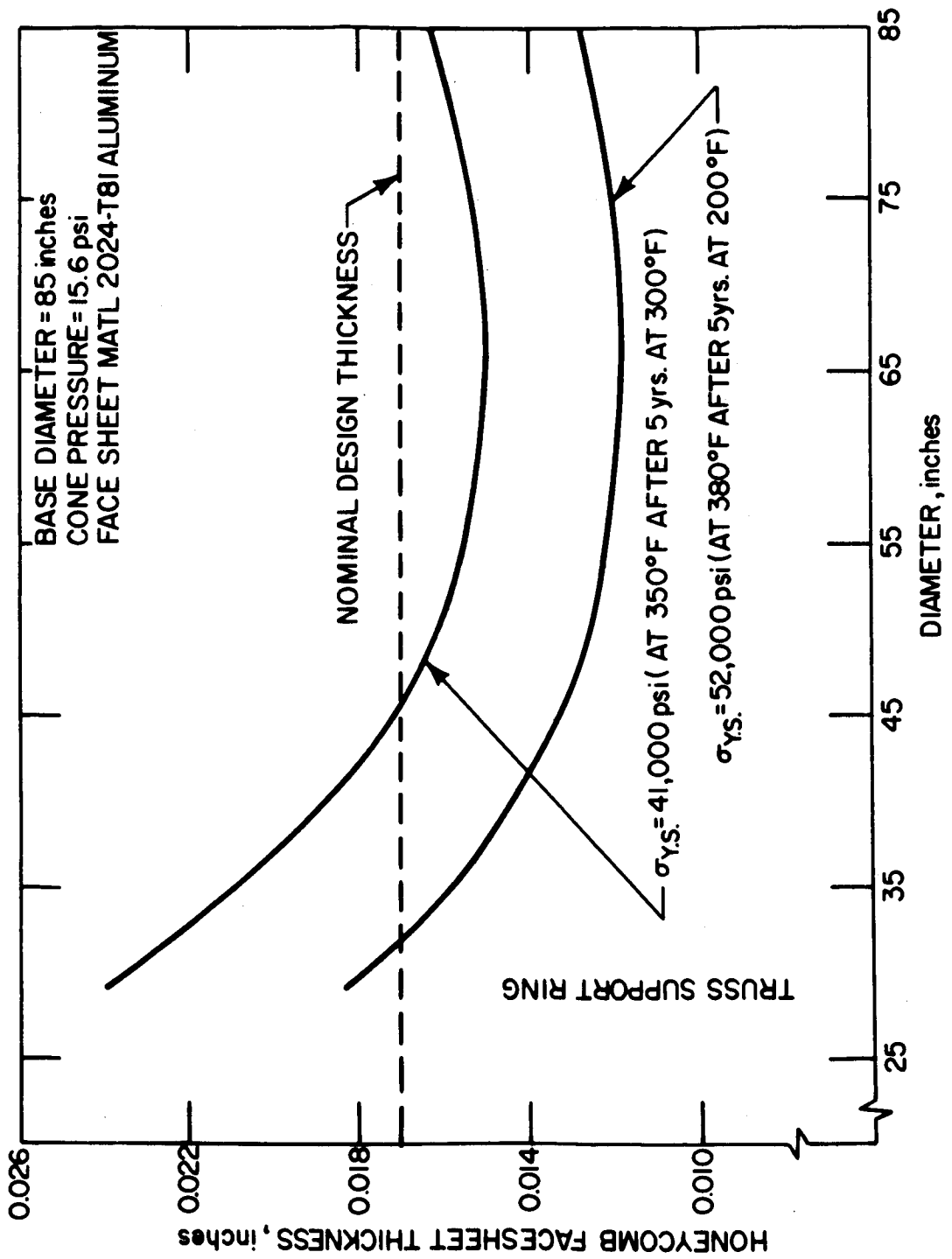


NO.	STRUCTURAL COMPONENT	MATERIAL AND CONSTRUCTION	DESIGN LOAD ENVIRONMENT	FAILURE MODE	STRUCTURAL REQUIREMENTS
1	CONICAL SHELL	HONEYCOMB 2024 - T81 AL.	ENTRY ($A_x = -38.8$ $A_n = 3.25$) $P_c = 15.6$ PSI $T = 350^\circ\text{F}$	FACESHEET - YIELD CORE - GENERAL BUCKLING: PRESSURE	FACESHEET, $t_f = 0.017$ INCH (NOMINAL); CORE, $t_c = 0.52$ INCH
2	CYLINDRICAL SHELL	MONOCOQUE 2024-T81 AL.	INTEGRAL LAUNCH (MORL) $A_x = 2.0$; $A_n = 10.0$	COMBINED AXIAL COMPRESSION AND SHEAR INSTABILITY	$t = 0.06$ INCH
3	TRUSS-SUPPORT RING (a) UPPER (b) LOWER	2024-T81 AL. (BOTH SECTIONS) CHANNEL BUILT-UP BOX RING SECTION	ENTRY $A_x = 38.8$ $A_n = 3.25$ $P = 15.6$ PSI $T_c = 350^\circ\text{F}$	COMBINED OUT-OF-PLANE AND IN-PLANE BENDING	
4	IRV INTERFACE RING	2024-T81 AL. CHANNEL	INTEGRAL LAUNCH (MORL) $A_x = 2.0$; $A_n = 10.0$	COMBINED OUT-OF-PLANE AND IN-PLANE BENDING	2.25 INCHES X 1.75 INCHES X 1.15 INCHES
5	SPACER RINGS	7075-T6 AL. CHANNEL RINGS	SEPARATE LAUNCH (ATLAS - CENTAUR) $A_x = 10.0$; $A_n = 2.0$	COMBINED OUT-OF-PLANE BENDING AND LOCAL FLANGE BENDING	SPACER HINGE DESIGN REQUIRES 2 RINGS 4.0 INCHES X 1.75 INCHES X 0.08 INCHES 3.0 INCHES X 1.75 INCHES X 0.08 INCHES



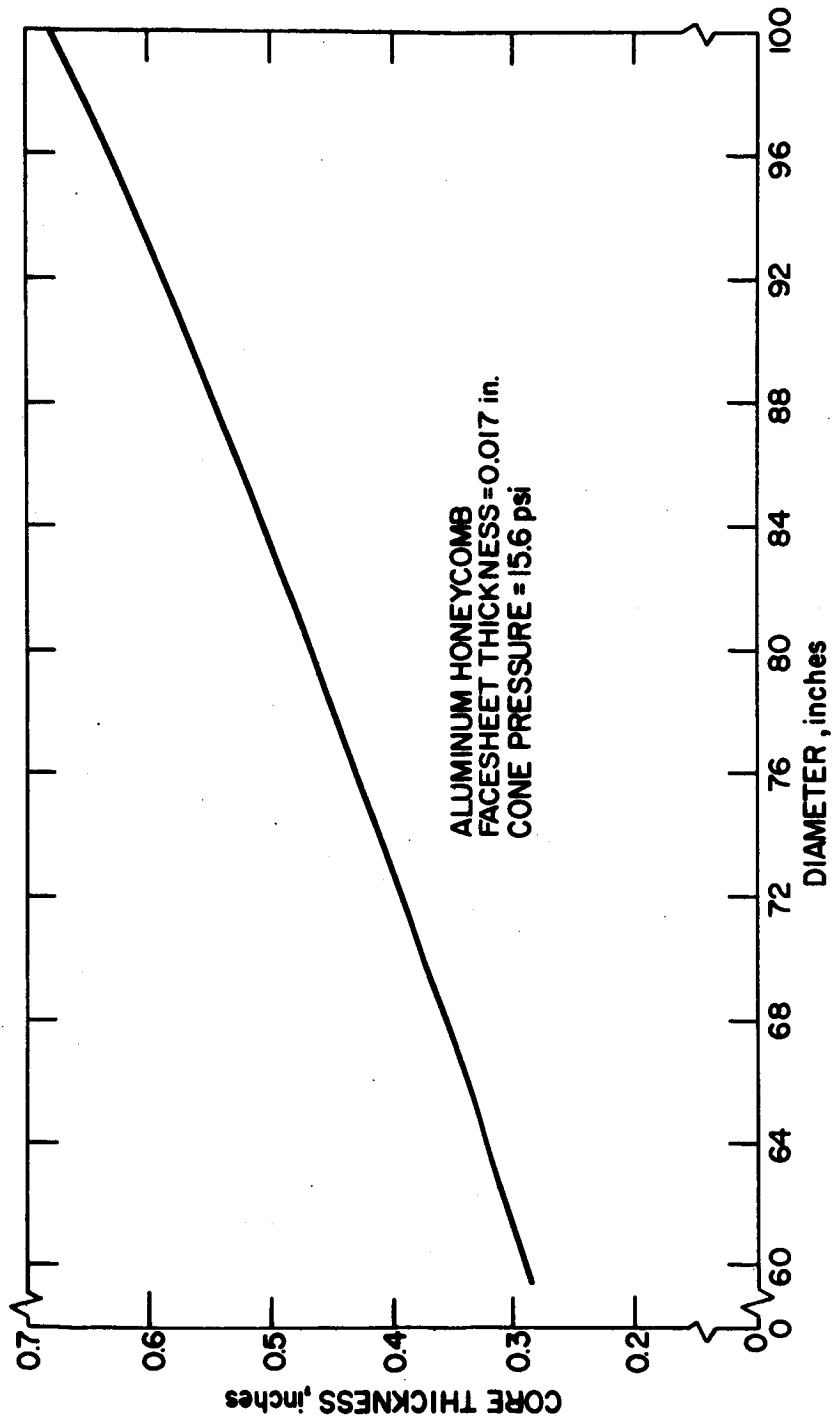
78-2930

Figure 6.2.3-3 CONE PRESSURE (WINDWARD MERIDIAN) AND ANGLE OF ATTACK PROFILES



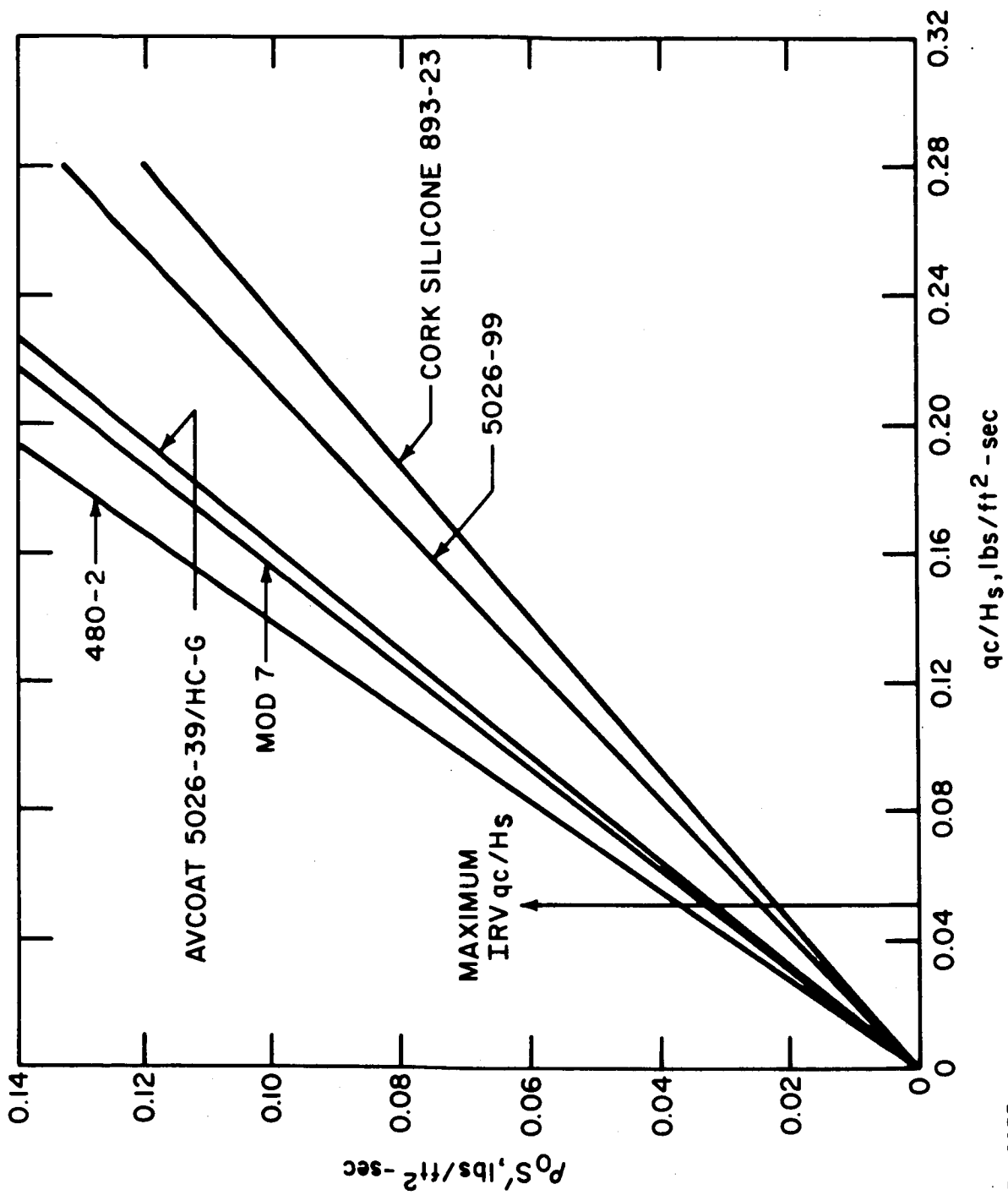
78-2931

Figure 6.2.3-4 MINIMUM HONEYCOMB FACESHEET THICKNESS VERSUS DIAMETER



78-2932

Figure 6.2.3-5 HONEYCOMB CORE THICKNESS VERSUS VEHICLE DIAMETER



78-2933

Figure 6.2.3-6 MODEL 500 DATA

and governing failure modes which were used to establish the structural requirements of these components are presented. In general, 2024-T81 aluminum alloy was specified for the aeroshell components since it appears to retain better strength capabilities after long exposure at elevated temperatures than other aluminum alloys (Reference 6.2.3-1). The aeroshell must withstand the severe reentry load and heating environment after long-time space operation at elevated temperatures. The spacer rings, however, do not reenter with the capsule and experience only major loads during launch; hence, any high-strength alloy such as 7075-T6 could be used.

REFERENCES

6.2.3-1. "Metallic Materials and Elements for Aerospace Vehicle Structures," MIL-HDBK-5A (February 8, 1966).

6.2.3-2. Weingarten, V. I., and P. Seide, "Elastic Stability of Thin-walled Cylindrical and Conical Shells under Combined External Pressure and Axial Compression," AIAA Journal, vol. 3, pp. 913-20 (1965).

6.2.3.2 Heat Shield Design

6.2.3.2.1. Preliminary Material Evaluation--As indicated in the Phase IA report the most efficient (low weight) design should include the use of a low-density charring heat shield. Alternate systems such as ablation/radiation or high-temperature integrated wall concepts offer no significant weight advantage and introduce thermostructural design and insulation complexities. The use of more sophisticated thermal protection systems such as transpiration cooling or liquid metals could result in increased weight and reliability problems for a 5-year mission. The main difficulty with the use of a low-density ablator is the uncertainty in reentry performance of the heat shield due to possible degradation caused by the heat source nuclear radiation and material instability in vacuum (see Section 6.2.3.3).

Among the low-density ablator materials under consideration are cork silicone, silicone ablator Mod 7, Avcoat 5026-99 and a super low-density candidate silicone 480 ($\rho \approx 16 \text{ lb/ft}^3$). In addition, the heat shield material used on the Apollo vehicle (Avcoat 5026-39/HC-G) is considered a strong candidate because of its state of development and the experience gained from actual flights including extensive data interpretation work at Avco. A description of these various materials and their fabrication procedures are given in Section 6.2.3.3.

In order to determine which of the candidates is more efficient from a purely thermal standpoint, it is necessary to investigate both the ablation and insulation characteristics of the material. Figure 6.2.3-6 indicates the surface mass removal as a function of a heat transfer coefficient \dot{q}_c/H_S . These curves were obtained by least squaring results from ground tests conducted in the Avco Model 500 facility.

Figure 6.2.3-6 indicates that the 5026-99 and cork silicone materials are better performers as ablators than the other three candidates. It should be noted that the actual ablation of these materials is a function of more parameters than \dot{q}_c/H_s and when a transient calculation is made the relative ablation performance of the various materials could be altered.

The insulation properties of the materials can best be described by the parameter $\rho k/c_p$ which is an indicator of the weight required to maintain a specified back-face temperature. A simplified assumption can be made which states that the material weight requirement is proportional to the square root of $k\rho/c$. Table 6.2.2-II lists the values of virgin density, conductivity and specific heat for the candidate materials together with the above parameter.

A review of Table 6.2.3-II indicates that the 480-2 material is the best insulator with Avcoat 5026-99 and cork silicone following. It is interesting that the insulative properties of 480-2 could compensate for its relatively high surface mass loss as indicated in Figure 6.2.3-6. Note that the 480-2 material was developed primarily for environments where the heating level is considerably lower than that experienced on IRV. These insulation properties in Table 6.2.3-II are only virgin values and if any significant differences between materials exist when charred then the relative performance could be changed.

This cursory analysis of both ablation and insulation characteristics of the candidates seems to indicate that Avcoat 5026-99 and cork silicone would result in the lowest overall weight with the silicone ablator 480-2 a strong contender if the insulative characteristics can compensate for its rather large surface recession.

6.2.3.2.2. Material Tradeoff--Figures 6.2.3-7 and 6.2.3-8 indicate the local heat shield thickness and weight requirements for the various candidate materials at the stagnation point of the IRV vehicle. The calculations were based on the double skip trajectory condition ($V_e = 25,000$ fps and $\gamma_e = -0.7$ degree) and an initial entry temperature of 100°F . These results include the effects of internal degradation of the material and oxidation effects at the surface. Figure 6.2.2-8 shows that the weights for 480-2, cork silicone, and Avcoat 5026-99 are comparable while Avcoat 5026-39 and silicone ablator Mod 7 are significantly heavier. Table 6.2.3-III summarizes the stagnation point heat shield requirements (for a 350°F maximum structure temperature) and the amount ablated for the various candidates. It should be noted that the confidence in the Avcoat 5026-39 values is considerably higher than for the other materials since flight test results have been incorporated. Only a small amount of ground test data exists on the other candidates.

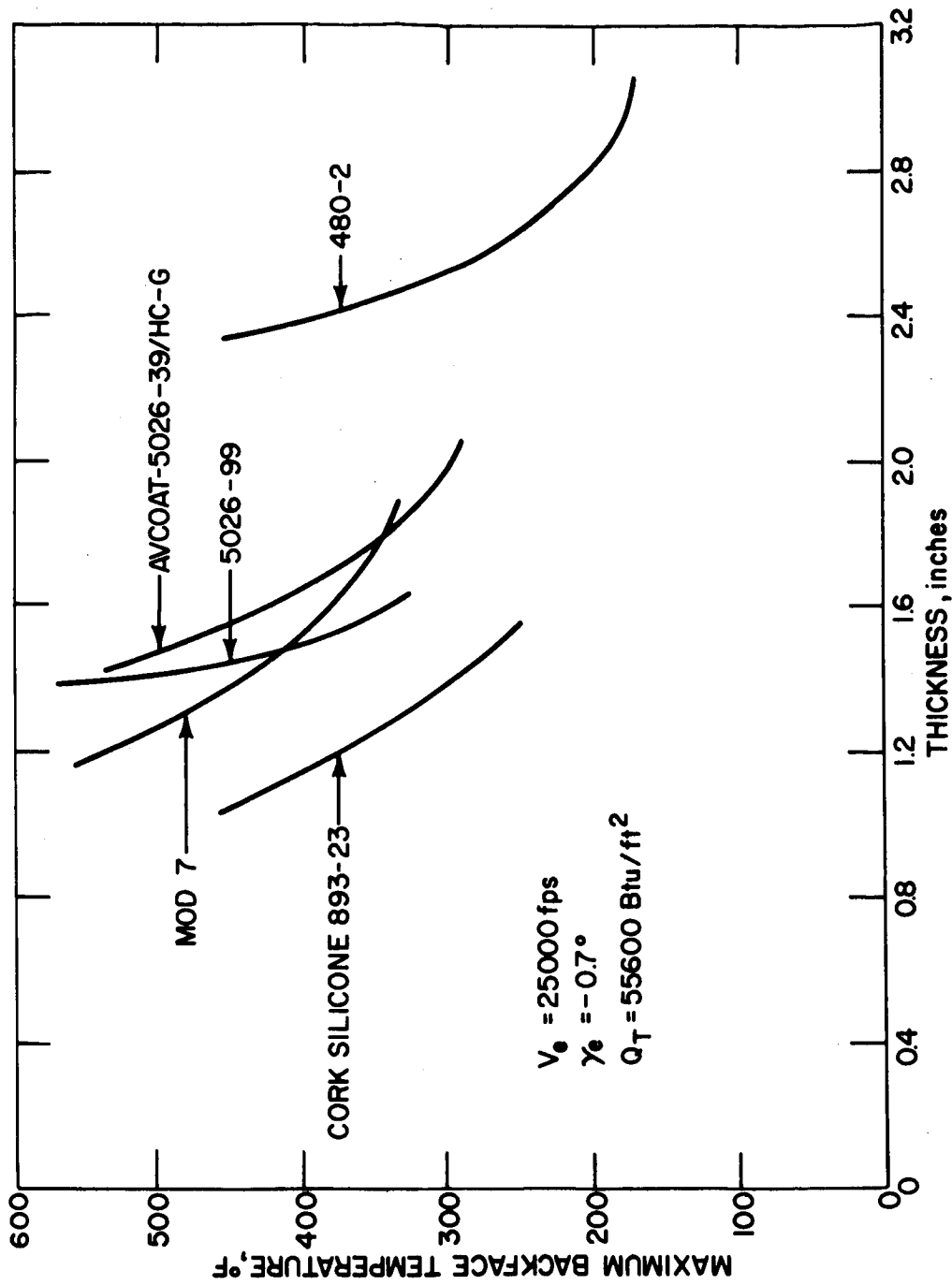
The results in this section bear out those obtained from Section 6.2.3.2.1 in that cork silicone, Avcoat 5026-99, and 480-2 appear to be the most efficient thermal protection systems for the IRV application. Since it is desirable to minimize ablation because of its effect on aerodynamic characteristics (e.g., shape) it would be preferable to eliminate 480-2 (See Table 6.2.3-III). While it may be possible to develop a stable Avcoat 5026-99 the use of a silicone system is preferred.

These results would appear to dictate the use of cork silicone for the IRV heat

TABLE 6.2.3-II

INSULATION CHARACTERISTICS OF IRV CANDIDATE MATERIALS

Material	k (Btu/ft hr ^o F)	ρ (lb/ft ³)	C_p (Btu/lb ^o F)	$k\rho/C_p$ (lb ² /ft ⁴ hr)	$\sqrt{k\rho/C_p}$ (lb/ft ²)
Cork Silicone	0.05	32	0.47	3.41	1.85
Silicone Ablator Mod 7	0.05	36	0.39	4.61	2.16
Avcoat 5026-99	0.04	25	0.45	2.23	1.50
Silicone 480	0.03	16	0.36	1.33	1.16
Avcoat 5026-39/HC	0.07	32	0.35	6.40	2.54



78-2934

Figure 6.2.3-7 IRV -- HEAT SHIELD THICKNESS DOUBLE SKIP ENTRY STAGNATION POINT

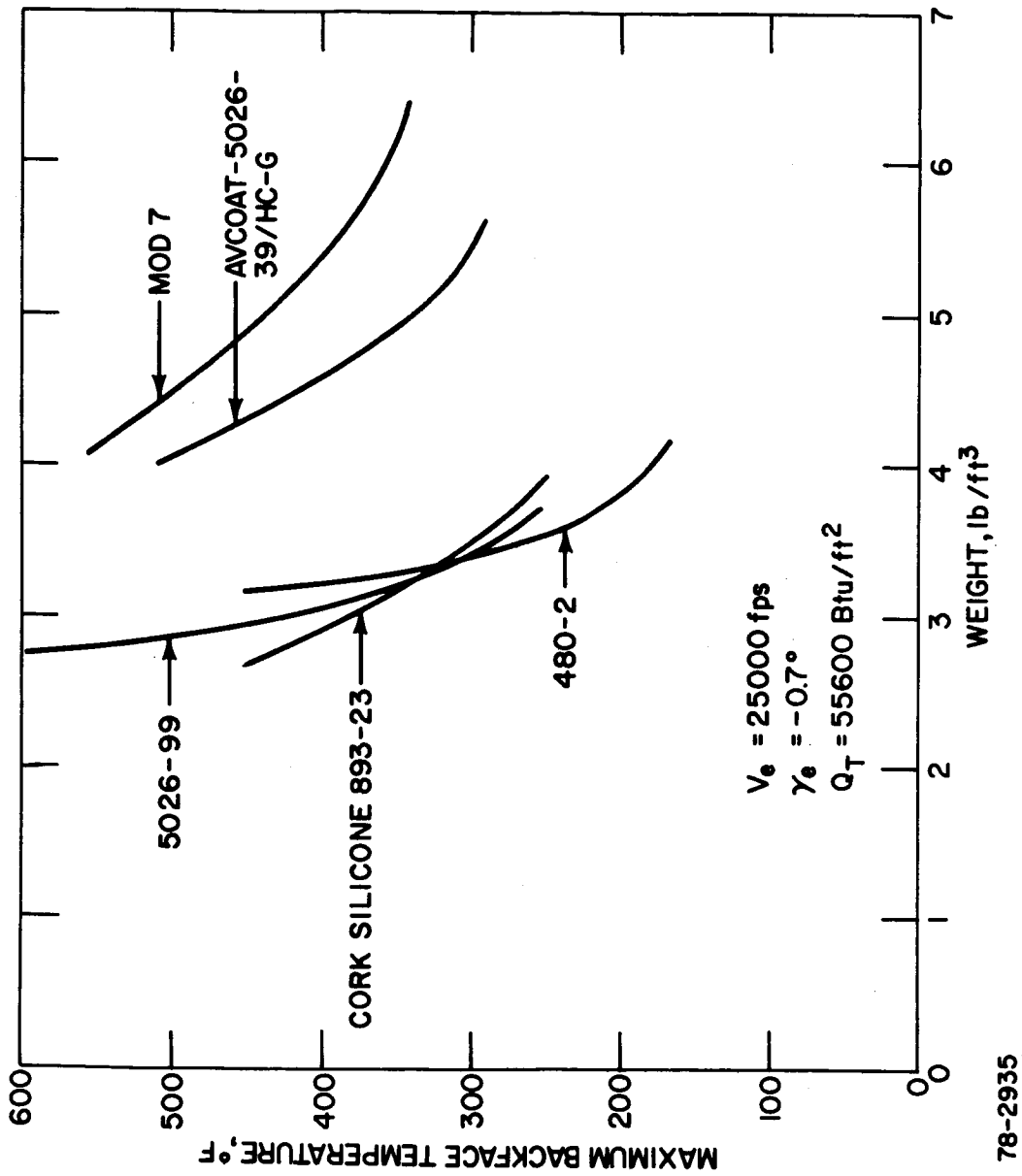


Figure 6.2.3-8 IRV -- HEAT SHIELD WEIGHT DOUBLE SKIP ENTRY STAGNATION POINT

78-2935

TABLE 6.2.3-III

MATERIAL COMPARISON FOR IRV HEAT SHIELD AT STAGNATION POINT

$$V_c = 26000 \text{ FPS} \left. \vphantom{V_c} \right\} \text{Double Skip}$$

$$\gamma_c = -0.7 \text{ degree}$$

MAXIMUM STRUCTURAL TEMPERATURE = 350°F

INITIAL ENTRY TEMPERATURE = 100°F

Material	Local Heat Shield Thickness (in)	Local Heat Shield Weight (lb/ft ²)	Surface Recession (inches)
Cork Silicone	1.26	3.17	0.81
Mod 7	1.76	6.15	0.57
Avcoat 5026-39	1.78	4.90	0.59
Avcoat 5026-99	1.58	3.22	0.73
480-2	2.43	3.28	2.31

shield. However, as mentioned in Section 6.2.3.3.4, the state of development of Avcoat 5026-39 is such that it should be selected for the thermal protection system. Indeed there is no guarantee that cork silicone will prove to be as superior to the Apollo material as indicated in Figure 6.2.3-7 once a complete development test program and flight test of this material become available. Therefore, although at the present time Avcoat 5026-39 does not appear to be the most efficient (low weight) heat shield, Avco recommends its selection as the primary candidate with the stipulations on a vacuum exposure ground test as indicated in Section 6.2.3.3.4.

6.2.3.3 Heat Shield Material Selection

As mentioned previously the candidate low-density heat shield materials include Avcoat 5026-39/HC-G (Apollo material), cork silicone, silicone ablator Mod 7, Avcoat 5026-99, and Silicone 480. Since the heat shield weight is such a small proportion of overall vehicle weight, other factors will have a strong effect on material selection. Among the factors are:

- a. The stability of the material in a vacuum environment for 5 years.
- b. Ease of fabrication, and
- c. The influence of nuclear radiation on material.

Of the three items under consideration, least is known about the stability of the materials since no long-term tests have been conducted and only extrapolations can be made. The influences of the factors on the various materials are discussed in the following sections.

6.2.3.3.1 Thermal Stability of Low-Density Charring Ablators--There are a number of charring resin systems which are stable to various degrees at 250° to 500°F. Among these are silicones, epoxies, phenolics, polyimides, polybensimidazoles, etc. Of these resin systems only the first three have been successfully used to formulate low-density ablative heat shield materials. The relative stability of the heat shield materials formulated from these resin systems is discussed below.

It should be noted that virtually no long-time stability tests have been performed under vacuum/temperature conditions on the candidate heat shield materials. The estimates of stability are based on engineering judgment in extrapolating thermogravimetric analysis (TGA) data which measures only the short-time effects of heating on weight loss. Most of these tests were conducted on the components separately and were run in a helium environment instead of a vacuum.

A. SILICONES

Silicone Ablator Mod 7

This material consists of a flexible silicone resin (RTV 655) with phenolic microballoons and silica fibers. The resin is comparatively stable and from TGA of the components Mod 7 should be stable for long times in a vacuum to about 300°F.

Silicone 480

This is an extra-low-density ablator based on the same flexible silicone resin as Mod 7 (RTV 655). Fillers are phenolic microballoons, silica eccospheres and silica fibers. No long-time thermal stability tests have been run on 480 yet, but from TGA data on its components, it should be stable for 5 years in a vacuum to about 300°F.

Cork Silicone (893-23)

This is a medium low-density flexible silicone ablator consisting of cork particles, silicone resin, and glass fibers. It should have stability characteristics similar to 480 above.

B. EPOXIES

AVCOAT 5026-39/HC-G (Apollo Heat Shield)

This material consists of an epoxy-novolac resin with various flexibilizers, phenolic microballoons, glass fibers and silica fibers. The mixture is gunned into fiberglass honeycomb cells edge bonded to a substructure. Due to the nature of the material and the fabrication sequence, it cannot be post-cured above 250°F. Therefore, it is not dimensionally stable for long times in a vacuum above about 150°F. If this ablator is bonded to an aluminum substructure, it should be possible to post-cure it at a somewhat higher temperature than 250°F without cracking. This may improve its elevated temperature stability enough to make it a candidate for IRV.

AVCOAT 5026-99

This is a low-density form of the 5026-39 ablative filler molded into panels (no honeycomb matrix). Since it has no honeycomb matrix, it can be post-cured at a higher temperature than 250°F. Therefore, it should be possible to make this material stable in a vacuum to about 250° to 300°F.

C. PHENOLICS

Low-density Nylon Phenolic

This material has not been used to any extent on flight vehicles primarily due to the complicated fabrication procedures required. Therefore, no definitive data exists on long-time stability at elevated temperatures. The presence of nylon powder in the formulation would tend to hurt the stability somewhat. Basically the phenolic resin and the phenolic microballoons should be stable to 300° to 400°F in a vacuum provided the composite was post-cured at 400° to 475°F (in a vacuum or inert atmosphere).

6.2.3.3.2 Fabrication

Silicone Ablator Mod 7 and Silicone 480

These materials are fabricated by first mixing up the components to form a

clay-like compound. This compound can be die molded or vacuum bag molded against a contoured mandril. In applying these materials to an actual vehicle, the most efficient method is to coat the vehicle surface with a silicone primer and after it is partially cured, to apply the compound by handputtying (followed by vacuum bag curing and finally post-curing). The heat shield is thus self-bonded to the substructure. After final machining to size, the heat shield is complete.

Cork Silicone (893-23)

This material starts out as a very light, fluffy mixture of cork particles, resin, and fibers. It must be compressed over seven times in volume during molding to final density. Therefore, it is made only in rigid metal dies. The normal method of fabrication is to mold a panel several inches thick and one to two feet square and then to slice it into sheets of the desired thickness which are, in turn, bonded onto the substructure using an epoxy resin. The material is flexible enough to conform to most two-dimensionally curved surfaces (cylinders, cones, etc.) However, for three-dimensionally curved surfaces the sheets must be cut fairly small and pieced together before bonding. It should be noted that the adhesive joints in low-density ablators of this type usually have superior ablation resistance (compared to the base heat shield) because the adhesive is about two to three times more dense.

AVCOAT 5026-39/Hc-G

This material was developed for and used on the Apollo vehicle. It consists of a fiberglass honeycomb filled with a low-density charring epoxy ablator. It is fabricated by first bonding the fiberglass honeycomb onto the substructure (with HT-424 adhesive tape) with the cells essentially perpendicular to the surface. Then each cell is "gunned" full of ablator by operators using air-powered, hand-held "guns". After a large area has been gunned full of green ablator, it is vacuum bag cured. When the entire heat shield is completed, it is given one final post-cure and is finish machined.

AVCOAT 5026-99

This is a low-density form of the 5026-39 ablative filler used above but without a honeycomb matrix. It is normally molded in dies into a flat or contoured panel. Each panel must then be machined on all edges (overlapping flanges) and on the inner surface to mate the specific vehicle contour for its location. The panels are then fitted and bonded in place.

Low-density Nylon Phenolic

This is a NASA/Langley developed heat shield consisting of phenolic resin and microballoons plus nylon powder. It is fabricated by mixing the components in a vacuum blender. It is cast into a mold by placing the mold in a vacuum chamber and feeding the above mixture into the chamber through a funnel. This procedure is very awkward and the sizes of parts produced is quite limited.

6.2.3.3.3 Radiation Effects

Table 6.2.3-IV summarizes the threshold damage level for the various materials. Since applicable data is not available on these specific materials, best estimates were made from the available data on the constituents as obtained from Reference 6.2.3-1. Since the expected dosage level from the heat source is approximately 10^5 rads, no problem is anticipated. In addition, the materials can withstand 10^{13} neutrons/cm² which is larger than the 10^{12} neutrons/cm² expected from the heat source.

6.2.3.3.3 Summary--In view of the above factors, it appears that the best candidate for the IRV would be the Apollo material (AVCOAT 5026-39/HC-G) because of the state of development, background in fabrication problems, and experience in flight tests. However, the possibility of stability problems with this material would dictate the existence of a back-up material with a silicone system such as Mod 7 or cork silicone. In any case, it would appear that a ground test program to determine the effects of long-time vacuum exposure on these materials would be required before any final selection is made. Table 6.2.3-V compares the relative performance of the materials from a structural and thermal property standpoint. Low-density nylon phenolic has not been included in the table since its fabrication complexity indicates it to be a less promising candidate.

REFERENCES

- 6.2.3-1 Space Materials Hand Book, Second Edition, Technical Documentary Report No. ML-TDR-64-40 (January 1965).

TABLE 6.2.3-IV

RADIATION THRESHOLD LEVELS FOR CANDIDATE MATERIALS

Material	Threshold Damage Level (Rads)
AVCOAT 5026-39/HC-G	2×10^9
Cork Silicone	10^7
Mod 7	10^7
AVCOAT 5026-99	2×10^9
Low-density Nylon Phenolic	8×10^9
Silicone 480	10^7

TABLE 6.2.3-V

PROPERTIES OF TYPICAL LOW-DENSITY ABLATORS

Material	Mod 7	480-2	893-23	Avcoat 5026-99	Avcoat 5026-39/HC-G
<u>Composition</u>	Low-density filled silicone elastomer	Low-density filled silicone elastomer	Glass-reinforced cork silicone elastomer	Low-density charring epoxy	Low-density charring epoxy in FG H/C
<u>Density (lb/ft³)</u>	36	16	32	25	32
<u>Tensile Properties</u>					
<u>Tensile Strength (psi)</u>					
-150°F	695	478	540 (-100°F)	1400 (-35°F)	680
75°F	328	135	170	640	560
400°F	203	100	96 (300°F)	263 (350°F)	210
<u>Total Strain to Failure (percent)</u>					
-150°F	8.0	4.0	3.0 (-100°F)	1.6 (-35°F)	0.6
75°F	5.2	1.7	9.0	2.9	0.8
400°F	3.3	4.4	4.0 (300°F)	0.2 (350°F)	0.4
<u>Elastic Modulus (psi x 10⁻⁶)</u>					
-150°F	0.024	0.024	0.009 (-100°F)	0.130 (-35°F)	0.15
75°F	0.008	0.009	0.002	0.040	0.12
400°F	0.007	---	0.001 (300°F)	0.036 (350°F)	0.03
<u>Coefficient of Thermal Expansion (in./in./°F x 10⁻⁶)</u>					
-150 to 75°F	35	19	23	17	19
-100 to 75°F					
<u>Thermal Properties</u>					
<u>Thermal Conductivity (Btu/hr-ft-°F at 250°F)</u>	0.055	0.030	0.054	0.043	0.072
<u>Specific Heat (Btu/lb-°F from 750 to 450°F)</u>	0.389	0.360	0.471	0.455	0.35

7.0 TERMINAL SURVIVAL SYSTEMS

The analyses described in the previous sections defined IRV requirements in terms of reentry survival. In addition, it is a desirable goal to ensure intact impact of the HS, thereby minimizing potential nuclear hazards during and subsequent to impact. To this end then, considerable effort has been expended in evaluating the utility of drag augmentation (and recovery) system, impact attenuation schemes, and location aids for inclusion in the basic IRV. At the conclusion of the Phase IA effort a decision was made to cease investigation of aerial recovery systems. Therefore, Phase IB effort has been limited to a review of parachutes and ballutes as drag augmentation devices to limit terminal impact velocities. It also should be noted that parachutes can exhibit an unacceptable failure mode, i.e., a deployment failure in which the partially deployed parachute wraps itself around the descending IRV thereby causing the IRV to become unstable and tumble during descent. A tuck-back ballute system also shows potential as a drag augmentation device and study of such a system was initiated during Phase IB.

Impact attenuation studies were based primarily on an optimization and parametric study of the "Rotating Plate Concept" introduced in the Phase IA task.

This section also includes a brief review of location aid requirements for the IRV system.

7.1 DRAG AUGMENTATION DEVICES

The application of drag augmentation devices to the IRV was originally intended to allow for aerial recovery. The system under consideration included a main chute, recovery chute, and the ancillary equipment to package and deploy these devices.

During Study Phase IB, the requirement for drag augmentation to reduce impact was identified. The impact attenuation system must be designed to protect the heat source under the most extreme impact conditions (i.e., drag augmentation failure). However, inclusion of a drag augmentation device can significantly decrease the probability of failure upon impact by reducing the impact structural loads.

For this application, two drag augmentation devices have been examined briefly. Further study will follow during Study Phase II if applicable to the preliminary design. The ring sail parachute system and the tuck-back ballute system have been examined for a deployment at a dynamic pressure of 48 pounds per square foot and terminal velocities of 100 feet per second and 50 feet per second as shown in Figures 7.1-1 and 7.1-2. The ballute system was significantly heavier and required more packaging volume than the parachute. This volume can take the form of a toroidal package which is more easily packaged in the IRV. The ballute has a better probability of inflation under off-nominal conditions such as a rolling or tumbling reentry situation. The possibility of large angle of attack oscillations at deployment due to wind gusts make the ballute a better selection if the larger weight can be accommodated. The ballute, particularly the tuck-back ballute, have had comparatively less development and represent a possibly costly development program to achieve a comparable confidence level. The trade-off between these two drag augmentation devices requires more study with the particular IRV design selected for Study Phase II. The comparison is shown in Figure 7.1-3.

DEPLOY AT $q = 48 \text{ LB/FT}^2$

STABILITY $\pm 10^\circ$

TERMINAL VELOCITY - 100 FPS

PARACHUTE SYSTEM WEIGHT - 20.6 LB

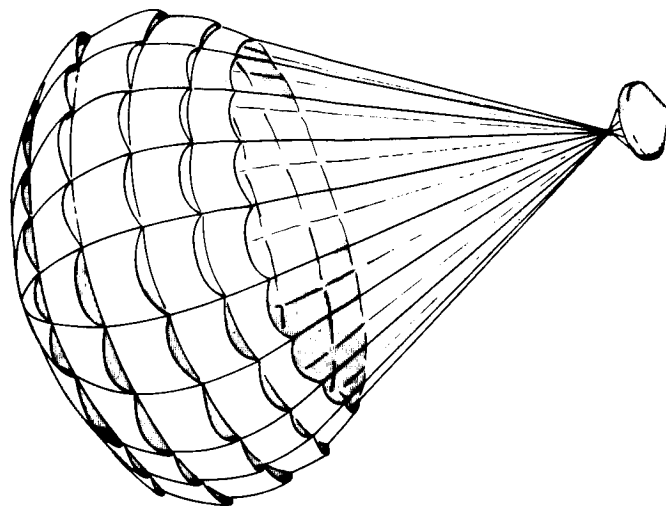
PARACHUTE SYSTEM VOLUME - 0.6 CU FT

TERMINAL VELOCITY - 50 FPS

PARACHUTE SYSTEM WEIGHT - 68.5 LB

PARACHUTE SYSTEM VOLUME - 2.0 CU FT

NO AERIAL RECOVERY CAPABILITY

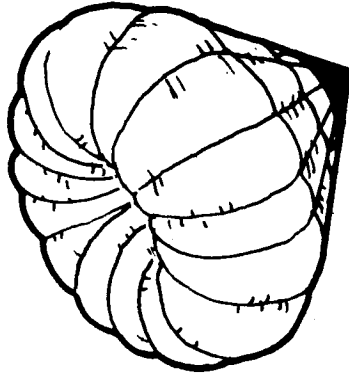


DEPLOY AT $q = 48 \text{ LB/FT}^2$

TERMINAL VELOCITY - 100 FPS

BALLUTE SYSTEM WEIGHT - 42 LB

BALLUTE SYSTEM VOLUME - 1.2 CU FT



TERMINAL VELOCITY - 50 FPS

BALLUTE SYSTEM WEIGHT - 102 LB

BALLUTE SYSTEM VOLUME - 4.7 CU FT

NO AERIAL RECOVERY CAPABILITY

Figure 7.1-2 TUCK-BACK BALLUTE (CD = 0.5)

78-0629

	PARACHUTE	BALLUTE
WEIGHT	LIGHTER BY FACTOR OF 1.5 TO 2.0	--
PACKAGING	REQUIRES LESS VOLUME	BETTER CONFIGURATION
INFLATION RELIABILITY	VERY RELIABLE UNDER NOMINAL DEPLOYMENT CONDITIONS	MORE RELIABLE INFLATION UNDER OFF NOMINAL DEPLOYMENT CONDITIONS
STATE OF ART	WELL WITHIN STATE-OF-ART	LIMITED TEST DATA AVAIL. DEVELOPMENT REQUIRED
MATERIALS	PROBABLY NOMEK	DACRON OR NYLON NEOPRENE COATED

78-0631

Figure 7.1-3 AERODYNAMIC DECELERATOR COMPARISON

7.2 IMPACT ATTENUATION

7.2.1 Summary

The Rotating Plate Concept, introduced and discussed in the Phase IA Report, Section 5.4.5.4, has been modified by the addition of a "cold plate" (a structural honeycomb plate located below the insulation and the heat source). This section presents the results of parametric studies conducted for the purpose of determining the effect of the modified impact attenuation system on overall vehicle weight and diameter.

7.2.2 Cold Plate Concept

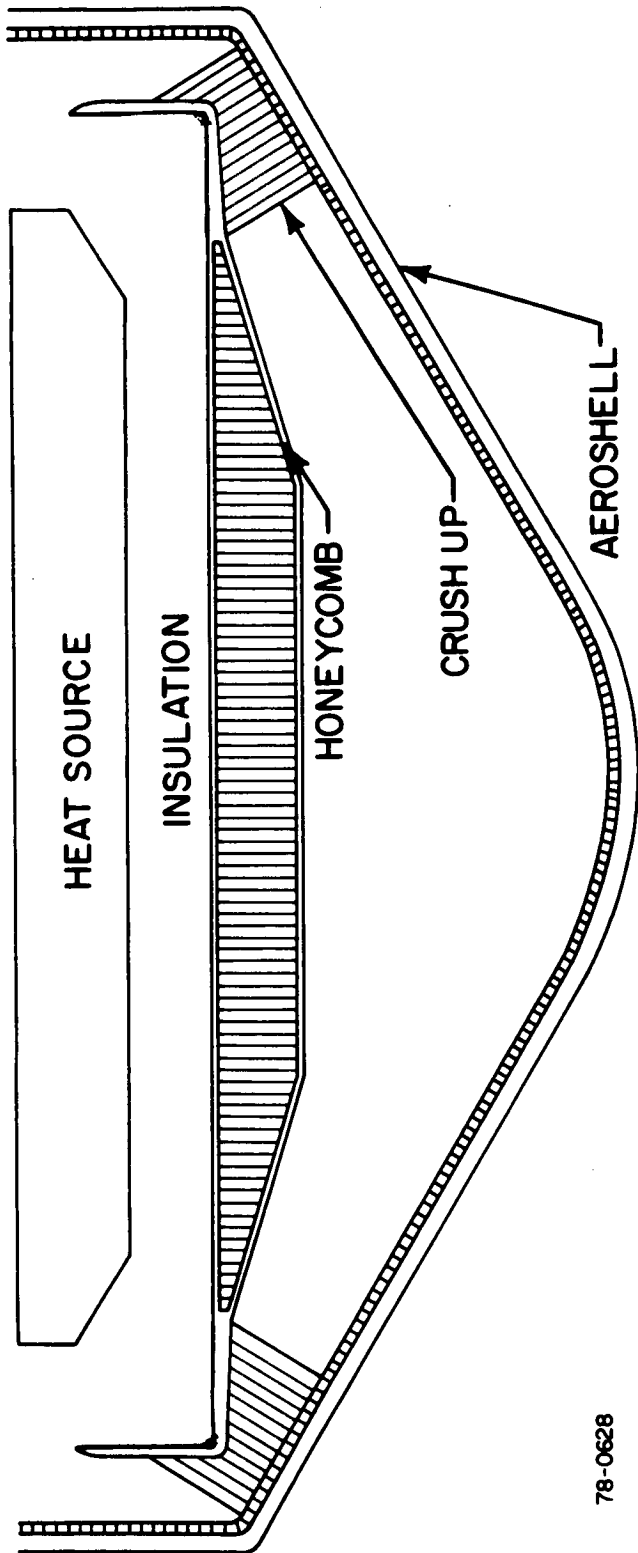
Previously, the Rotating Plate Concept utilized a strengthened heat source plate to enhance its own ability to withstand the impact loads. The heat source plate however is operating at a low design bending stress (approximately 20,000 psi) because of the severe thermal environment to which it is subjected. The Cold Plate Concept takes advantage of the much lower temperatures which exist outside the super insulation (see Figure 7.2-1). Consequently, different materials which have much higher strength/weight ratios can be utilized.

The rotating maneuver proceeds as before, except that during impact, after the supporting truss system has failed, the HS compresses the insulation and is supported in turn by the cold plate. Lateral motion is prevented by the peripheral ring around the outside of the cold plate and friction. The heat source plate is constrained to rotate with the cold plate until flat impact is achieved. The cold plate is designed to withstand the shear and bending loads caused by the localized loads at the edge of the plate and the inertial loads imposed on it by the heat source. In addition, the cold plate aids in distributing and reducing the flat impact loads transmitted to the heat source. It also will reduce the concentrated loading effect due to sharp projections and surface irregularities.

7.2.3 IRV Optimization Study

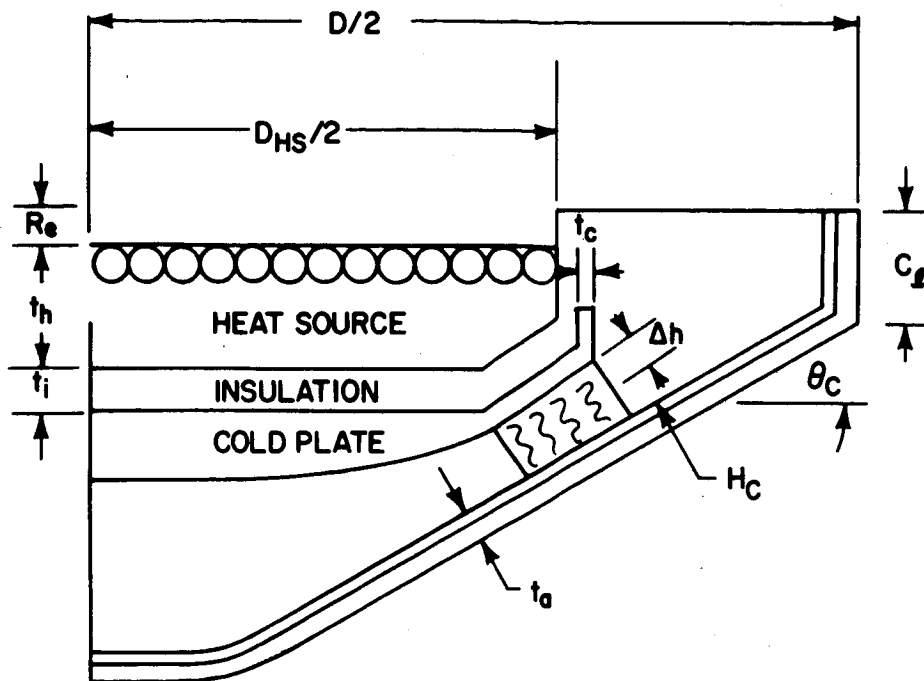
Integration of the impact attenuation system with the IRV results in a direct weight and increased diameter penalty. The increased diameter is geometrically related to the crush-up stroke as seen in Figure 7.2-2. Consequently, a reduction in the stroke requirement can significantly reduce the IRV's diameter. A decrease in stroke however means that a greater force must be transmitted to the cold plate and this, because of the more severe structural requirements, results in an additional weight penalty. This trend is further reinforced by the fact that a smaller diameter vehicle will exhibit higher terminal velocities and will consequently see even higher impacting loads. A tradeoff therefore exists between vehicle diameter and weight. This section presents the analytical approach and the results of the indicated vehicle tradeoff optimization study.

The analytical treatment developed in Appendix E of the Phase IA report has been modified to include the cold plate concept (see the Appendix). These equations have been mechanized in order to determine the parametric relationships between heat source geometry and weight, cold plate geometry and weight, terminal impacting velocity, and required crush-up stroke. Typical results of these studies are presented in Figures 7.2-3 and 7.2-4. For each heat source configuration of interest (including assumed cold plate geometry), the cold plate weight has been



78-0628

Figure 7.2-1 COLD PLATE CONCEPT



D = IRV Diameter

D_{HS} = Heat Source diameter

R_e = Capsule recess

t_h = Heat Source thickness

t_i = Insulation thickness

t_c = Cold plate edge thickness

t_a = Aeroshell thickness

ΔH = Corner recess

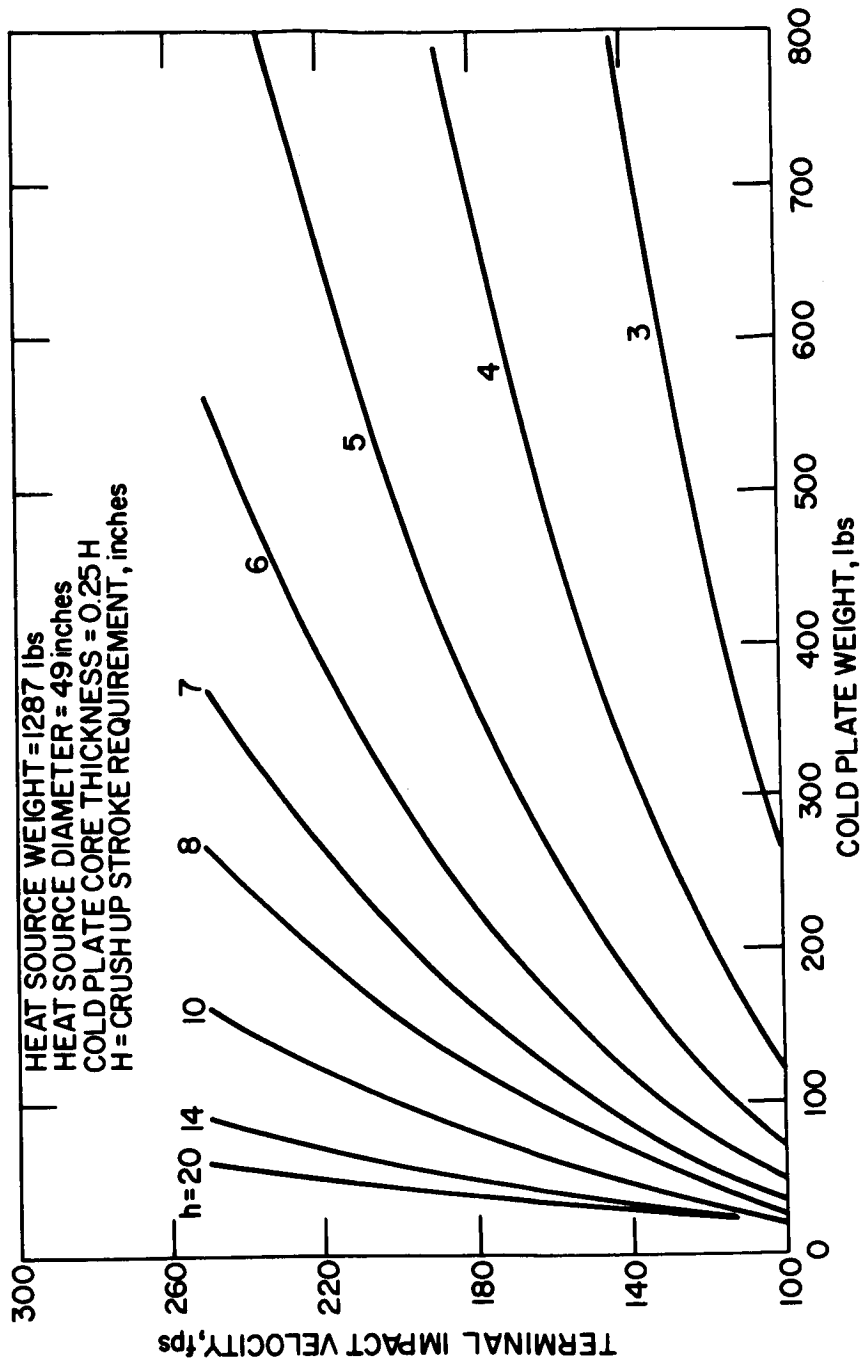
H_c = Crush-up height

θ_c = Blunt cone angle

C = Cylinder length = kD

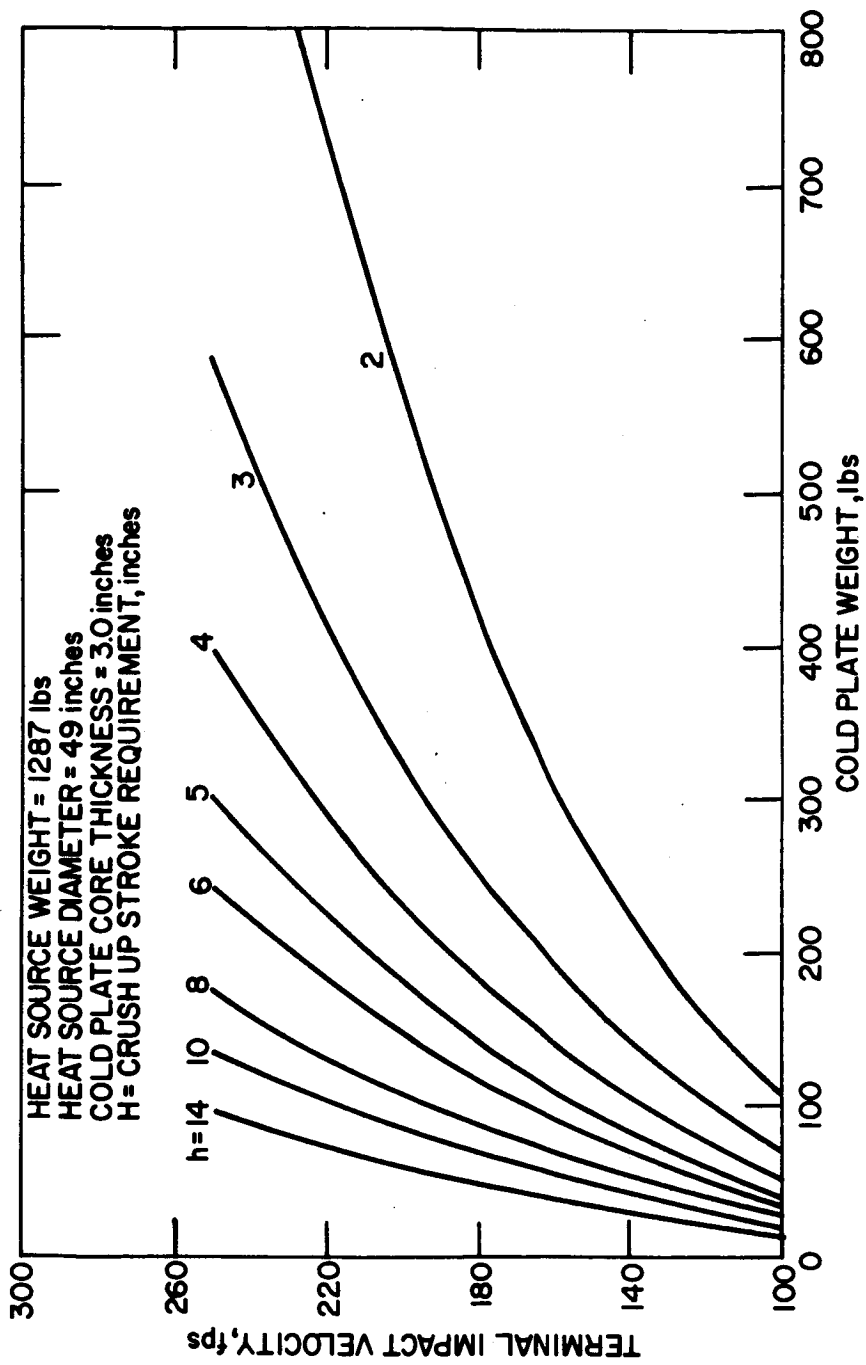
$$D = \frac{2}{\tan \theta + k/2} \left[R_e + t_h + \frac{t_i}{\cos^2 \theta} + \frac{t_c + t_s}{\cos \theta_c} + \frac{h - \Delta h}{\cos \theta_c} + \frac{D_{HS}}{2} \tan \theta_c \right]$$

Figure 7.2-2 IRV GEOMETRY



78-2937

Figure 7.2-3 STROKE AND COLD PLATE WEIGHT REQUIREMENTS
(PLATE THICKNESS = f(H))



78-2938

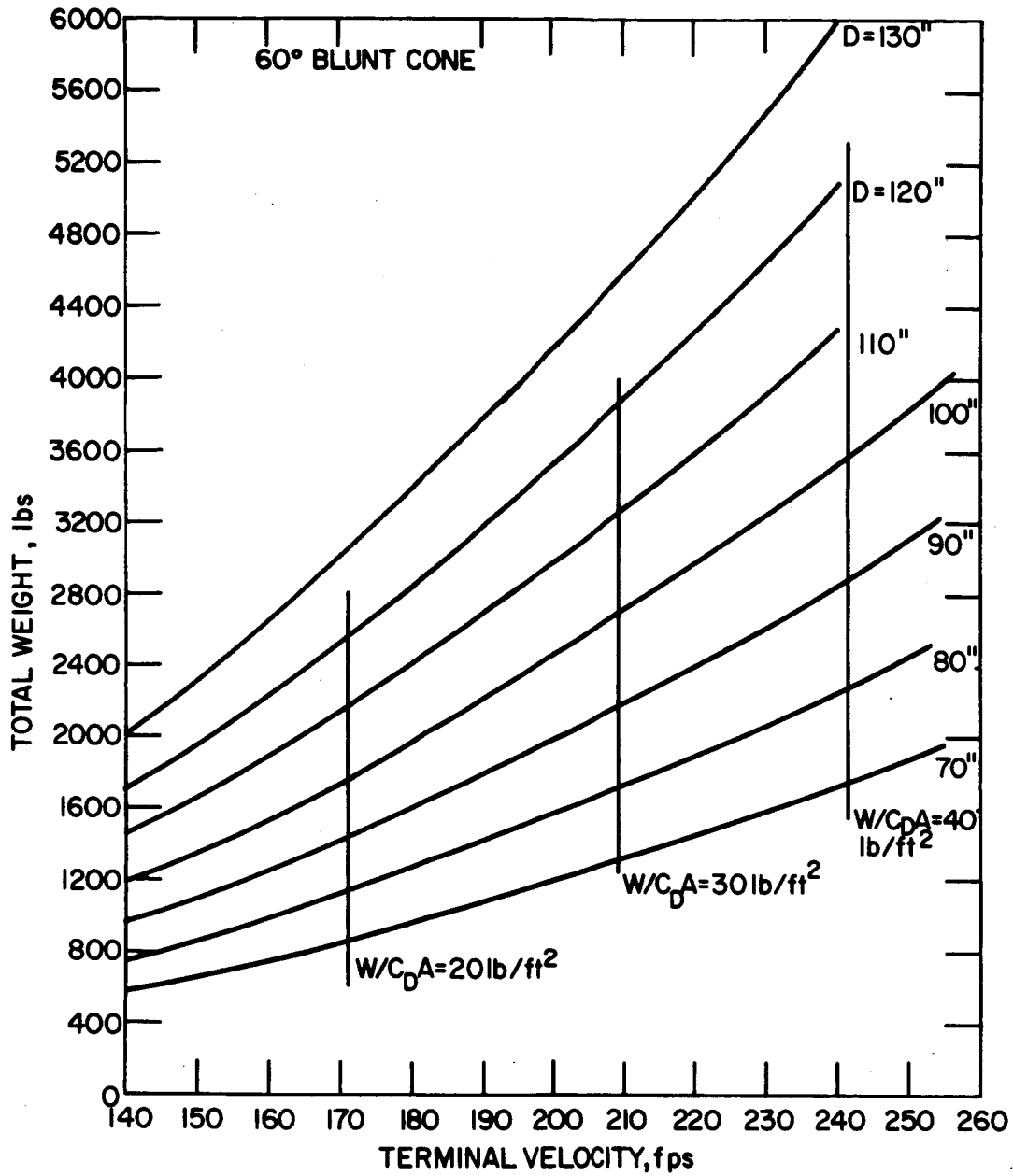
Figure 7.2-4 STROKE AND COLD PLATE WEIGHT REQUIREMENTS
(PLATE THICKNESS = CONSTANT)

determined for the entire range of terminal velocities and crush-up heights. The terminal velocity is a direct function of the vehicle ballistic parameter which in turn contains vehicle gross weight and diameter (see Figure 7.2-5). Vehicle diameter is geometrically related to crush-up stroke as indicated by the relationship presented in Figure 7.2-2. This expression considers all the pertinent design layout parameters including, specific design modifications such as capsule recess, cylinder height, and cold plate corner recess. The corner recess innovation has been instituted for the purpose of increasing the available volume for crush-up material without the subsequent penalty of increased vehicle diameter (see Figure 7.2-6). Total weight of the vehicle is the sum of fixed weights, the impact attenuation system weight, and component weights which are a function of the vehicle diameter. These include the structural and heat shield weights and have been combined as shown in Figure 7.2-7.

Interrelated considerations have been combined to produce a graphical and analytical iteration procedure which allows the determination of point designs for the basic weight-diameter optimization studies. The procedure also allows the isolation and study of specific design modifications so as to determine their effect on overall vehicle weight and/or size.

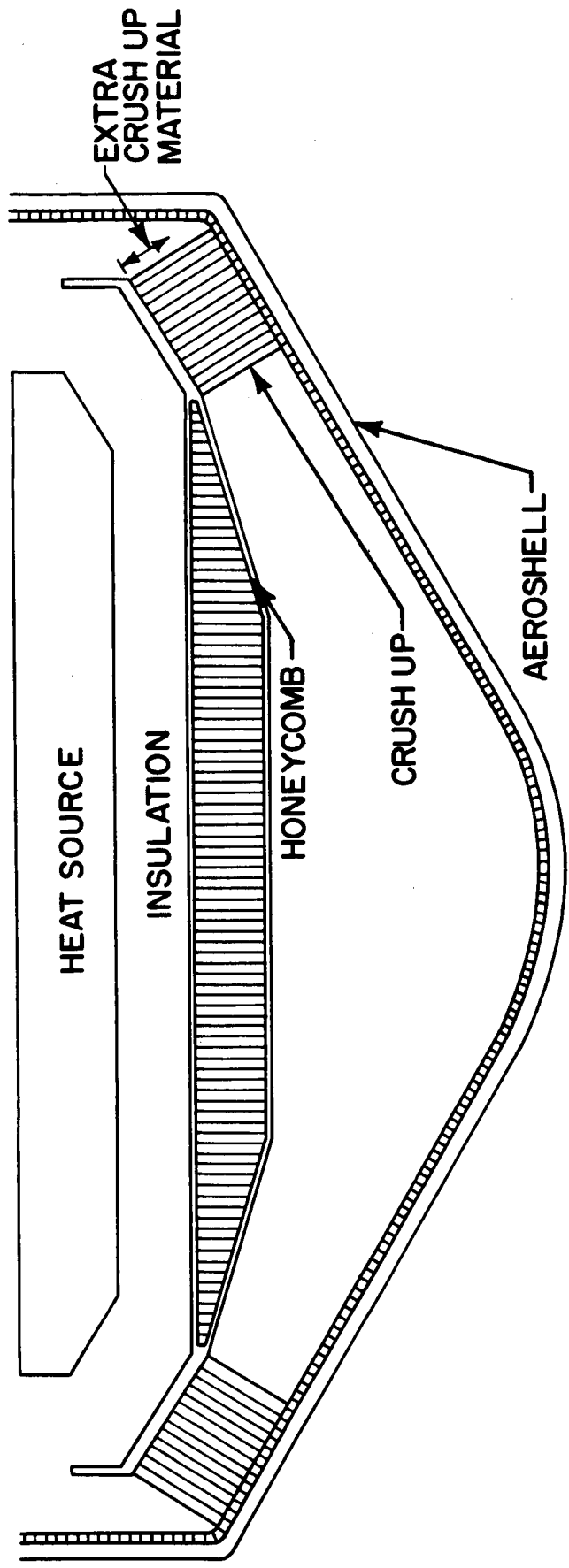
Data presented in Figure 7.2-8 is typical of the results obtained in these optimization studies and indicates the specific effect of variations in the capsule mounting geometry. It is evident that employment of an exposed capsule configuration directly increases the available volume for crush-up material and therefore reduces the required vehicle diameter. It should be noted that these results are representative of the IRV without the other possible modifications; i.e., no corner recess and with the cold plate honeycomb thickness set at 25 percent of the crush-up material height. This criterion is established by the fact that 25 percent of a typical crush-up material is unusable, and if full rotation is considered necessary, without the cold plate itself contacting the ground, then the thickness of the cold plate cannot be greater than 25 percent of the crush-up height.

As is noted, capsule mounting geometry is one of the design options which have a direct effect on the impact attenuation system and therefore on vehicle weight and size. Another such parameter is basic heat sources weight. The effect of reducing heat source weight is shown in Figure 7.2-9. This reduction could be accomplished by modifying the fuel capsule to the vented capsule design. The effect of corner recess is presented in Figure 7.2-10. The weight saving is not significant, but the diameter reduction of 10 inches is, and the 2-inch recess has been employed in the 85-inch-diameter circular planar (ORNL) design. The parametric data of Figures 7.2-9 and 7.2-10 are also based upon the honeycomb core thickness of the cold plate of 25 percent of the crush-up height. Figure 7.2-11 presents comparison data for the case where the core thickness is held constant at 3.0 inches. A significant reduction in diameter can be realized; however, the cold plate will now contact the ground before full rotation has been achieved. This will result in some local failure but it is difficult to ascertain the overall effect without further study and possibly testing. Figure 7.2-12 presents the effect that a reduction in terminal velocity would have on the integrated vehicle design. Such a design, however, must be based upon the successful operation of an active device such as an aerodynamic decelerator.



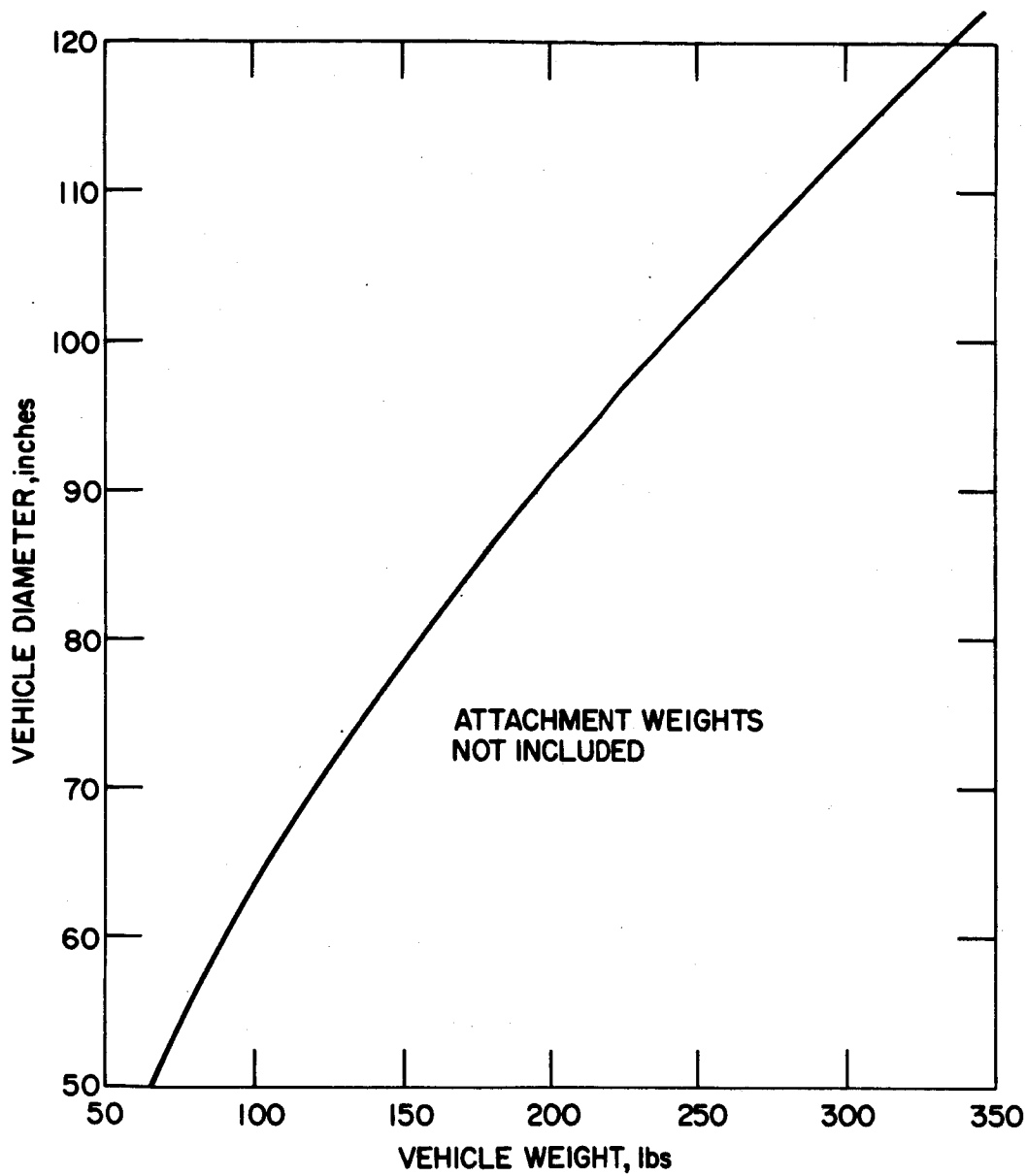
78-2939

Figure 7.2-5 IRV WEIGHT VERSUS TERMINAL VELOCITY



78-0627

Figure 7.2-6 COLD PLATE CONCEPT WITH RECESSED CORNER



78-2940

Figure 7.2-7 IRV AEROSHELL DIAMETER (HEAT SHIELD, BOND, AND ALUMINUM HONEYCOMB) VERSUS AEROSHELL WEIGHT 60-DEGREE BLUNT CONE, 15-PERCENT CYLINDER

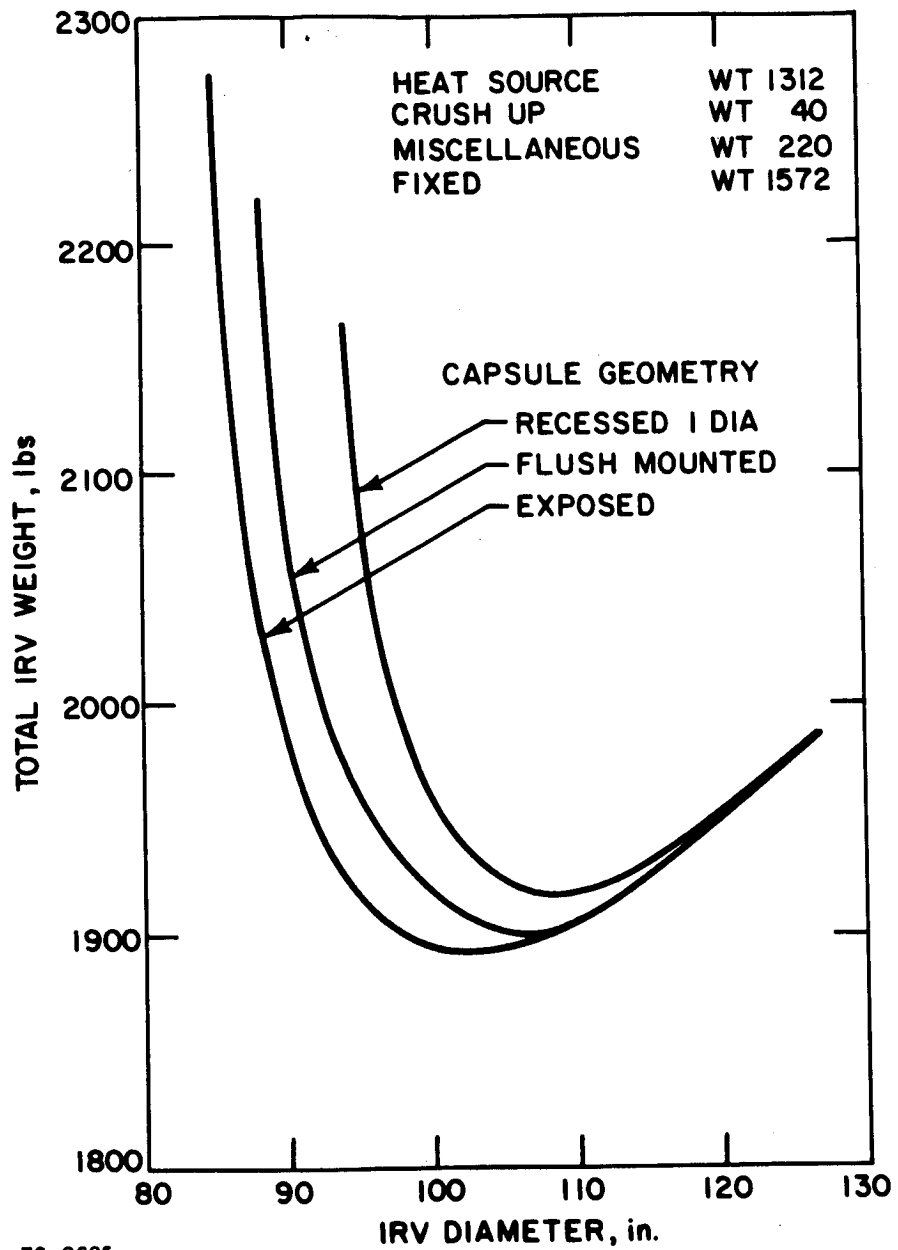


Figure 7.2-8 IRV WEIGHT OPTIMIZATION STUDY (CAPSULE MOUNTING OPTIONS)

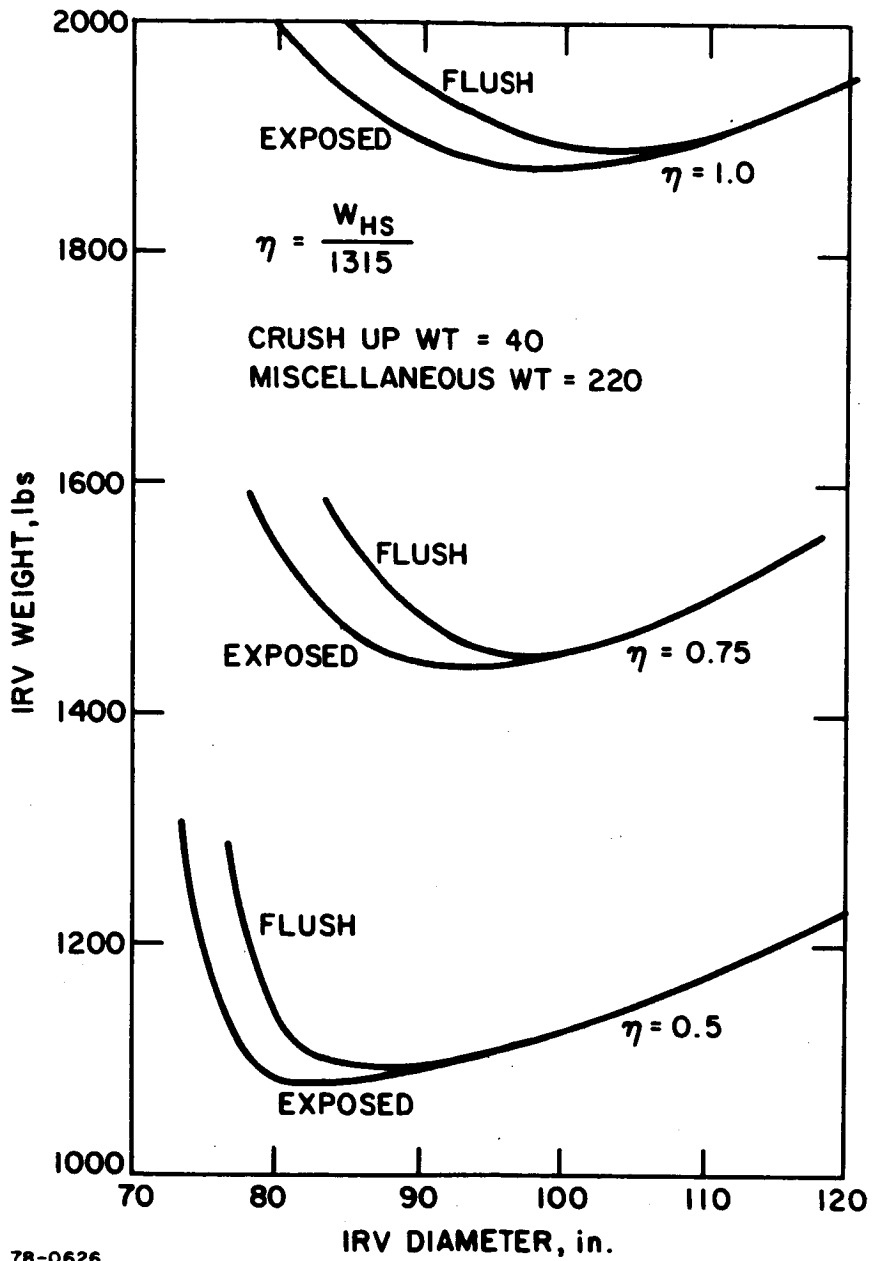
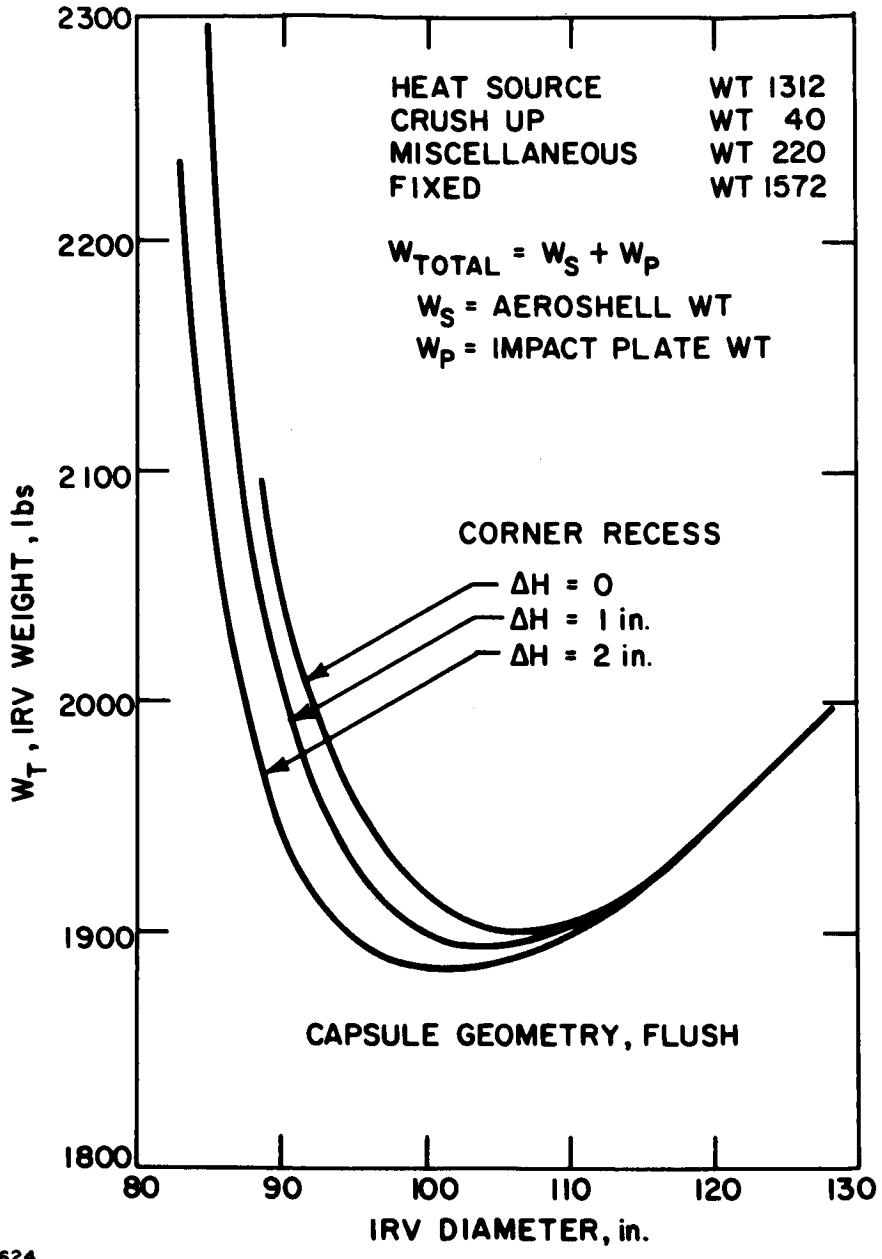
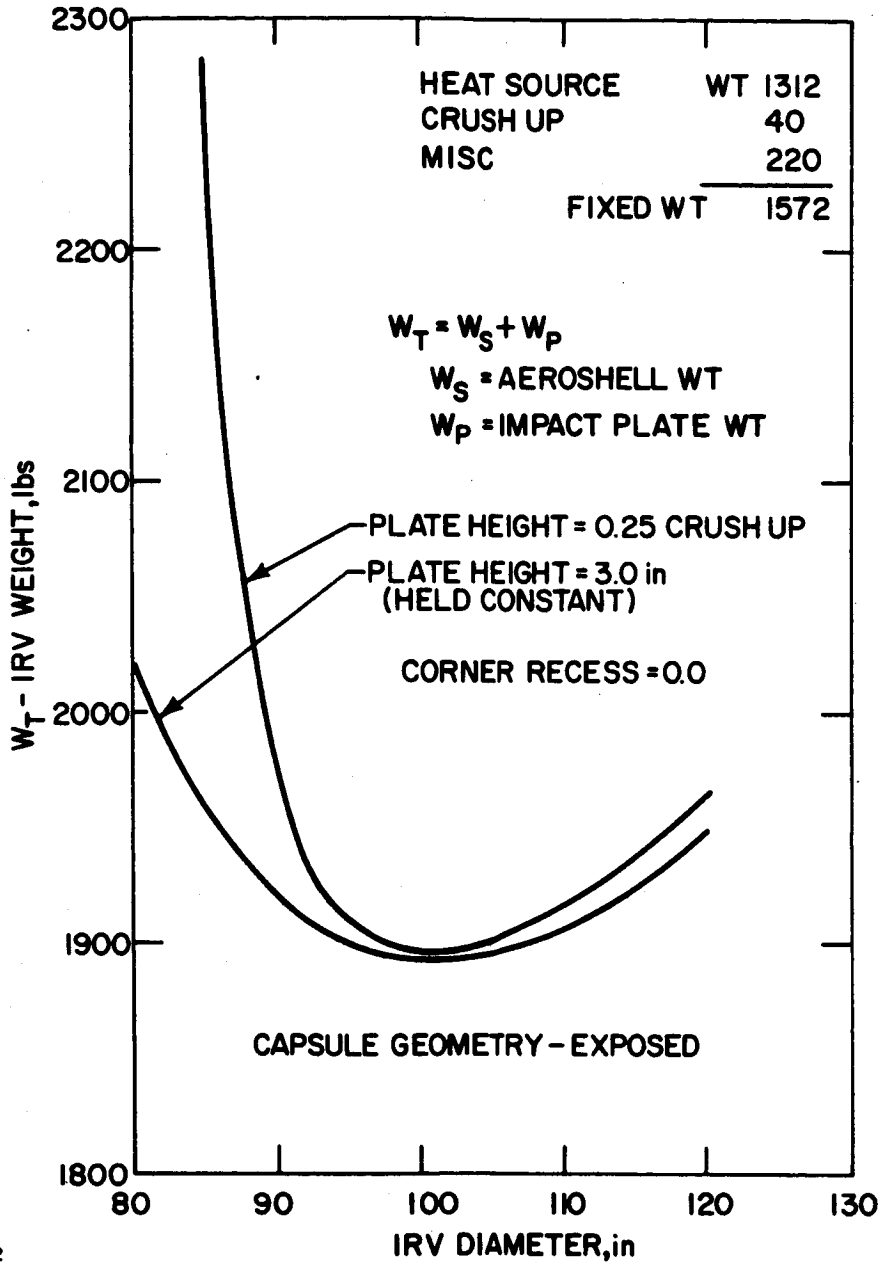


Figure 7.2-9 IRV WEIGHT, DIAMETER TRADEOFF (HS WEIGHT OPTION)



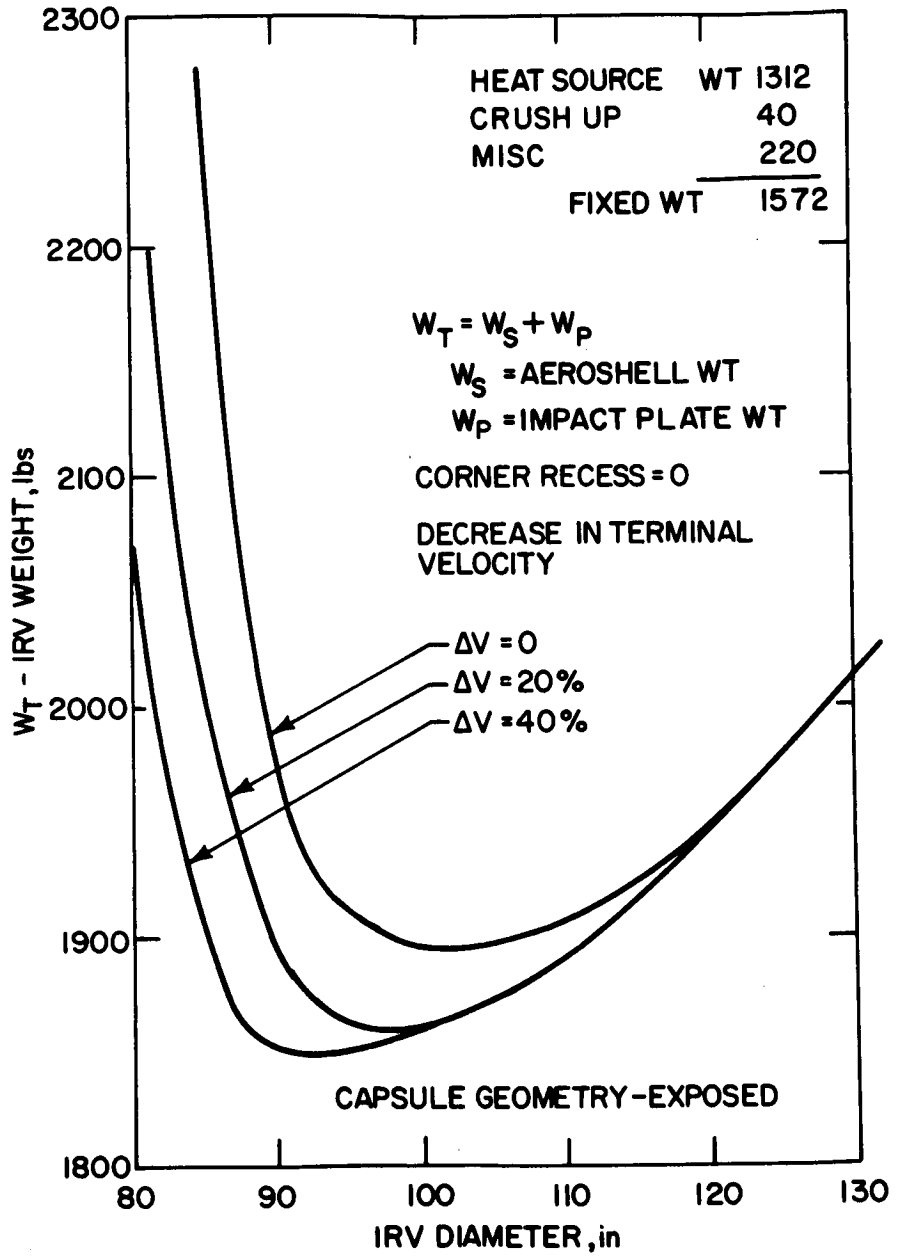
78-0624

Figure 7.2-10 IRV WEIGHT VERSUS DIAMETER (CORNER RECESS EFFECT)



78-0622

Figure 7.2-11 IRV WEIGHT VERSUS DIAMETER (COLD PLATE THICKNESS OPTION)



78-0623

Figure 7.2-12 IRV WEIGHT VERSUS DIAMETER (IMPACT VELOCITY EFFECT)

If successful, it would increase the probability of impact survival of the HS by significantly reducing the impact loading environment.

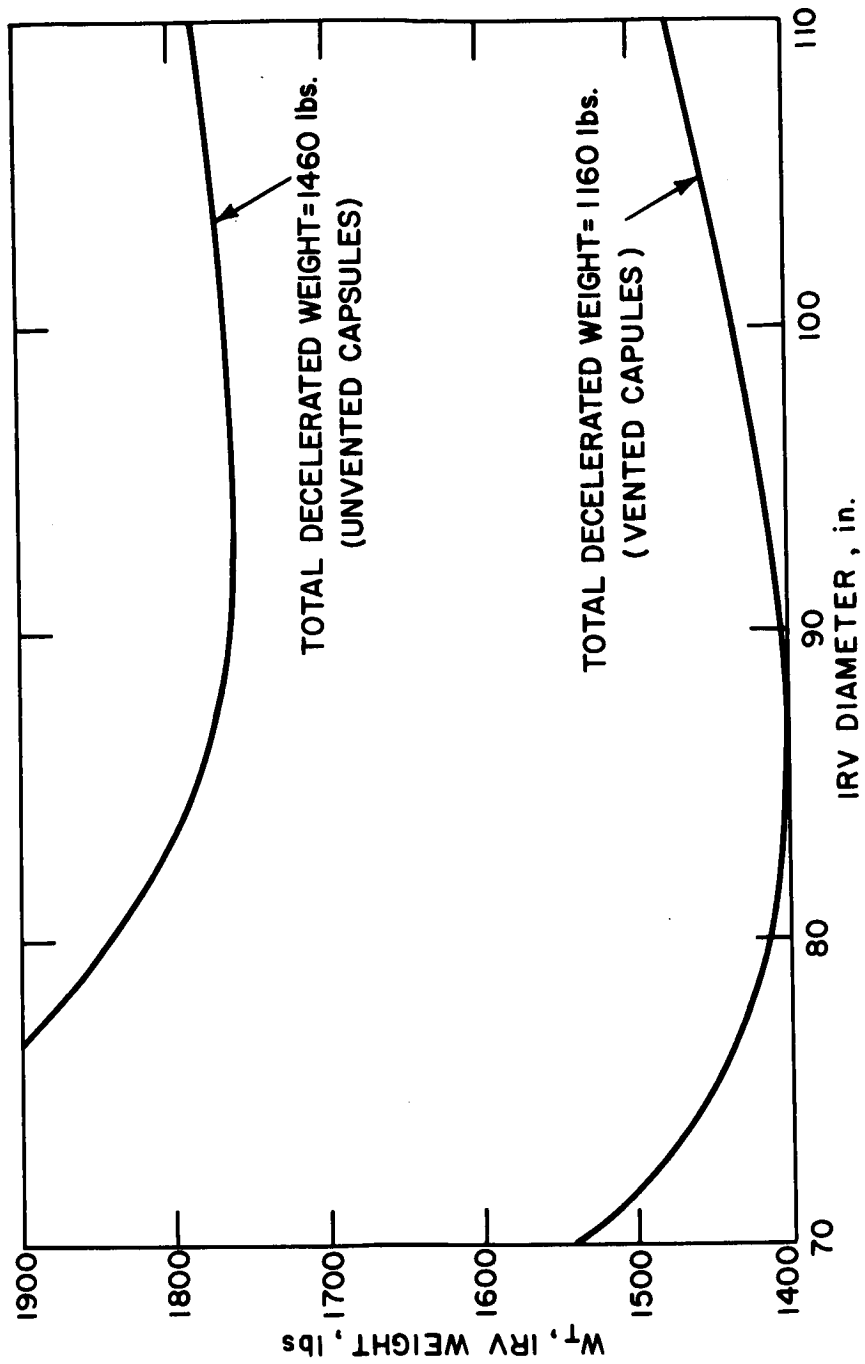
The data presented in Figure 7.2-13 considers the effect of combining four of the pertinent design modification parameters: heat source weight, capsule mounting geometry, cold plate honeycomb core thickness, and corner recess. The modifications are readily accommodated and the resulting vehicle designs are therefore considered realizable.

7.3 LOCATION AIDS

The primary location aids are shown in Figure 7.3-1. The recovery beacon operates in the 230 to 250-mhz region with standard aircraft direction finding equipment over a 25 to 50-mile range. The antenna is a whip which is deployed at impact. A beacon of this class has been used for many recovery operations, both land and water, and is designed to survive land impact. The beacon is powered by a sealed wet cell nickel cadmium battery, or if replaceability is possible, mercury batteries can be used. The nickel cadmium battery must be continuously or periodically trickle charged to maintain its charge for the possible 5-year life in space. Primary nickel cadmium or silver zinc batteries (dry charged with electrolyte added remotely when power is needed) are a possibility, but represent a one-shot active mechanism which reduces the reliability of the power subsystem.

A flashing light can be used as an auxiliary recovery aid for terminal recovery operations at night. The flashing light has not proven to be an effective primary location aid unless the recovery beacon fails and then the payload is seldom recovered. The search pattern necessary with a flashing light is restrictively narrow.

Other location aids which are available are the use of luminous color on the upper surface of the flotation balloon for water recovery, and the use of IR detectors on aircraft or helicopters for land recovery. The forest rangers in the northwestern states and Canada have been locating campfires and other small potential fire hazards by this technique with great success during the last 5 years.



78-0621

Figure 7.2-13 REFERENCE DESIGN WEIGHT, DIAMETER TRADEOFF STUDY

	WEIGHT	VOLUME		
RECOVERY BEACON (230 TO 250 MH ₇) (25 TO 50 MILE RANGE)	2 OZ	3.5 CU IN	PRIMARILY FOR WATER RECOVERY	
FLASHING LIGHT (NIGHT SEARCH) (25-MILE RANGE)	16 OZ	4 CU IN		MAY NOT SURVIVE LAND IMPACT IF >5-10,000 G's
BATTERY (60-HR LIFE)	25 LB	350 CU IN		TRICKLE CHARGE FOR 5-YEAR LIFE
LUMINOUS COLOR	FLOTATION BALLOON			
IR SOURCE	IRV		PRIME LAND RECOVERY AID	

Figure 7.3-1 LOCATION AIDS

8.0 IRV SYSTEM

This section summarizes the design and integration effort performance on the IRV system, its associated S/C on Launch Vehicle interface and specific systems integration analyses completed during Task IB. It also includes a comprehensive discussion of the HSHX Task IB design effort as well as a brief review of the Task IA HSHX conceptual design ground rules and results. Specific details of the IRV and HSHX conceptual designs, weights, and geometry constraints are presented in the following discussion.

8.1 IRV DESIGN DESCRIPTION

A typical IRV vehicle is shown in Figure 8.1-1. It consists of a 49-inch-diameter planar array heat source supported on a refractory tubular truss within an 85-inch-diameter, 60-degree conical aeroshell. The aeroshell thermoprotection system consists of a low-density charring ablator supported by a bonded aluminum substructure. The attachment of ablator to substructure is through an adhesive system. The aluminum sandwich substructure is reinforced through the use of ring stiffeners at strategic locations, i.e., at the heat source support juncture, at the transition from cone to cylinder, and at the adapter interface to the booster vehicle. In order to accomplish assembly at the heat source within the aeroshell, a removable nose cap is utilized. This nose cap is bolted around its periphery by a series of structural bolts protected by removable ablator plugs (see Figures 8.1-2 and 8.1-3).

In addition to the 49-inch-diameter planar heat source configuration, a pin cushion and vented capsule circular array heat source configurations were investigated and are shown in Figures 8.1-4 and 8.1-5 respectively. Figure 8.1-6 depicts weight and vehicle diameter for various configurations and a detailed weight summary for the three reference configurations is shown in Table 8.1-I.

8.1.1 Heat Source Attachment

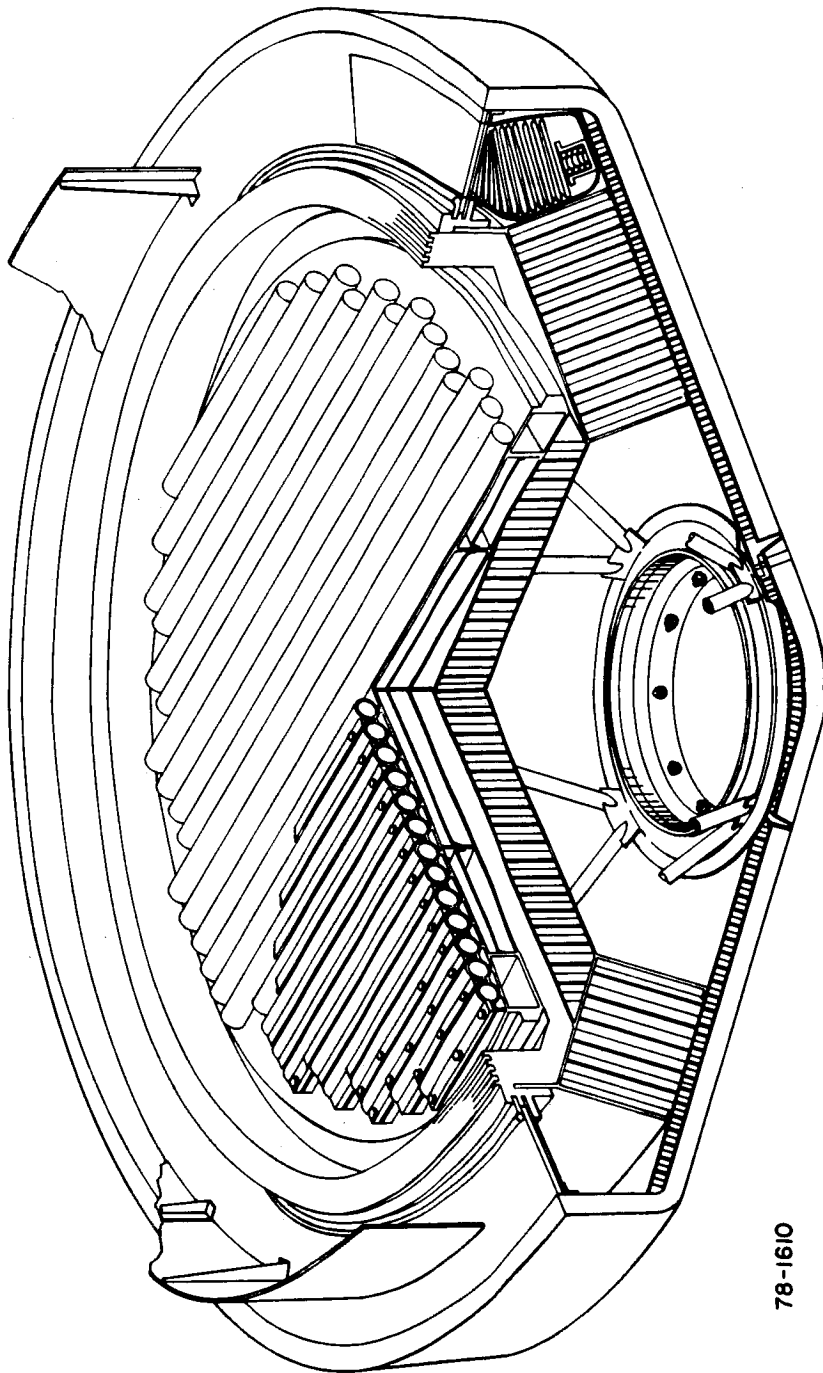
The heat source primary support is by a tubular truss arrangement terminating in a continuous ring which interfaces with a mating ring within the aeroshell. This tubular truss forms a four-point load path into the aeroshell and is attached through the use of bolts accessible with the nose cap removed as described above. This heat source attachment configuration is depicted in Figure 8.1-7. A possible temperature problem is envisioned in the immediate locale of the heat source truss attachment to the aeroshell ring and this local area requires further detailed analysis. A change of material within the tubular struts may be required to minimize heat leakage and ensuing temperature of the aeroshell attachment ring. Insulators or thermal barriers may be required at the bolt locations. If it is possible to maintain the desired temperatures at the heat source/aeroshell interface, then an aluminum ring as shown in Figure 8.1-7 will be employed. Otherwise, titanium or other higher temperature materials must be considered. Through the process of chemical milling or doubler attachment (bonding), the inner face sheet of the aluminum sandwich aeroshell substructure is reinforced, thickness wise, in the area of this support ring attachment assuring proper distribution of the design loads. In addition to the face sheet reinforcement it is expected that detailed analysis in Task II will dictate increased density core material in this ring area.

TABLE 8.1-I

IRV REFERENCE DESIGNS - MASS PROPERTIES COMPARISON

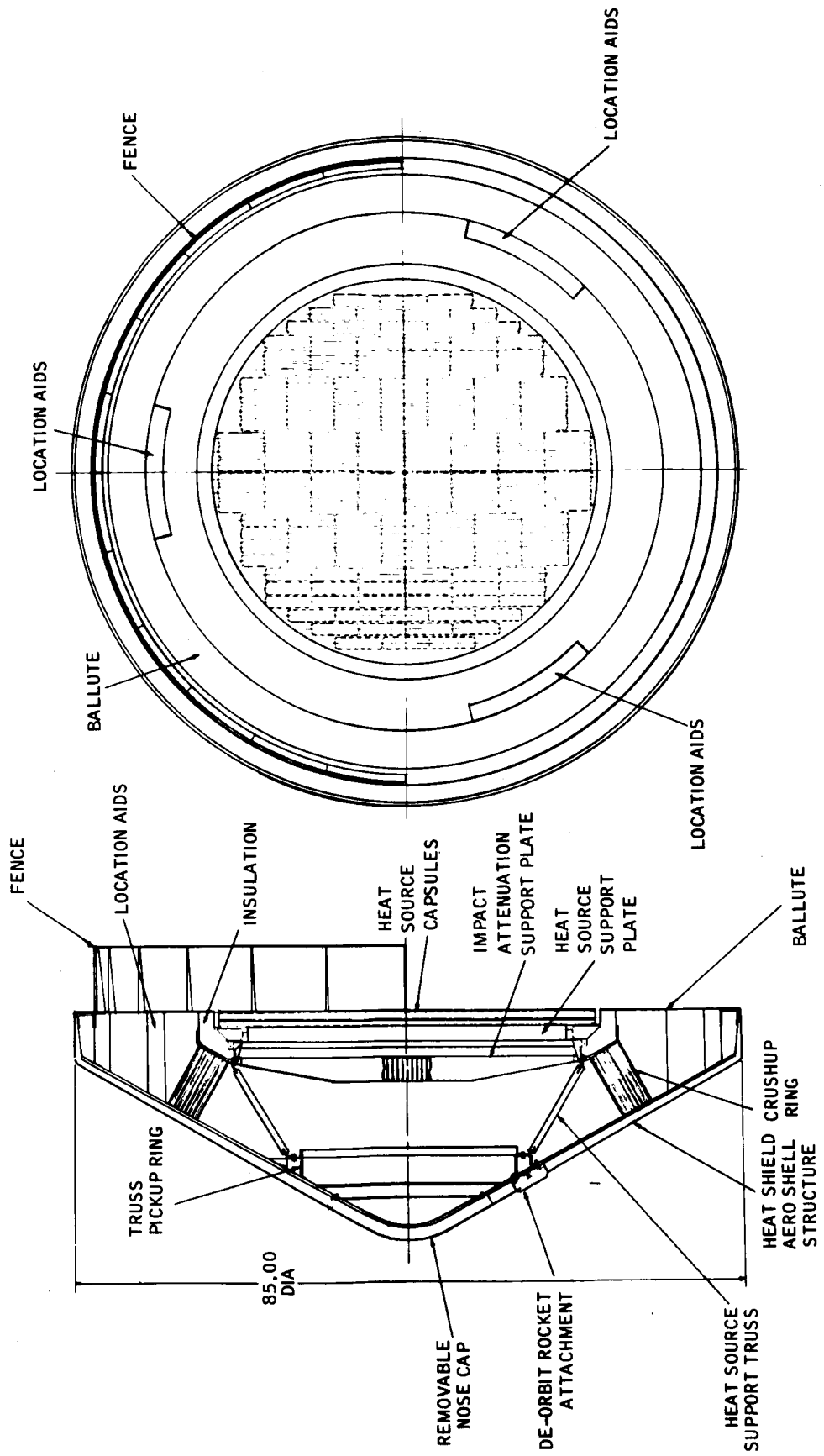
	WEIGHT (POUNDS)		
	85" VEHICLE DIAMETER 49" DIAMETER HEAT SOURCE (PLANAR)	70.5" VEHICLE DIAMETER 39" DIAMETER HEAT SOURCE (PINCUSHION)	75.0" VEHICLE DIAMETER 46" DIAMETER HEAT SOURCE (VENTED CAPSULE - PLANAR)
A. HEAT SOURCE	(1288.0)	(1365.0)	(984.9)
CAPSULES	755.0	760.0	475.6
SUPPORT SYSTEM	165.5	285.0	115.9
RETENTION SYSTEM	98.0	----	79.3
HEAT SINK (B ₂ O) AND PLATE	160.0	220.0	218.0
TRUSS SUPPORT SYSTEM	67.5	59.0	54.1
INSULATION	42.0	41.0	42.0
B. AEROSHELL	(552.0)	(281.2)	(480.7)
HEATSHIELD	122.2	84.1	95.1
BOND	6.9	4.7	5.4
STRUCTURE	66.3	45.6	51.6
ATTACHMENTS	12.0	12.0	12.0
FENCE	31.9	26.3	28.1
CRUSHUP	60.0	----	60.0
COLD PLATE	145.0	----	120.0
BALLUTE	42.0	42.0	42.0
RECOVERY AIDS	38.5	38.5	38.5
CONTINGENCY	28.0	28.0	28.0
C. IRV ENTRY WEIGHT	1840.8	1646.2	1465.6
D. ADDITIONAL SYSTEMS	(195.0)	(195.0)	(195.0)
SPACER AND HINGE	30.0	30.0	30.0
ABORT/DEORBIT SYS.	165.0	165.0	165.0
E. IRV LAUNCH WEIGHT	(2035.8)	(1841.2)	(1660.6)
F. MASS PROPERTIES OF RE-ENTRY VEHICLE			
WEIGHT (POUNDS)	1840.8	1646.2	1465.6
CG (INCHES)*	25.9	23.9	25.0
I _{xx} (ROLL SLUG FT ²)	202.0	108.1	122.4
I _{yy} (PITCH SLUG FT ²)	110.3	61.9	71.8

*CG REF. AX = 0) IS AT THE STAGNATION POINT



78-1610

Figure 8.1-1 ISOTOPE REENTRY VEHICLE, 49-INCH DIAMETER PLANAR ARRAY



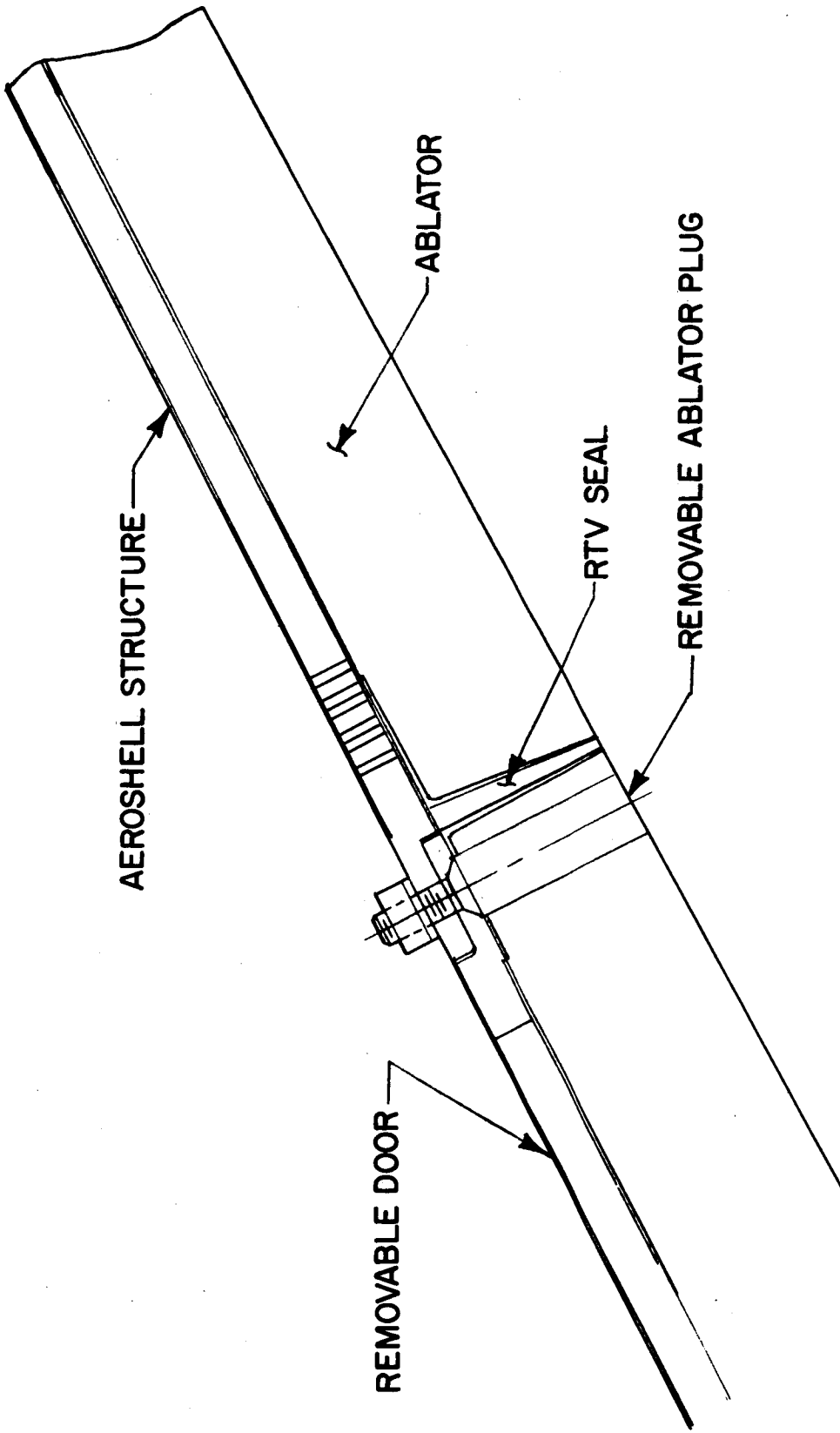
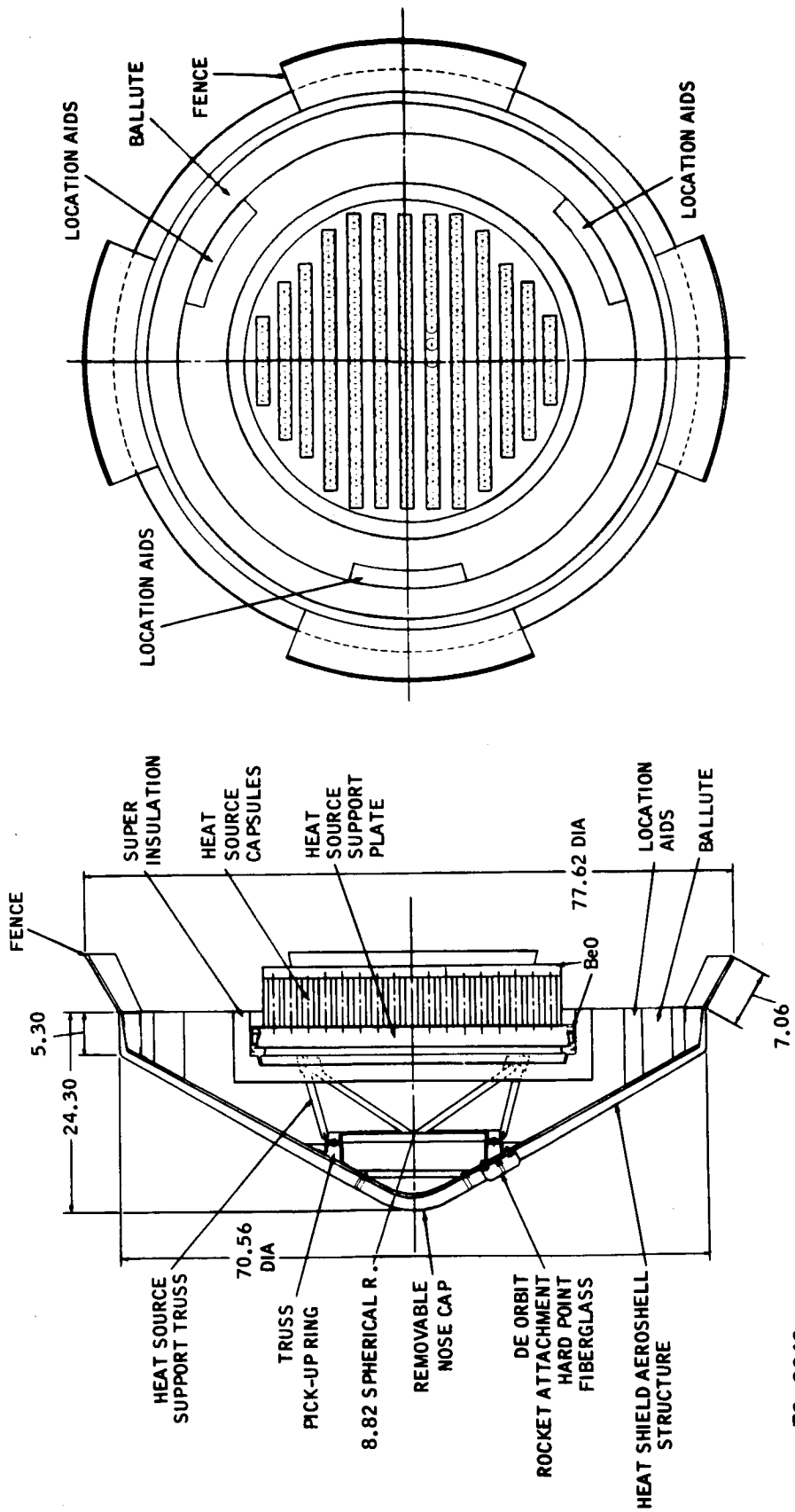


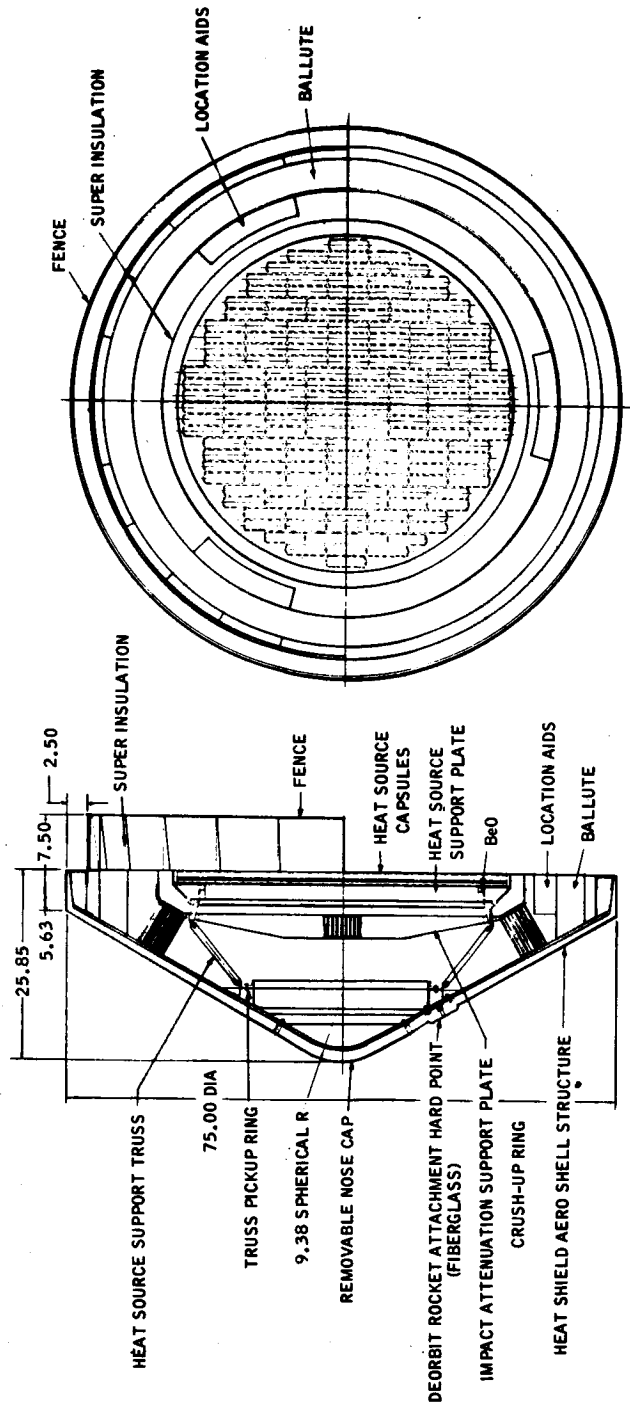
Figure 8.1-3 DETAIL OF IRV REMOVABLE DOOR

78-0616






78-0648

Figure 8.1-4 IRV PIN CUSHION ARRAY REFERENCE DESIGN



78-0649

Figure 8.1-5 IRV CIRCULAR PLANAR ARRAY REFERENCE DESIGN (VENTED CAPSULES)

PERTURBATION (1) HEAT SOURCE CONFIGURATION	REF. DESIGN	A MIN. DIA. (BARE)		B ISOTROPIC CRUSH-UP		C CRUSH-UP		D CRUSH-UP WITH RECESS	
		DIA. IN.	WT. LB.	MIN. DIA. 75.0	MIN. WT. 1826	MIN. DIA. 75.0	MIN. WT. 1851	MIN. DIA. 75.0	MIN. WT. 2083
A 49.0 CIRC. PL. 	85	66.0	1551	66.0	2151	75.0	1464	75.0	1585
B 46.0 CIRC. PL. - VENTED 	75.0	62.3	1232	62.3	1772	75.0	1464	71.1	1585
C 39.0 PIN CUSHION 	70.5 1646	70.5	1646	70.5 (2) 82.5	1916 (2) 1893				

(1) ALL CONFIGURATIONS HAVE BALLUTE & FLUSH HEAT SOURCE UNLESS OTHERWISE SPECIFIED

(2) PROTRUDING (4.0") HEAT SOURCE

78-0658

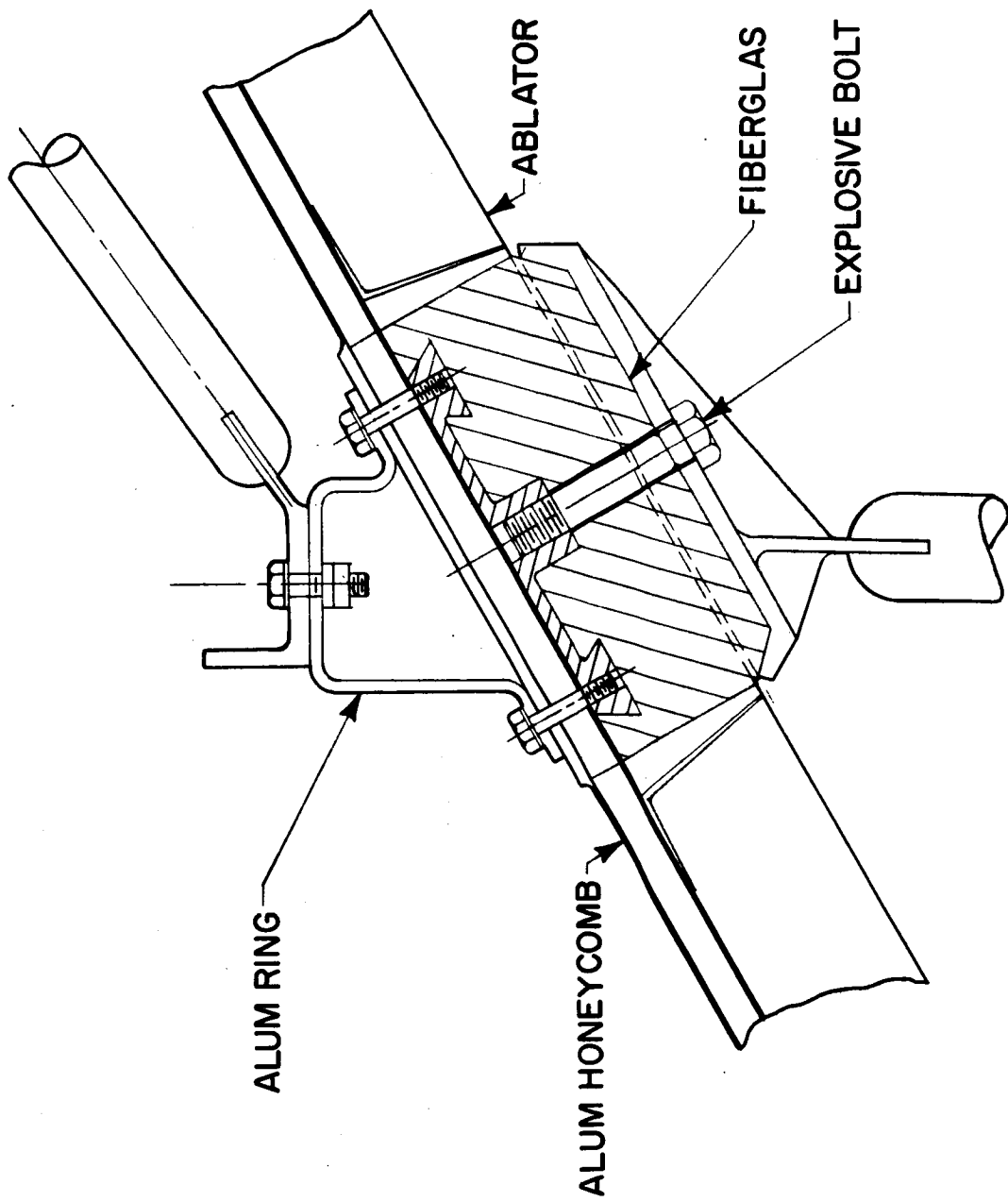


Figure 8.1-7 DETAIL OF TRUSS AEROSHELL ATTACHMENT POINT

78-0612

8.1.2 Abort/Deorbit System Attachment

In an effort to shorten the load pad and in the interest of weight saving, the abort system attachment is located at the same points through which the heat source is supported (see Figure 8.1-7). A circular fiberglass shear compression pad is inserted through the heat shield and rigidly attached to the aeroshell substructure. A metallic cup or pad through an explosive bolt attaches the abort deorbit system tower to this fiberglass structural pad. A flexible RTV gasket cast around the circumference of the fiberglass pad between the pad and the ablator will form a thermal seal and reduce transmission of loads into the ablator which could result in structural deformation and/or failure. This design applications is currently utilized on the Apollo spacecraft and has progressed through fabrication and a series of successful flight tests.

In order to simplify and reduce the number of separation systems, the spin motors can be attached to the abort tower and jettisoned with the abort tower. Otherwise, they would require a separate release system if mounted directly to the IRV. A detail of the spin motor attachment is shown in Figure 8.1-8.

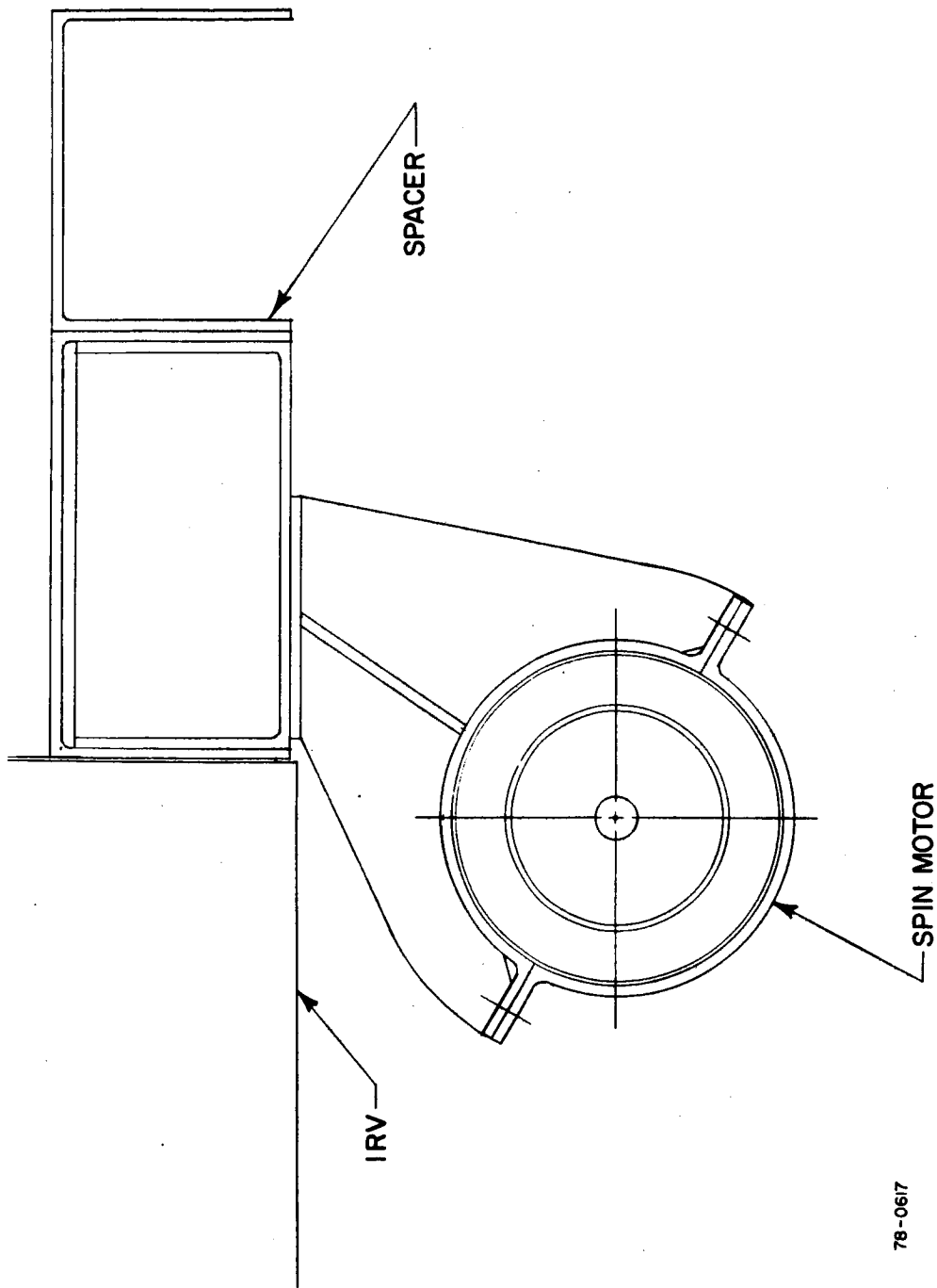
8.1.3 IRV/Heat Exchanger Launch Vehicle Interface

A transition from the cone to a short cylinder (15 percent R_B) is accomplished at the aft end of the IRV. This short cylinder section is currently envisioned as a stiffened aluminum skin construction, locally reinforced to resist launch load conditions (Figure 8.1-9). The aft end of this section is terminated in a "C" shaped channel as a primary structural member. This channel is used as the main attachment to the spacer section which contains the hinging for the emergency cooling mode as well as forming the attachment to the launch vehicle. The aerodynamic fence utilized for turning the vehicle around in the case of a rearward reentry situation is also attached to the "C" channel. The backface of the "C" channel is protected by a thin layer of structural ablator material (fiberglass) and the separation of the IRV from the heat exchanger is accomplished at this interface through the use of four explosive bolts.

8.1.4 Deceleration and Impact Attenuation

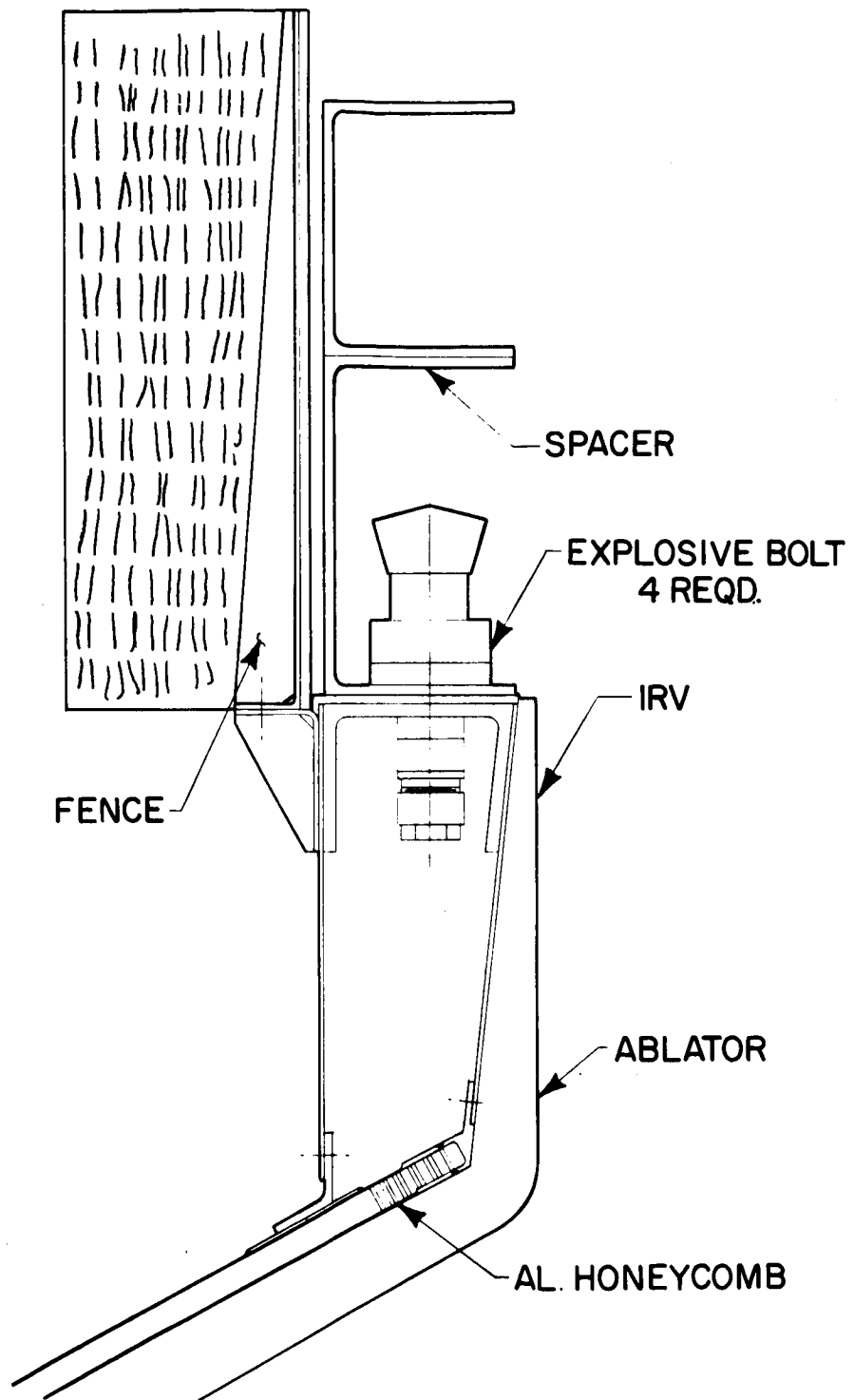
Within an annulus cavity in the back surface of the IRV surrounding the heat source and insulation a ballute is packaged and deployed after reentry to augment drag and ensure survival at impact. The aft cover over the area of the ballute storage annulus will be separated and jettisoned from the vehicle through the use of pyrotechnic devices to allow ballute deployment. The ballute system and other deceleration devices are discussed in Section 7.0 of this document.

An impact attenuation system which utilizes the heat source support design to provide rotation of the heat source for impact conditions other than vertical in combination with a honeycomb crushup system is contained in the forward portion of the aeroshell. The IRV design is such that it provides a stroke of approximately 8 inches during the impact of the vehicle thus dissipating the energy to ensure fuel capsule survival. A thick honeycomb sandwich is utilized immediately outside the heat source insulation and is used to reduce the possibility of heat source support plate breakup and distribute the load into the honeycomb crushup system. Figure 7.2-6 shows a detail of the Rotating Plate Concept attenuation system reference employed in circular planar HS array IRV's.



78-0617

Figure 8.1-8 DETAIL OF SPIN MOTOR ATTACHMENT



78-0618

Figure 8.1-9 DETAIL OF AFT CYLINDRICAL RING STRUCTURE

8.2 HSHX DESIGN

System Definition

The HSHX is a part of the closed gas loop of the Brayton-cycle power conversion system. The other major elements of the Brayton-cycle gas loop are contained in a package as illustrated in Figure 8.2.1-1. They consist of the Brayton-cycle rotating unit (BRU), the recuperator, and the heat-sink heat exchanger. This package is referred to as the Power Conversion Module (PCM).

For the purposes of this study, the PCM package is assumed to be mounted in a rectangular frame with the dimensions as noted in the figure.

The HSHX system includes the following items:

- a. The HSHX itself
- b. The ducting between the HSHX and the PCM package
- c. The structural support between the HSHX and the PCM package
- d. That portion of the insulation system which is removable with the complete closed gas loop

The elements of the HSHX system are illustrated in Figure 8.2.1-2. It is seen that the HSHX, ducts, structure, PCM package, and insulation form a single integral unit.

System Requirements

The requirements imposed on the HSHX (summarized in Table 8.2-I) consist of specified operational and performance goals. The overall power system is comprised of a single IRV-isotope heat source and two independent Brayton-cycle power conversion systems (PCM) shown schematically in Table 8.2-I. Each PCM is capable of delivering full output power (6.8 kw_e), but only one of the systems is in operation at a given time. In order to provide inplace redundancy of the power conversion system, PCM No. 1 and PCM No. 2 must each be capable of operation without removal of the other. PCM No. 1 and PCM No. 2, including the HSHX's, are to be separately removable as integral units. PCM No. 1 and PCM No. 2 are to be interchangeable, or, stated another way, one PCM must be able to be utilized as either PCM No. 1 or No. 2. The packaging configurations of the PCM-HSHX are to be compatible with the Atlas/Centaur separate-launch-to-orbit vehicle, and the SATURN-IB integral-launch MORL type of installation. The differences between these two installations would be confined to the ducting and the HSHX-PCM interface only.

The performance requirements imposed on the HSHX, also listed in Table 8.2-I consist of a set of specified temperatures, flow rates, pressure drops, etc. which are required to obtain full electrical output power. In addition to the internal performance of the HSHX, the HSHX system must keep the maximum fuel capsule temperature below 2000°F during normal operation and keep the heat leaks associated with the HSHX system to less than 1 kw_t.

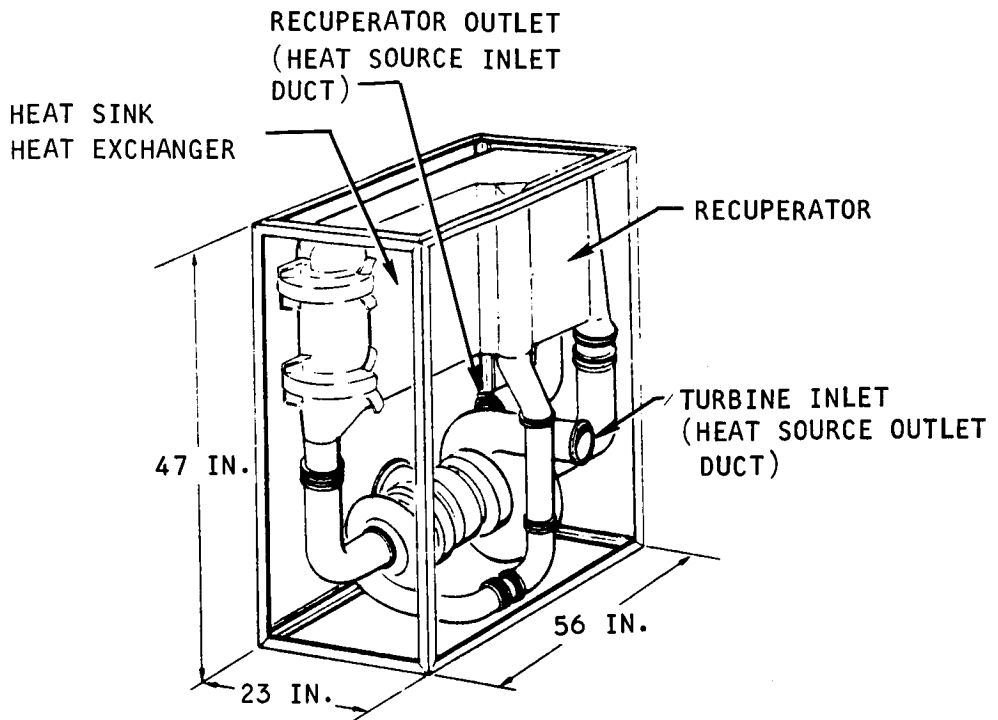
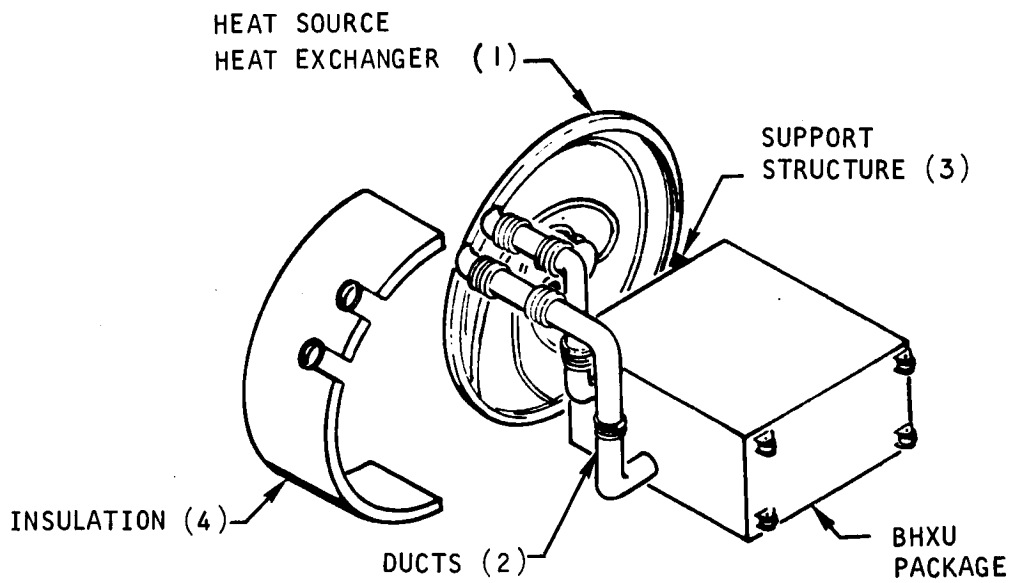


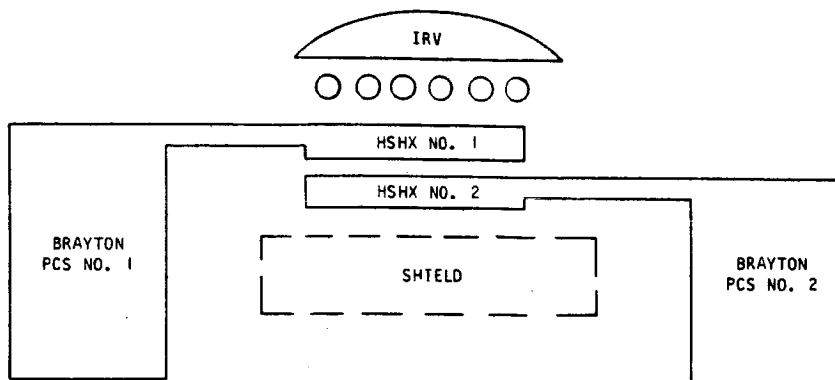
Figure 8.2.1-1 BRAYTON-CYCLE POWER CONVERSION MODULE



A-33454

Figure 8.2.2-2 HEAT-SOURCE HEAT EXCHANGER SYSTEM

TABLE 8.2-1
HSHX - SYSTEM REQUIREMENTS



OPERATIONAL

- INPLACE REDUNDANCY
 EITHER SYSTEM NO. 1 OR NO. 2 CAPABLE
 OF FULL POWER OPERATION WITHOUT
 MOVEMENT OF MAJOR COMPONENTS
- REPLACEABILITY
 PCS'S INCLUDING HSHX'S TO BE REMOVABLE
 AS A COMPLETE UNIT
- INTERCHANGEABILITY
 PCS NO. 1 AND NO. 2 TO BE INTERCHANGEABLE
- COMPATIBLE WITH
 ATLAS/CENTAUR (SEPARATE LAUNCH)
 SATURN I-B (INTEGRAL LAUNCH-MORL)

PERFORMANCE

- RADIATION HEAT TRANSFER FROM ISOTOPE SOURCE
- 1600°F EXIT GAS TEMPERATURE
- 1200°F INLET GAS TEMPERATURE
- 23.5 KW_t TRANSFERRED TO GAS
- MAX OPERATING SOURCE TEMP ≤ 2000°F
- $\Delta P/P \leq 3.3\%$ (1.05 PSI)
- Xe-He, (83.8 MWt) @ 0.94 LB/SEC
- HEAT LEAK ≤ 1.0 KW_t

A-33455

During the Phase I-a studies, full power output from PCM No. 2 was required when PCM No. 1 was inoperative. For the Phase I-b studies, this ground rule was relaxed in preference to one which would require full power output from PCM No. 1 but would accept less than full power output from PCM No. 2. The maximum source temperature associated with full power output from PCM No. 1 was treated as the maximum allowable source temperature for operation of PCM No. 2. The resulting reduced power output from PCM No. 2 was accepted as the emergency or standby power capability. This results in a significant reduction in required source temperatures.

8.2.1 Planar Circular Heat-Source Array

8.2.1.1 Source Description

The heat source for this system consists of a 49-inch-diameter planar array of 164 fuel capsules. A scalloped metal cover plate is used over the fuel capsule as a part of the fuel capsule retention scheme. The temperature distribution around the fuel capsule for this heat source is shown in Figure 8.2-1. The design of the heat source heat exchangers (HSHX) is based on an effective source temperature which is defined as

$$T_{\text{eff}} = \left[\frac{1}{A_c} \int_{A_c} T_s^4 dA_c \right]^{1/4} \quad (8-1)$$

where

T_{eff} = effective source temperature

A_c = source surface area

T_s = source surface temperature

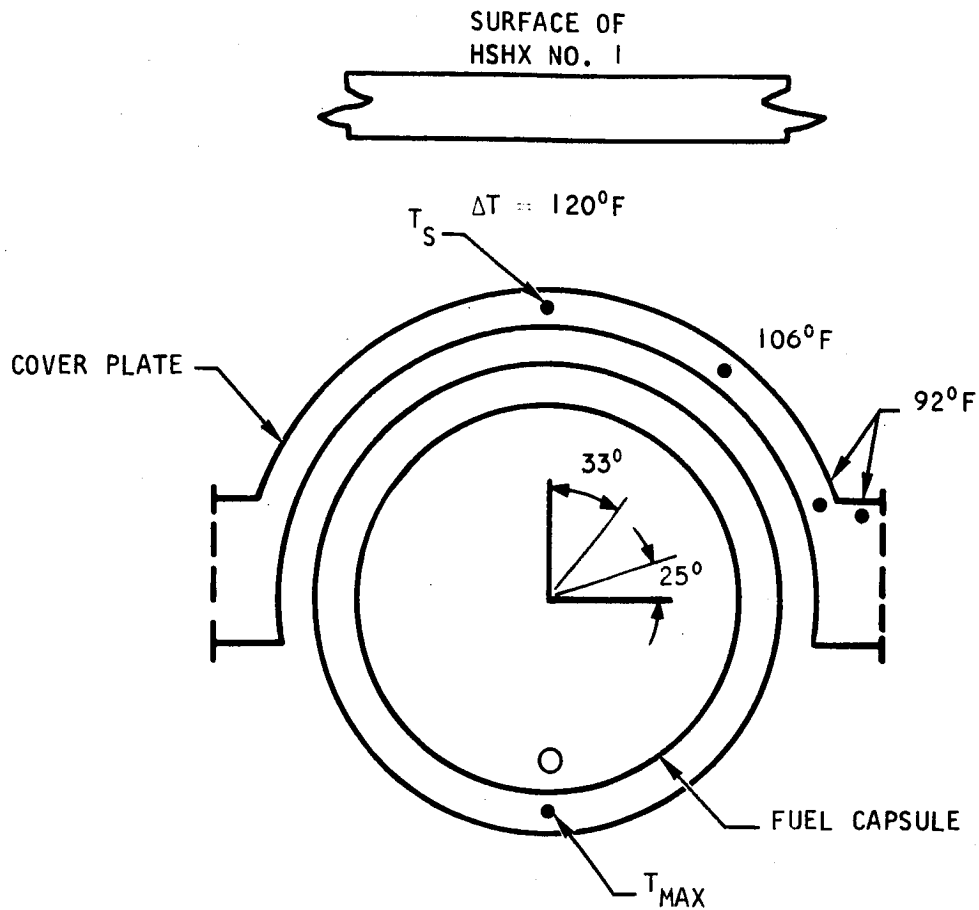
In addition, to provide a conservative estimate of the temperature levels, the effective temperature was set as equal to the temperature existing on the capsule cover plate. Thus, for this system (referring to Figure 8.2-1) the effective temperature is taken as

$$T_{\text{eff}} = T_{\text{max}} - 120^\circ \quad (8-2)$$

where

T_{max} = maximum fuel capsule temperature

8.2.1.2 Involute Tubular Heat-Source Heat Exchanger



CAPSULE DIAMETER = 1.55 IN.
 COVER THICKNESS = 0.060 IN.
 SPACING = 1.75 IN.

CALCULATION BASED ON $T_{MAX} = 2000^{\circ}F$

$$\Delta T = T_{MAX} - T_S$$

T_S = SURFACE TEMPERATURE

T_{MAX} = MAXIMUM CAPSULE SURFACE TEMPERATURE

Figure 8.2-1 TEMPERATURE GRADIENT AROUND NONVENTED FUEL CAPSULE
(CIRCULAR PLANAR HEAT SOURCE)

Description

The detailed involute HSHX design is shown in Figure No. 8.2-2. The basic heat transfer portion of the HSHX occupies a 49-inch-diameter circle to correspond to the size of the heat source. The Brayton fluid both enters and exits from the heat exchanger at the periphery and flows around the circumference in annular manifolds. The inlet manifold has a constant diameter of 2.75 inches and a wall thickness of 0.03 inch; it is located above the outlet manifold, which has a diameter of 3 inches and a wall thickness of 0.042 inch. The 49-inch-diameter active portion of the heat exchanger is composed of 18 tubes, each with an OD of 1.34 inches and a wall thickness of 0.030 inch. The weight of the heat exchanger is 89 pounds.

The Brayton fluid flows along the inlet manifold, enters alternate tubes and follows an involute path toward the center, where it enters a header box and then reenters adjacent tubes, flows back out to the periphery, and leaves through the outlet manifold. The central header box is 4.0 inches in diameter. This requires that the tubes be staggered around the circumference, with the inlet legs located above the outlet legs. Staggering is begun 4 inches from the center of the header box, with the outlet legs undergoing a downward bend and the inlet legs joining the header box above the outlet legs.

The inlet and outlet legs are separated by a gap of 0.056 inch and are joined together by a weld bead. The all-welded construction offers a structurally sound approach to the HSHX design and permits thermal conduction between the hot and cold legs, which results in a reduction of the maximum temperature on the heat source.

The actual physical layout of the tubes for the involute HSHX design is not easy to visualize. The design objective is to maintain the tube spacing at a specified value in a direction normal to the tube axis, regardless of the radial distance from the center of the circular HSHX. This arrangement is in contrast to aligning the tubes radially inward; it will result in a constant thermal resistance for heat transfer within the heat exchanger regardless of the location along the radius.

Let

$2N$ = the number of tubes in the heat exchanger

D = the OD of each tube

r_i = the radius of the smallest circle for which the specified tube spacing can be maintained

$\frac{A_{\text{tube}}}{A_{\text{total}}}$ = the ratio of projected tube area to total heat exchanger projected area (a measure of the tube spacing)

Referring to Figure 8.2-3, θ is the angle the tube axis makes with a radial line at a radius, r , and ϕ is the angle the radial line makes with respect to some reference line drawn through the center of the circle.

FOLDOUT FRAME 1

FOLDOUT FRAME 2

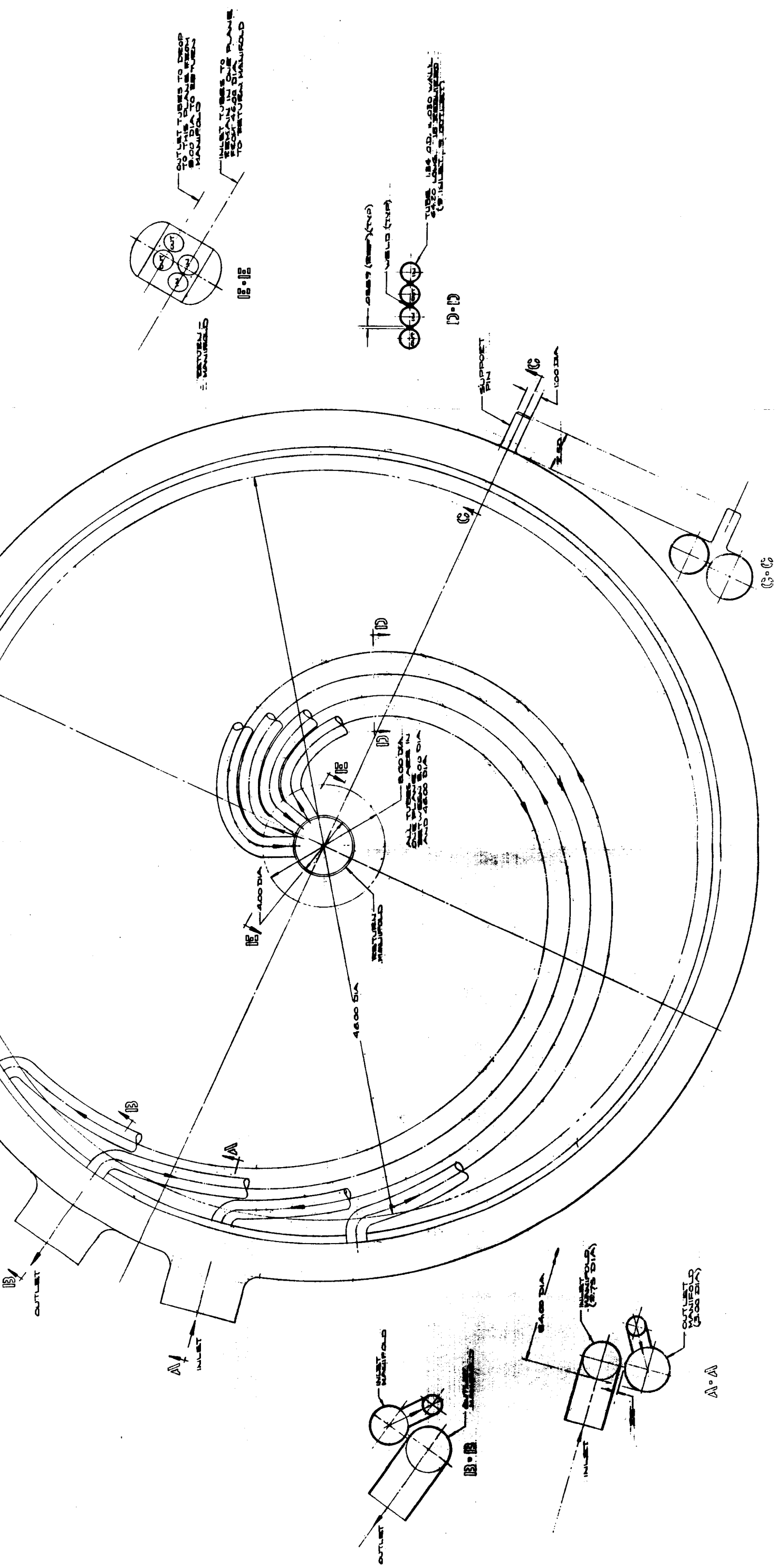


Figure 8.2-2 LAYOUT OF HEAT EXCHANGER INVOLUTE -- 49-INCH DIAMETER

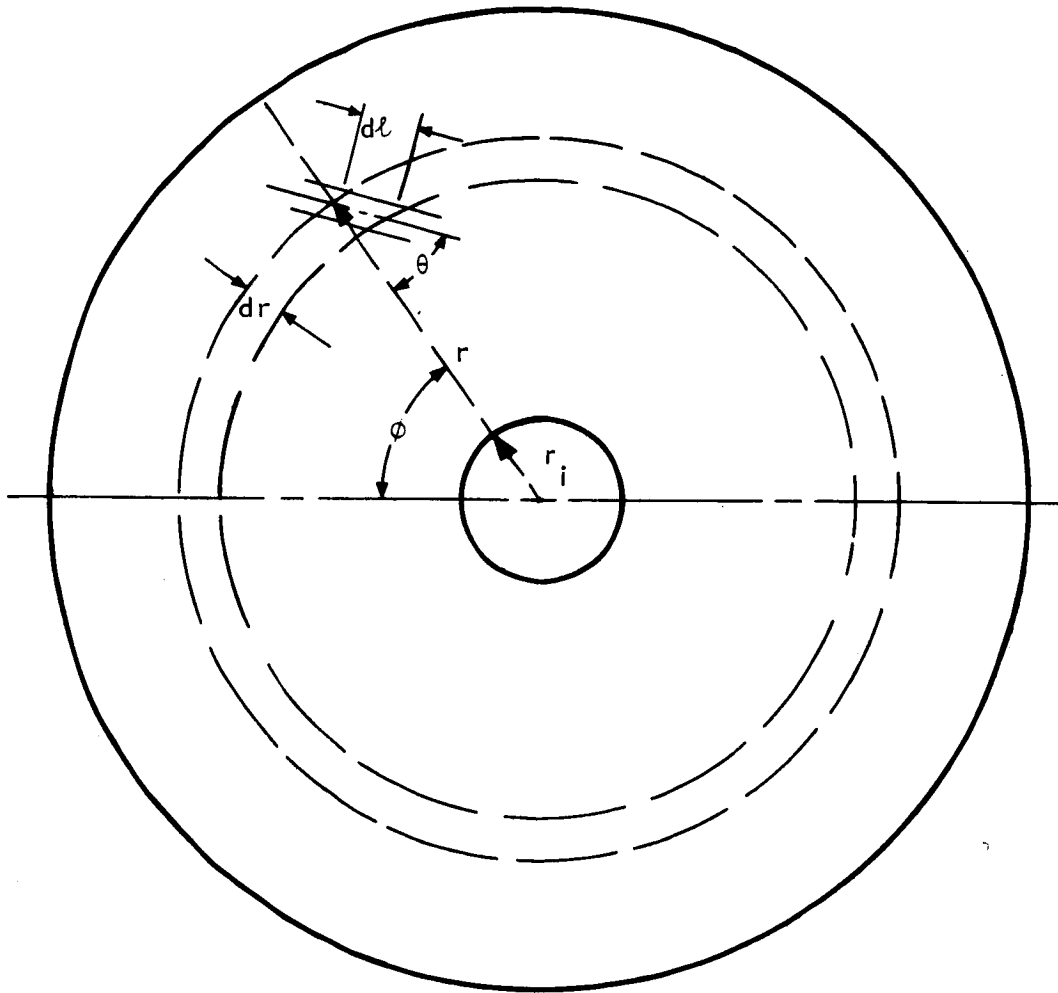


Figure 8.2-3 PHYSICAL MODEL FOR DETERMINATION OF INVOLUTE TUBE LAYOUT

Based on the above definitions, it can be seen that

$$\frac{2ND}{\frac{A_{\text{tube}}}{A_{\text{total}}} \cos \theta} = 2\pi r \quad (8-3)$$

But based on the definition of

$$\frac{2ND}{\frac{A_{\text{tube}}}{A_{\text{total}}}} = 2\pi r_i \quad (8-4)$$

and therefore,

$$\cos \theta = \frac{r_i}{r} \quad (8-5)$$

It can also be seen from Figure 8.2-2, that

$$\cos \theta = \frac{dr}{d\ell} \quad (8-6)$$

where $d\ell$ is a differential element of tube length. From Figure 8.2-2,

$$d\ell = \frac{r d\phi}{\sin \theta} \quad (8-7)$$

Therefore

$$\frac{dr}{d\ell} = \frac{\sin \theta dr}{r d\phi} \quad (8-8)$$

and

$$d\phi = \tan \theta \frac{dr}{r} \quad (8-9)$$

From Equation (8-5), $\tan \theta = \frac{\sqrt{r^2 - r_i^2}}{r_i}$

and therefore

$$\int_0^\phi d\phi = \int_{r_i}^r \frac{\sqrt{r^2 - r_i^2}}{r r_i} dr \quad (8-10)$$

for which the angle ϕ in radians can be found to be

$$\phi = \sqrt{\left(\frac{r}{r_i}\right)^2 - 1} - \arccos \frac{r_i}{r} \quad (8-11)$$

Equation (8-11) completely describes the tube layout for the involute HSHX.

Design Analysis

The heat-source heat exchangers were required to exhibit inplace redundancy, replaceability, and full power output from PCM No. 2 with PCM No. 1 in place. The latter objective was to be met within the 2000°F temperature limitation imposed on the fuel capsules, and therefore, it represented the HSHX design point.

While this was the HSHX design point, operating PCM No. 2 at a reduced power permits lowering the source temperature.

The design procedure of the HSHX's is discussed in the following paragraphs. A design of the HSHX was first obtained on the basis of the pressure drop requirements, and based on this design, the heat transfer performance of the system was checked. Wall temperature and heat flux distributions in the HSHX were obtained, and these values were utilized to refine the first design. The following paragraphs describe a) the selection of a design which would meet the pressure drop requirements, b) the thermal analysis of the heat transfer process in the heat source-HSHX cavity, and c) the procedure used in designing the inlet and outlet manifolds.

1. Pressure Drop

The available pressure drop imposes a severe restriction on the HSHX and is the primary consideration in undertaking the design. Neglecting entrance effects, turning losses, and momentum changes, the pressure drop in the HSHX is equal to the frictional pressure drop, i.e.,

$$\Delta P = \Delta P_f = \frac{2G^2 fL}{q\rho D} \quad (8-12)$$

Let

N = the number of "in" legs = number of "out" legs

L = the combined length of an "in" leg and "out" leg

D = the tube ID \approx tube OD

D_o = the overall diameter, less manifolds, of the HSHX

D_i = the diameter of the inner circle where staggering of the tubes begins

$\frac{A_{\text{tube}}}{A_{\text{total}}}$ = the ratio of the projected tube area to the total projected area of the HSHX

Therefore, neglecting the thickness of the tube wall,

$$ND = \frac{\pi D_i A_{\text{tube}}}{2 A_{\text{total}}} \quad (8-13)$$

also

$$NDL = \frac{\pi}{4} \frac{A_{\text{tube}}}{A_{\text{total}}} (D_o^2 - D_i^2) \quad (8-14)$$

$$G = \frac{4 W_{\text{total}}}{\pi ND^2} \quad (8-15)$$

where W_{total} = the total Brayton fluid flow rate in the HSHX

The friction factor, f , can be represented by the following expression for turbulent flow

$$f = 0.046 \text{Re}^{-0.2} \quad (8-16)$$

where

$$\text{Re} = \frac{GD}{\mu} \quad (8-17)$$

Utilizing Equations (8-13), (8-14), (8-15), (8-16), and (8-17), Equation (8-12) becomes

$$\Delta P = \frac{0.000983 (D_o^2 - D_i^2) W_{\text{total}}^{1.8} \mu^{0.2}}{\rho D_i^{2.8} \left(\frac{A_{\text{tube}}}{A_{\text{total}}} \right)^{2.8} D^3} \quad (8-18)$$

which may be rearranged to yield the tube diameter.

$$D = 0.0995 \left[\frac{(D_o^2 - D_i^2) W_{\text{total}}^{1.8} \mu^{0.2}}{\Delta P \rho D_i^{2.8} \left(\frac{A_{\text{tube}}}{A_{\text{total}}} \right)^{2.8}} \right]^{1/3} \quad (8-19)$$

Selecting values for D_o , D_i , ΔP , and $\frac{A_{\text{tube}}}{A_{\text{total}}}$ permits a straightforward calculation of the tube diameter based on pressure drop considerations. The number

of tubes comprising the heat exchanger and their length can be determined by going back to Equations (8-13) and (8-14). After the HSHX design has been selected, additional pressure drop due to entrance, turning, and momentum effects can be calculated and added to the specified frictional losses to yield the total pressure drop.

2. Thermal Design

An analysis of the heat transfer between the heat source and the HSHX should consider the radiant heat interchange between the heat source and HSHX No. 1, as well as between HSHX No. 1 and HSHX No. 2; the conduction across the heat exchangers; and the convection between the Brayton fluid and the walls of the HSHX in operation. The interaction between radiation, conduction, and convection results in a very complex heat transfer process. Therefore, an accurate determination of the temperature distribution over the heat source and the HSHX's requires the use of computers.

A thermal analysis was carried out for the present case (planar circular heat-source array and an involute tabular heat exchanger). The diameter of the heat source as well as the heat exchangers was taken as 49 inches. It was assumed that full output power from PCM No. 2 is required when HSHX No. 1 is inoperative, i.e., outleg gas temperature from HSHX No. 2 is 1600^oF.

The physical model treated in this analysis is sketched in Figure 8.2-4. The heat flow in the system is simulated by a thermal-resistance thermal-capacitance network. Each element in the system is represented by a node in this electrical analog.

The surface of the heat source facing HSHX No. 1 is divided into five elements of equal areas. It is assumed that all the heat generated in the fuel capsules is radiating from this surface and is distributed uniformly over the surface. The heat-source temperatures in this analysis should be considered as effective source temperatures. Therefore, any temperature drop in the fuel capsules should be added to these temperatures to get the maximum source temperature.

Since HSHX No. 1 is not in operation, heat is transferred primarily by conduction between the various portions of the heat exchanger. Each of the upper and lower surface areas of HSHX No. 1 is divided into five circular elements of equal areas as shown in Figure 8.2-4. Heat is transferred between these two halves by conduction and radiation.

The Brayton fluid flows in and out of the tubes of HSHX No. 2 as shown in Figure 8.2-4. Both the fluid and the wall temperature as well as the wall heat flux vary along the tube. An accurate determination of these variations is necessary for the proper design of the HSHX. Therefore, the upper and lower halves of each tube are divided into several elements along the tube. Each of these elements is thermally connected, through convection, to the Brayton fluid. Heat is transferred between the upper and lower elements of the tube by conduction. Heat transfer between inlet and outlet tubes is important and is taken into consideration in the thermal network.

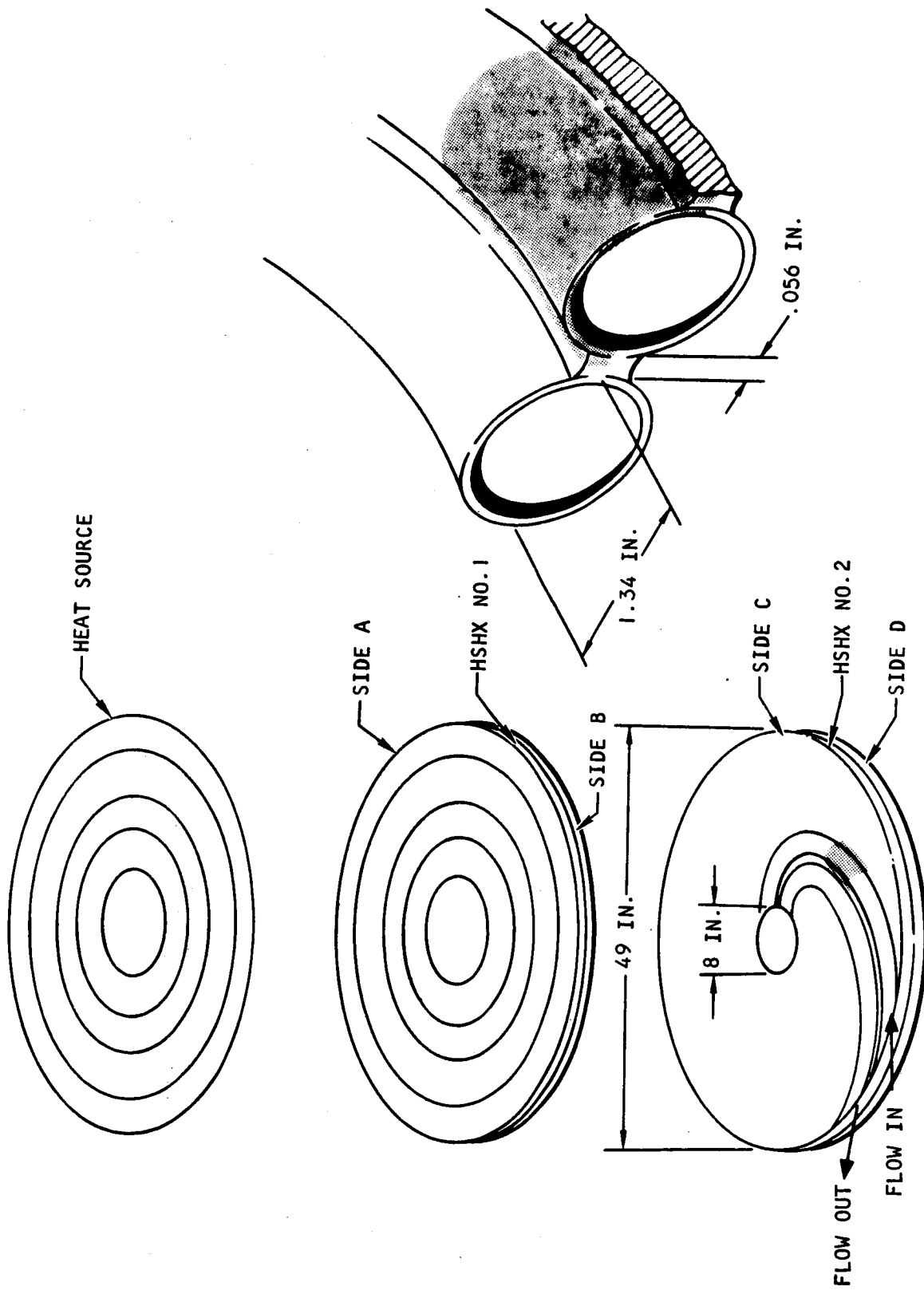


Figure 8.2-4 THERMAL MODEL FOR INVOLUTE HEAT-SOURCE HEAT EXCHANGER

The assumptions used in the analysis are summarized below:

- a. Each element is isothermal and assumes one discrete temperature.
- b. Each surface is gray.
- c. The radiation reflected and emitted from each element is diffusely distributed. The fact that the radiating surfaces of these elements are gray and that heat is emitted as well as reflected by each element, is accounted for by assuming an effective emissivity $\epsilon_{eff} = 0.74$.
- d. The top surfaces of the heat source, the side walls, and the lower surface of HSHX No. 2 are perfectly insulated. (This assumption is unnecessary and can be eliminated in the analysis of the final system.)
- e. A prescribed and uniform heat flux exists at the elements of the heat source.
- f. Heat is transferred between the two halves of the heat exchanger by conduction and radiation. A suitable value of the thermal resistance between the two halves was determined by separately analyzing the tube and fin combination.
- g. The Brayton fluid in HSHX No. 2 is also divided into elements. Heat is transferred between each element and the two halves of the HSHX by convection.
- h. The heat transfer coefficient inside the tubes of the HSHX is constant and is predicted by fully developed turbulent-flow correlations for moderate temperature differences such as the Dittus-Boelter correlation.

Using assumptions (a) and (c), the radiation view factors between various elements in Figure 8.2-4 are computed by a computer program CONFAC-11 (Reference 8.2-1). Knowing these view factors and using the remainder of the above assumptions, the various elements are represented as discrete nodes in an electric network simulating the heat transfer processes. This, in turn, is analyzed using a second computer program MLFTHAN-MARK-1 (Reference 8.2-2) to obtain the temperature distribution for the physical system shown in Figure 8.2-4.

It may be noted that some modification of the MARK-11 program was necessary to allow for the large number of the radiation resistances in the present application. A brief description of this program and the modifications is given in Reference 8.2-3.

3. Manifold Design

Based on structural considerations, the inlet and outlet manifolds were made with a circular cross section. The manifolds must be judiciously sized to keep the maldistribution of the flow to the heat exchanger tubes within acceptable limits. As fluid is drained from the inlet manifold into the tubes, conservation of momentum will result in a tendency for the static pressure to increase in the direction of the manifold flow. Proper selection of the inlet and outlet manifold sizes along with a U-flow configuration will result in the momentum

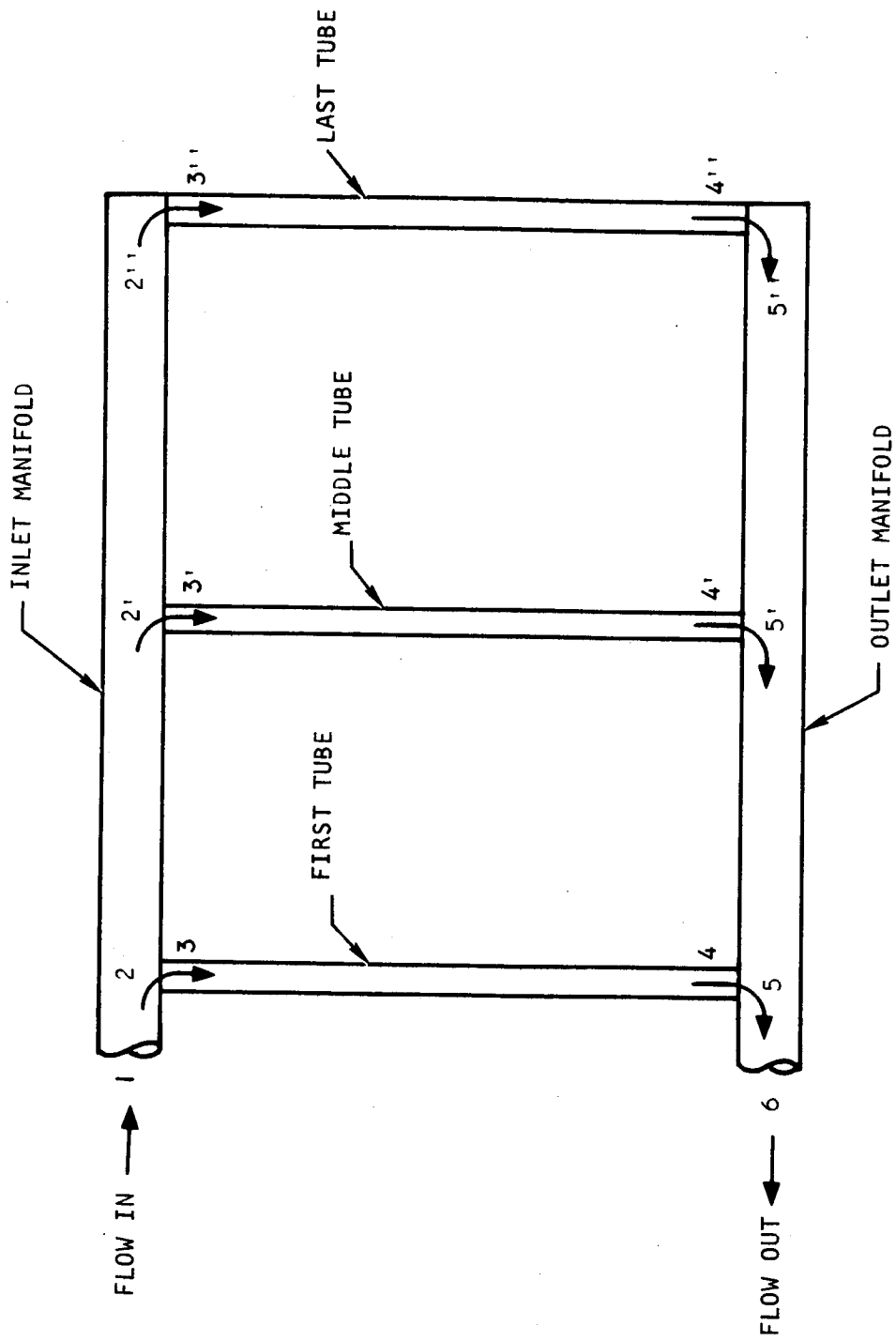


Figure 8.2-5 U-FLOW CONFIGURATION FOR EQUALIZING FLOW DISTRIBUTION IN THE HEAT-SOURCE HEAT EXCHANGER

recovery along the inlet manifold offsetting pressure drops due to cumulative inlet manifold friction and outlet manifold friction and momentum changes. Experience has shown that if the manifolds are sized so that, by assuming uniform flow distribution, the calculated pressure drop incurred by flowing along a path from the inlet flange, through the nearest heat exchanger tube, and back to the outlet flange is the same as for flowing between the flanges but through the furthest heat exchanger tube, the calculated flow maldistribution due to varying pressure drops for other flow loops will be less than 5 percent.

An algebraic representation of the flow distribution problem takes the following form. Consider the flow diagram in Figure 8.2-4. It is a U-flow pattern consisting of the inlet and outlet manifolds and the first, middle, and last tubes of the heat exchanger. Assume uniform flow distribution a priori. For the first flow path, i.e., path 1-2-3-4-5-6,

$$P_1 - P_6 = (P_1 - P_2) + (P_2 - P_3) + (P_3 - P_4) + (P_4 - P_5) + (P_5 - P_6) \quad (8-20)$$

While taking the last flow path, i.e., path 1-2''-3''-4''-5''-6,

$$P_1 - P_6 = (P_1 - P_{2''}) + (P_{2''} - P_{3''}) + (P_{3''} - P_{4''}) + (P_{4''} - P_{5''}) + (P_{5''} - P_6) \quad (8-21)$$

where

$$P_1 - P_{2''} = \Delta P_{f, 1-2} + \Delta P_{\text{mom}, 1-2}$$

$$P_{2''} - P_{3''} = \Delta P_{\text{ent loss}, 2''-3''}$$

$$P_{3''} - P_{4''} = \Delta P_{f, 3''-4''} + \Delta P_{\text{header}, 3''-4''}$$

$$P_{4''} - P_{5''} = \Delta P_{\text{exit loss}, 4''-5''}$$

$$P_{5''} - P_6 = \Delta P_{f, 5''-6} + \Delta P_{\text{mom}, 5''-6}$$

and for the middle flow path, i.e., path 1-2'-3'-4'-5'-6,

$$P_1 - P_6 = (P_1 - P_{2'}) + (P_{2'} - P_{3'}) + (P_{3'} - P_{4'}) + (P_{4'} - P_{5'}) + (P_{5'} - P_6) \quad (8-22)$$

where

$$P_1 - P_{2'} = \Delta P_{f, 1-2'} + \Delta P_{\text{mom}, 1-2'}$$

$$P_{2'} - P_{3'} = \Delta P_{\text{ent loss}, 2'-3'}$$

$$P_{3'} - P_{4'} = \Delta P_{f, 3'-4'} + \Delta P_{\text{header}, 3'-4'}$$

$$P_{4'} - P_{5'} = \Delta P_{\text{exit loss}, 4'-5'}$$

$$P_{5'} - P_6 = \Delta P_{f, 5'-6} + \Delta P_{\text{mom}, 5'-6}$$

For the inlet manifold

$$\Delta P_{\text{mom, inlet man.}} = -(q_{\text{in, o}} - q_{\text{in}})$$

where $q_{\text{in, o}}$ is the velocity head at the entrance to the inlet manifold, and q_{in} is the velocity head in the inlet manifold at the entrance to a particular tube. In the outlet manifold,

$$\Delta P_{\text{mom, outlet man.}} = 2(q_{\text{out, o}} - q_{\text{out}})$$

In this case, $q_{\text{out, o}}$ is the velocity head at the exit of the outlet manifold, and q_{out} is the velocity head in the outlet manifold at the exit of a particular tube.

Inspection of the foregoing equations reveals that in order to make the pressure drops through the first and last legs equal, the inlet manifold size must be smaller than the outlet manifold size. There are actually an infinite number of combinations of inlet and outlet manifold sizes that will result in equal pressure drops for the first and last legs. Setting a value for the total pressure drop between the inlet and outlet flanges, however, will result in a single combination of inlet and outlet manifold sizes.

The amount of maldistribution can be estimated by comparing the pressure drop for the flow path through the middle tube with the pressure drop for flow paths containing the first or last tubes, i.e.,

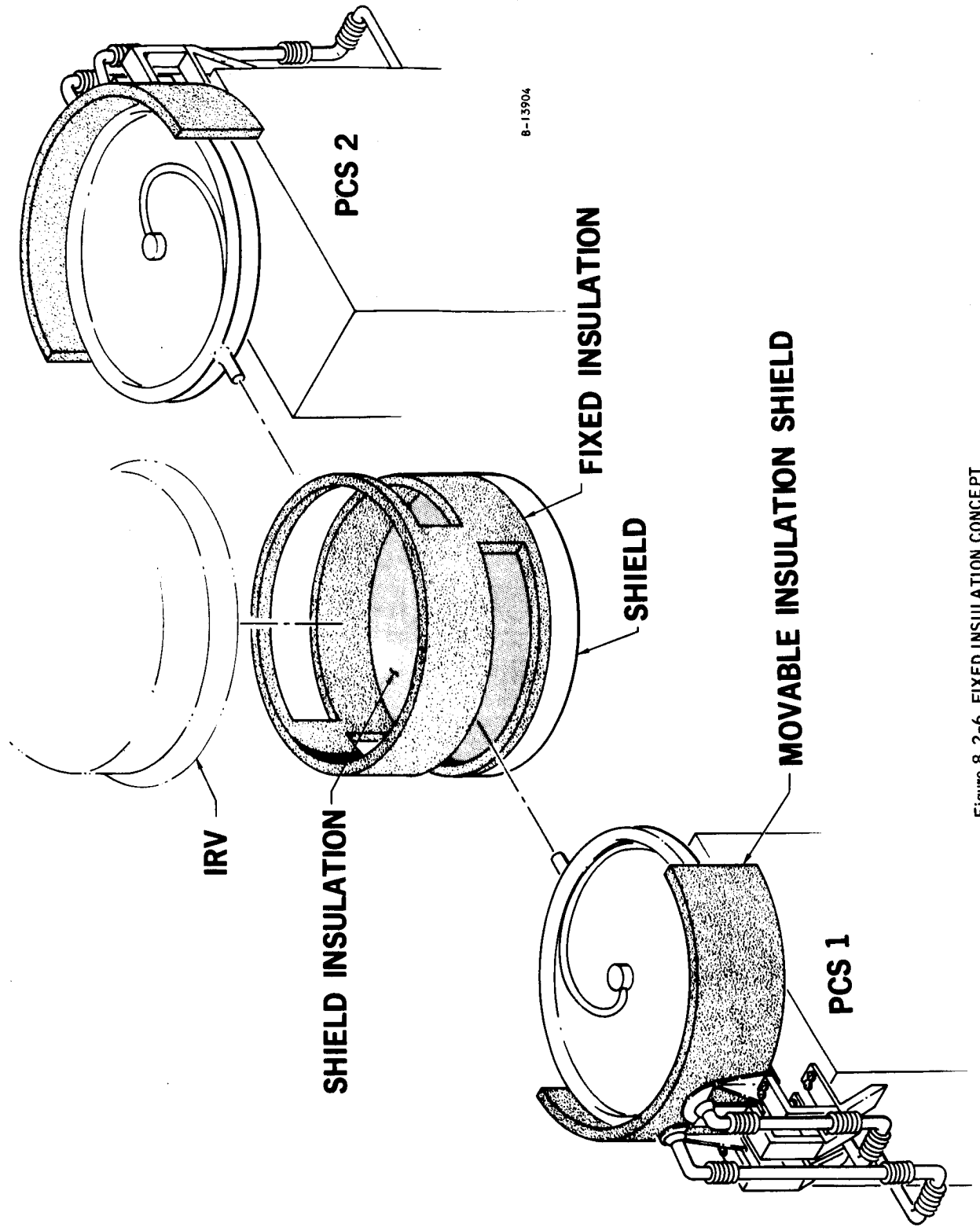
$$\text{maldistribution} \approx \frac{\sqrt{\Delta P_{1-2-3-4-5-6}} - \sqrt{\Delta P_{1-2'-3'-4'-5'-6}}}{\frac{1}{2} \left[\sqrt{\Delta P_{1-2-3-4-5-6}} + \sqrt{\Delta P_{1-2'-3'-4'-5'-6}} \right]} \quad (8-23)$$

Installation

1. Fixed Insulation Concept

Figure 8.2-6 illustrates the general approach to the installation of the HSHX-BHXU with the IRV system. A fixed superinsulation system forms the boundaries of a cavity between the IRV and the radiation shield. Openings on either side of the cavity are provided to accept the two system HSHX's. Insulation panels attached to the HSHX are sized to overlap the openings on the fixed insulation so that, when the heat exchangers are in place, the cavity is completely closed. The HSHX's are supported on one end by a bracket attached to the PCM and on the other end by brackets attached to the radiation shield for the bottom heat exchanger and to the IRV support ring for the top heat exchanger. The PCM packages are offset in a supporting frame network to allow the two heat exchangers to overlap each other in the cavity.

Figure 8.2-7 shows the installation of the 49-inch-diameter circular involute HSHX in a configuration suitable for the separate launch concept; the insulation approach shown schematically in Figure 8.2-6 is incorporated. A truss and



8-13904

Figure 8.2-6 FIXED INSULATION CONCEPT

WILDOUT FRAMES /

WILDOUT FRAMES 2

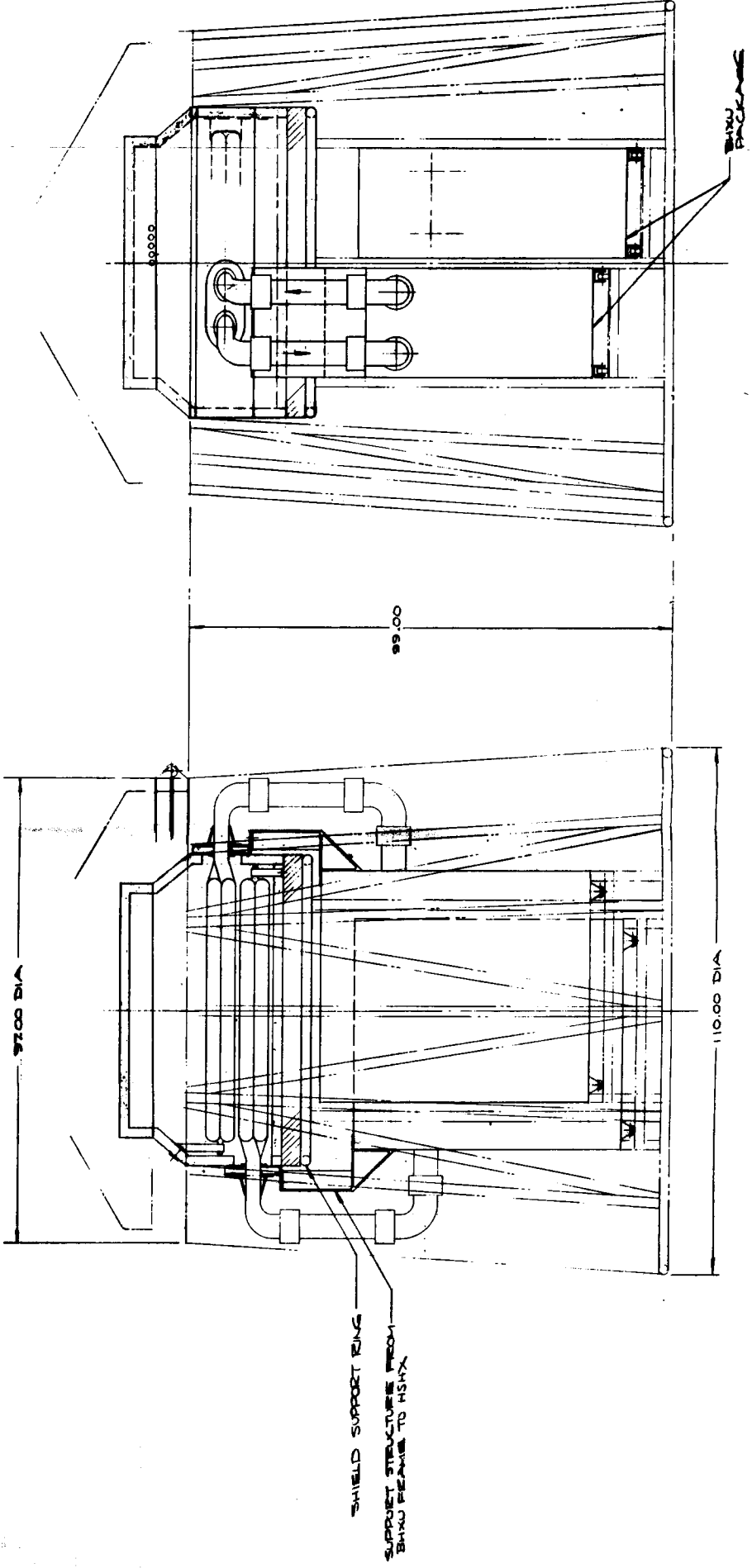
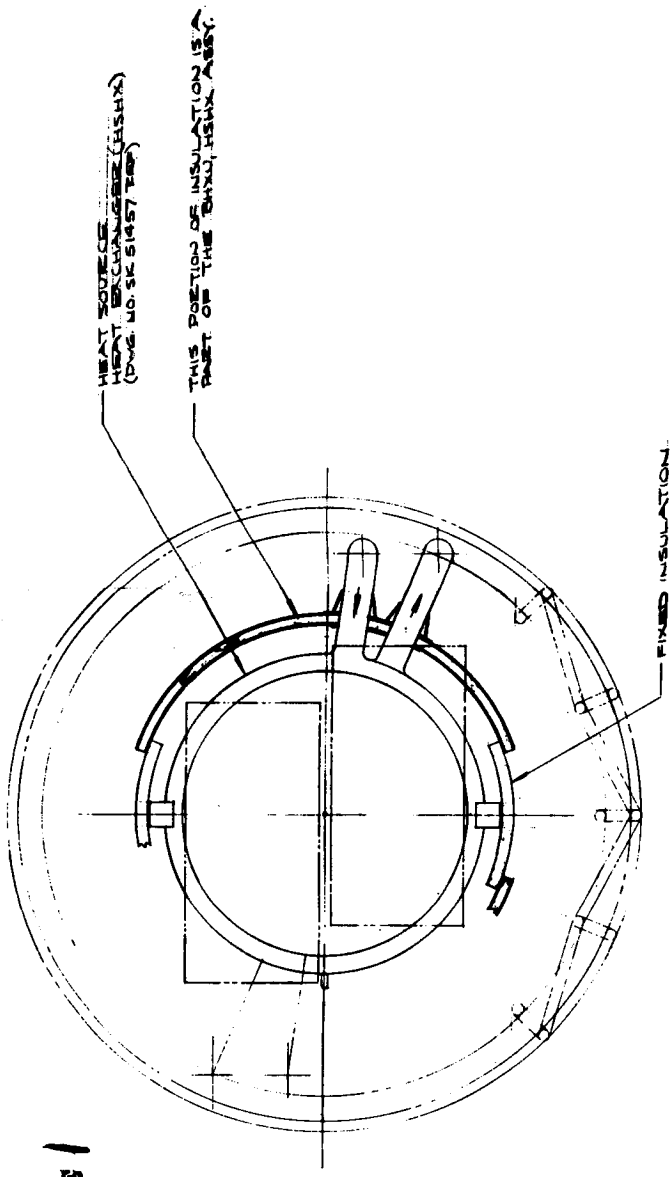


Figure 8.2-7 CIRCULAR PLANAR SOURCE -- INVOLUTE TUBE HEAT EXCHANGER (49-INCH DIAMETER)

ring framework beneath the shield provides the support for the two PCM packages which slide in on tracks and are locked into place to the truss framework.

2. Heat Dump System

An alternate approach to the rotation of the heat source for the emergency heat dump mode could be provided by removing a portion of the fixed insulation from under the IRV. The advantage of this approach is that it would be simpler to move a few pounds of insulation than to move the complete IRV.

Figure 8.2-8 shows the involute HSHX installation incorporating a heat dump system. A portion of the fixed insulation on either side of the cavity slides down to expose the source to space. Since the large manifolds associated with the involute HSHX would still be between the heat source and the outside, it was necessary to increase the separation distance between the source and HSHX No. 1 from 5 inches to about 12 inches. This gives better view factors between the heat source and the outer environment and, hence, results in a reasonable maximum source temperature (1900^oF) in the heat dump mode.

3. Heat Leaks

The main areas to be insulated are the heat exchanger cavity, the inlet and outlet ducts to both heat exchangers, and the structural supports to the heat exchangers.

The Linde Super Insulation, a product of Union Carbide Corporation, was assumed as the insulating material for the heat exchanger cavity. The thermal conductivity of the superinsulation is at least one order of magnitude less than any of the available conventional insulating materials. Moreover, superinsulation systems have shown excellent performance while withstanding rigorous conditions of mechanical shock, vibration, and severe radiation and temperature environments.

Thermal conductivity performance data for load-bearing and non-load-bearing superinsulation is presented in Figure 8.2-9. Load-bearing insulation has higher thermal conductivity due to an increased solid conduction. This difference is less significant at the higher temperatures, where radiation becomes the dominant mode of heat transfer.

The superinsulation covers the shield at the bottom of the HSHX cavity as well as the inner surface of the side walls of the cavity. In the fixed insulation concept, the side walls are made of a fixed part and two movable parts, as shown in Figure 8.2-6 and Figure 8.2-7. In the heat dump concept, the superinsulation consists of a fixed part and two sliding parts, as shown in Figure 8.2-8.

A certain number of penetrations through the superinsulation are required at locations where the various parts of the insulation are joined. Conservative estimate has been made for the heat leak at these joints.

Flexible MIN-K 2000, a product of Johns-Manville, has been selected to insulate inlet and outlet ducts and flanges. MIN-K is a fibrous material which contains

FOLDOUT FRAME 2

FOLDOUT

FOLDOUT FRAME 1

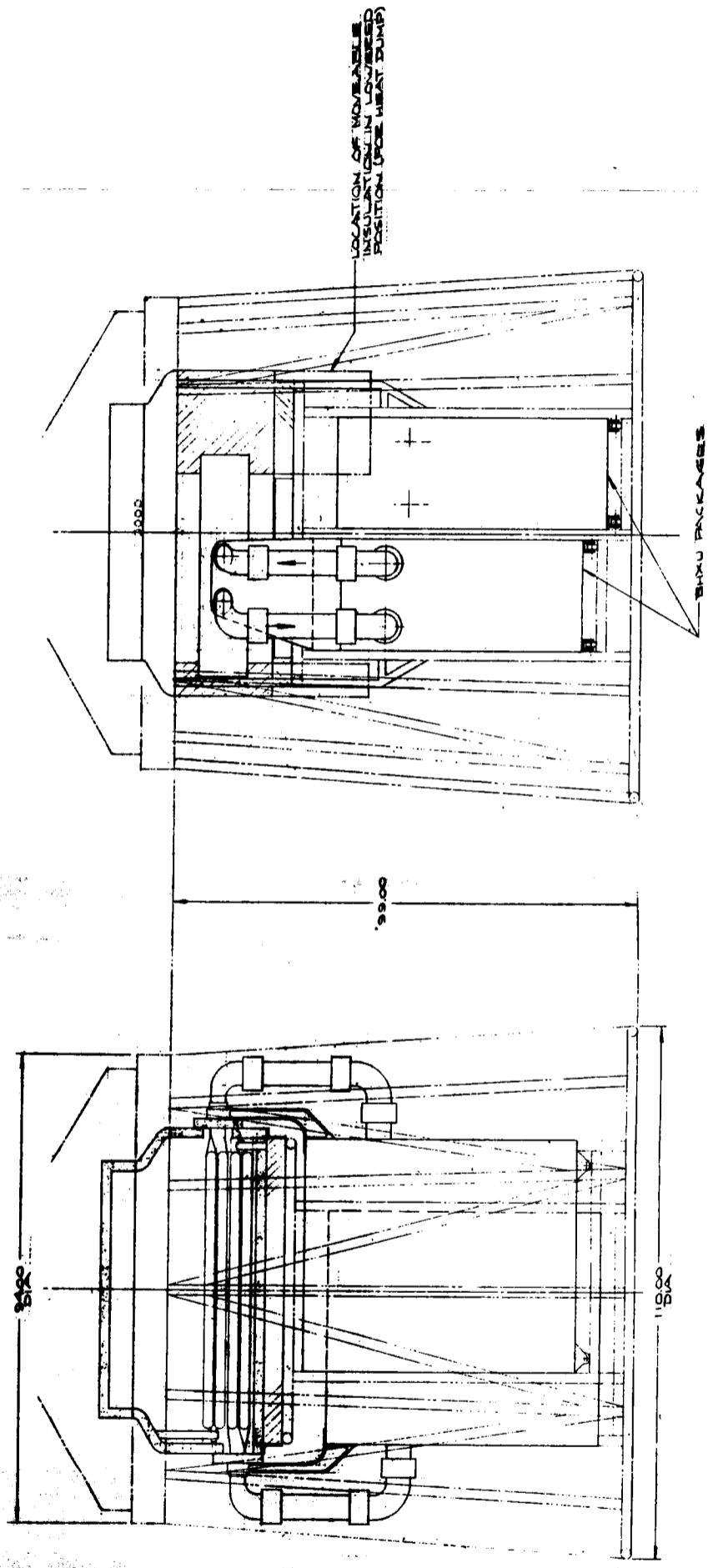
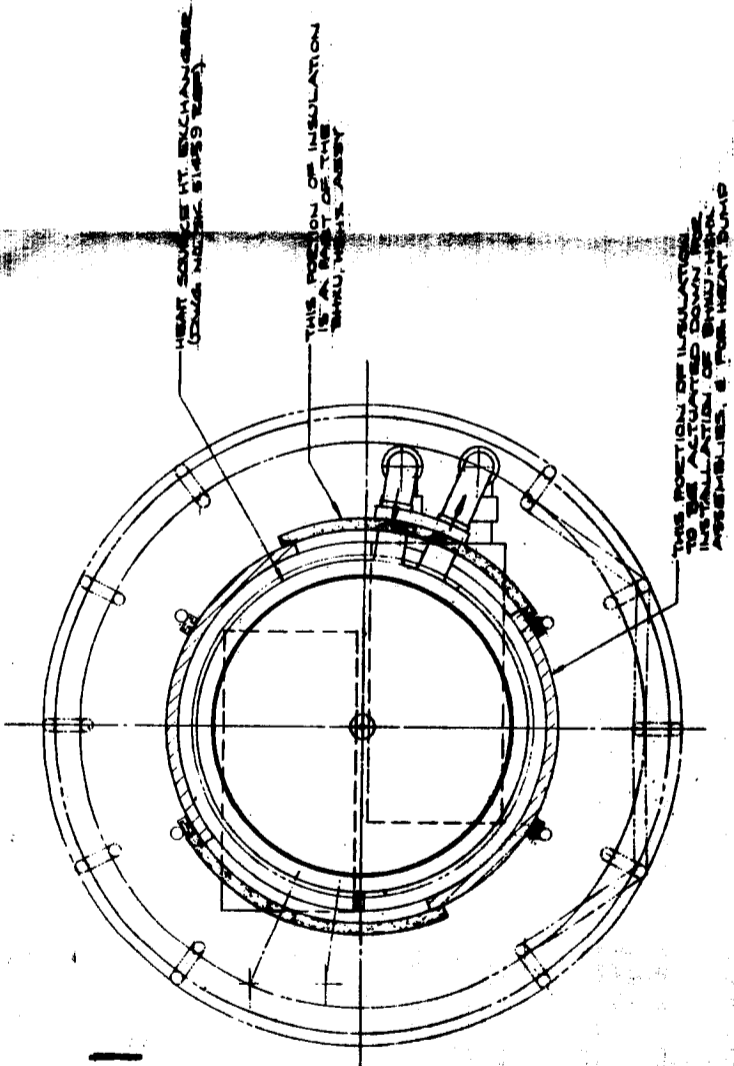
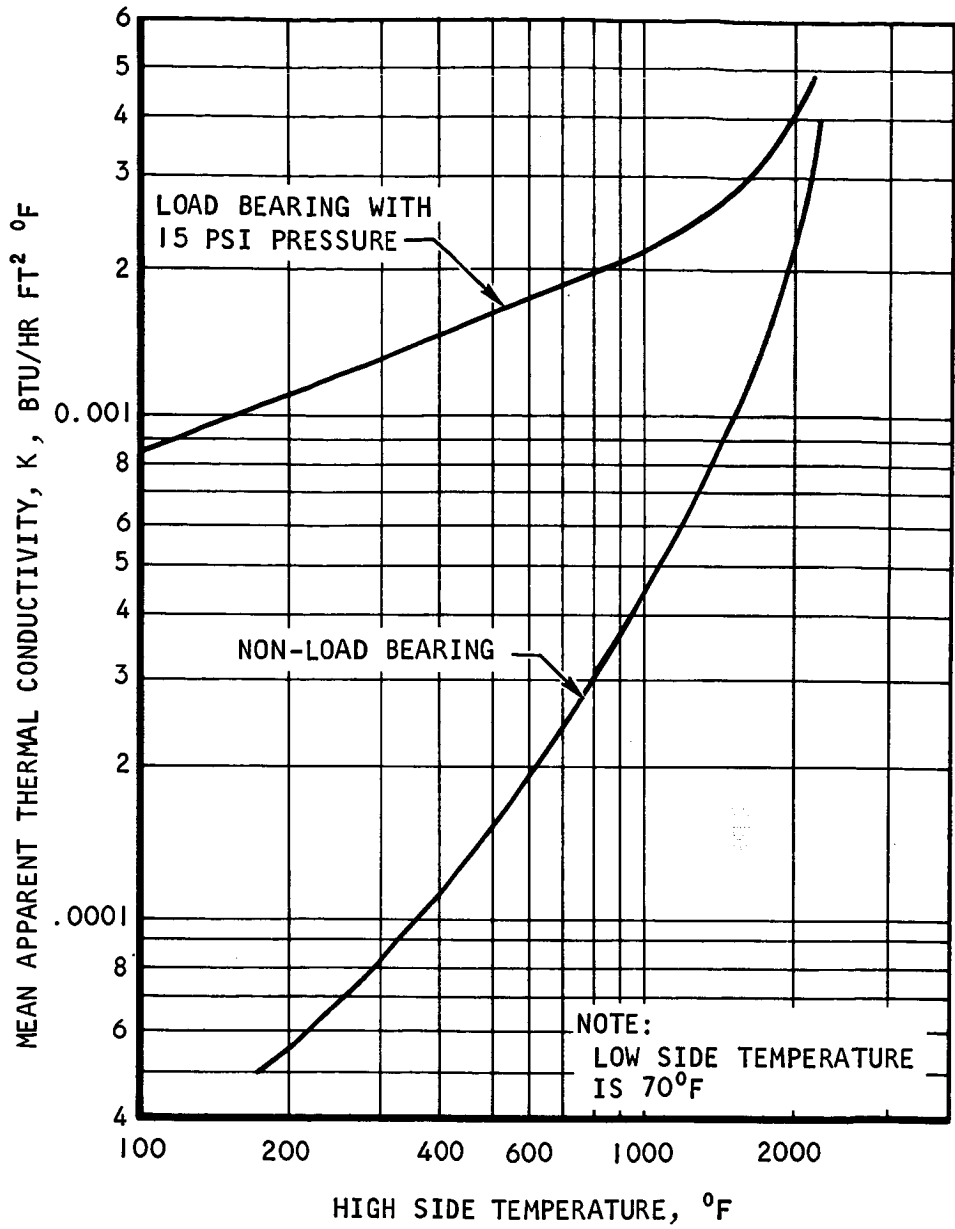


Figure 8.2-8 CIRCULAR PLANAR SOURCE -- INVOLUTE TUBE HEAT EXCHANGER (49-INCH DIAMETER) (HEAT DUMP SYSTEM)



A-33318

Figure 8.2-9 THERMAL CONDUCTIVITY VERSUS TEMPERATURE AS A FUNCTION OF BEARING LOAD

appreciable quantities of exceedingly fine particulate matter. The pore structure of MIN-K is so minute that it has a thermal conductivity lower than the molecular conductivity of still air. The thermal conductivity decreases appreciably at higher altitudes. For example, at an altitude of 10 miles, Figure 8.2-9 shows the conductivity decreases by as much as 50 percent. This characteristic is directly attributable to the extremely small pore size of MIN-K. Figure 8.2-10 shows the thermal conductivity of MIN-K 2000 versus temperature in air.

Figure 8.2-11 shows the various areas of heat leaks and the recommended insulating materials at these locations. A minimum thickness of 2 inches of superinsulation is used to cover the cavity boundaries. At the aft support see Figure 8.2-11, penetrations through the insulation are necessary for installation purposes. Therefore, the thickness of the superinsulation is increased to about 3 inches to limit the heat leak in this area. A thickness of 2 1/2 inches of flexible MIN-K 2000 was estimated to be satisfactory for the insulation of the ducts and to cover the flanges and the outer mounting brackets. The MIN-K will have stainless steel with gold coating as a facing material. This will decrease the heat loss by radiation to the environment. A thickness of 1 inch of asbestos is used between the flanges of the inlet and outlet ducts to reduce the heat conducted along the tube walls. While the HSHX is not in operation, the asbestos minimizes the heat conducted to the PCM. The supports of the PCM act as heat leaks, dissipating the small amount of heat conducted to the PCM through the ducts. As a result, no significant temperature rise will occur in the inoperative PCM unit.

Assuming a sink temperature of 0°F, the magnitude of the heat leaks are listed in Figure 8.2-12.

The larger heat losses in the heat dump system are caused by the larger HSHX cavity and the sliding portions of the insulation.

Performance

A typical temperature distribution along one of the tubes in HSHX No. 2 is depicted in Figure 8.2-13. The Brayton fluid temperature rise is also shown in the same figure. The fluid enters the tube at 1200°F; the temperature gradient along the tube is large in the first pass due to the high heat flux in this pass and decreases gradually in the second pass. The fluid outlet temperature in this case is 1600°F which corresponds to full output power from PCM No. 2.

The results of the effective and maximum heat-source temperature distribution and the temperature distribution on HSHX No. 1 on the side facing the heat source are also shown in Figure 8.2-13. The ΔT from the effective radiating temperature to the fuel capsule hot spot is taken from the capsule thermal analysis as 120°F. It is obvious in this figure that the design temperature limitation of 2000°F is exceeded by approximately 60°F. This can be attributed to: a) a slight increase in ΔT around the fuel capsule due to the smaller capsule spacing, b) an increase due to the 17-percent decrease in radiating area attendant in going from a 53- to a 49-inch-diameter, and c) an increase in temperatures indicated by the more accurate machine calculations over the previous hand calculations.

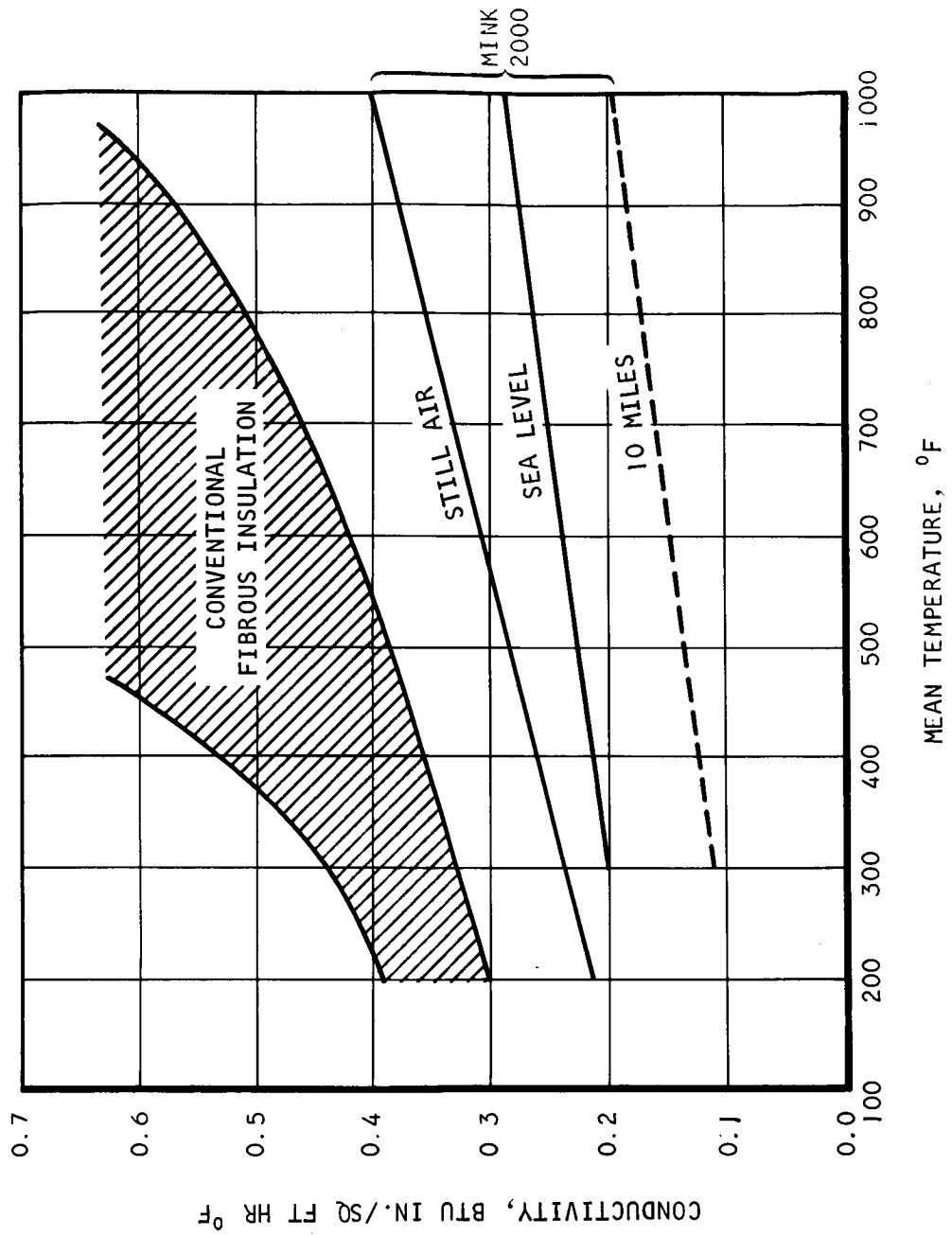


Figure 8.2-10 THERMAL CONDUCTIVITY COMPARISON

A-33317

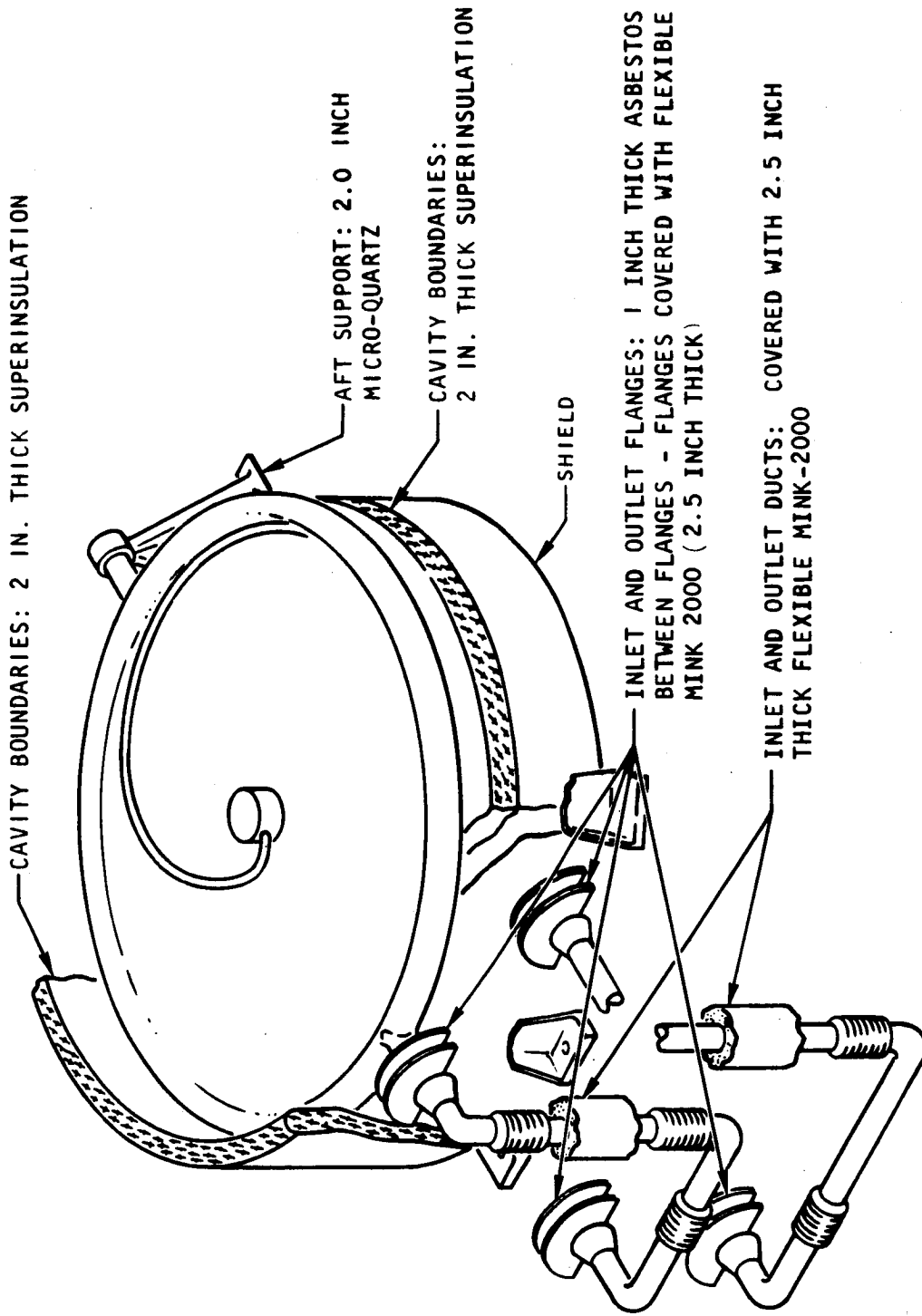
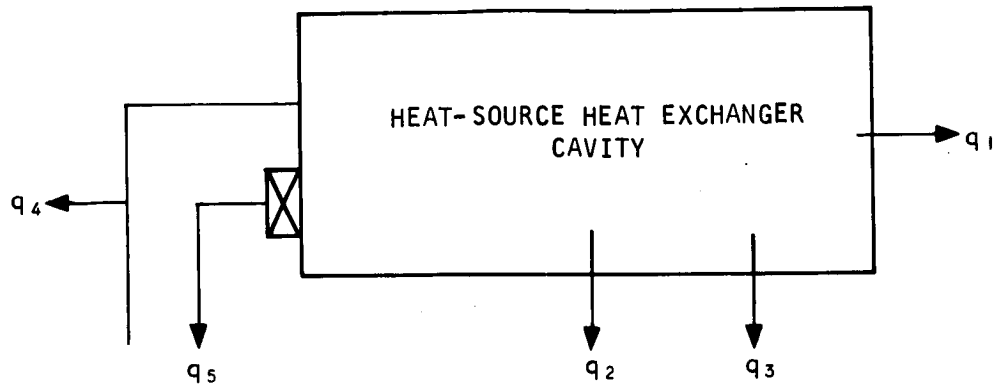


Figure 8.2-1.1 ASSUMPTIONS FOR HEAT LEAK ESTIMATES

A-33006



q_1 = heat loss from side walls of HSHX cavity in watts

q_2 = heat loss from base of HSHX cavity in watts

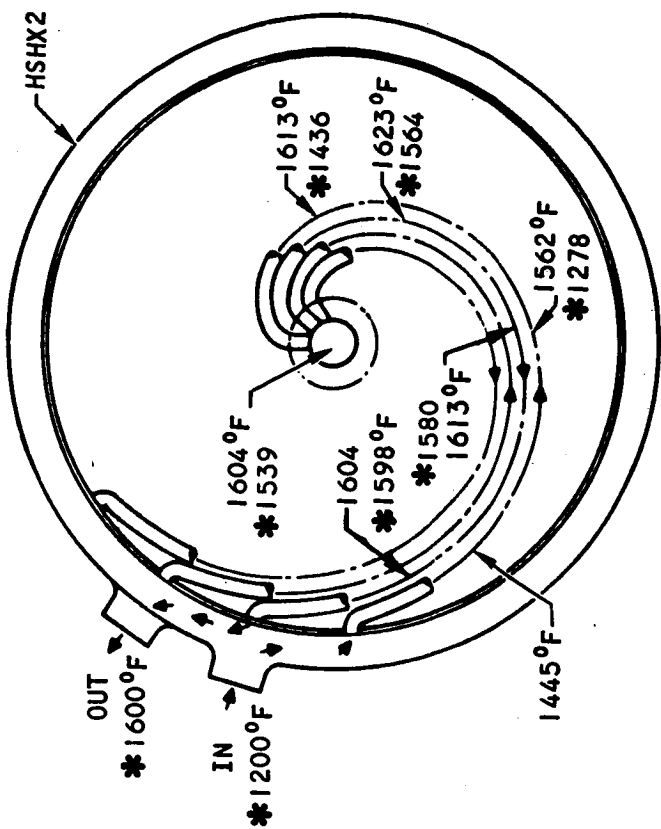
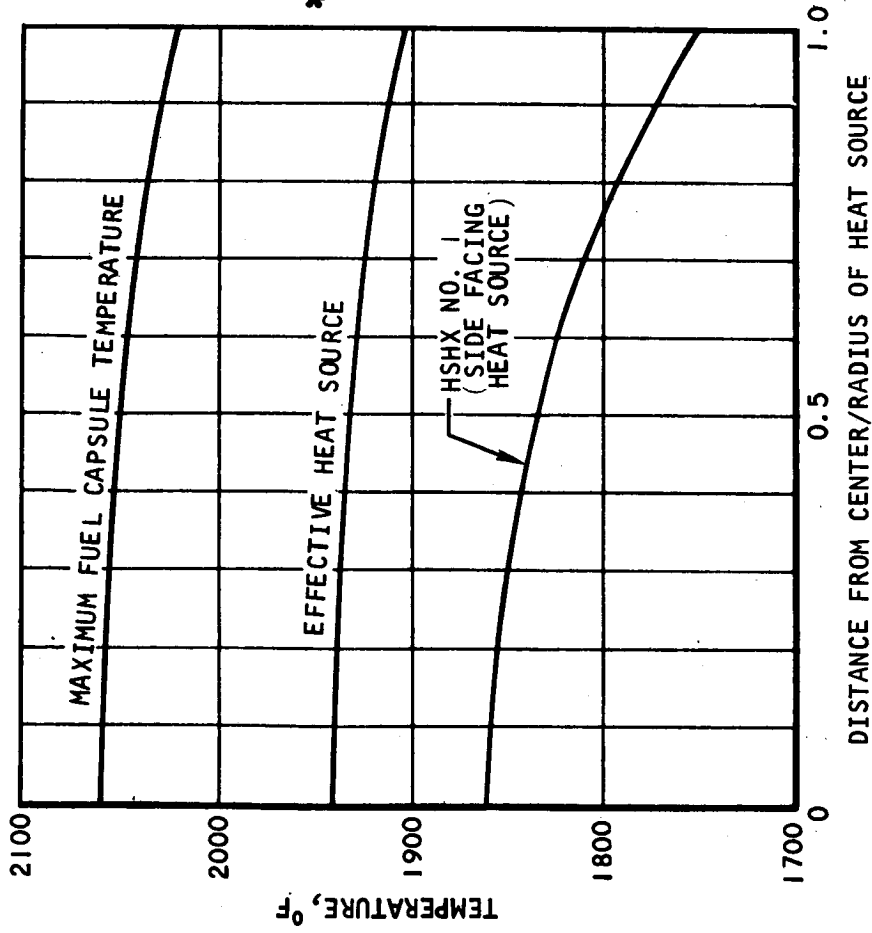
q_3 = heat loss from aft support in watts

q_4 = heat loss from inlet and outlet ducts in watts

q_5 = heat loss from mounting brackets in watts

System	$q_1 + q_2$	q_3	q_4	q_5	Total
Fixed insulation system (no heat dump)	255	61	404	202	922
Heat dump system	324	61	404	202	991

Figure 8.2-12 HEAT LEAKS -- PLANAR CIRCULAR HEAT SOURCE



* INDICATE FLUID TEMPERATURE

Figure 8.2-13 INVOLUTE HEAT-SOURCE HEAT EXCHANGER PERFORMANCE (SECOND HEAT EXCHANGER IN OPERATION) (49-INCH-DIAMETER)

At the conclusion of the Phase IA studies, the ground rule which required that the second power system operate at full power with the 2000°F capsule limit was relaxed in favor of one in which a reduction in power level on the second unit would be traded for a reduction in source temperature. In other words, the full output power requirement would only be imposed on the first HSHX. Figure 8.2-14 shows the temperature distributions with HSHX No. 1 operating at full turbine inlet temperature. The data presented in this figure are not a result of a computer calculation; they were estimated from the computer results shown in Figure 8.2-13. It is clear in this figure that, under such a condition, the maximum source temperature is 1870°F which is considerably lower than 2000°F.

The maximum source temperature was shown in Figure 8.2-13 to be 2060°F when HSHX No. 2 is in operation and full output power is required from PCM No. 2. The reduction of this temperature to the 2000°F limit can be accomplished by one or more of the following ways:

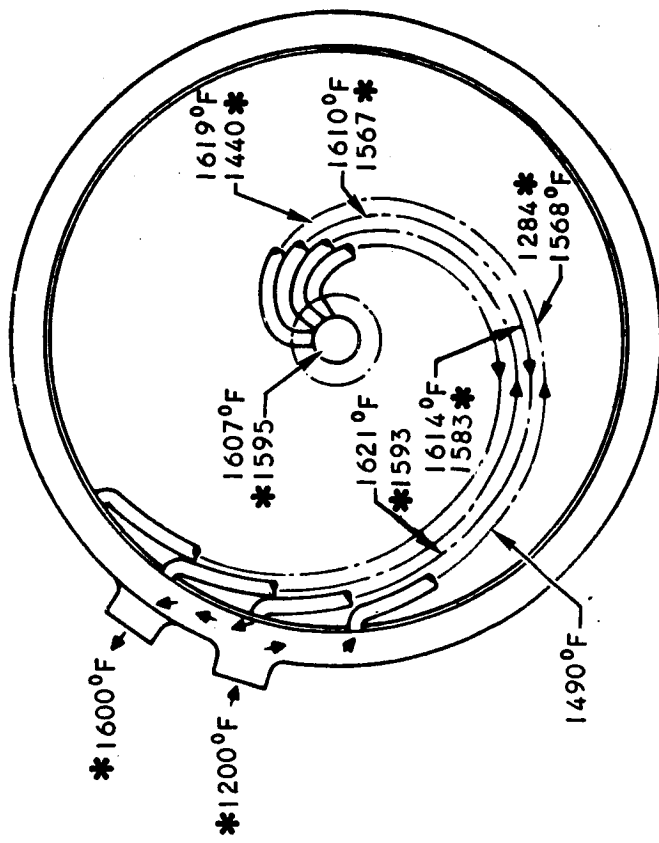
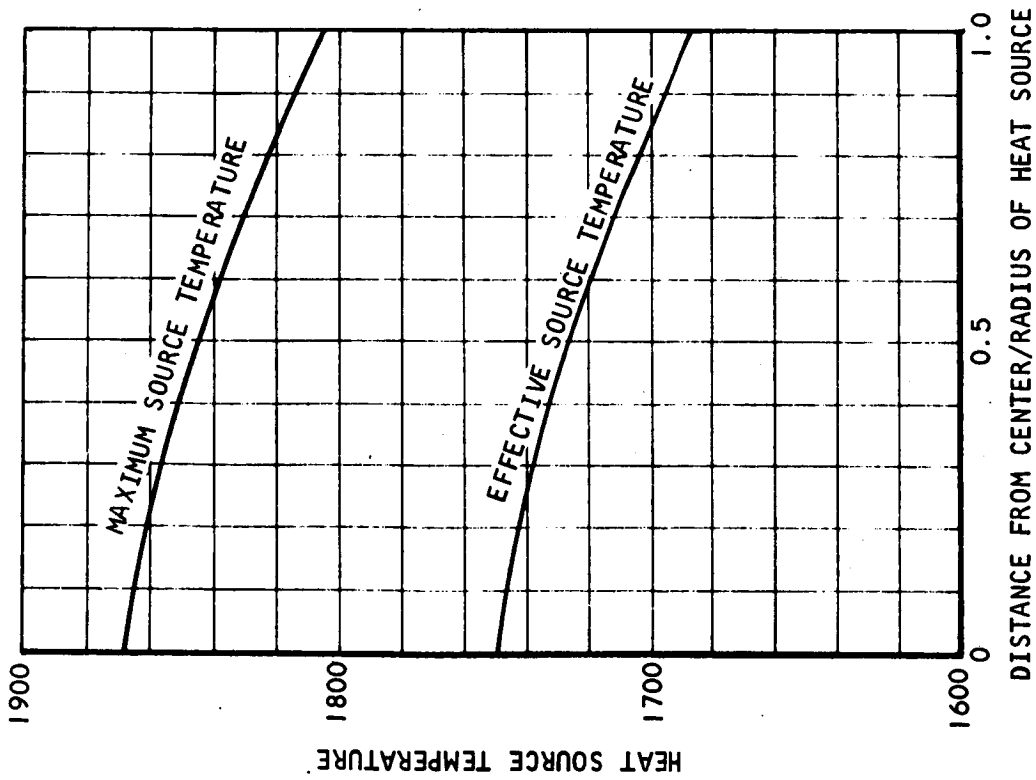
- a. Increase the diameter of the HSHX
- b. Increase the diameters of both the HSHX and the heat source
- c. Increase the wall thickness of the HSHX tubes
- d. Relax the requirement of full output power from PCM No. 2.

The effect on the maximum source temperature of increasing the diameter of the HSHX is shown in Figure 8.2-15 for a source diameter of 49 inches. An increase in the diameter of the HSHX results essentially in an increase in the geometric shape factor between the heat source and the HSHX. As shown in this figure, the diameter of the HSHX has to increase to about 61 inches to reduce the maximum source temperature by 60°F.

A more effective way to reduce the source temperature is to increase the diameter of both the heat source and the HSHX. This increases the geometric shape factor between the heat source and the HSHX, and at the same time, it decreases the heat flux per unit area of the heat source. The maximum effective source temperature is shown in Figure 8.2-16 versus the HSHX diameter when either HSHX No. 1 or HSHX No. 2 is in operation. In both cases, the turbine inlet temperature is kept at 1600°F. If HSHX No. 2 is in operation, to have a maximum effective source temperature of 1880°F (to allow for a 120°F temperature drop in the fuel capsules), the diameters of the heat source and the HSHX have to be greater than 55 inches.

A third way to decrease the maximum heat-source temperature consists of a) increasing the wall thickness of the HSHX tubes to reduce conduction losses and b) providing a better thermal conduction path between the hot and cold legs by depositing additional weld material between the tubes. A simple relationship can approximately describe the source temperature reduction. Temperature degradations due to conduction effects can be cut in half by doubling metal thickness. Figure 8.2-17 indicates the reduction in heat-source maximum temperature based on the preceding assumption.

The effect of relaxing the full power requirement for the PCM No. 2 is revealed in Figures 8.2-18 and 8.2-19. Figure 8.2-18 shows the decrease in the maximum



* FLUID TEMPERATURE

Figure 8.2-14 INVOLUTE HEAT-SOURCE HEAT EXCHANGER PERFORMANCE (FIRST HEAT EXCHANGER IN OPERATION) (49-INCH-DIAMETER)

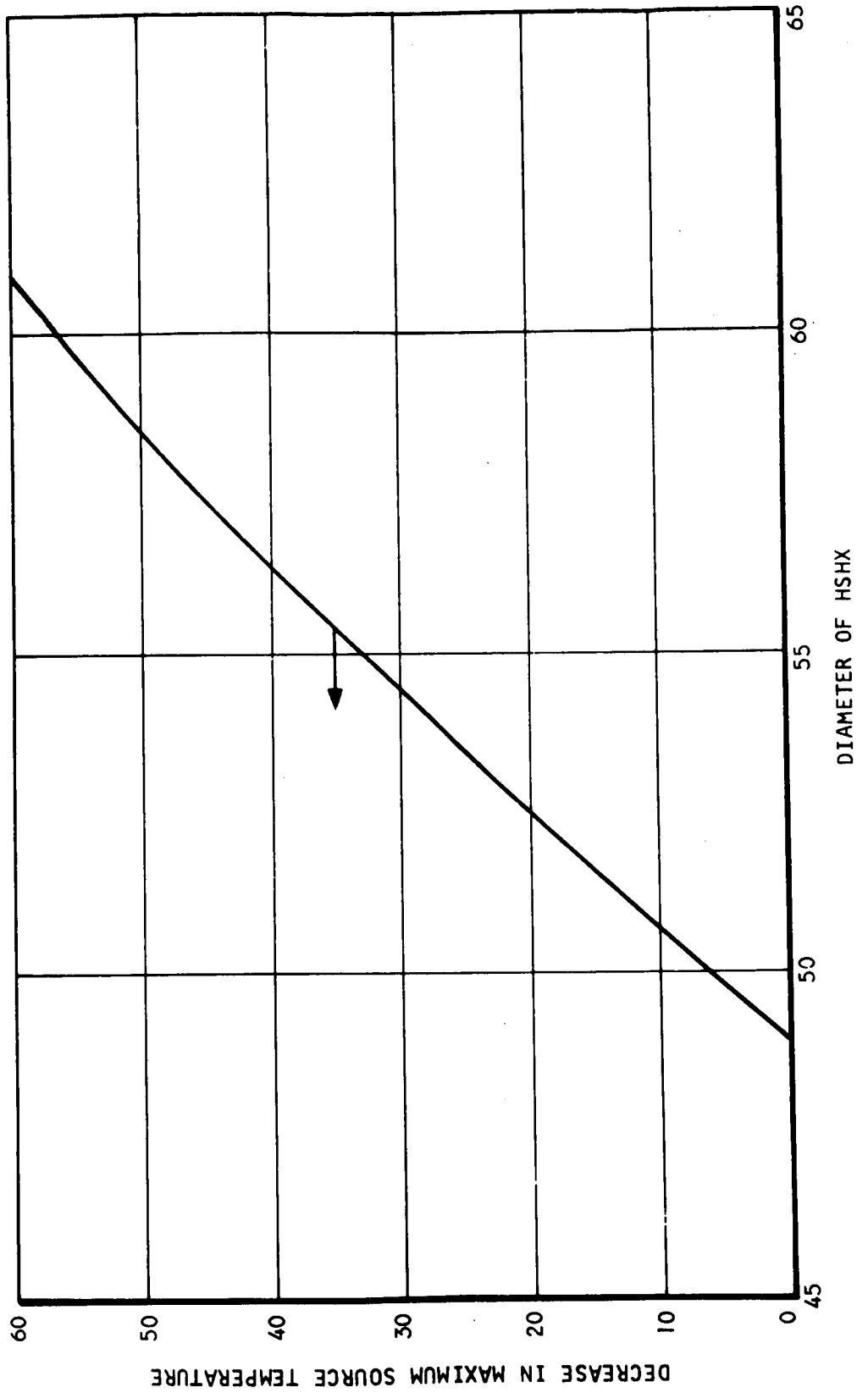


Figure 8.2-15 EFFECT OF INCREASING HEAT-SOURCE HEAT EXCHANGER DIAMETER

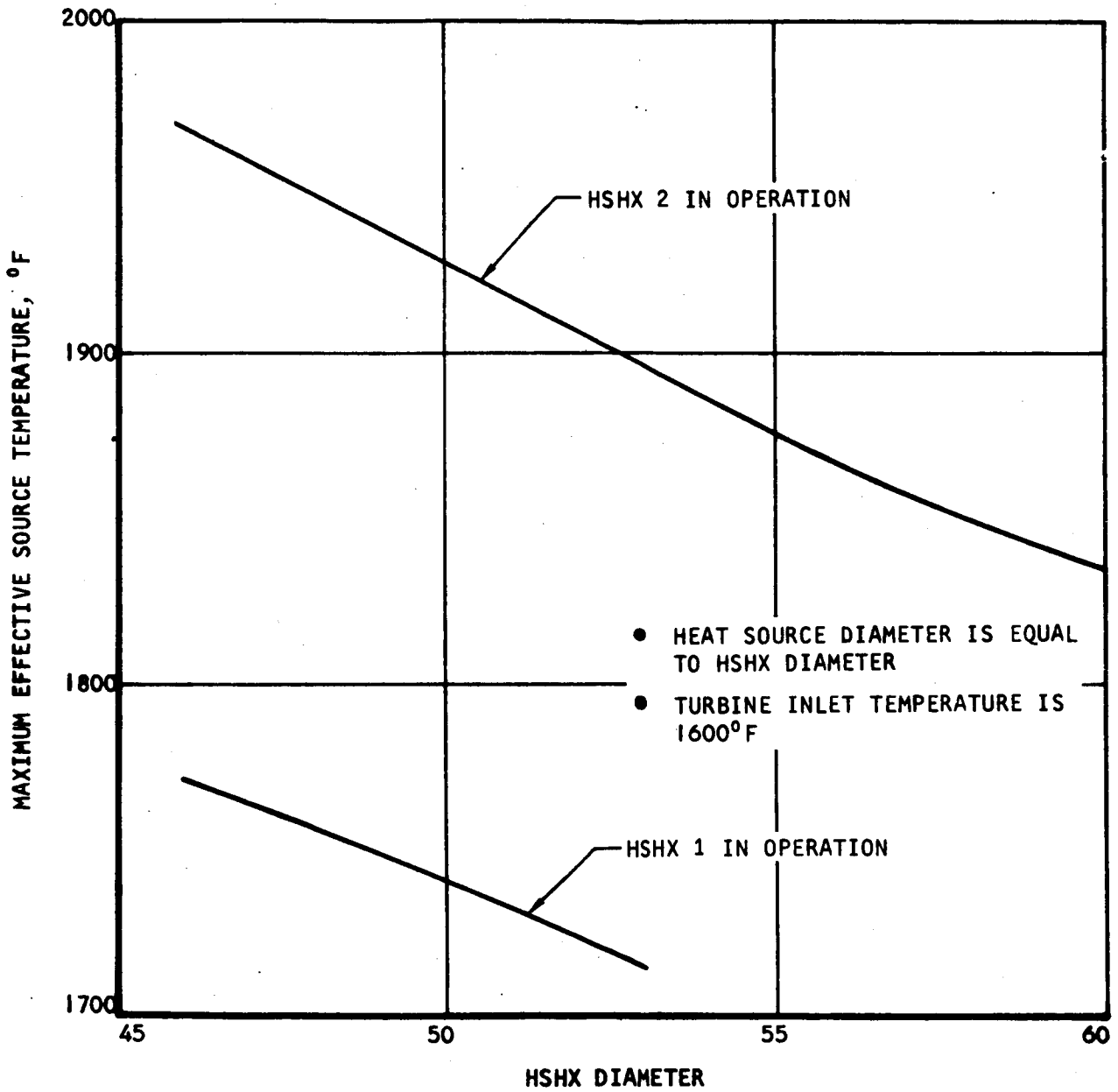


Figure 8.2-16 HEAT-SOURCE HEAT EXCHANGER AREA REQUIREMENTS

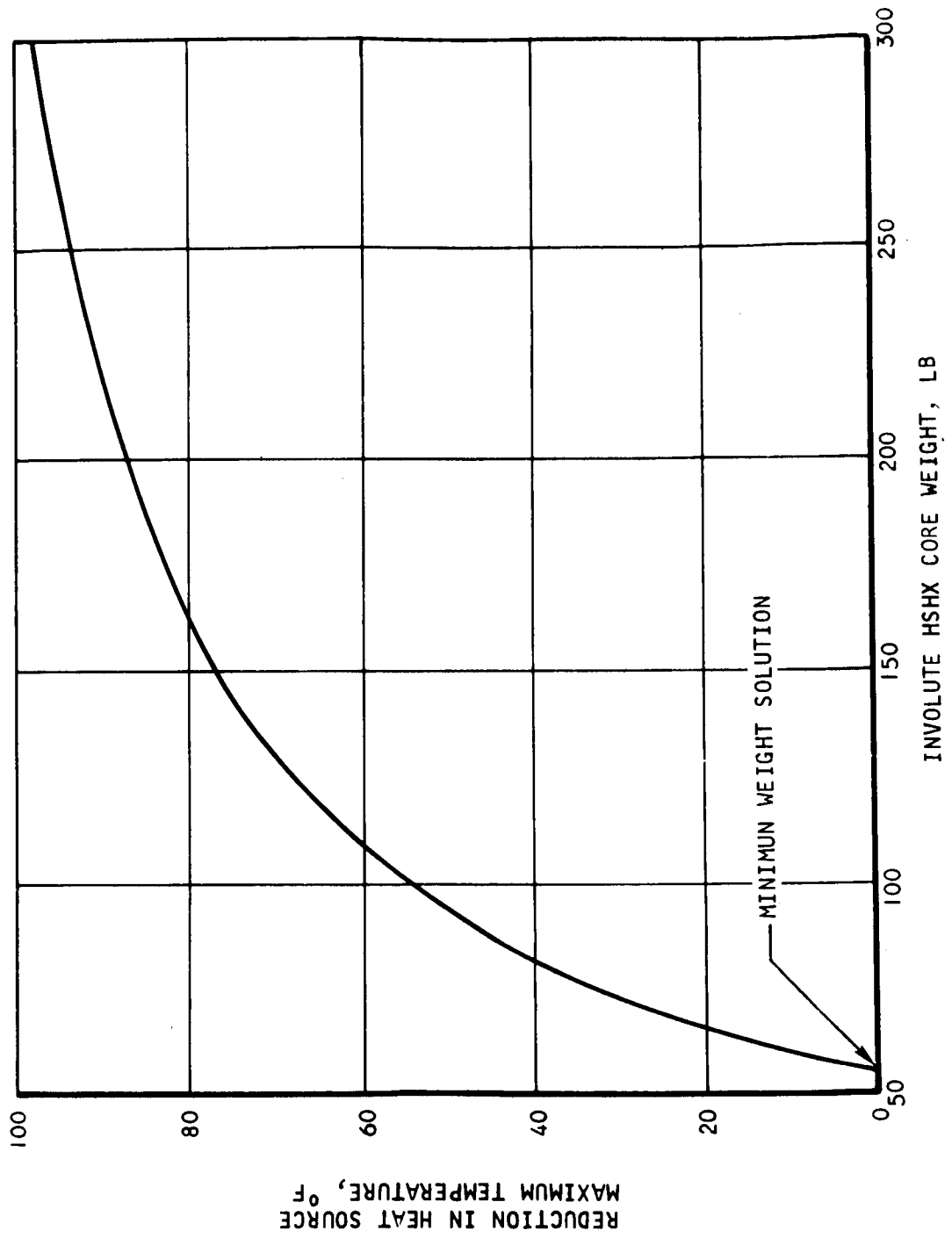


Figure 8.2-17 HEAT-SOURCE HEAT EXCHANGER -- WEIGHT VERSUS REDUCTION IN SOURCE TEMPERATURE (49-INCH- DIAMETER SOURCE)

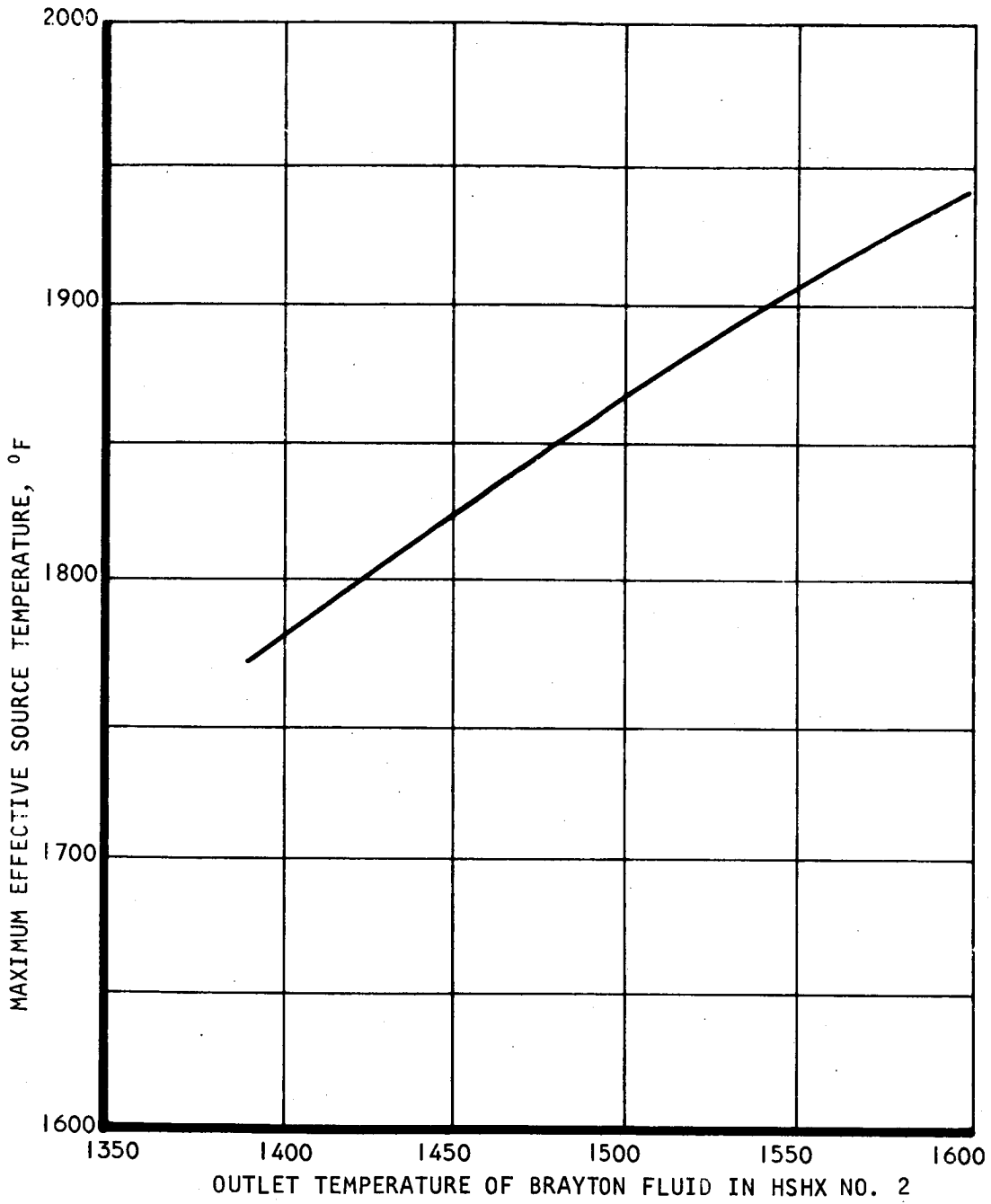


Figure 8.2-18 BRAYTON FLUID OUTLET TEMPERATURE VERSUS EFFECTIVE SOURCE TEMPERATURE (CIRCULAR GEOMETRY)

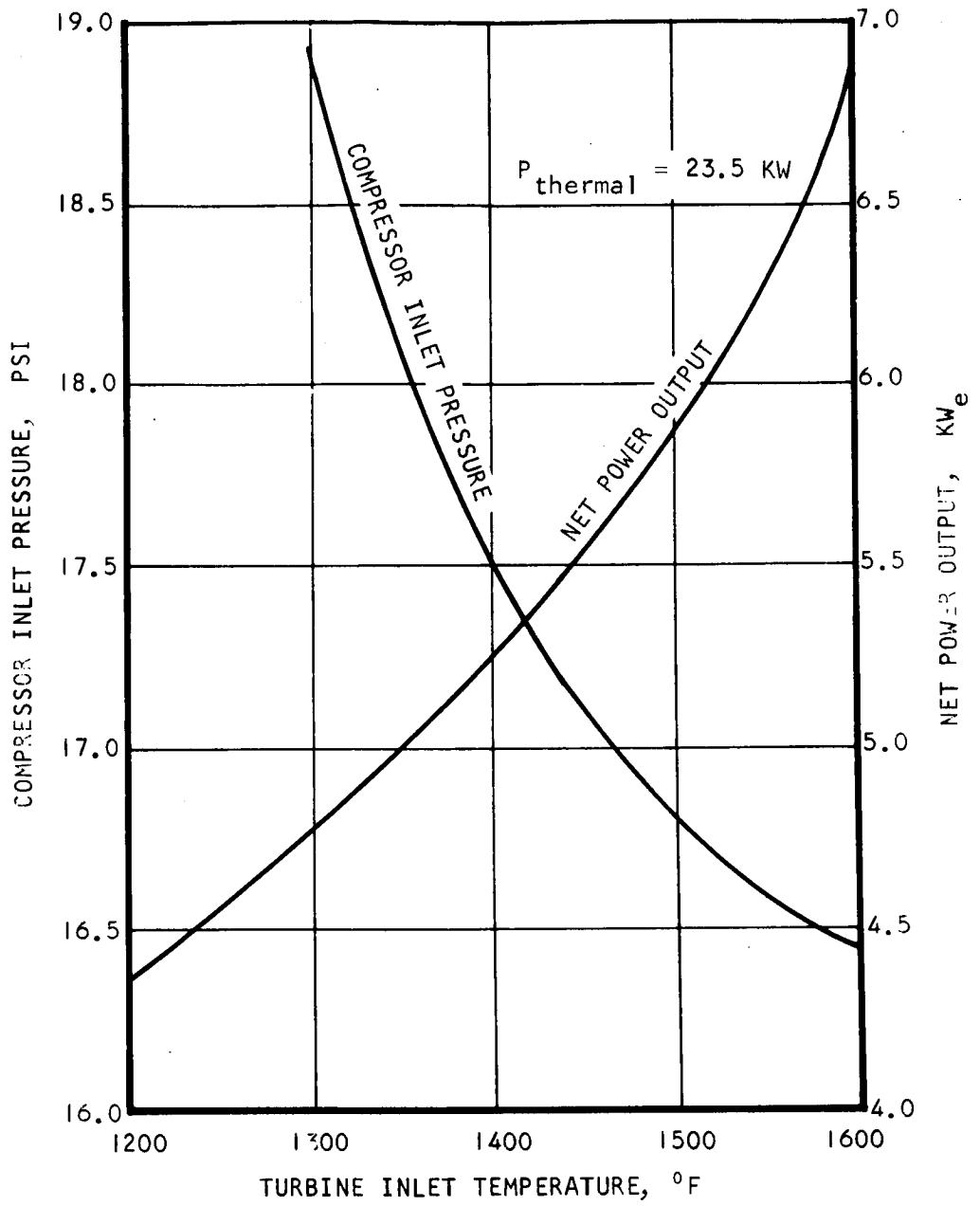


Figure 8.2-19 TURBINE INLET TEMPERATURE VERSUS POWER OUTPUT

effective source temperature as a result of the decrease in the Brayton fluid outlet temperature in HSHX No. 2. It is clear in this figure that decreasing the gas outlet temperature by 80°F results in about a 60°F decrease in the maximum effective source temperature, and hence the maximum source temperature would not exceed 2000°F. A reduction of the turbine inlet temperature from 1600°F to 1520°F results in a reduction of electrical power output of about 12 percent (from 6.86 to 6.05 kw_e) as indicated in Figure 8.2-19

Reducing turbine inlet temperature is accomplished by increasing the system pressure level, as shown in Figure 8.2-19 in terms of the required compressor inlet pressure. The gas management system would be utilized to effect this pressure level change. This approach offers a potential for reducing source temperatures at some penalty of operational capability.

8.2.1.3 Rectangular Heat-Source Heat Exchanger

Description

The rectangular HSHX for the 49-inch-diameter heat source is shown in Figure 8.2-20. The active portion of the heat exchanger consists of 48 tubes, each with an OD of 1.0 inch and a wall thickness of 0.030 inch. A spacing of 0.021 inch is left between tubes to provide for a weld bead. The fluid enters alternate tubes along the length of the 3.0-inch-diameter inlet manifold, flows across the face of the heat source, enters a 1.5-inch-diameter header, is turned, enters adjacent tubes, flows back across the face of the heat source, and enters the 3.0-inch-diameter outlet manifold. The wall thickness of the inlet and outlet manifolds are 0.030 inch and 0.042 inch, respectively. The length of the outer legs is 37 inches, and the center legs are 49 inches long. The wall thickness of the tubes is 0.030 inch, and the overall weight of the heat exchanger is 85 pounds.

Design Analysis

The same design procedure described for the involute tubular HSHX was used for the rectangular HSHX.

1. Thermal Design

The thermal analysis of the heat transfer process in the heat source HSHX cavity was carried out using the approximate method described in Reference 8.2-3. Profiles of the wall temperature and heat flux along the tubes of HSHX No. 2 are depicted in Figure 8.2-21. These profiles were calculated for the tubes in the center of the HSHX. The source temperature distribution shown in this figure is along the centerline of the heat source in the Y-direction.

The ratio of the local heat flux for various tubes of HSHX No. 2 to the local heat flux in the center tube is shown in Figure 8.2-21 versus the distance from the center. This distribution is shown for locations 1, 2, 3, 4, and 5 depicted in Figure 8.2-22. At location 2, for example, which is at a distance ± 10 inches from the y=0 plane, the local heat flux in a tube located 16.2 inches from the plane x = 0 is about 48 percent of the local heat flux in the tube at the center. At locations close to the end of the tubes, the variation of the local heat flux

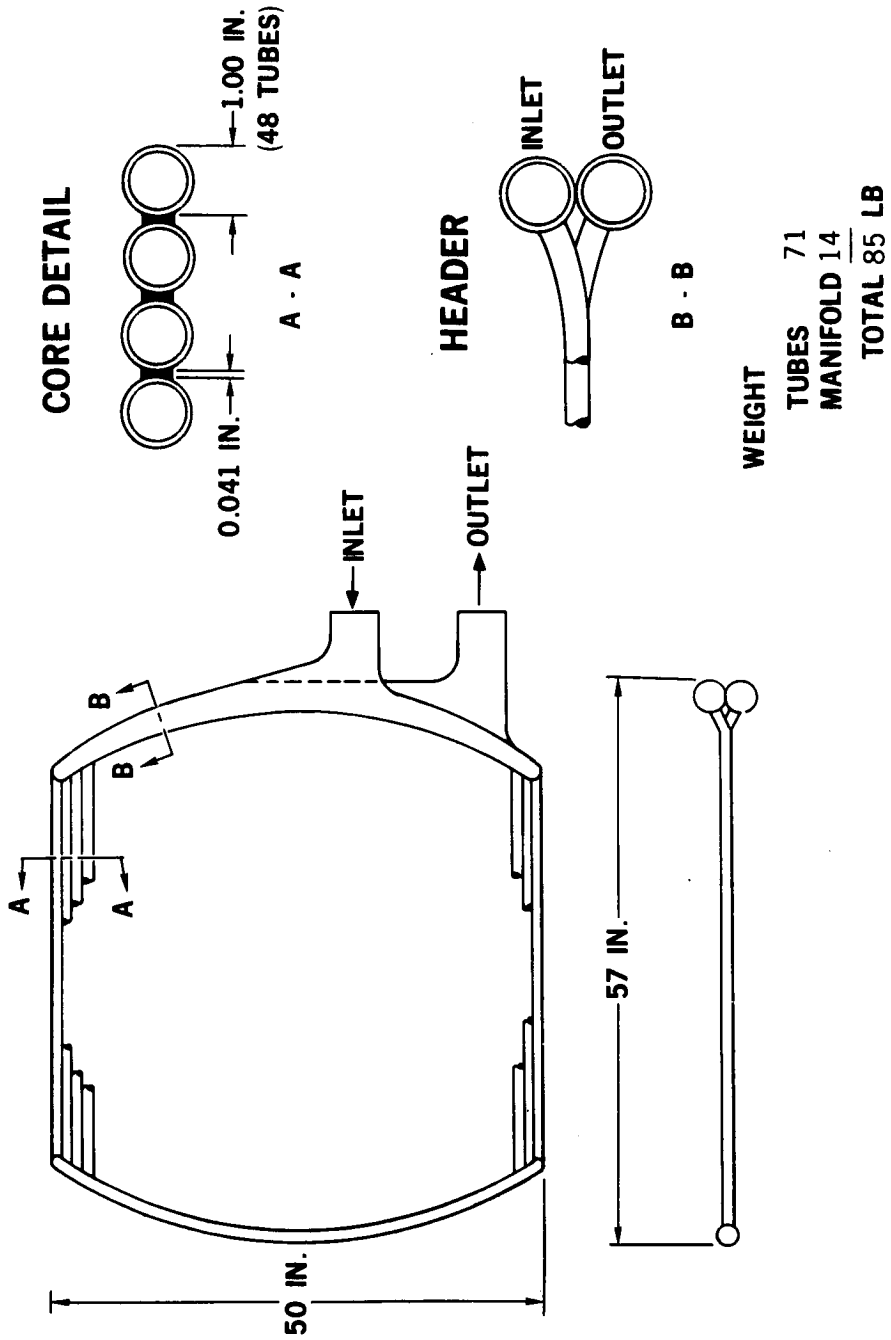


Figure 8.2-20 RECTANGULAR HEAT-SOURCE HEAT EXCHANGER CIRCULAR SOURCE
49-INCH-DIAMETER)

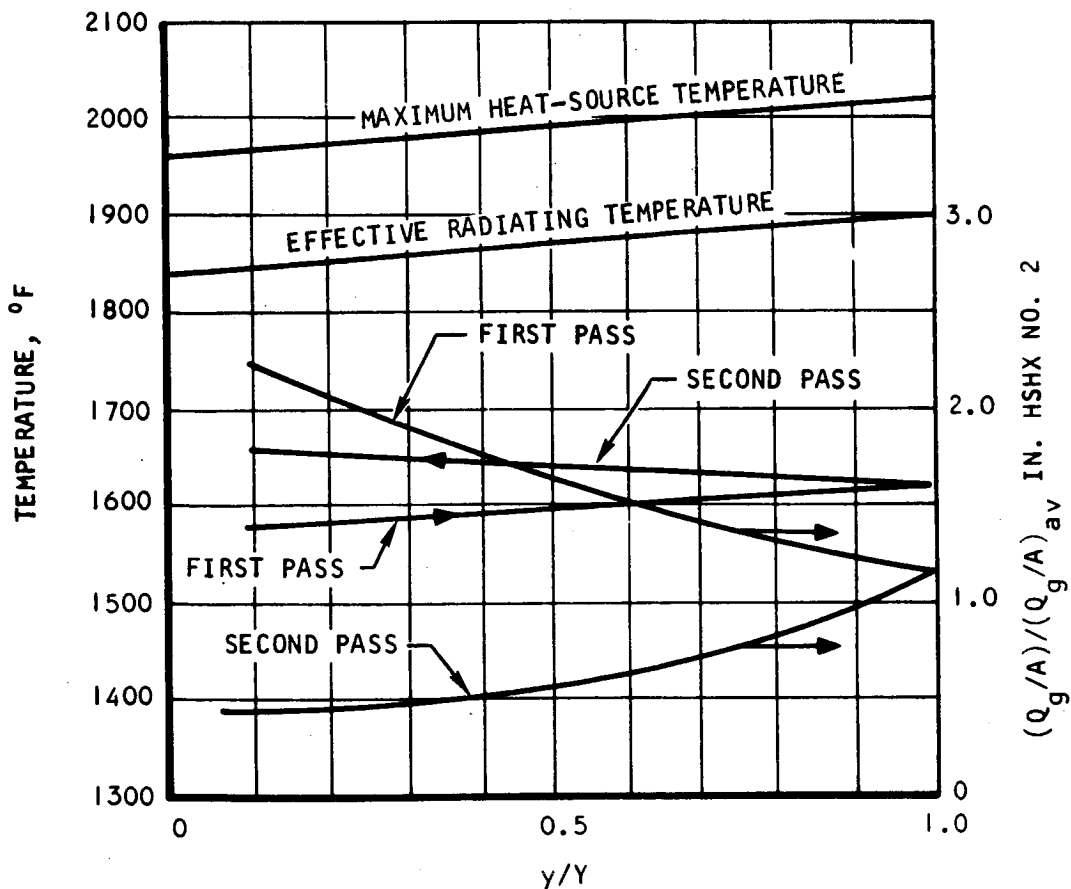
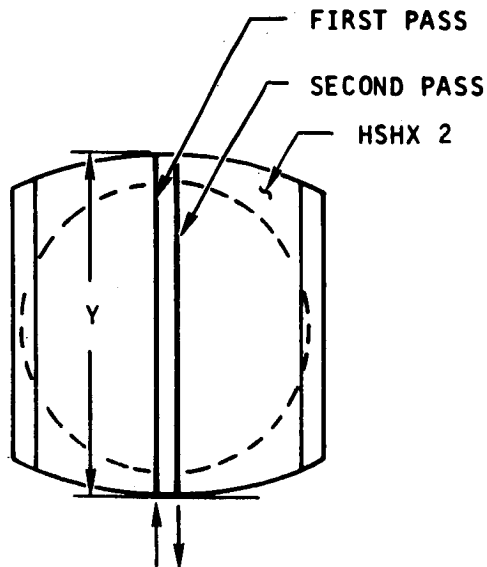


Figure 8.2-21 RECTANGULAR HEAT-SOURCE HEAT EXCHANGER -TEMPERATURE DISTRIBUTIONS (49-INCH-DIAMETER)

among various tubes becomes more severe. Figure 8.2-22 reveals that, for a tube located at a distance $x = 16.2$ inches and at a location $y = 18.5$ inches, the heat flux is about 7 percent that of the center tube. Hence, these portions of the tubes are contributing very little to the required heat transfer area.

2. Pressure Drop

Figures 8.2-21 and 8.2-22 describe the heat input to the various flow paths across the face of the heat source. It can be seen that the amount of heat input along any particular flow path is approximately proportional to the distance that the fluid traverses across the face of the heat source in that region. On this basis, the Brayton fluid, in order to have a constant exit temperature as it enters along the length of the outlet manifold, should also be distributed in proportion to the distance it traverses over the face of the heat source.

Let

N = the number of "in" legs = number of "out" legs

D = tube OD \approx tube

n = number of "in" legs away from the center flow path (center path = 0)

The half-length, y , that leg n traverses across the face of the heat source is

$$y = r \sqrt{1 - \frac{4n^2}{N^2}} \quad (8-24)$$

Therefore, the local Brayton fluid flow rate through leg n should be

$$\dot{W} = \dot{W}_0 \sqrt{1 - \frac{4n^2}{N^2}} \quad (8-25)$$

where \dot{W}_0 is the Brayton fluid flow rate through the central leg.

Therefore

$$\begin{aligned} \dot{W}_{\text{tot}} &= 2 \int_0^{N/2} \dot{W} \, dn = 2 \dot{W}_0 \int_0^{N/2} \sqrt{1 - \frac{4n^2}{N^2}} \, dn \\ &= \frac{\pi \dot{W}_0 N}{4} \end{aligned} \quad (8-26)$$

where \dot{W}_{tot} is the total Brayton fluid flow rate to the HSHX.

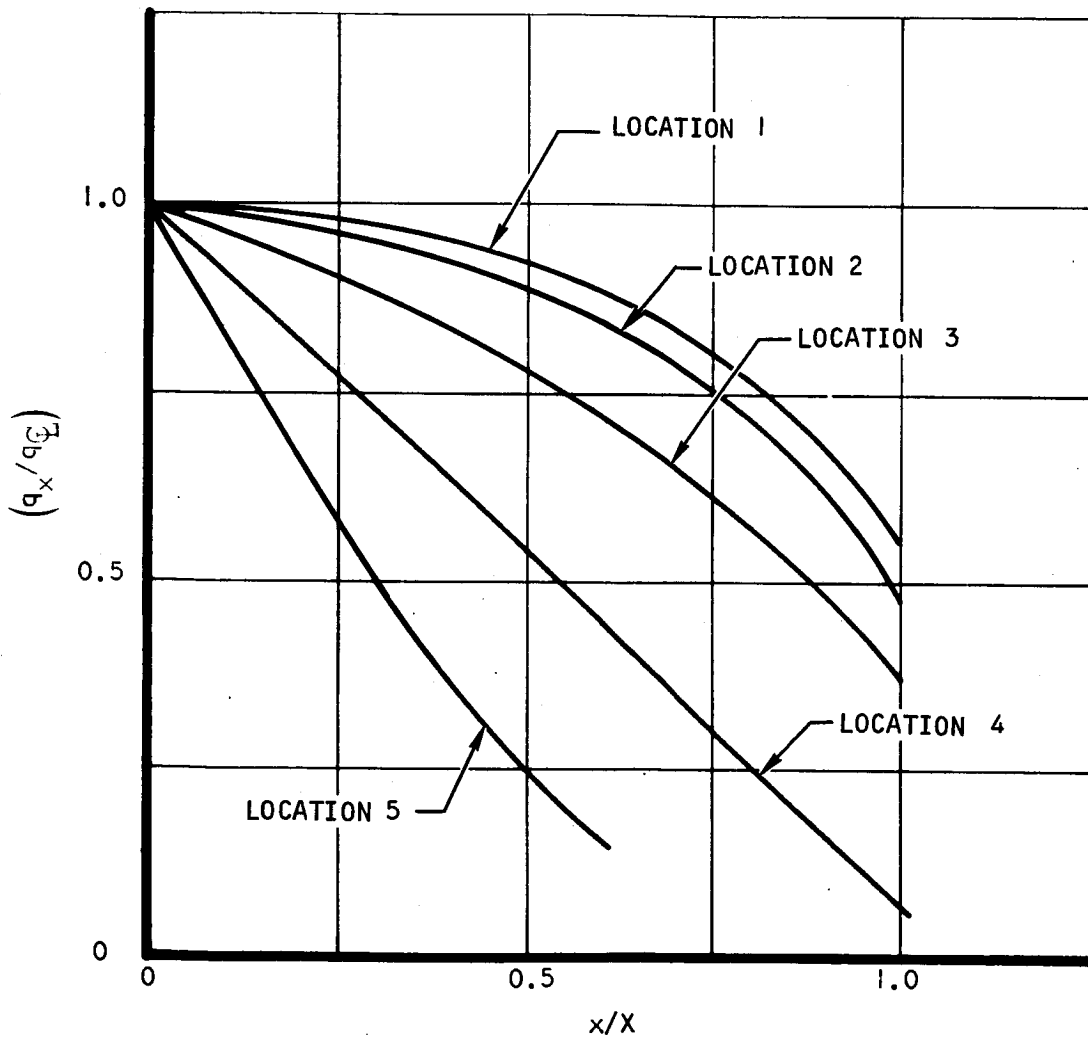
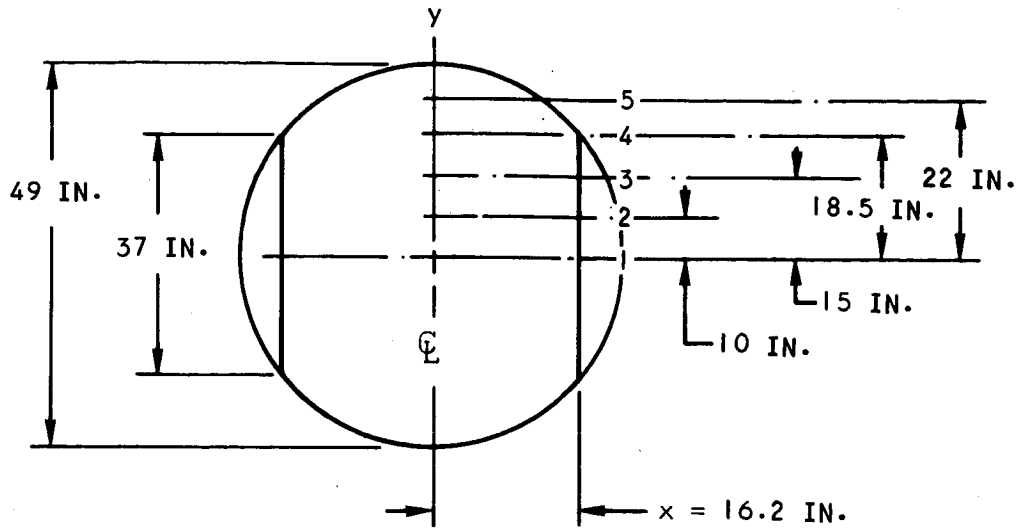


Figure 8.2-22 RECTANGULAR HEAT-SOURCE HEAT EXCHANGER CIRCULAR PLANAR SOURCE-VARIATION OF HEAT FLUX ALONG VARIOUS TUBES

Utilizing Equations (8-12), (8-15), (8-16), and (8-17) the frictional pressure drop through any leg becomes

$$\Delta P_f = 0.00442 \frac{\mu \cdot 2 \dot{W}^{1.8} L}{\rho D^{4.8}} \quad (8-27)$$

Utilizing Equations (8-24) and (8-25)

$$L \dot{W}^{1.8} = 4rW_o^{1.8} \left[1 - \frac{4n^2}{N^2} \right]^{1.4} \quad (8-28)$$

while

$$D = r/N \quad (8-29)$$

and by applying Equations (8-26), (8-28), and (8-29) to (8-27)

$$\Delta P_f = 0.0273 \frac{\mu \cdot 2 \dot{W}_{tot}^{1.8}}{\rho r^{3.8}} N^3 \left[1 - \frac{4n^2}{N^2} \right]^{1.4} \quad (8-30)$$

Now for the center leg, $n = 0$, and therefore Equation (8-30) can be rearranged to give

$$N = \left[\frac{r^{3.8} \Delta P_f \rho}{0.0273 \mu \cdot 2 \dot{W}_{tot}^{1.8}} \right]^{1/3} \quad (8-31)$$

Equation (8-31) permits calculation of the number of legs comprising the heat exchanger, while Equation (8-29) yields the tube diameter. The flow distribution can be calculated from Equations (8-25) and (8-26).

3. Manifold Design

Equations (8-25) and (8-26) yield the desired flow distribution based on the thermal energy input to each leg of the HSHX. It can be seen from Equation (8-30), however, that the pressure drop due to friction will vary greatly for various legs of the heat exchanger; therefore, additional means have to be utilized to obtain the flow distribution specified by Equations (8-25) and (8-26). It would ideally be desirable to achieve proper flow distribution by utilizing the appropriate inlet and outlet manifold design. Due to the unusual distribution of flow that is required, however, it is more realistic to orifice the flow to each leg, with the orifice size for each leg resulting in the desired flow distribution. The inlet and outlet manifold diameters have therefore been set at 3.0 inches, and the orifices are relied upon to yield the desired distribution of flow. The 3.0-inch manifold diameter is large enough so that the manifold pressure drop represents only a small portion of the pressure drop through the HSHX.

Installation

1. Heat Dump System

The heat dump concept with the rectangular HSHX is illustrated in Figure 8.2-23. The large inlet and outlet manifolds are now located on one end of the heat exchanger, and they do not block the view of the heat source when the two side panels are moved down in the heat dump mode. In fact, radiation can occur both from the heat source and from the surfaces of the heat exchangers in the heat dump mode. At the nominal 5-inch separation distance from the source, the maximum source temperature is only 1700°F. A sliding panel was selected, instead of a hinged door, to eliminate interference with the shroud around the vehicle. In operation, the system would be launched with the doors open. After a very short time, the shroud would be ejected, and the temperature of the heat source would climb to 1700°F.

The installation concept for the rectangular HSHX with heat dump capability is shown in Figure 8.2-24. Two sides of the insulation cavity are rectangular panels that slide down and expose the heat source, the four surfaces of the heat exchangers, and the shield insulation surface (the manifolds do not obstruct the view of these surfaces to space in that direction). The equilibrium maximum source temperature under the heat dump condition is approximately 1700°F, which is 150°F to 200°F below that for the circular involute HSHX for the particular geometries analyzed.

2. Heat Leaks

The insulating materials and the thicknesses in this system are identical with those shown in Figure 8.2-11 for the circular HSHX. Assuming a 0°F sink temperature, the magnitude of the heat leaks at various locations in the system are shown in Figure 8.2-25.

Performance

The temperature distribution in HSHX No. 2 was shown in Figure 8.2-21 when HSHX No. 1 is inoperative and the outlet temperature of the Brayton fluid is 1600°F. The maximum source temperature was shown to be around 2020°F.

In a manner similar to that utilized for the involute HSHX, the maximum heat-source temperature can be reduced either by relaxing the requirement of full output power from PCM No. 2 or by increasing the wall thickness of the tubes of the HSHX.

Figure 8.2-26 shows the reduction in the maximum effective source temperature as a result of the reduction in the Brayton fluid outlet temperature in HSHX No. 2. Using this figure and Figure 8.2-19 one can conclude that a reduction of 20°F in the source temperature results in a reduction of about 5 percent in the electrical power output from PCM No. 2.

A reduction in the maximum source temperature also can be obtained at the expense of increased HSHX weight. Figure 8.2-27 which has been obtained for the rectangular HSHX, shows the penalty in HSHX weight as a function of the reduction in the source temperature.

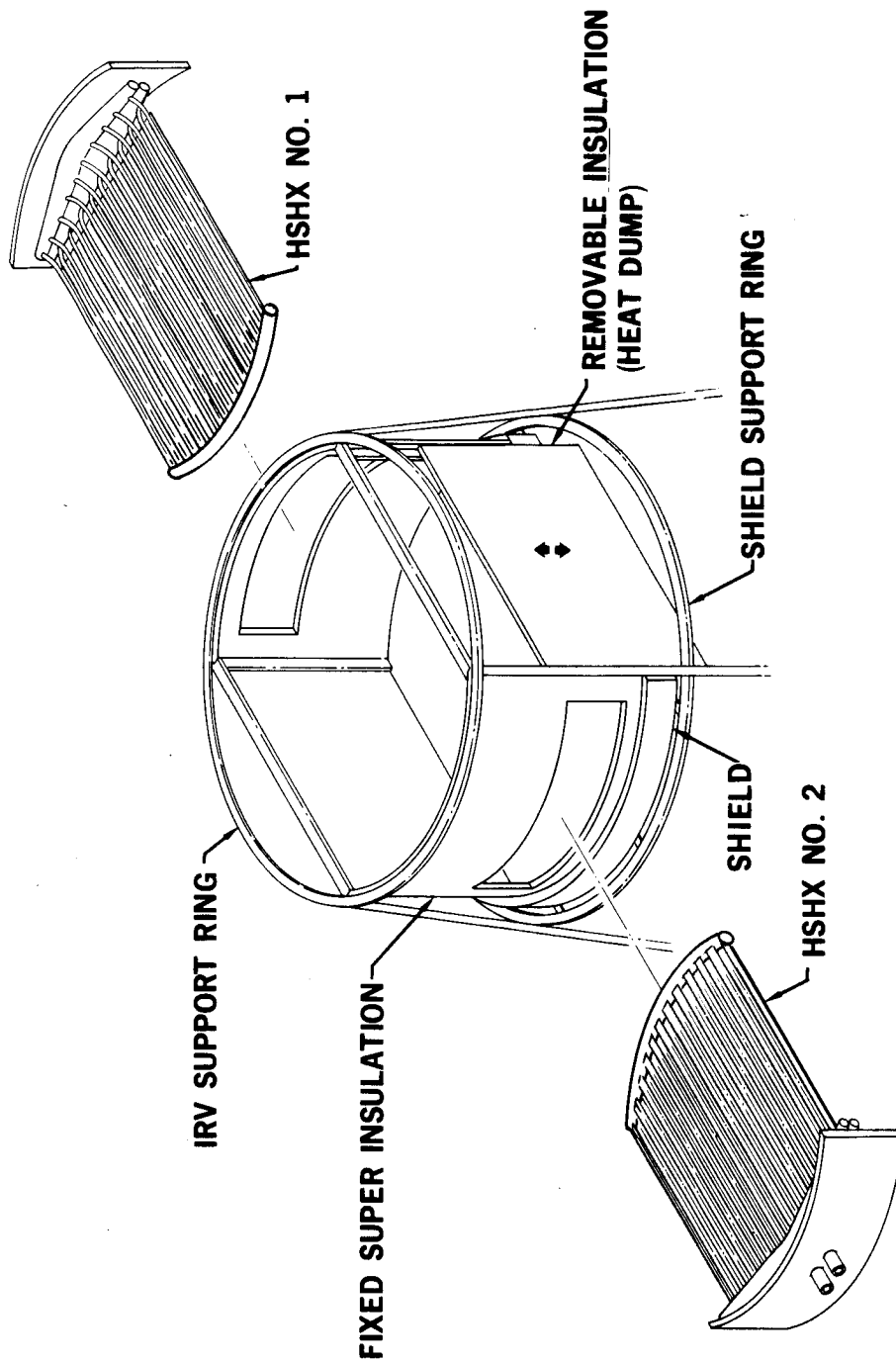
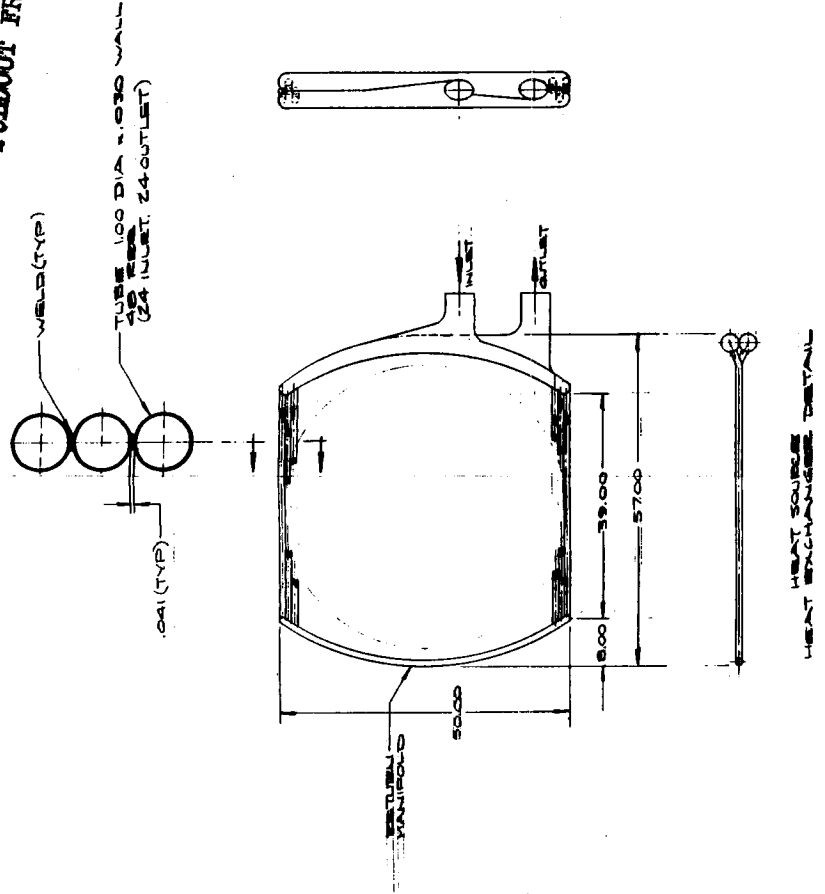


Figure 8.2-23 RECTANGULAR HEAT-SOURCE HEAT EXCHANGER-HEAT DUMP CONCEPT

FOLDOUT FRAME 2



FOLDOUT FRAME 1

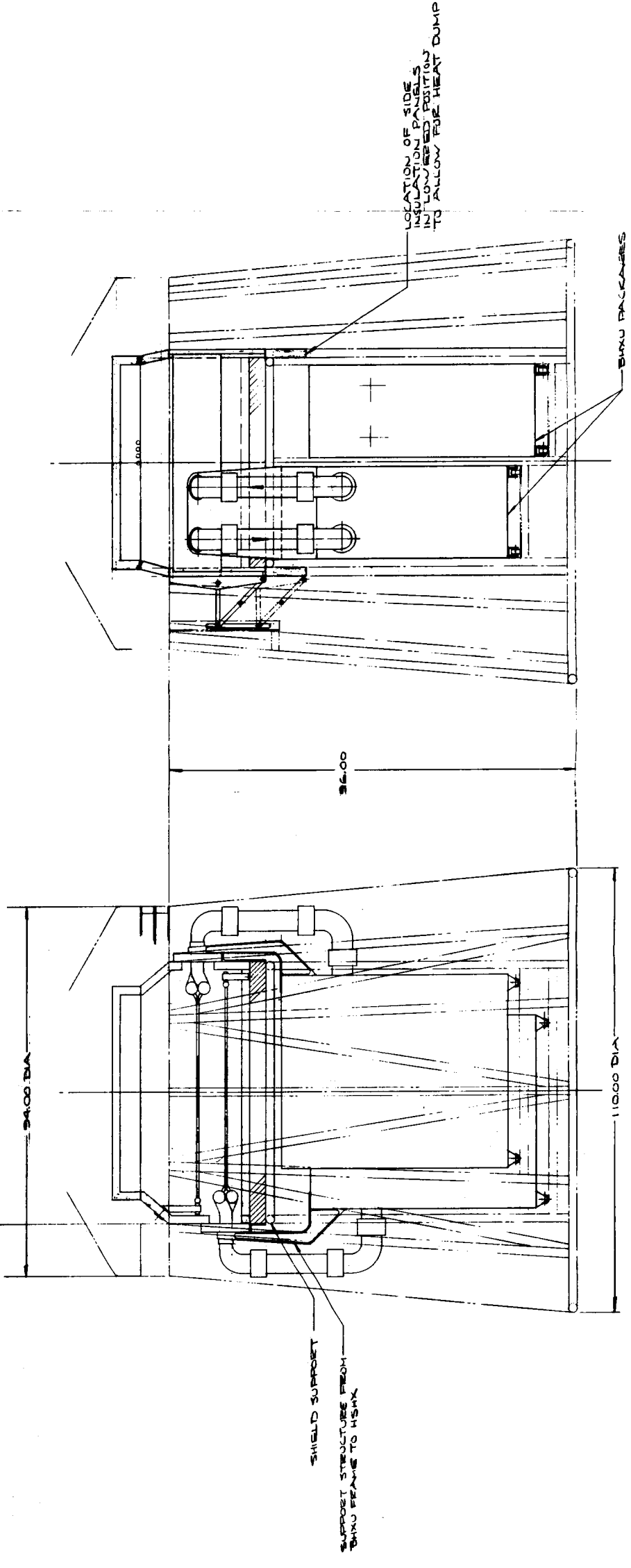
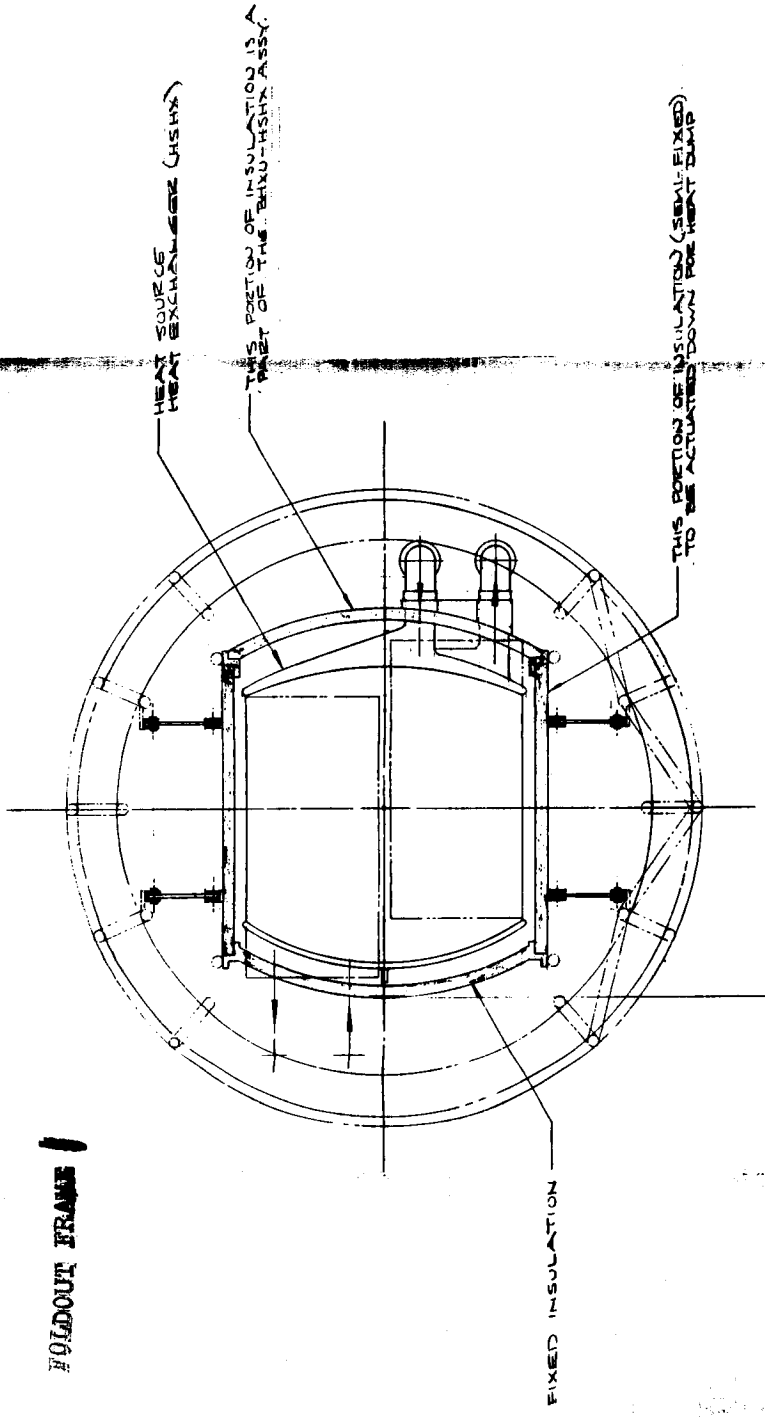
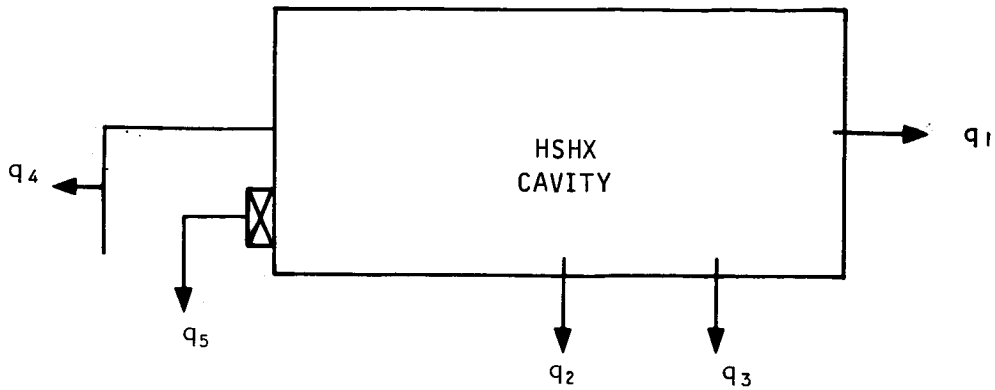


Figure 8.2-24 CIRCULAR PLANAR SOURCE -- RECTANGULAR HEAT EXCHANGER (HEAT DUMP SYSTEM)



q_1 = heat loss from side walls of HSHX cavity in watts

q_2 = heat loss from bottom surface of HSHX cavity in watts

q_3 = heat loss from aft support in watts

q_4 = heat loss from inlet and outlet ducts in watts

q_5 = heat loss from mounting brackets in watts

System	$q_1 + q_2$	q_3	q_4	q_5	Total
Fixed insulation system (no heat dump)	220	51	404	212	887
Heat dump system	258	51	404	212	945

Figure 8.2-25 HEAT LEAKS

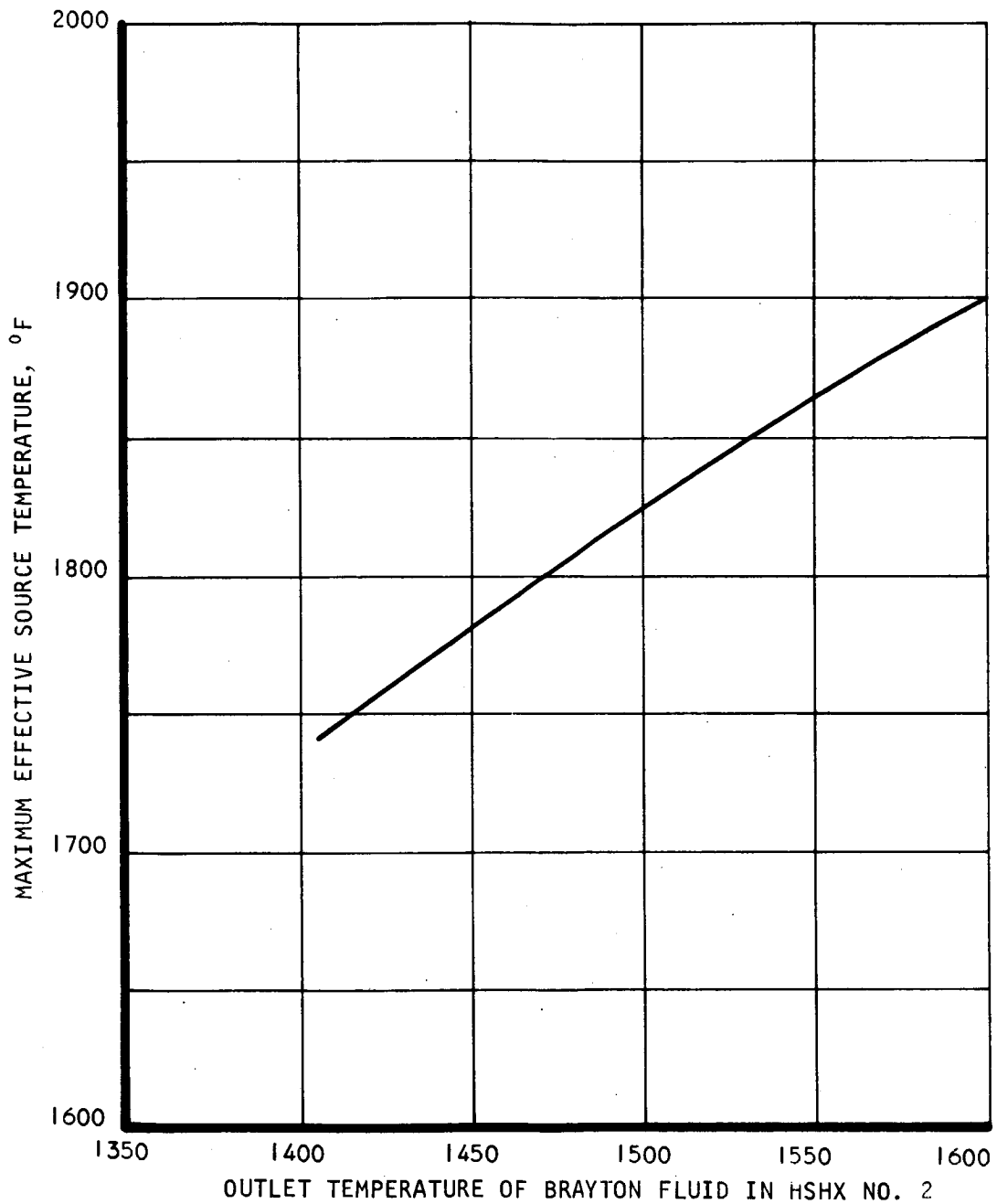


Figure 8.2-26 BRAYTON FLUID OUTLET TEMPERATURE VERSUS EFFECTIVE SOURCE TEMPERATURE (RECTANGULAR GEOMETRY)

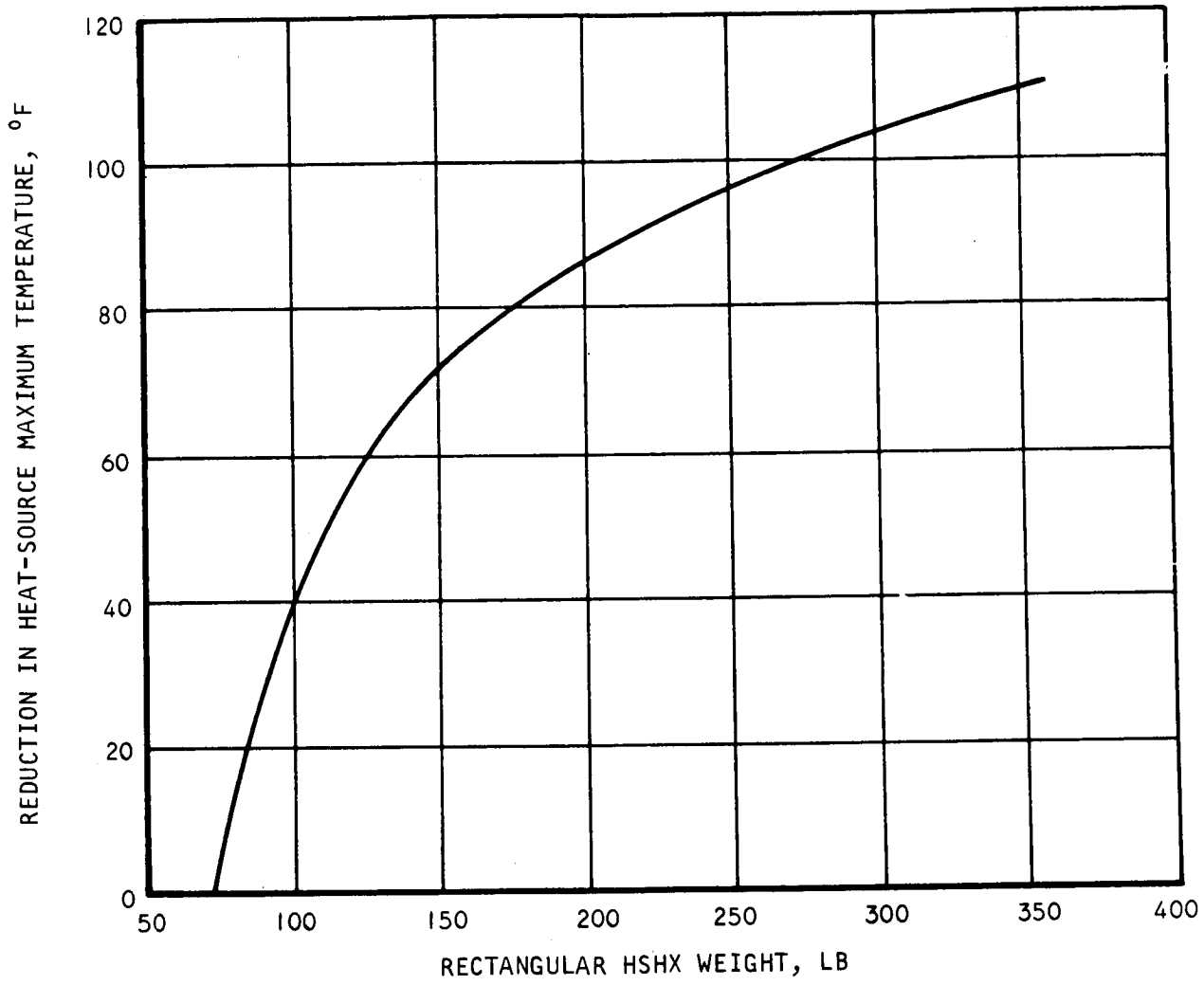


Figure 8.2-27 HEAT-SOURCE TEMPERATURE REDUCTION VERSUS HEAT-SOURCE HEAT EXCHANGER WEIGHT FOR RECTANGULAR GEOMETRY

8.2.2 Pin Cushion Heat-Source Array

8.2.2.1 Source Description

The pin cushion heat source is a 39-inch-diameter cylindrical unit made up of 13 parallel rows of axially mounted fuel capsules. The rows of fuel capsules form cords of different lengths on the circular source plate. A cross section of a typical fuel capsule is shown in Figure 8.2-28 which also shows the temperature distribution around the capsule and in one of its adjoining auxiliary coolant heat exchanger (ACHX) passages. In this design, there is no coverplate between the fuel capsule and the HSHX; consequently, the difference between the maximum capsule temperature and the effective source temperature is only 70°F.

The HSHX design for this system represented a significant departure from the HSHX approach developed in the Phase IA studies. Figure 8.2-29 shows the design approaches used for the HSHX's for the Phase IA and Phase IB pin cushion heat sources.

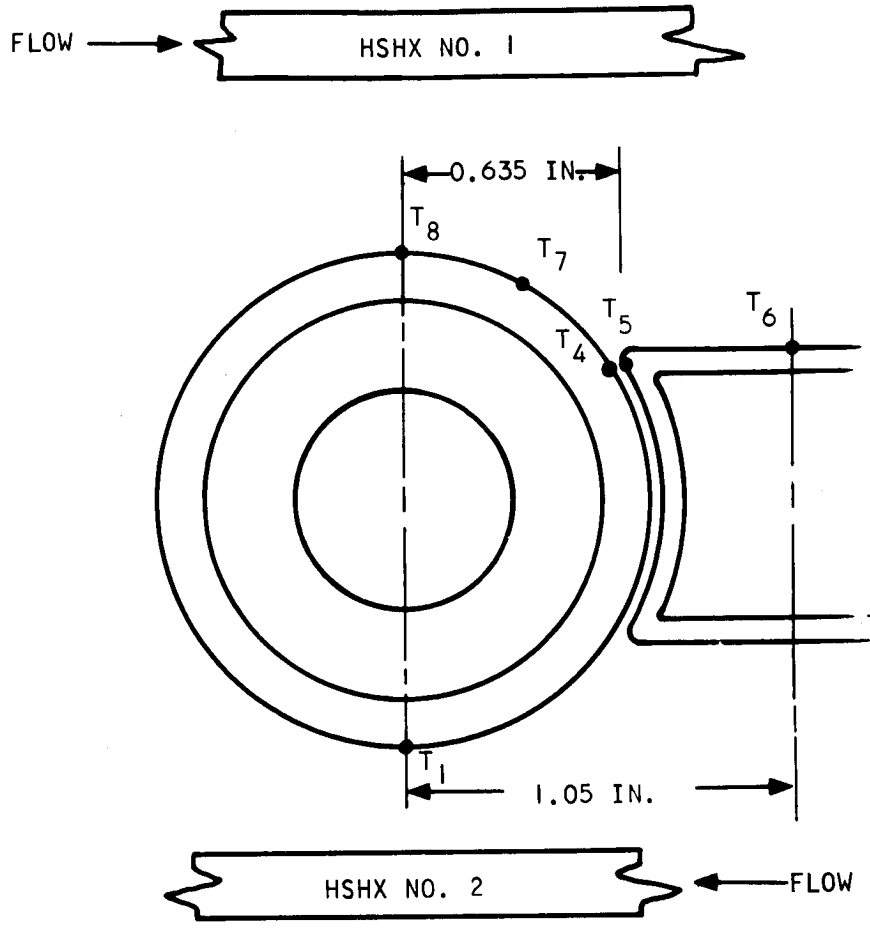
In the Phase IA configuration, heat was extracted from both sides of the fuel capsules, and two heat exchanger legs were placed between each row of capsules. In an effort to reduce the source diameter to a minimum, however, the Phase IB configuration shown in Figure 8.2-29 was adopted. This configuration has a single heat exchanger leg between each fuel capsule row. A single leg picks up heat from two rows of fuel capsules. HSHX No. 1 and HSHX No. 2 are offset in a horizontal plane and occupy the space between alternate rows of fuel capsules. The spacing of the rows of fuel capsules is set by the OD of the HSHX tubes plus a clearance of 0.5 inch.

8.2.2.2 Heat-Source Heat Exchanger Design

Description

The general arrangement of the HSHX and the rows of fuel capsules is shown in Figure 8.2-30 and the arrangement of the two HSHX's and the heat source array is shown in Figure 8.2-31. The heat exchanger legs are inserted between alternate rows of fuel capsules, and each leg is heated by two rows of fuel capsules. Figure 8.2-30 presents pertinent design data for the HSHX; the weight of the HSHX is 39 pounds. The number of tubes and the lengths and diameters of the tubes vary in the different sections of the heat exchangers. Both HSHX No. 1 and HSHX No. 2 include seven banks of tubes. Because of the alternate spacing of sections of each HSHX between the rows of capsules, operation of either HSHX No. 1 or HSHX No. 2 is equivalent from the standpoint of heat transfer and heat-source operating temperature. The HSHX layout is shown in Figure 8.2-32.

The active heat transfer portion of the HSHX consists of banks of tubes that are inserted between the rows of isotope fuel capsules. Brayton fluid flows along the primary inlet manifold and through the secondary inlet manifolds to the tube banks. The fluid enters alternate tubes and flows the length of the isotope fuel capsule rows. It then enters a tubular header, executes a 180-degree turn, re-enters the active portion of the heat exchanger through the adjacent tubes, and flows back along the rows of isotope fuel capsules. It then exits from the HSHX via the secondary and primary outlet manifolds.



$T_{MAX} - T_1$		$T_6 - T_1 = 81^{\circ}F$
$T_4 - T_1$	$51^{\circ}F$	$T_7 - T_1 = 60^{\circ}F$
$T_5 - T_1$	$72^{\circ}F$	$T_8 - T_1 = 70^{\circ}F$
CALCULATION BASED ON $T_{MAX} = 2000^{\circ}F$		

Figure 8.2-28 FUEL CAPSULE TEMPERATURE GRADIENT IN A VERTICAL PIN CUSHION ARRAY

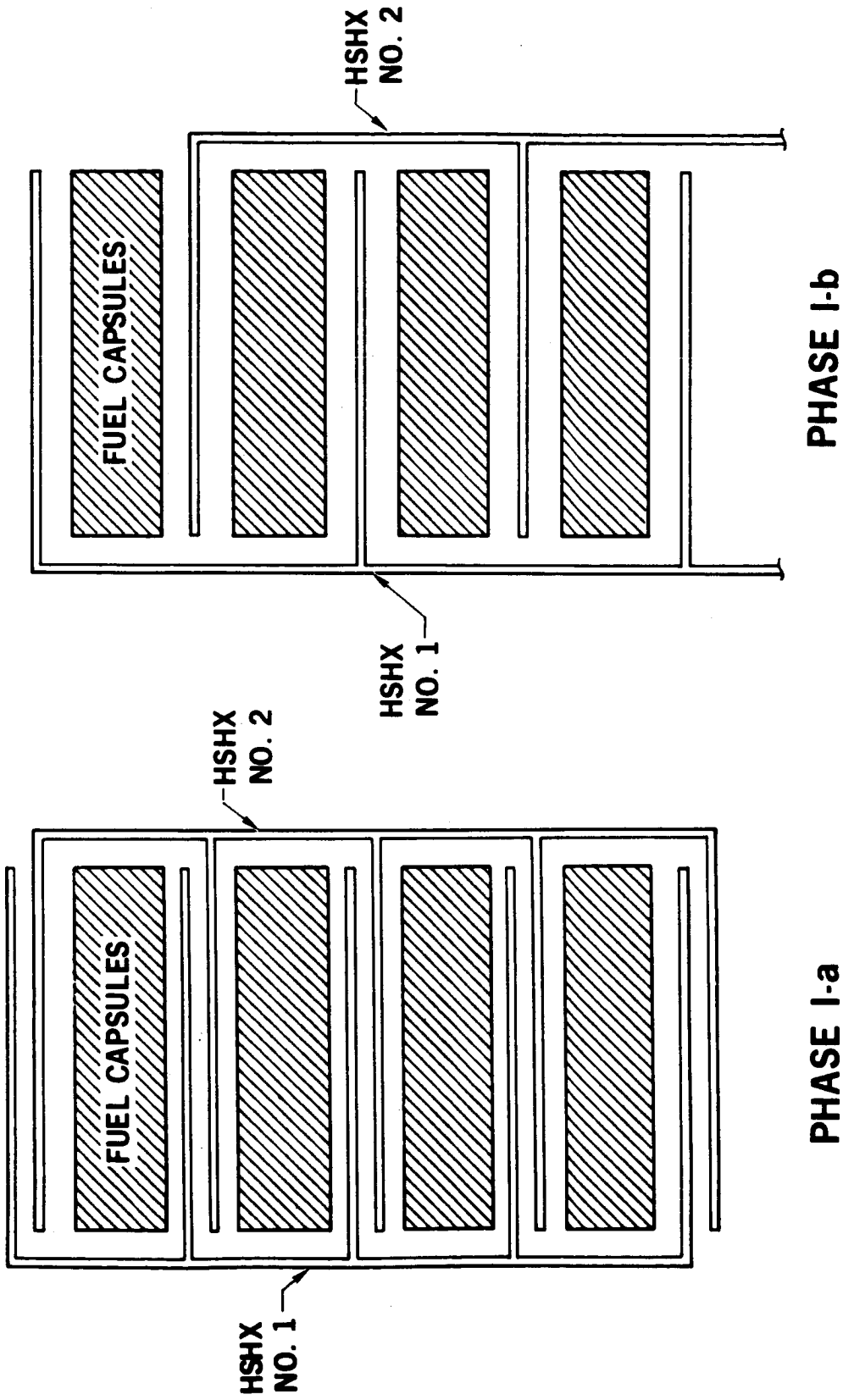
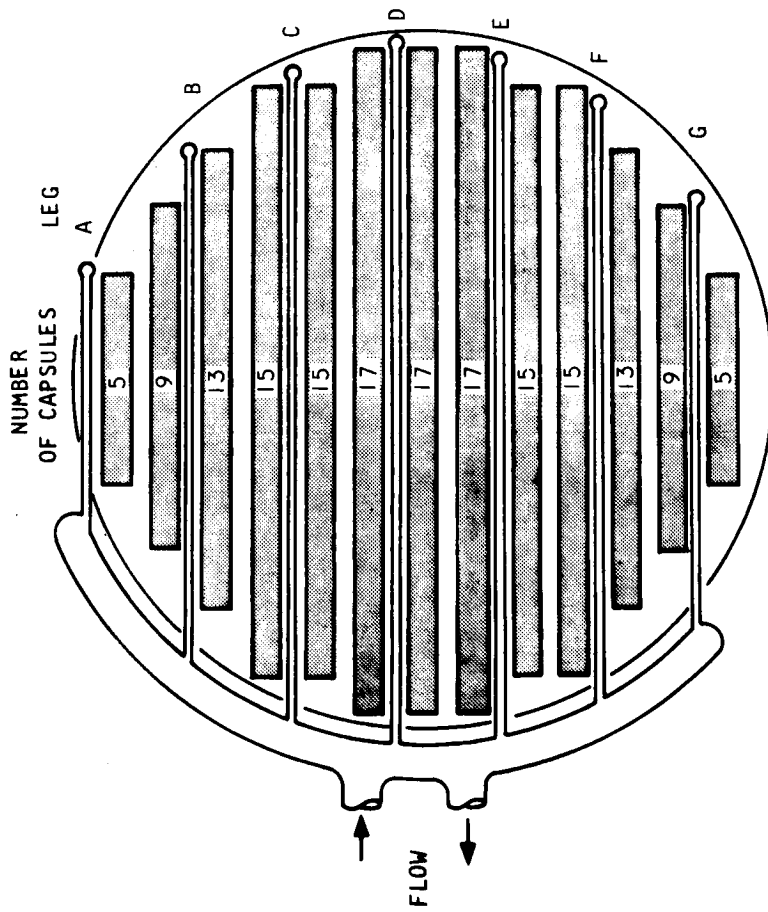


Figure 8.2-29 PIN CUSHION HEAT-SOURCE HEAT EXCHANGER APPROACHES



LEG ▼	W (#/SEC)	NUMBER OF TUBES	TUBE DIAMETER (INCHES)	LENGTH (INCHES)
A	0.0285	16	0.297	18
B	0.1254	8	0.594	28
C	0.1710	4	1.06	34
D	0.1938	4	1.123	36
E	0.1825	4	1.08	34
F	0.1595	6	0.871	27
G	0.0798	10	0.491	15

HEIGHT OF EACH
LEG = 5.5 IN.

Figure 8.2-30 PIN CUSHION HEAT-SOURCE HEAT EXCHANGER (39-INCH-DIAMETER SOURCE)

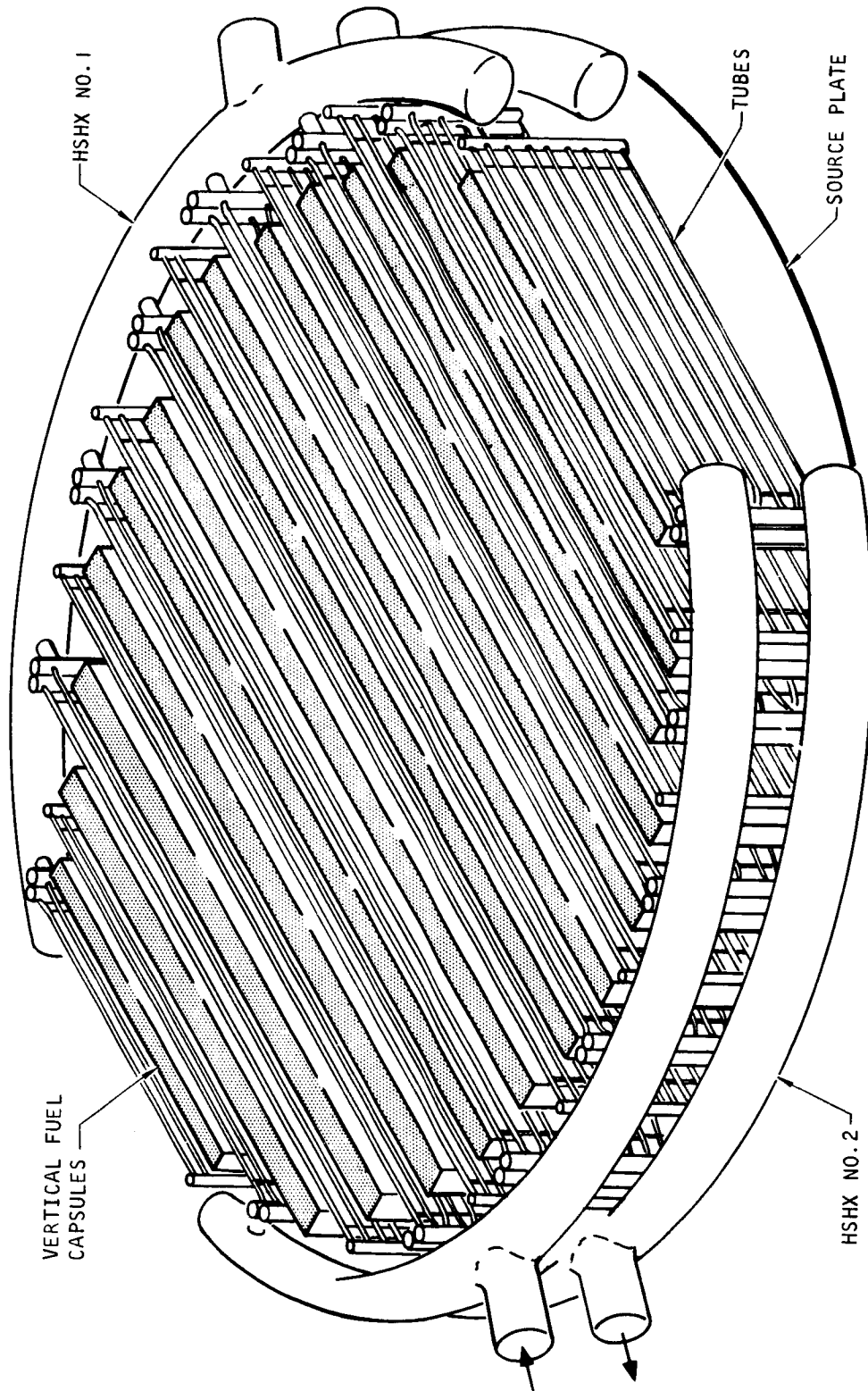


Figure 8.2-31 PIN CUSHION HEAT-SOURCE HEAT EXCHANGER

FOLDOUT FRAME 1

FOLDOUT FRAME 2

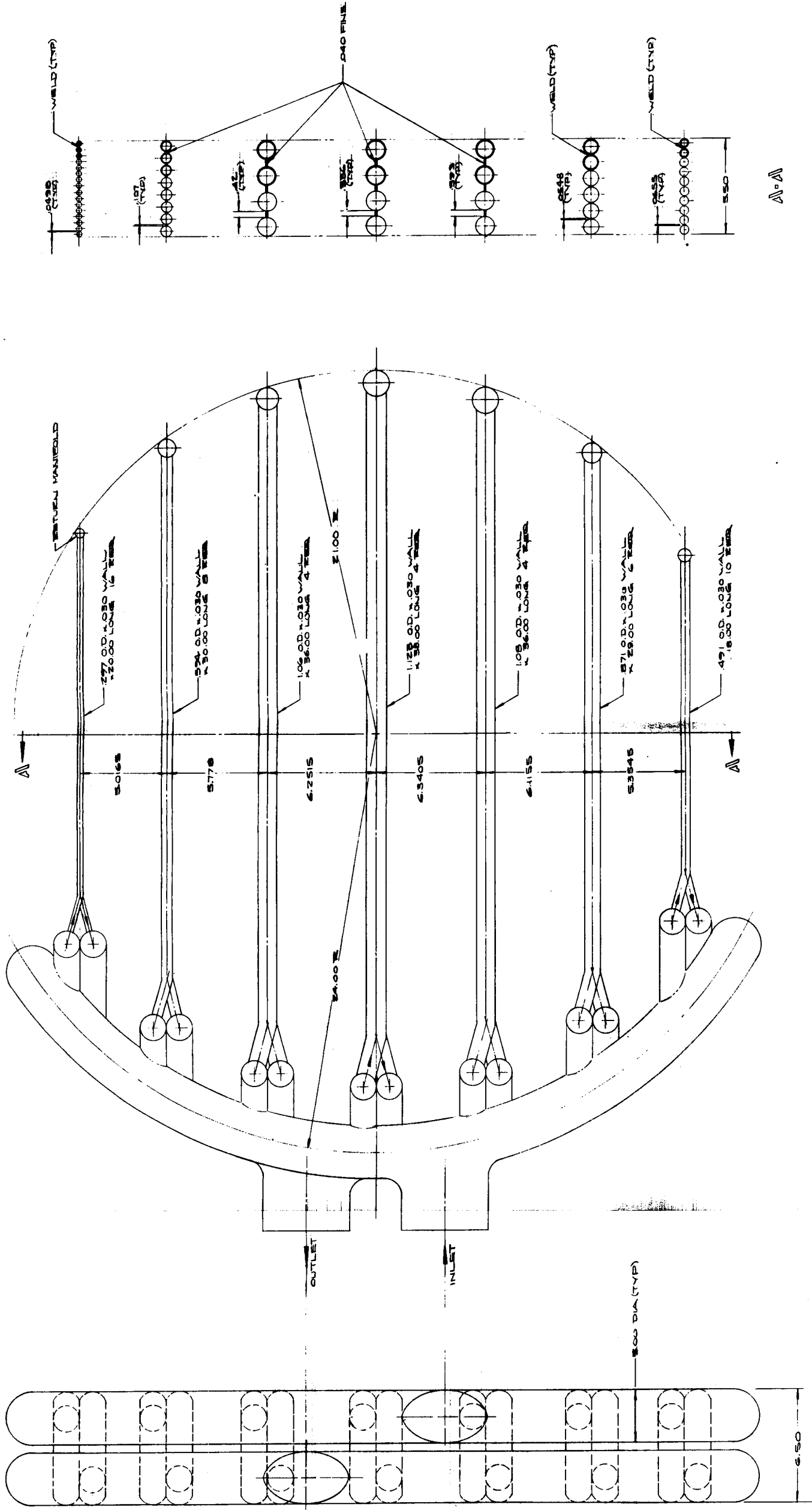


Figure 8.2-32 LAYOUT -- HEAT EXCHANGER, VERTICAL PIN CUSHION

Design Analysis

1. Thermal Design

Figure 8.2-33 shows the distribution of the wall temperature and the effective and maximum source temperature for a pin cushion heat-source array. This system is characterized by a lower maximum source temperature (1790°F) because of 1) the absence of a second radiation gap and 2) the absence of conduction temperature drop in the inactive HSHX. Moreover, the maximum capsule temperature is only 70°F above the effective source radiating temperature instead of the 120°F difference that occurs in the involute-tube design. The heat-source temperature distribution remains the same whether HSHX No. 1 or HSHX No. 2 is active.

2. Pressure Drop

The desired distribution of fluid among the various sections of the HSHX is determined by the thermal input from the rows of isotope fuel capsules. Utilizing the flow values given in Figure 8.2-30 each section of the HSHX was designed to yield a specified pressure drop, in a manner similar to that outlined for the involute and rectangular HSHX's.

3. Manifold Design

Because of the complicated flow arrangement involving both primary and secondary distribution manifolds, it may be necessary to incorporate orifices to obtain proper pressure profiles in the manifolds. This possibility was not studied in detail during this phase of the design study effort.

8.2.2.3 Installation

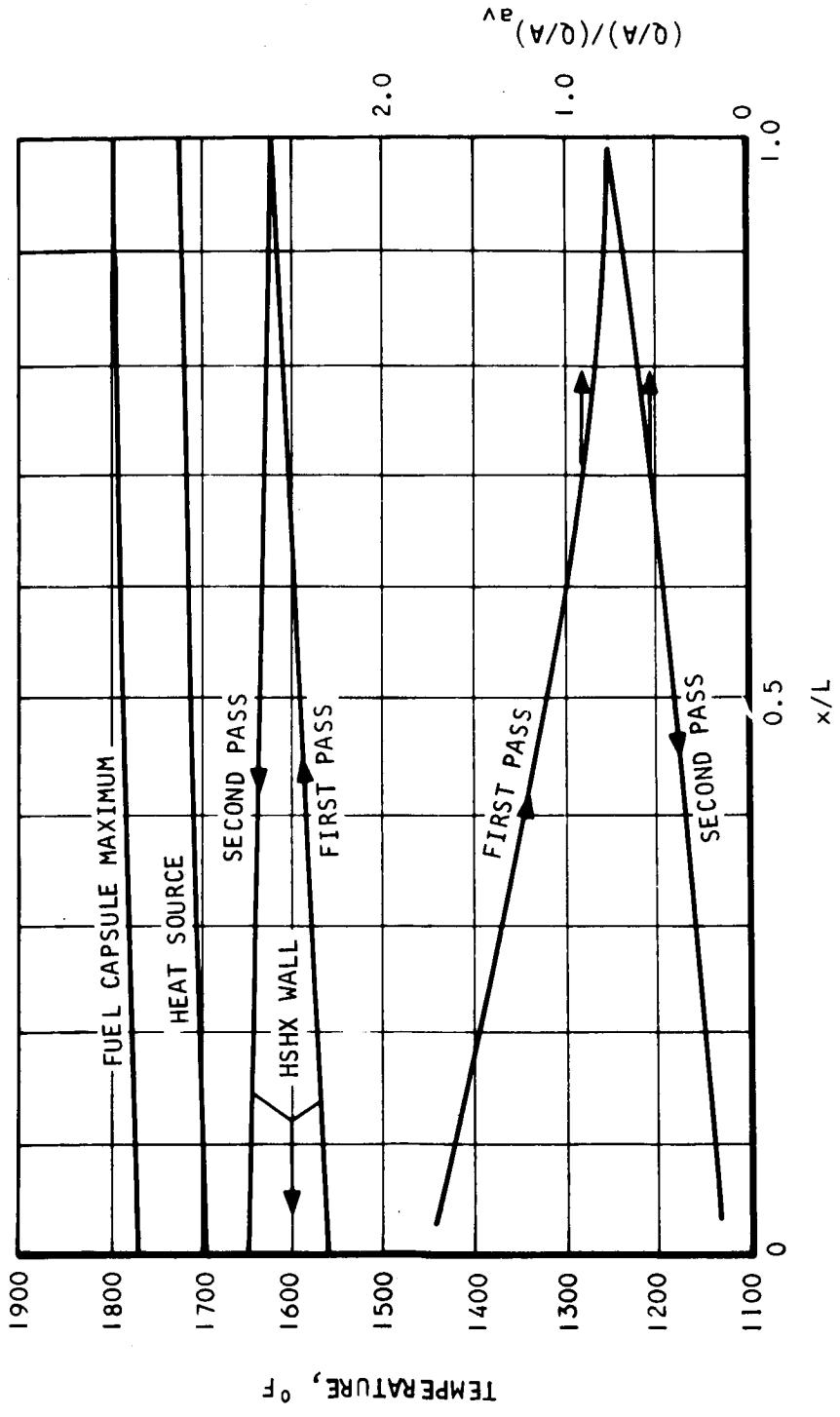
The vehicle installation of the pin cushion HSHX is shown in Drawing 8.2-34. Comparison of the concept shown on this drawing with the other concepts reveals that this is a considerably more compact arrangement. In this design, the PCM's are displaced in the horizontal plane rather than in the vertical to allow the HSHX legs to fit down between the rows of fuel capsules. This installation concept may place some restrictions on the back side of the IRV because of the proximity of the HSHX ducts to the IRV. This aspect of the problem has not been fully explored for this configuration.

The insulating materials and thicknesses are identical to those shown in Figure 8.2-11 for the 49-inch circular HSHX. The heat leaks at various locations in the system are listed in Figure 8.2-35. The total heat loss is estimated to be 823 watts.

8.2.3 Planar Circular Heat-Source Array (Vented Capsule)

8.2.3.1 Source Description

The vented capsule heat source consists of 164 fuel capsules arrayed on a 39-inch-diameter source plate. A scalloped coverplate is employed to hold the fuel capsules to the source plate. A cross section of a typical fuel capsule, indicating the temperature distributions, is shown in Figure 8.2-36. For the design of the HSHX's, the effective radiating temperature is taken as the minimum source surface temperature.



A-34490

Figure 8.2-33 TEMPERATURE DISTRIBUTIONS IN PIN CUSHION HEAT-SOURCE HEAT EXCHANGER

FOLDOUT FRAME 1

FOLDOUT FRAME 2

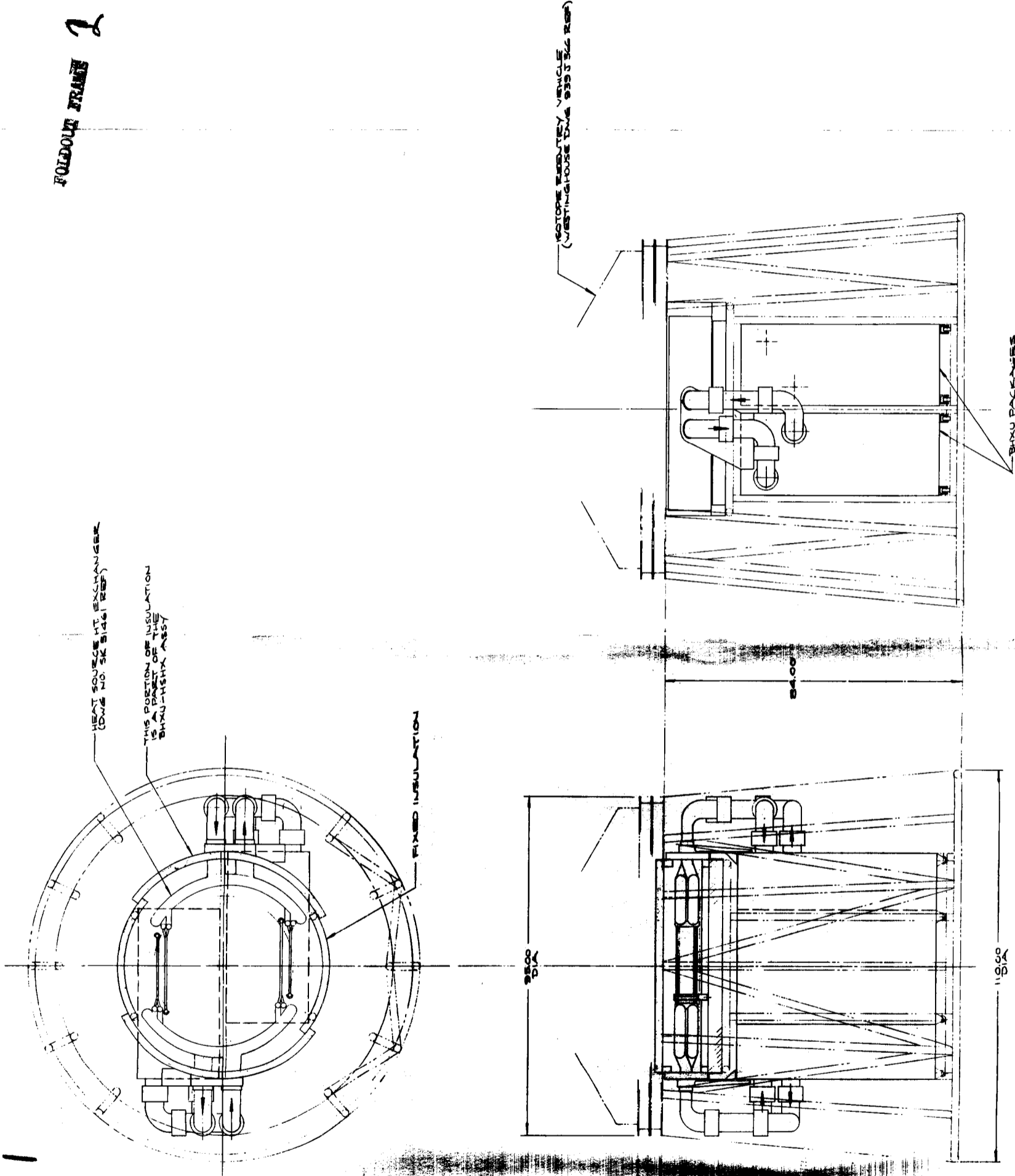
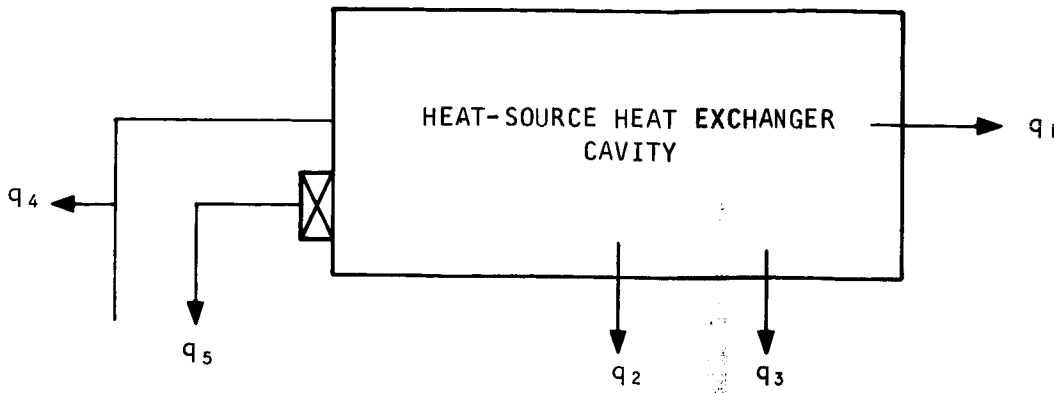


Figure 8.2-34 PIN CUSHION SOURCE -- TUBE-FIN HEAT EXCHANGER



q_1 = heat loss from sidewalls of HSHX cavity in watts

q_2 = heat loss from base of HSHX cavity in watts

q_3 = heat loss from aft support in watts

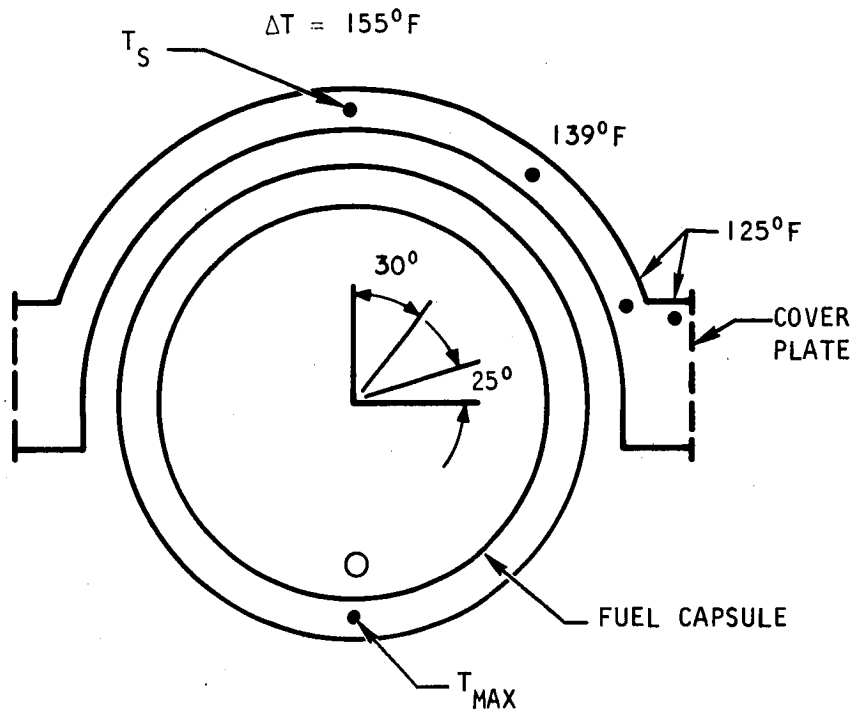
q_4 = heat loss from inlet and outlet ducts in watts

q_5 = heat loss from mounting brackets in watts

System	$q_1 + q_2$	q_3	q_4	q_5	Total
Fixed insulation system	210	61	371	181	907

Figure 8.2-35 HEAT LEAKS FOR PIN CUSHION SYSTEM

HSHX NO. 1



CAPSULE DIAMETER = 1.4 IN.
 COVER THICKNESS = 0.060 IN.
 SPACING = 1.6 IN.

A-34841

$$T_S = T_{MAX} - \Delta T$$

T_S = SOURCE SURFACE TEMPERATURE

CALCULATION BASED ON $T_{MAX} = 2000^\circ\text{F}$

T_{MAX} = MAXIMUM FUEL CAPSULE TEMPERATURE

Figure 8.2-36 TEMPERATURE GRADIENT AROUND VENTED CAPSULE (CIRCULAR PLANAR HEAT SOURCE)

8.2.3.2 Involute Tubular Heat-Source Heat Exchanger

Description

Figure 8.2-37 shows the HSHX for the 46-inch-diameter heat source. The design of this HSHX is essentially equivalent to the involute HSHX that is employed for the 49-inch-diameter heat source that utilizes nonvented isotope fuel capsules. The tube diameter and spacing is identical, as is the cross section of both the inlet and outlet manifolds. The only difference between the two designs is that the diameter of the active portion of the former is 49 inches while for the latter it is 46 inches. The smaller heat exchanger has a slightly lower pressure drop than the larger, but it is not enough to warrant a redesign. The weight of this heat exchanger is 79 pounds.

Installation and Heat Leaks

The installation of the HSHX-BHXU with the IRV system is shown in Figure 8.2-38. The heat dump system approach, described in Section 8.2.1 for the 49-inch system, is used in this case. The main areas to be insulated are the heat exchanger cavity, the inlet and outlet ducts to both heat exchangers, and the structural supports to the heat exchangers. The thicknesses of the insulating materials are the same as those shown in Figure 8.2-11. The magnitudes of the heat leaks at various locations in the system are listed in Figure 8.2-39.

Performance

The design of the HSHX's was carried out in the same way described in the previous sections. The thermal analysis resulted in the temperature and heat flux distributions presented in Figures 8.2-40 and 8.2-41. Figure 8.2-40 shows the fluid temperature, wall temperature, and heat flux profiles in HSHX No. 2 when HSHX No. 2 is in operation and full output power is required from PCM No. 2. Figure 8.2-41 shows the effective and maximum source temperatures when either HSHX No. 2 or HSHX No. 1 is in operation. In both cases, full output power is assumed to be required, i.e., outlet gas temperature from the HSHX in operation is 1600°F. For the case with HSHX No. 2 in operation, the maximum source temperature is 2115°F which is 55°F higher than the maximum for the 49-inch system.

This increase in source temperature is due to the decrease in the heat source and in the HSHX areas and to the increase in the temperature drop in the fuel capsules. For the case when HSHX No. 1 is in operation, Figure 8.2-41 shows that the maximum source temperature is considerably lower than 2000°F.

Figure 8.2-42 shows the maximum effective radiation temperatures as a function of diameter for circular sources with a matching involute HSHX. The top curve is for full output power on the HSHX No. 2, and the bottom curve is for full output power on the HSHX No. 1. To obtain the maximum fuel capsule temperatures, the temperature drop in the fuel capsules (ΔT) must be added to these curves. This ΔT also increases as the diameter gets smaller; it is 120°F at 49 inches and 155°F at 46 inches. Decreasing the diameter below 50 inches results in a significant power drop of HSHX No. 2, but considerable reduction below 45 inches is possible with HSHX No. 1 yielding full power output.

FOLDOUT FRAME 1

FOLDOUT FRAME 2

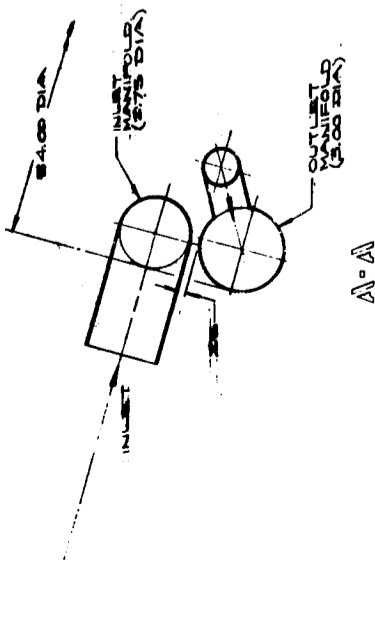
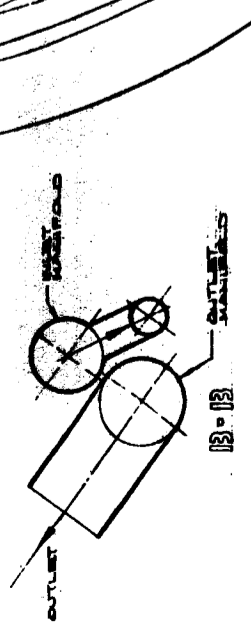
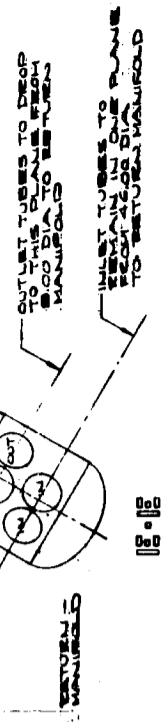
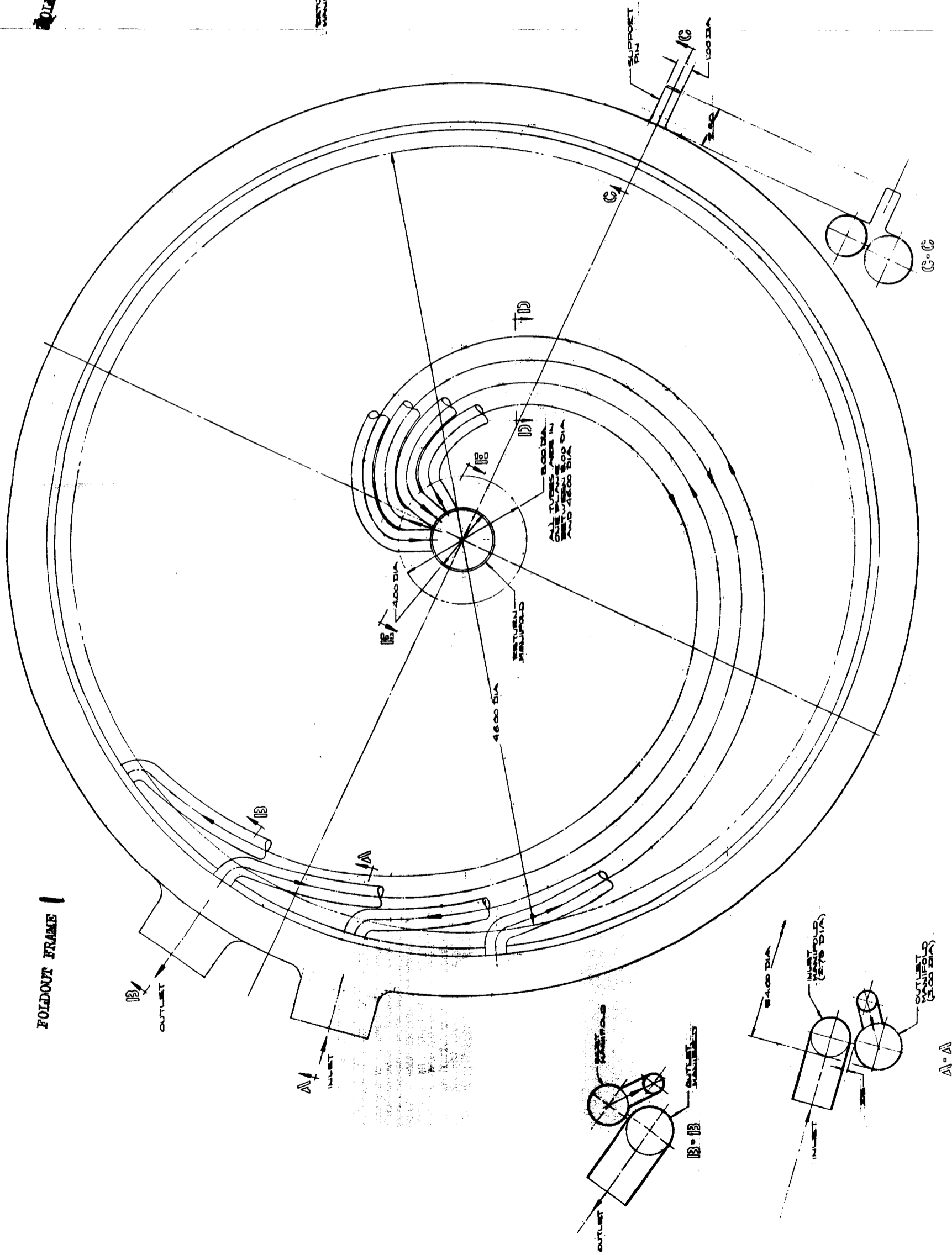


Figure 8.2-37 LAYOUT -- HEAT EXCHANGER INVOLUTE (46-INCH-DIAMETER)

FOLDOUT FRAME

FOLDOUT FRAME 2

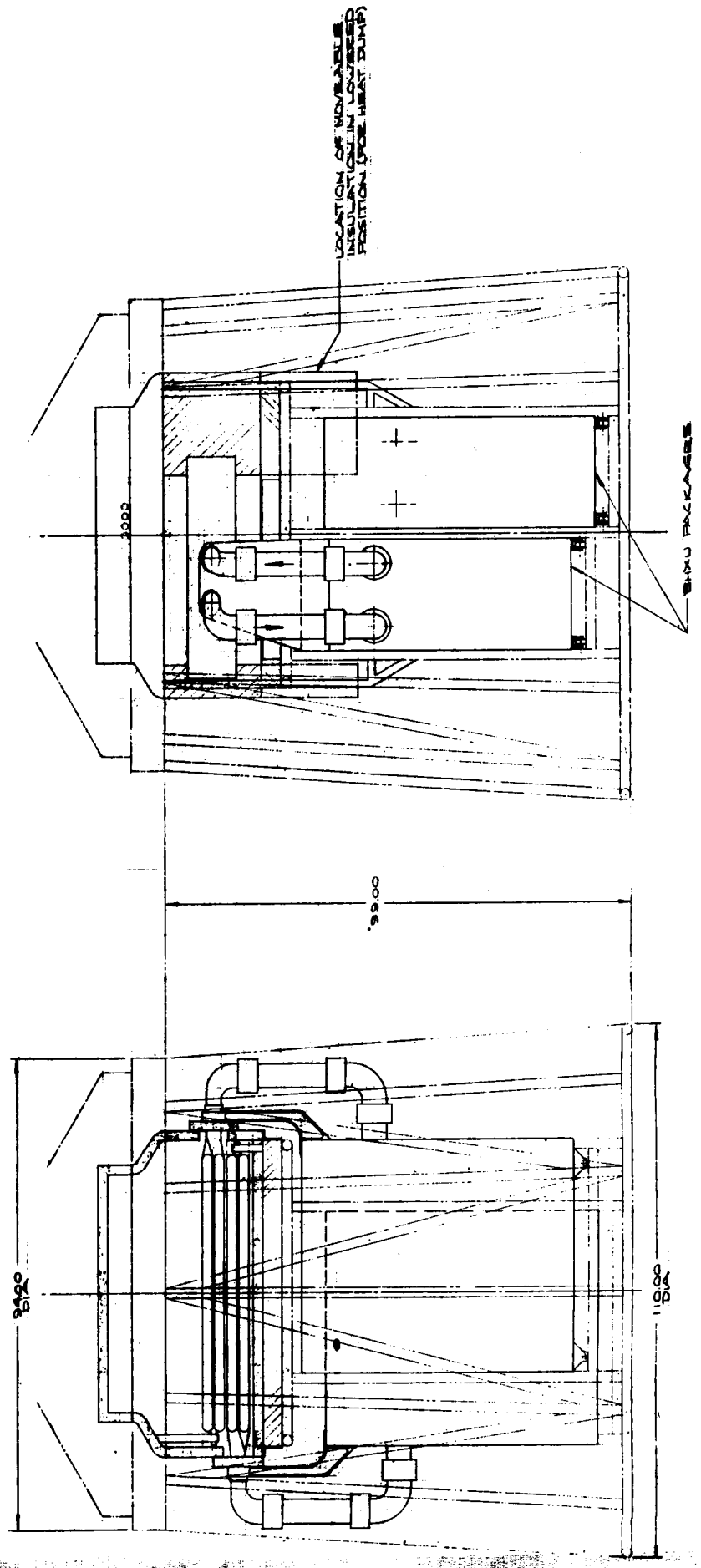
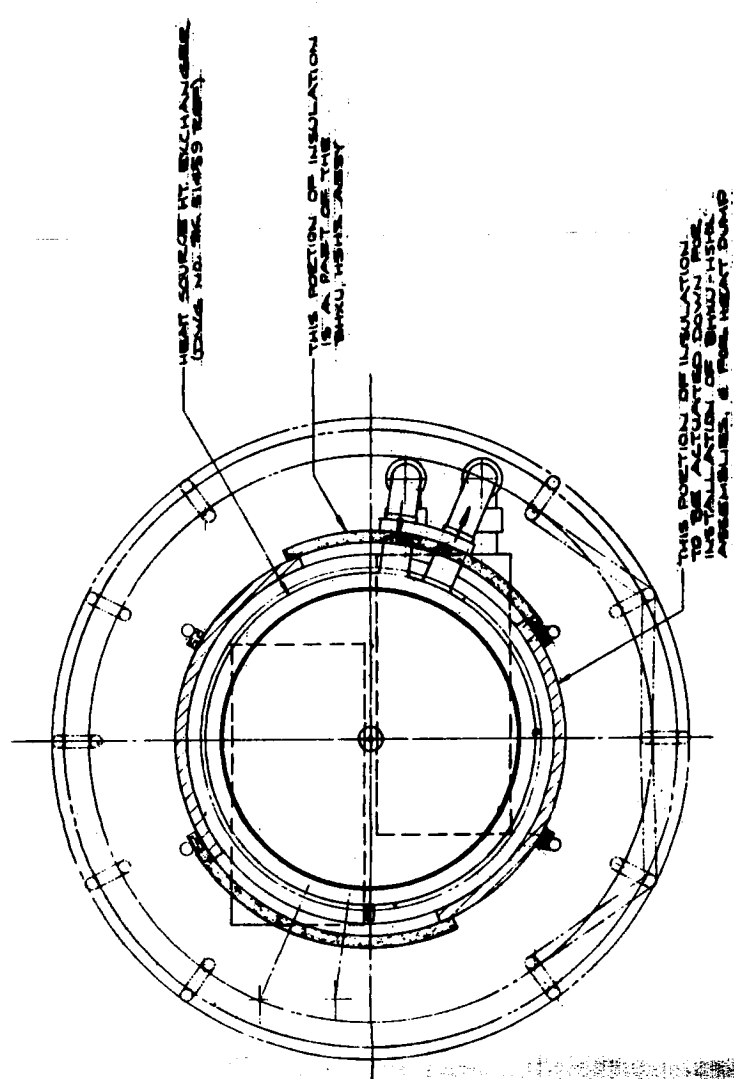
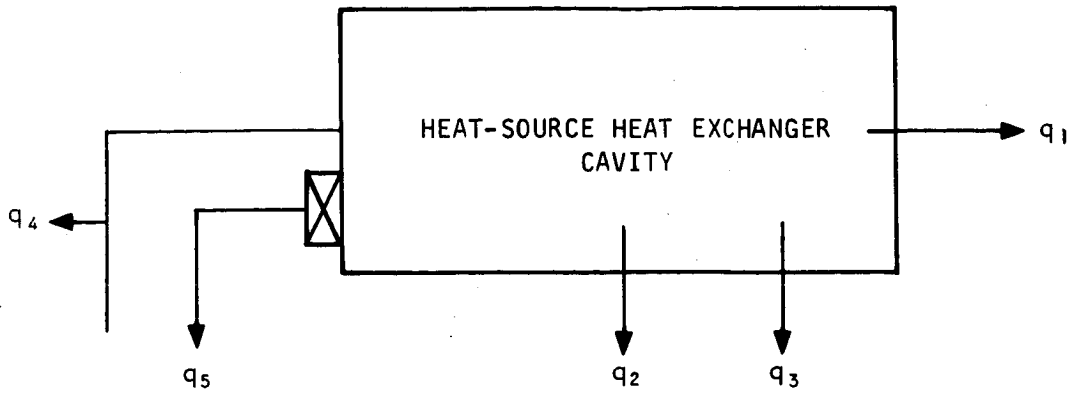


Figure 8.2-38 CIRCULAR PLANAR SOURCE -- INVOLUTE TUBE HEAT EXCHANGER (46-INCH-DIAMETER) (HEAT DUMP SYSTEM)



q_1 = heat loss from sidewalls of HSHX cavity in watts

q_2 = heat loss from base of HSHX cavity in watts

q_3 = heat loss from aft support in watts

q_4 = heat loss from inlet and outlet ducts in watts

q_5 = heat loss from mounting brackets in watts

System	$q_1 + q_2$	q_3	q_4	q_5	Total
Fixed insulation system (no heat dump)	240	61	404	202	907
Heat dump system	304	61	404	202	971

Figure 8.2-39 HEAT LEAKS -- CIRCULAR PLANAR HEAT SOURCE (VENTED CAPSULES)

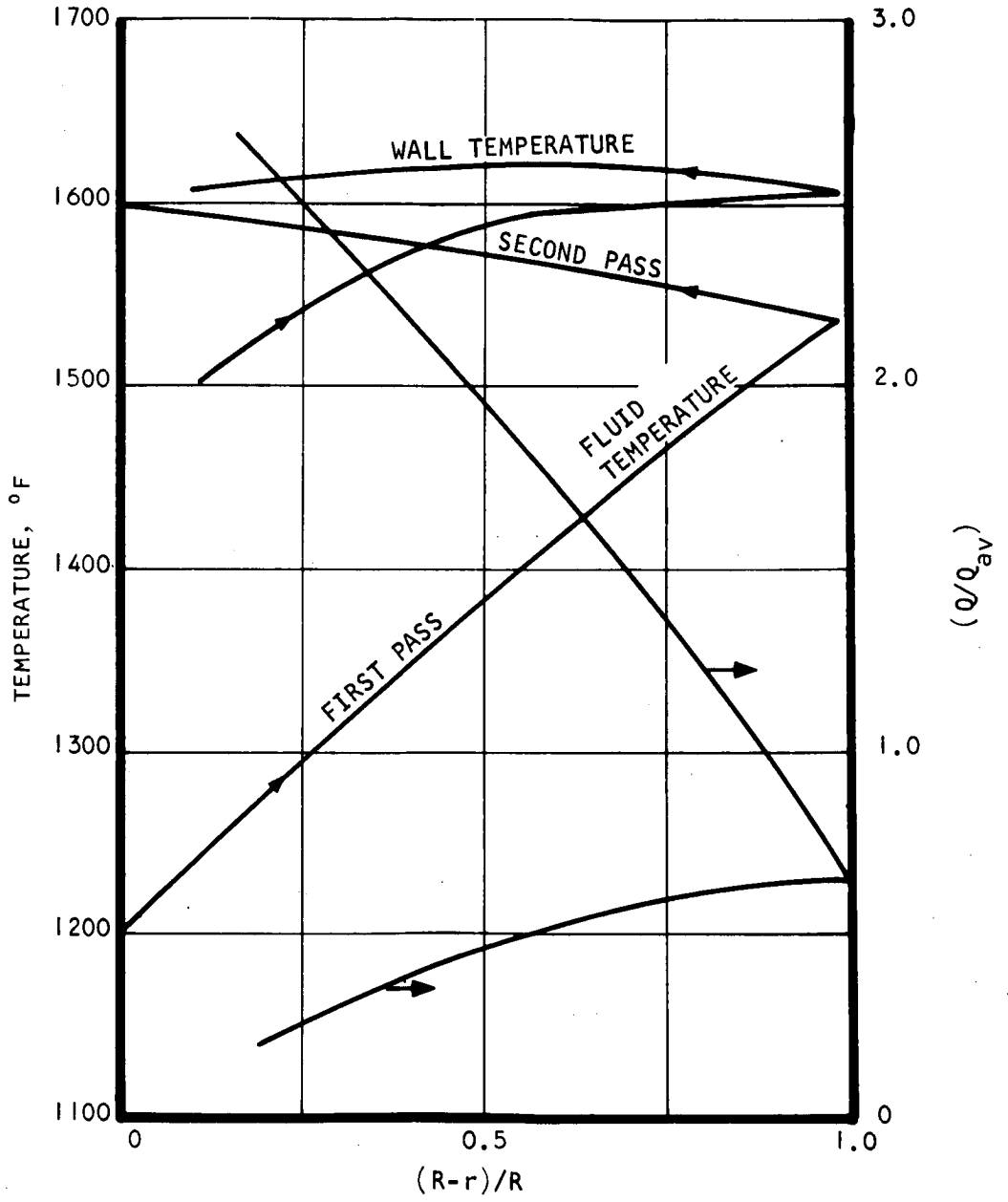
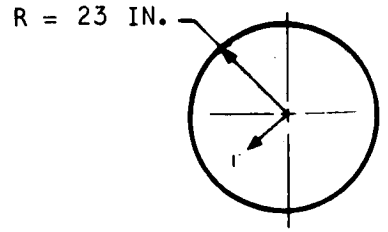
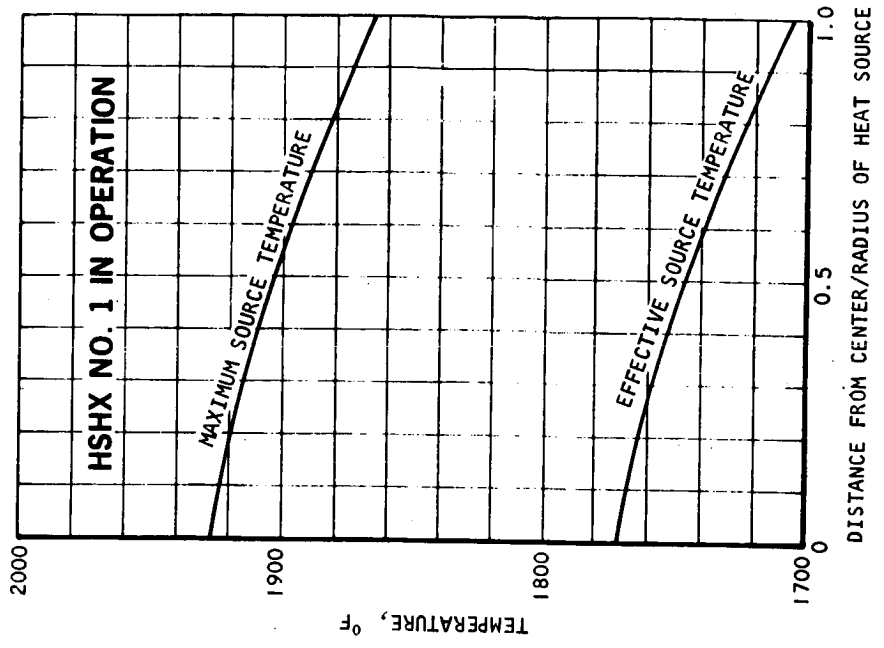


Figure 8.2-40 TEMPERATURE AND HEAT FLUX DISTRIBUTIONS IN HSHX NO. 2 -- PLANAR CIRCULAR SOURCE (VENTED CAPSULE)



A-34491

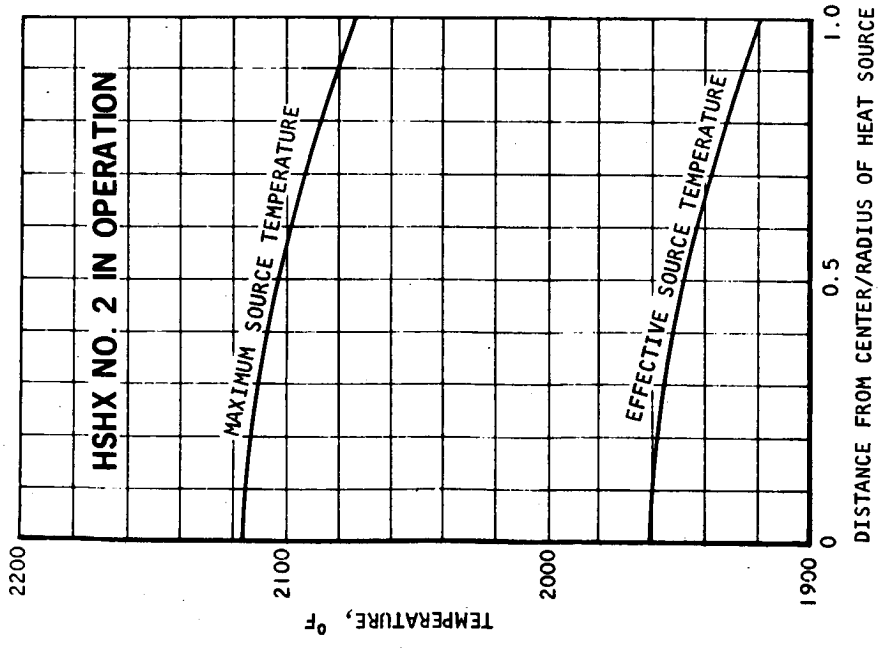


Figure 8.2-4I INVOLUTE-TUBE CIRCULAR HEAT-SOURCE HEAT EXCHANGER (VENTED CAPSULE) (46-INCH-DIAMETER)

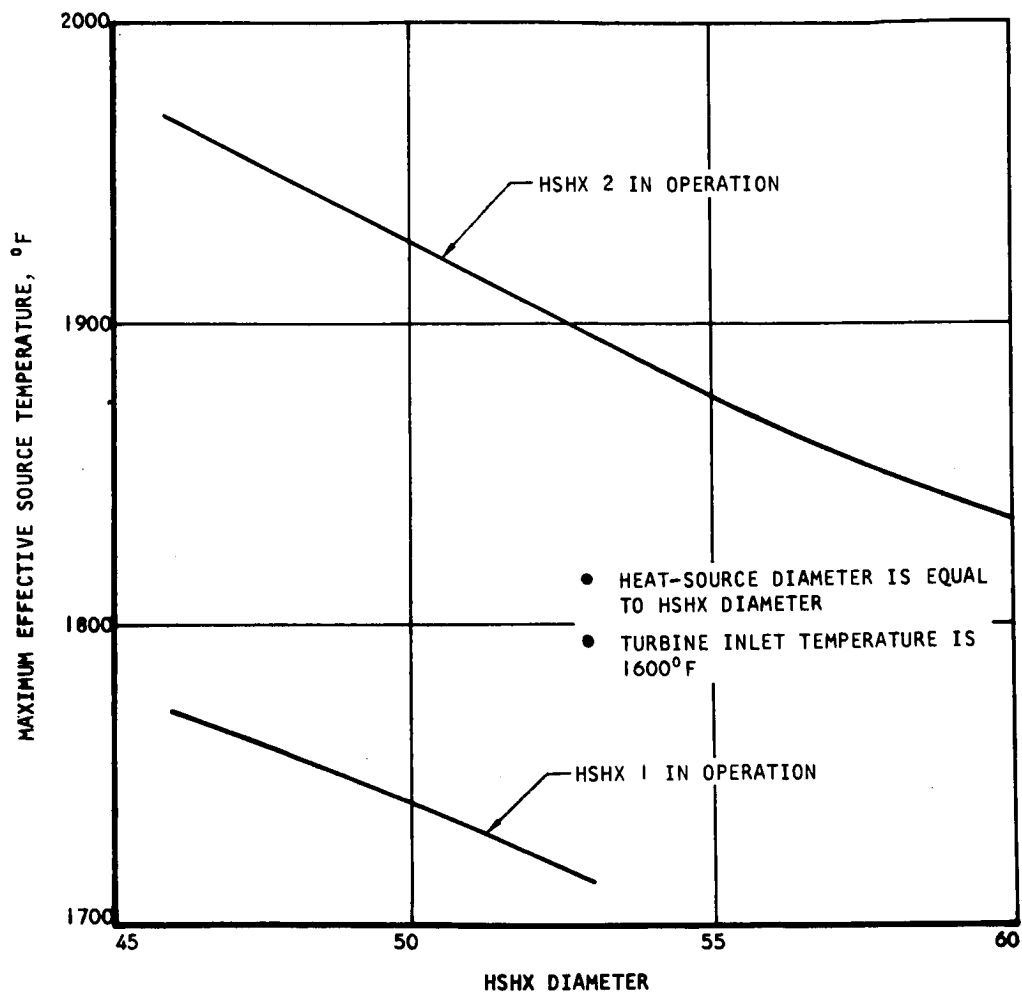


Figure 8.2-42 HEAT-SOURCE HEAT EXCHANGER -- AREA REQUIREMENTS

8.2.4 Structural Analysis

8.2.4.1 Introduction

The structural characteristics of the three design approaches under consideration (involute, rectangular, and pin cushion) were compared. This preliminary analysis indicated that all three were acceptable from the standpoint of structural integrity. Analyses were performed for pressure containment and for thermal loads.

The pressure containment analysis was performed to determine preliminary wall thicknesses for the various designs. Typical mechanical loads in the tube arrays, caused by restraint of free thermal expansion, were determined to indicate one of the major design considerations for operation for the HSHX at elevated temperatures. The tube loads in the unwelded transition from the basic array to the collector manifolds were shown to be highly dependent upon unwelded length.

8.2.4.2 Structural Design Criteria

A variety of load conditions, stress conditions, and possible failure modes will be experienced by the HSHX during its 5-year service life. The detailed set of design criteria discussed below will be used to design the various components.

Allowable Stresses for Internal Pressure Containment

The design pressure for the heat exchanger is 56 psi, and design temperatures, as noted in the calculations, are associated with a gas inlet temperature of 1200°F and outlet temperature of 1600°F.

The Cb-1Zr material properties that must be considered for components operating at temperatures below about 1300°F are the short-time yield and ultimate strength properties. For higher operating temperatures, the stress-rupture properties at temperature for the 50,000-hr service life will govern the design.

The standard design practice employed by AiResearch for pressure containment in the low-temperature regime is to use proof pressures of 1.5 times the working pressures and burst pressures of 2.0 times the working pressures. The structure must not yield at proof pressure or rupture at burst pressure. This implies that the proof pressure is the governing design condition if the ratio of yield stress to ultimate stress is less than 0.75 and that the burst pressure will govern if the ratio is greater than 0.75. The allowable stress at working pressure is, therefore, the lesser of the following:

$$\sigma_{\text{all}} = (f_{\text{tu}})/2 \quad (8-31)$$

$$\sigma_{\text{all}} = (f_{\text{ty}})/1.5 \quad (8-32)$$

The extended life requirements of the unit demand that creep deformation and stress rupture also be considered. These stress limitations are more stringent than the allowable stresses obtained from the short-time properties. Standard industrial practice on pressure vessels is to employ factors of 1.5 on 1-percent creep and 2.0 on stress rupture. Allowable stresses at working pressures must, therefore, be the lesser of the following:

$$\sigma_{all} = (1\text{-percent creep stress})_{50,000 \text{ hr}} / 1.5$$

$$\sigma_{all} = (\text{creep-rupture stress})_{50,000 \text{ hr}} / 2$$

These must be compared with the short-time allowable stresses to determine the governing design condition.

At elevated temperature, material properties are very sensitive to temperature. For Cb-1Zr, an increase in temperature of 100°F leads to a decrease of approximately 30 percent in creep- and stress-rupture strengths. Therefore, an allowance must be made to account for the possibility of over-temperature. The design temperature used to establish allowable stresses is taken to be the maximum operating temperature plus 100°F.

One modification to the above will be made for bending load designs that will be governed by the material creep properties. The maximum bending stress occurs at the extreme fibers, and creep relation will cause a redistribution of the load across the bending section. It is desirable to modify the allowable bending stress to take advantage of the increased creep-strength capability. Assuming that a constant stress is achieved on both the tension and compression portions of the section, the bending stress allowable will be 1.5 times the above creep- and stress-rupture allowables.

Allowable Stresses for Inertia Loads

Launch and liftoff loads, supplied by NASA for the Atlas/Centaur launch vehicle, were:

Maximum acceleration	6.4 g
Maximum normal acceleration	2.3 g
Limit load factors	1.25 times acceleration g's

The inertia loads on the HSHX may be experienced during any phase of the operating cycle of the unit. The mounting brackets must therefore be designed to carry the inertia loads at elevated temperature. Since the maximum loads occur for a relatively short time during vehicle launch, the short-time material properties will be used.

The design allowable stress used for the inertia loads is therefore the short-time tensile yield stress at the design temperature that is expected at the bracket location:

$$\sigma_{all} = \sigma_{ty}$$

(8-33)

This will lead to a conservative bracket design because the above criteria call for simultaneous application of the various inertia loads discussed below. In practice, these loads will not occur at the same time, and the peak loads experienced by the mounting system may be considerably less than the quoted combined maximum values. For example, application of the shock load and vibration

load at different times would produce maximum bracket loads of about 50 percent of the design load capability.

Allowable Thermal Fatigue Stresses

The design temperatures for steady-state conditions were based on temperature distributions for two-pass configurations given in the previous topical report. An assumed temperature lag of the headers of 400°F was used to illustrate possible transient conditions.

The magnitude of thermal stresses developed during the rapid heat-up cycle of the system will result in plastic deformations in various components. The minimum operating life requirement of the HSHX is 100 thermal cycles. A minimum calculated design life of 400 cycles will be used to ensure that the 100-cycle operating life is achieved.

The required analyses will be based on the accumulated plastic strain approach for estimating fatigue life. The number of cycles to failure, N , is determined from the formula:

$$N = \frac{2C^2}{(\epsilon_p)_{1-2}^2 + (\epsilon_p)_{3-4}^2} \quad (8-34)$$

where

N = cycles to failure

ϵ_p = plastic strain

C = ductility constant

The constant, C , is determined from the formula:

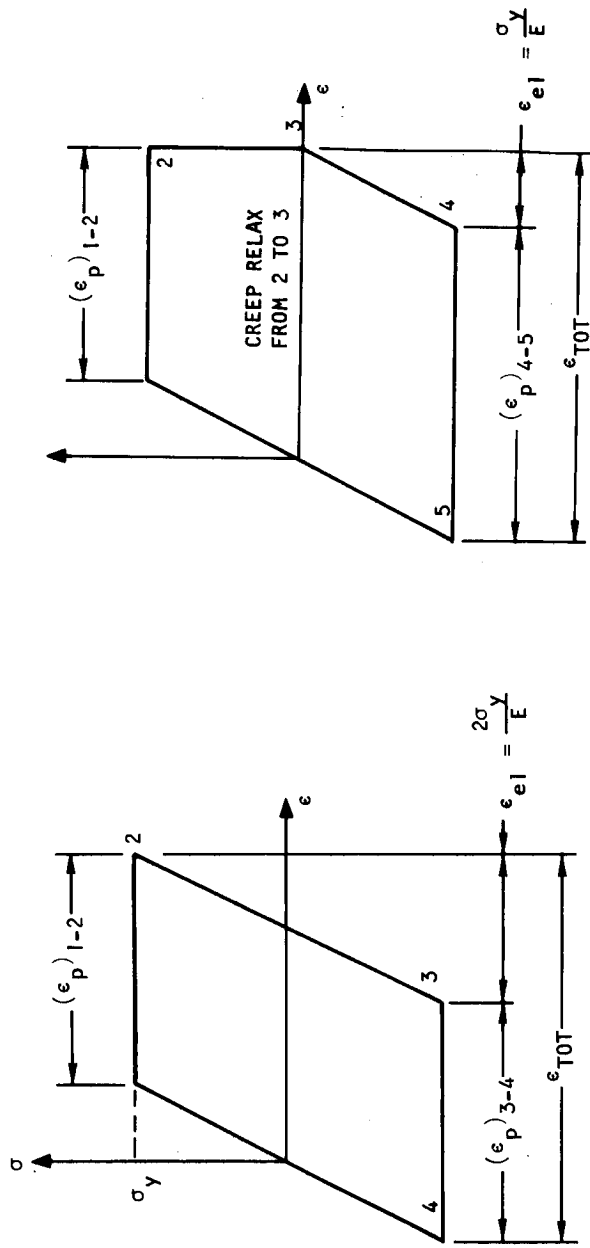
$$C = (0.7905 \epsilon_f)^{3/4} \quad (8-35)$$

where

ϵ_f = true reduction of area = $-\ln(100 - \text{percent RA})/100$

RA = reduction of area

The fracture ductility is determined from material properties, and the plastic strain is estimated from a typical load cycle for the material. Two examples of loading sequences are shown in Figure 8.2-43 with the associated expressions for determining ϵ_p . Cumulative effects for different load cycles during the material life are handled by a fatigue damage rule similar to Miner's rule. This may be expressed as



CYCLE WITHOUT CREEP

$$(\epsilon_p)_{1-2} = \epsilon_{TOT} - \frac{2\sigma_y}{E}$$

$$(\epsilon_p)_{3-4} = \epsilon_{TOT} - \frac{2\sigma_y}{E}$$

CYCLE WITH CREEP

$$(\epsilon_p)_{1-2} = \epsilon_{TOT} - \frac{2\sigma_y}{E}$$

$$(\epsilon_p)_{4-5} = \epsilon_{TOT} - \frac{\sigma_y}{E}$$

Figure 8.2-43 TYPICAL IDEAL ELASTIC-PLASTIC LOAD CYCLES

$$\sum_{i=1}^n \frac{C_i^2}{(N_i)^2} \leq 1.0 \quad (8-36)$$

Material Properties

The pertinent available physical and mechanical properties of Cb-1Zr are shown in Table 8.2-II. The design allowables based on the above criteria are shown in Table 8.2-III for stresses due to internal pressure and inertia loads.

8.2.4.3 Pressure Containment Analysis

Preliminary pressure containment analysis was performed to estimate tube and header wall thicknesses. Required thicknesses were determined from the formula for a uniform cylinder under internal pressure. The maximum stress is:

$$\sigma = Pr/t \quad (8-37)$$

so the required thickness is

$$t_{\text{req}} = Pr/\sigma_{\text{all}} \quad (8-38)$$

where

P = the internal pressure

r = the cylinder radius

A summary of tube and header estimated wall thicknesses along with the governing criteria and estimated maximum is presented in Table 8.2-IV for the three candidate designs at operating temperature. A preliminary tube wall thickness of 0.030 inch was selected as a reasonable minimum fabricable size.

The material thicknesses shown in the table do not reflect possible departures from straight tubular geometry. Curvature of the tubing, particularly in the case of the involute tubing, will require increased thickness since the stresses at outer fibers in these tubes are somewhat higher than those computed by the above cylinder equation. Joints between the tubes and manifolds will also require either local reinforcement or general wall thickness increases.

8.2.4.4 Thermal Stress Analysis

A preliminary thermal stress calculation indicated that substantial tube loads are possible in the unwelded transition region from the welded tube area to the inlet and outlet headers. The headers and tubes operate at different temperature levels in all three designs, and the unwelded lengths of tubing must accommodate the differential thermal movements. Calculations were performed for two lengths of unwelded tubing and two operating conditions: steady-state and a typical simulated heat-up condition. In the heat-up case, the headers were assumed to be 400°F lower than their steady-state operating temperatures.

TABLE 8.2-II

Cb-Izr MATERIAL PROPERTIES

Temperature, °F	σ_{ty}	50,000-hr Rupture Stress	Elastic Modulus, $\times 10^6$	Thermal Expansion, $\times 10^{-6}$
70	35,000	Not applicable	16.0	4.15
400	34,700	Not applicable	15.6	4.15
1000	34,000	Not Applicable	14.8	4.25
1200	33,500	Not Applicable		4.30
1300	33,000	45,000		
1400	32,000	24,100	14.3	
1500		13,500		
1600	30,000	7,300	14.1	4.35
1650		5,500		
1700	29,000	4,000	14.0	
1750		2,800		
1800	28,000	2,200		4.45

TABLE 8.2-III

Cb-Izr ALLOWABLE STRESSES

Temperature, °F	Tensile - Compressive Allowable, psi	Bending Allowable, psi	Inertia Load Allowable, psi
70	23,300	35,000	35,000
400	23,100	34,700	34,700
1000	22,600	34,000	34,000
1200	22,300	33,500	33,500
1300	22,000	33,000	33,000
1400	12,050	18,100	32,000
1500	6,750	10,100	31,000
1600	3,650	5,320	30,000
1650	2,750	4,120	29,500
1700	2,000	3,000	29,000
1750	1,400	2,100	28,500
1800	1,100	1,650	28,000

TABLE 8.2-IV

TUBE AND HEADER SUMMARY

Part	Wall Thickness	Governing Criterion	Maximum Temperature, °F
<u>Involute HSHX</u>			
Inlet header	0.030	Minimum gage	1425
Outlet header	0.042	σ_{all}	1620
Inlet tube	0.030	Minimum gage	1604
Outlet tube	0.030	Minimum gage	1620
<u>Rectangular HSHX</u>			
Inlet header	0.030	Minimum gage	1480
Outlet header	0.042	σ_{all}	1620
Inlet tube	0.030	Minimum gage	1628
Outlet tube	0.030	Minimum gage	1628
<u>Pincushion</u>			
Inlet header	0.031	σ_{all}	1550
Outlet header	0.065	σ_{all}	1660
Inlet collector header	0.030	Minimum gage	1560
Outlet collector header	0.030	σ_{all}	1650
Inlet tube	0.030	σ_{all}	1620
Outlet tube	0.030	σ_{all}	1646

The maximum tube bending moments occurring for each of the three designs is given in Table 8.2-V. Distances of 3.0 and 5.25 inches radially inward from the header to the edge of the welded tube region were used. The allowable tube moment based on Cb-1Zr allowable stresses for internal pressure containment is shown in Table 8.2-V. The bending moment required to initiate tube yielding is also included. The steady-state operating conditions are related to the pressure-containment allowable bending stresses that are governed by creep-rupture properties; the transient conditions are related to the short-time yield properties of the material.

The results in Table 8.2-V show that increased tube length decreases the applied bending moment in all cases. Furthermore, there is an acceptable unwelded tube length for each design. The involute design is acceptable both for steady-state and for the assumed transient conditions with a 5.25-inch radial transition length. The other two designs will require unwelded tube lengths greater than those shown in the table, and the pin cushion design would be acceptable with a smaller length increase than that required for the rectangular design.

REFERENCES

- 8.2-1 Toups, K. A., A General Computer Program for the Determination of Radiant Interchange Configuration and Form Factors - CONFACT II, Report No. SID 65-1043-2, North American Aviation, Inc. (October 1965).
- 8.2-2 Fick, J. L., MLFTHAN-LMSC Thermal Network Analyzer Mark I, Distribution No. 1295.
- 8.2-3 Coombs, M. G. et al., Heat-Source Heat Exchanger Design Study, AiResearch Topical Report No. 68-3257.

8.3 IRV/BRAYTON CYCLE/LAUNCH VEHICLE INTEGRATION

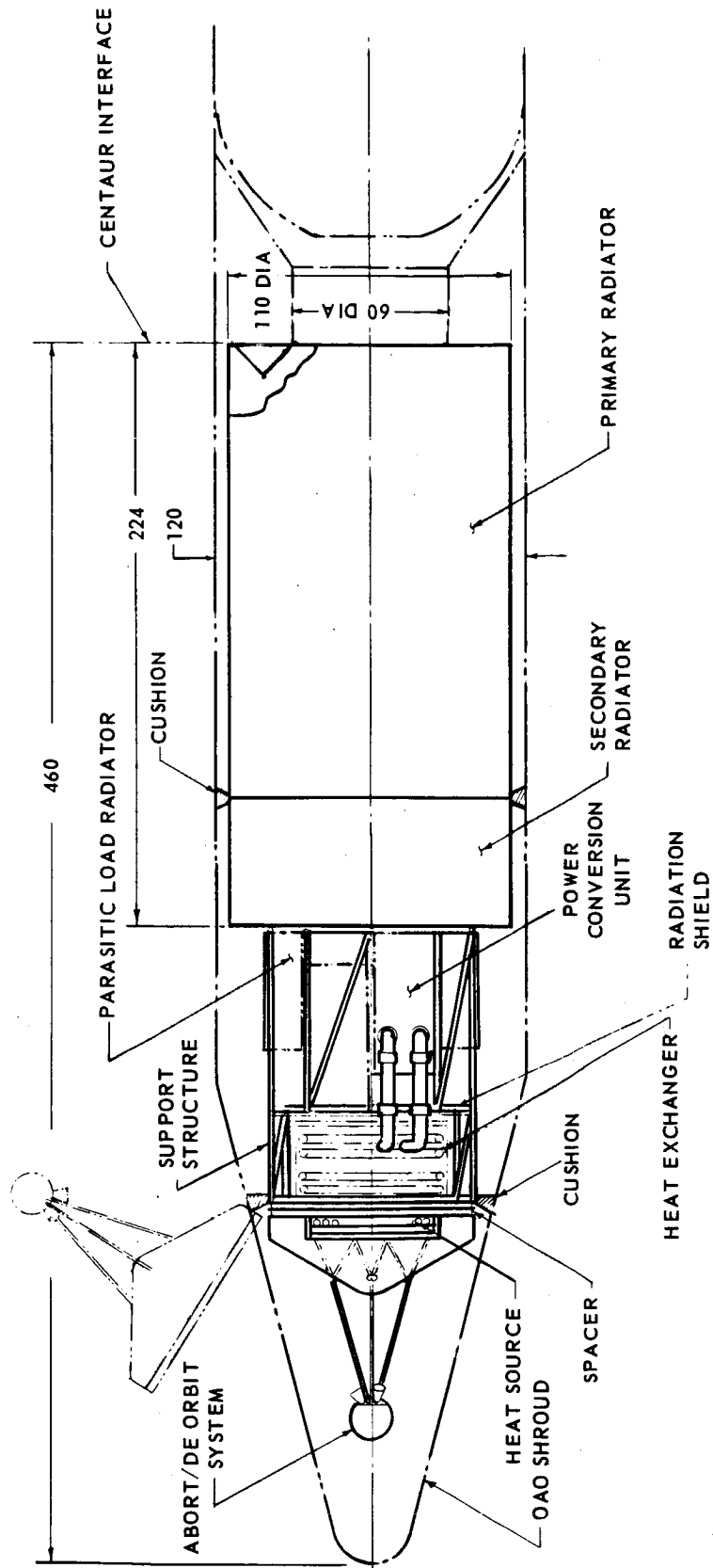
The integration of the IRV vehicle with the heat exchanger and associated systems is as depicted in the exploded configuration shown in Figure 1.0-1. The heat exchanger is supported in its proper position relative to the heat source by a tubular support structure. This structure also supports the PCM package and is the primary load carrying structure between the NASA Lewis radiator (launch vehicle) and the IRV. The hinged spacer discussed in Section 8.1.4 above is attached to the forward ring of this support truss. For the emergency cooling mode the IRV with its heat source is hinged away from the heat exchanger and radiates to space and is shown in Figure 8.3-1. An alternate method of emergency cooling, currently planned to be incorporated in conjunction with the IRV hinging is shown in Figure 8.3-2. This is accomplished by hinging or sliding insulation panels out of position and allowing heat rejection to outer space. This concept complicates the design of the primary support structure as well as adding an active actuating system but appears to warrant consideration in the preliminary design phase. The tubular support structure is designed to allow insertion and/or removal of the PCM package at any time once the aerodynamic shroud has been jettisoned. This is accomplished by mounting the PCM package at any time once the aerodynamic shroud has been jettisoned. This is accomplished

TABLE 8.2-V

UNWELDED TUBE THERMAL BENDING MOMENTS

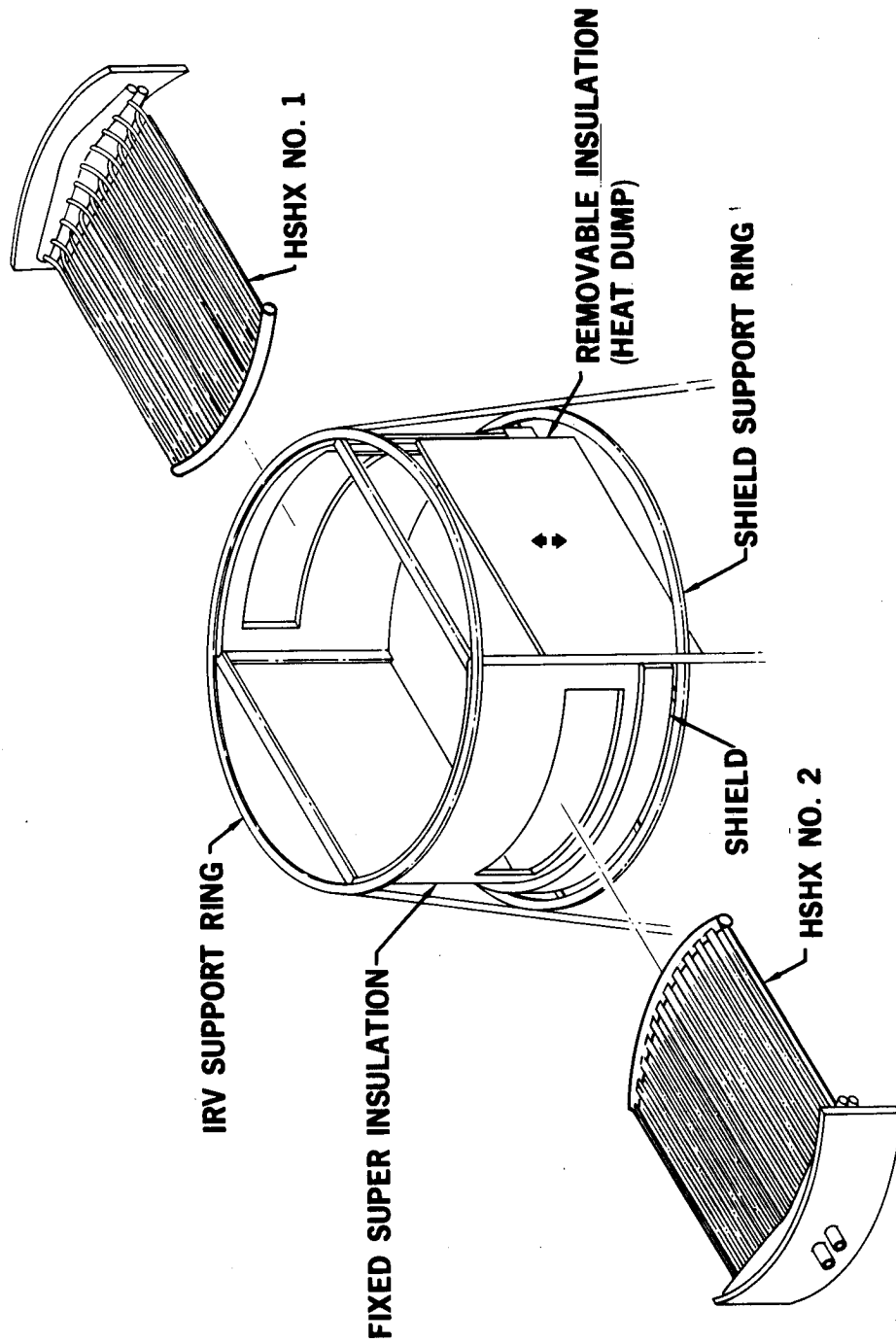
Design	Length of Transition Region, in.	Moment, lb-in.				Comments (see note)
		Steady State	Allowable for Steady State	400°F Header Transient	Yield	
Involute	3.0	3520	1080	11,600	4880	Both exceed allowables
	5.25	955		3040		
Rectangular	3.0	546	33	2020	334	Both greatly exceed allowables
	5.25	390		1445		
Pincushion	3.0	378	48	920	870	Both exceed allowables; transient moment is nearly acceptable
	5.25	141		344		

NOTE: The comments apply to listed transition lengths only. Increased separation between the manifolds and welded tube regions reduces the applied moments in all cases.



78-0639

Figure 8.3-1 IRV/BRAYTON CYCLE LAUNCH VEHICLE INTEGRATION



68-3608

Figure 8.3-2 RECTANGULAR HSHX -- HEAT DUMP CONCEPT

by mounting the PCM package on a track within the support truss and carrying the launch loads around the required structural envelope. Insulation and radiation shielding is packaged immediately aft of the heat exchanger.

8.3.1 Abort and Deorbit Analysis

This section describes an investigation of the abort and deorbit performance of the IRV. Three candidate configurations are compared on the basis of their relative spin-rate requirements, ease of integration, reliability, weight, volume, and operational features. The calculation of required spin-rate draws upon the general analysis of spin-stabilized thrusting presented in Appendix A.

The possibility of using the deorbit spin-up and thrust rockets for pad-abort is examined and found to be feasible for two of the three candidate configurations. The nominal deorbit thrust level (2800 pounds) was chosen with this possibility in mind.

8.3.1.1 Candidate Configurations

Three essentially different deorbit system configurations have been considered (see sketches in Figure 8.3-4). They are:

1. Tower-mounted retrorocket - In this configuration, a single combustion chamber feeding three canted nozzles is mounted on a tower attached to the heat shield.
2. Nose-mounted retrorocket - In this configuration, a single rocket is mounted directly on the heat shield. The thrust vector direction is opposite to that of Case 1.
3. Peripheral-mounted retrorockets - In this configuration, three separate rockets are mounted on the periphery of the vehicle. The thrust direction is the same as in Case 1.

8.3.1.2 Required Spin-Rate

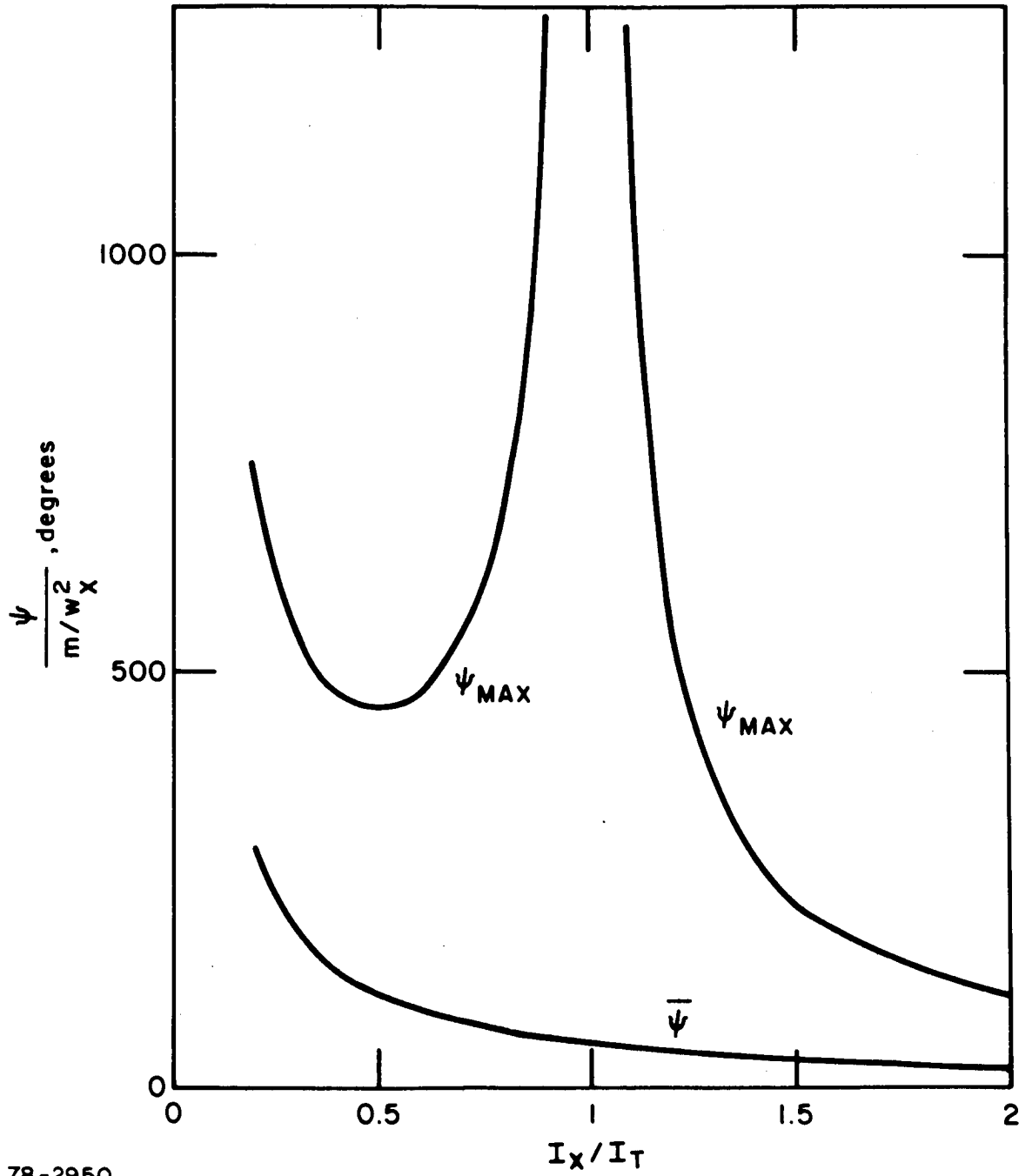
Appendix A summarizes some useful approximate solutions which describe the deviation of the spin axis away from its initial direction, caused by initial transverse rates and a transverse torque associated with a thrust misalignment and/or a c.g. offset. Normalized curves for the long term average deviation and the maximum deviation due to transverse torque are plotted versus inertia-ratio in Figure 8.3-3. The curves are normalized by the dimensionless ratio m/ω^2 where

ω = spin rate

m = M_T/I_T

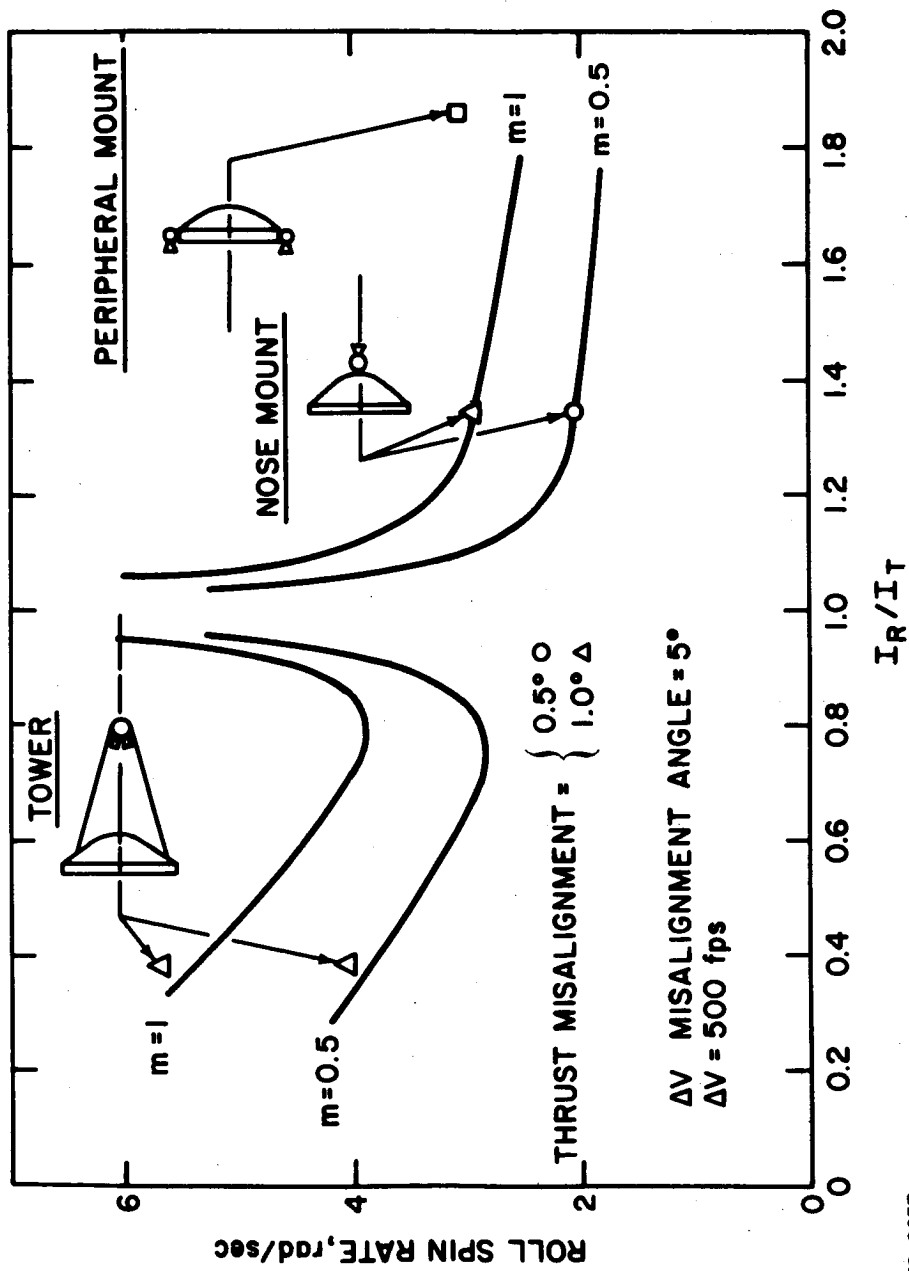
M_T = transverse torque

I_T = transverse inertia



78-2950

Figure 8.3-3 TRANSVERSE MOMENT EFFECTS



78-0637

Figure 8.3-4 DEORBIT SYSTEM CONSIDERATIONS

The average deviation, $\bar{\psi}$, is a measure of the thrust application angle error. Detailed examination of the complete solution shows that if thrusting lasts for a few revolutions or longer, the average value $\bar{\psi}$ is close to the plotted curve, except when the inertia ratio, I_X/I_T , is near unity.

The required spin-rate is given by

$$\omega_{req'd} = \left[\frac{m_{max}}{\bar{\psi}_{allowed} I_X/I_T} \right]^{1/2} \quad (8-38)$$

where m_{max} is the maximum expected value of M_T/I_T and $\bar{\psi}_{allowed}$ is the allowable thrust application angle error. The maximum expected value of transverse torque is given by

$$M_Z = d \sin \beta T \quad (8-39)$$

for Configurations 1 and 2, and

$$M_Z = \frac{r}{3} \Delta T \quad (8-40)$$

for Configuration 3. In the above equations

d = the axial distance from the c.g. to the point of application of thrust.

r = the radial distance from the c.g. to the point of application of thrust.

β = the angular deviation of the thrust vector from its nominal line through the c.g.

T = the nominal thrust magnitude

ΔT = the deviation in thrust magnitude. (We assume one of the three engines differs from the other two.)

Table 8.3-I summarizes the moment arms, inertia, transverse torque estimates, and required spin-rates for the three configurations. The torque estimates shown in the table correspond to a thrust direction error (β) of 0.5 degree and a thrust magnitude error (ΔT) of 5 percent of the nominal value. The allowable error in the thrust application angle error ($\bar{\psi}$) was taken to be 5 degrees. Figure 8.3-3 shows that holding $\bar{\psi}$ below 5 degrees corresponds to holding ψ_{max} below 40 degrees as long as the region ($0.70 < I_X/I_T < 1.3$) is avoided. This limitation on ψ_{max} is necessary in order to prevent uncontrolled tumbling and also to prevent unacceptable ΔV losses associated with the difference between unity and the cosine of the deviation angle. Trajectory dispersion data shows that thrust application angle errors of 5 degrees cause reentry point dispersion errors on the order of 10 to 20 nautical miles.

The points indicated by Δ , \circ , and \square in Figure 8.3-4 correspond to the three configurations covered in Table 8.3-I. The solid curves plot Equation (8-38) for two values of m_{max} , except that they have been faired sharply upward in the

TABLE 8.3-1

SPIN-RATE CALCULATION SUMMARY

$\bar{\psi} = 5 \text{ deg}$

$\beta = 1/2 \text{ deg}$

$\Delta T = 5 \text{ percent}$

Configuration	d (ft)	r (ft)	I_x (slug ft ²)	I_T (slug ft ²)	$\frac{I_x}{I_T}$	M_z (ft lb)	$\frac{m}{[M_z/I_T]}$ (rad/sec ²)	$\left[\frac{m^x}{\bar{\psi} I_x / I_T} \right]^{1/2}$ (rad/sec)
1. Tower	8	--	155.2	406.3	0.38	187	0.46	4.05
2. Nose	2.5	--	151.1	112.5	1.34	59	0.52	2.10
3. Peripheral	--	3.75	208.1	112.2	1.86	175	1.56	3.10

vicinity of $I_x/I_T = 1$. These curves show graphically the effects of inertia-ratio and transverse torque on the required spin-rate.

8.3.1.3 Comparative Evaluation

Configuration 2 (nose-mounted retrorocket) has the smallest spin-rate requirement and is the smallest, lightest and most easily integrated design. It is also the most reliable deorbit system since it contains a single rocket with a single nozzle. The other two configurations, however, enjoy the following operational advantages:

1. The deorbit rocket can double as a pad-abort rocket.
2. Retro can occur immediately after separation from the parent vehicle, without danger of collision.
3. Reentry into the earth's atmosphere begins with a smaller angle of attack.

Figure 8.3-5 illustrates the relative disadvantage of the nose-mounted configuration in entering the atmosphere with a large angle of attack. This comes about because the nominal central angle of travel from retro to entry is approximately 120 degrees.

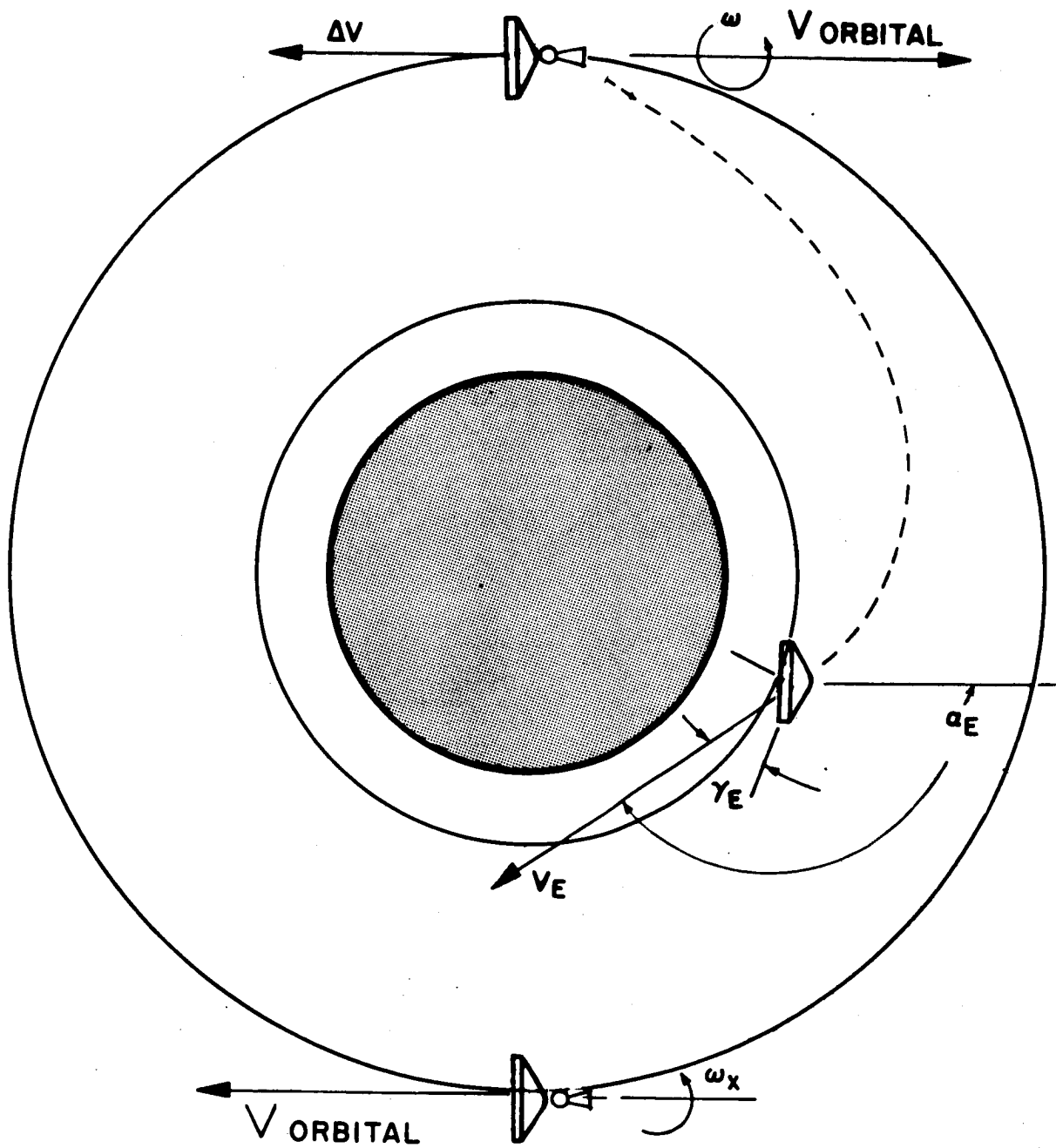
Table 8.3-II summarizes the relative advantages and disadvantages of the three systems.

8.3.1.4 Pad-Abort with Deorbit Rockets

The tower-mounted and peripheral-mounted configurations contain the possibility of accomplishing launch-pad aborts using the same thrust and spin-up rockets needed for deorbit. It is impossible to use the exact sequence of firings used in the deorbit case since the IRV must immediately thrust clear of the booster, without waiting for the completion of a spin-up maneuver.

The idea under consideration is to turn on both the thrust and spin-up rockets simultaneously; the spin-up rockets burn out first, allowing most of the thrusting to take place during a constant-spin-rate period. The total thrusting time period $(0, T_2)$ is thus divided into two parts: Phase I $(0, T_1)$ during which the spin-rate, ω , is steadily building up; and Phase II (T_1, T_2) during which the spin-rate remains constant (see sketch on the following page).

The applied torques are the spin-torque, M_x , and the unwanted transverse torque, M_T , due to thrust misalignment and/or c.g. offset. We are concerned with the time-history of the deviation of the thrust (spin) axis away from its initial direction during this maneuver. This deviation time-history during Phase II is affected by both the action of M_T during Phase II and the "initial conditions" in the transverse body rates and the Euler angles describing the deviation at time T_1 . These initial conditions are caused by the joint action of M_T and M_x during Phase I.



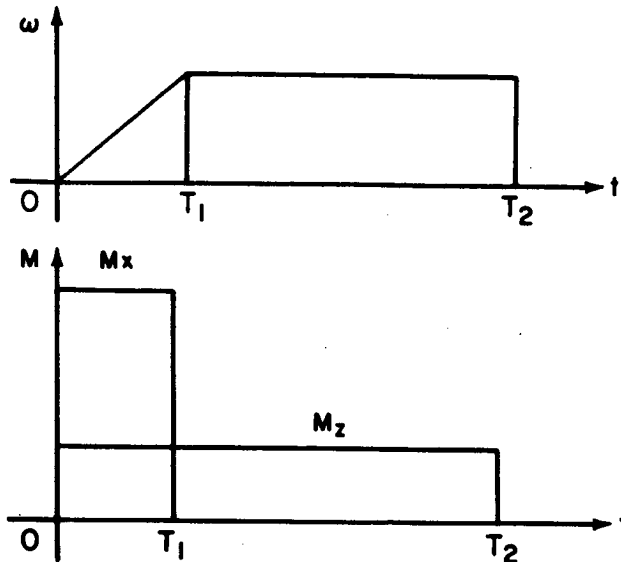
SEPARATE, SPINUP & WAIT 1/2 ORBITAL PERIOD

Figure 8.3-5 DEORBIT CONSIDERATIONS

776406P

TABLE 8.3-II
DEORBIT SYSTEM CONSIDERATIONS

Configuration	Spin Requirements	Integration	Reliability	Weight	Volume	Operation	Performance
Nose Mounted	Lowest spin	Easiest	Best	Lowest	Lowest	Requires separate abort system	Backward entry
Tower	Highest	Most difficult	Good	Highest	Highest	Can be used for abort mode	Low angle of attack entry
Peripheral	High	Not bad	Very poor	OK	OK	Can be used for abort mode too	Low angle of attack entry



In the deorbit case there is no appreciable M_T during spin-up, and the only important cause of misdirected thrust is the direct effect of M_T during the constant-spin-rate phase. In the pad-abort case, therefore, the deviation in thrust direction must be larger since there are additional terms associated with the "initial conditions" at T_1 . The question is: How quickly must the required spin rate be achieved before these additional contributions become intolerably large?

This problem was attacked by numerically integrating the exact equations of motion (see Appendix A) for various combinations of values of M_x and M_T . The following design procedure has emerged:

1. Estimate the maximum expected value of transverse torque, M_T , which might occur during thrusting.
2. Choose the spin-rate, ω_1 , required to accomplish the deorbit maneuver with acceptable accuracy, as in Section 8.3.1.2. This determines the total impulse of the spin-up system, but not the spin-up time, T_1 .
3. Choose a trial value of spin torque, M_x , in the range, 5 to 10 times M_z , and the accompanying spin-up time, $T_1 = \omega_1 / M_x$.
4. Numerically integrate the equations of motion with M_T and M_x until T_1 , then with M_T alone until T_2 . If the angular deviations and average deviation are larger than desired for pad-abort, increase M_x and decrease T_1 for the next trial and repeat Steps 3 and 4 until a satisfactory result is obtained.

An example set of calculations is as follows:

$$I_x = 180 \text{ slug ft}^2$$

$$I_T = 120 \text{ slug ft}^2$$

$$M_T = 120 \text{ ft lb}$$

$$\omega_1 = 2 \text{ rad/sec}$$

$$M_x = 720 \text{ ft lb}$$

$$T_1 = 0.5 \text{ sec}$$

$$\bar{\psi} = 15 \text{ deg}$$

$$\psi_{\max} = 60 \text{ deg}$$

The above values of $\bar{\psi}$ and ψ_{\max} would be too large for deorbit, but are probably acceptable for pad aborts. They could, of course, be reduced by spinning up faster.

8.3.2 Abort and System Integration

There appears to be two practical alternative approaches to the abort/deorbit rocket location; the first and generally more desirable is the utilization of a single solid propellant motor which can be utilized for either abort or the application of deorbit AV. This approach is shown in Figure 8.3-1 and is comprised of a spherical three nozzle canted solid propellant motor supported on a tubular tower structure. As discussed in Section 8.1 the attachment of this tower is accomplished through the same discrete hard points at which the heat source is attached to the aeroshell. The reliability of a single motor and its thrust application on the center line of the IRV make this approach more desirable.

The second approach utilizes separate abort and deorbit propulsion motors and is shown in Figure 8.3-6. The deorbit motor is mounted with its thrust vector rotated 180 degrees from the previous system with support supplied by a shorter truss structure, since there are no impingement problems on the IRV ablator. The attachment can be made to the IRV in a similar manner as mentioned previously and has the advantage of a thrust vector aligned with the IRV axis.

The abort motors are mounted to the periphery of the IRV or for the specific design discussed to the spacer section between the IRV and the heat exchanger/power conversion package. In this design, a minimum of two motors is required, and from a reliability standpoint three or more abort rockets are advantageous. Details of this analysis are given in Section 8.3.1 above.

The sequence of separation of the IRV and the abort and deorbit systems would be more complex for this configuration. To minimize the separation systems requirement for independent, both the spin motors and abort motors would be attached to the spacer. A separation plane would exist between the two sections of the spacer, and after application of spin and abort thrust the four explosive bolts

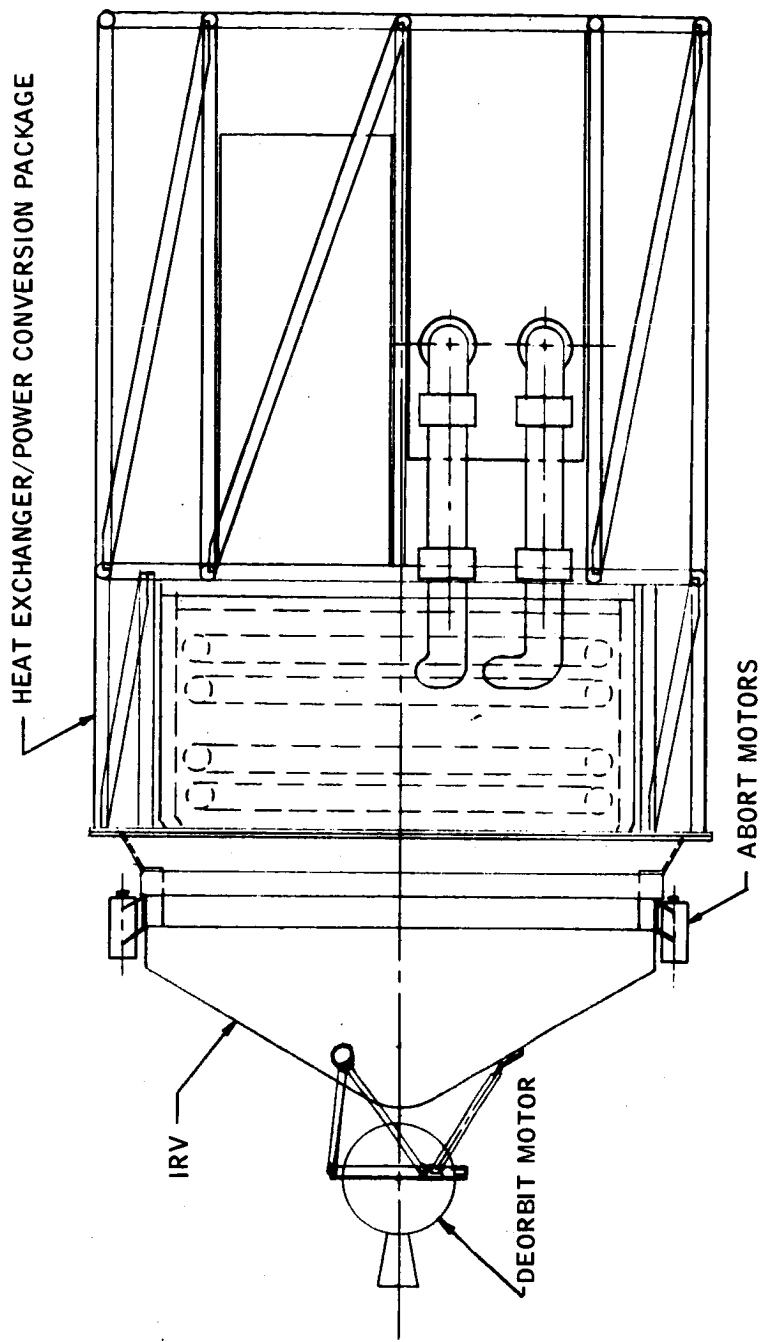


Figure 8.3-6 SEPARATE ABORT DEORBIT

78-0615

discussed in Section 8.1 above would separate the IRV, jettisoning both the spin and abort motor cases with the spacer. The deorbit motor would be jettisoned in the same manner as in the previous system.

8.3.3 Emergency Cooling

A problem which was given consideration in the Phase IB study was the determination of the peak capsule temperatures while the heat source is in a deployed state in space during periods of Brayton cycle shutdown. Scoping calculations for planar arrays indicated that the peak capsule temperature would be less than 1100°F with radiation to space, and a detailed analysis was not required. Preliminary calculations for the pin cushion arrays indicated, however, that very high capsule temperatures would be experienced because the capsules would be facing each other and radiation cooling would be deterred significantly. Since it was apparent that this deployed state would provide a constraint on the minimum row spacing, a detailed analysis was performed to determine minimum allowable spacings for this deployed state for the two pin cushion designs.

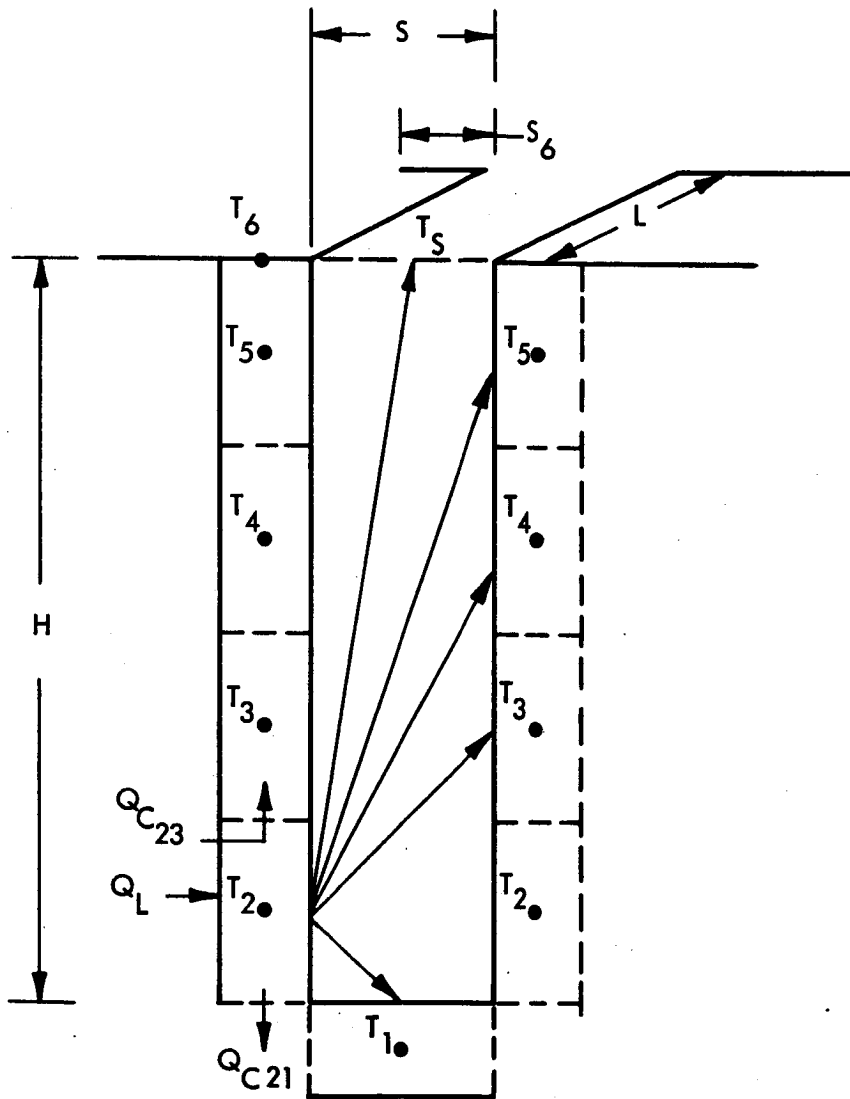
A nodal model was used as shown schematically in Figure 8.3-7. Taking a typical node designated by T_2 which represents a section of the capsule row, the internal heat generated is conducted to and from adjacent nodes. Heat is also radiated to and from nodes representing the adjacent capsule row, the heat source base, and space. By an iterative procedure, the temperature profile is determined as a function of nodal height, length, and thermal resistance and as a function of row spacing.

Two pin cushion arrays were compared: one being an array of fuel capsules standing vertically in rows with a 2-inch centerline distance between adjacent capsules in a row and the other being a log-type array of capsules stacked horizontally four high in rows. Figure 8.3-8 presents a plot of the peak fuel capsule temperatures of the vertical and horizontal capsule arrays as a function of row spacing and support metal thickness. The vertical array was found to have lower capsule temperatures at corresponding spacings for a combination of three reasons: 1) a shorter channel height, 2) a larger projected radiation area, and 3) less conduction path resistance. Based on a 2000°F capsule temperature limit for a long-time deployment, the row spacing could be as small as 1 inch for a vertical pin cushion array and 1.5 inches for a log-type pin cushion array with an 0.075-inch support metal thickness. HSHX hydraulic and thermal constraints indicate that a minimum of 1.5-inch spacing is necessary for the long rows of fuel capsules; however, shorter rows can be spaced closer. Based on these constraints, both arrays required the same heat source diameter. The more favorable beryllium oxide weight and distribution requirements for the vertical array resulted in its recommendation as the preferred design.

8.3.4 Launch Vehicle Integration

8.3.4.1 Separate Launch (Atlas-Centaur)

Figure 8.3-1 depicts the separate launch configuration considered in this study. A radiator design (furnished by NASA-LeRC) is used. It has been assumed that the radiator has load carrying capability and mates with the Atlas-Centaur on the 60-inch diameter payload attachment ring. The heat exchanger/power conversion unit support truss in the IRV are attached to the forward end of the radiator.



Q_L = INTERNAL HEAT GENERATION
 Q_C = HEAT TRANSFERRED BY CONDUCTION
 Q_R = HEAT TRANSFERRED BY RADIATION

612385-20B

Figure 8.3-7 PIN CUSHION HEAT SOURCE -- MODEL FOR RADIATION WHILE IN DEPLOYED STATE

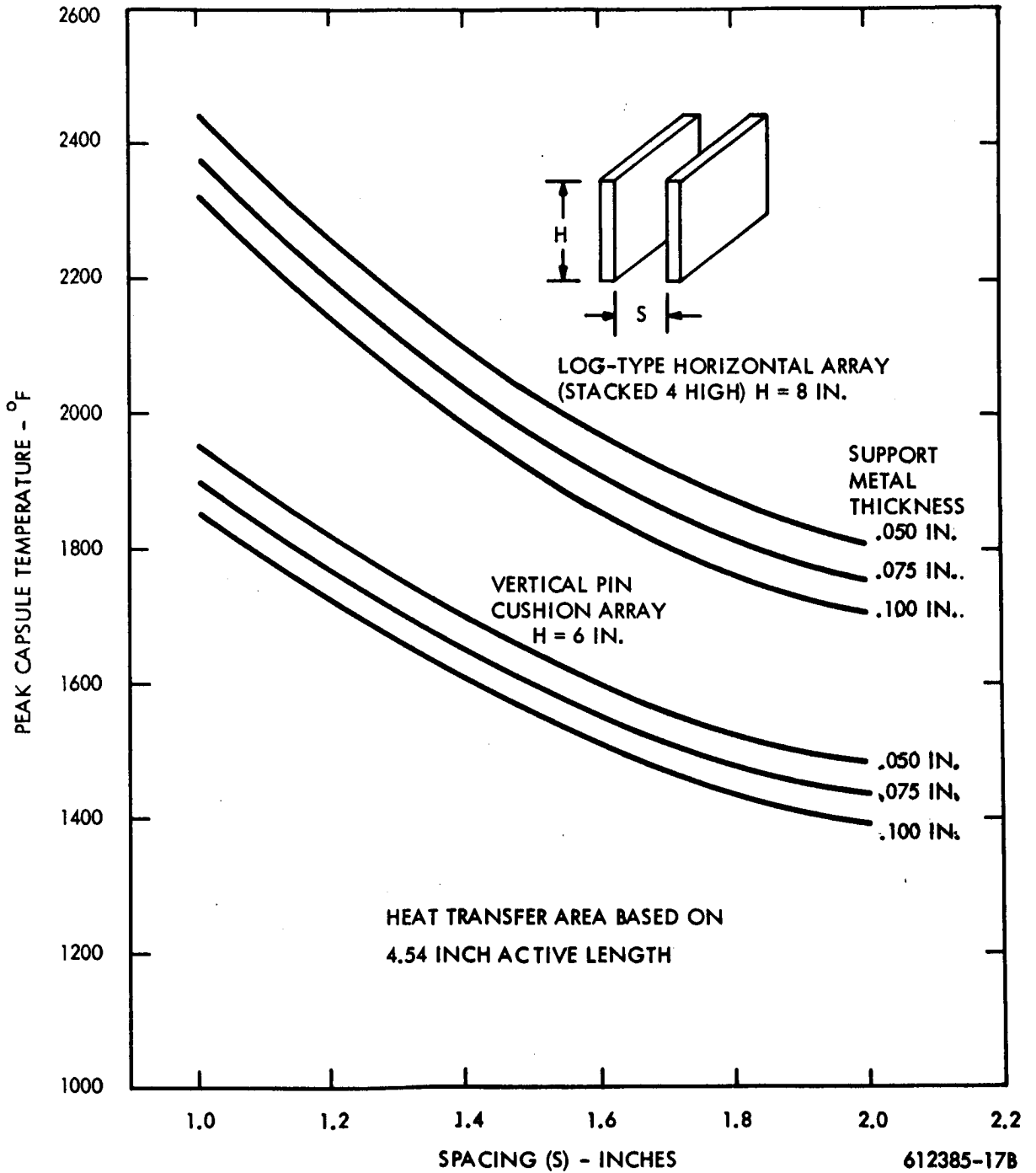


Figure 8.3-8 PIN CUSHION HEAT SOURCE -- EFFECT OF ROW SPACING ON PEAK CAPSULE TEMPERATURE

A critical problem in the integration with the launch vehicle appears to be one of aerodynamic shroud limitations. The OAO extended shroud was the primary consideration for utilization and for a limited length provides a dynamic clearance envelope of 120 inches in diameter which is compatible with the radiator design as shown. However, the length of the IRV and associated systems is such that OAO mid and aft fairings, or other means of lengthening the effective shroud total length are required. The current methods of accomplishing this do not appear to provide the 120-inch dynamic envelope clearance required. The OAO shroud can be extended through utilizing existing design, fabrication tooling, etc., but would not then reflect a proven and qualified shroud system and would in all likelihood require future testing. The dynamic envelope can be controlled and reduced by the utilization of snubbers or resilient support cushions between the shroud and the payload package. These are considered and shown in Figure 8.3.1.

8.3.4.2 Integral Launch (Saturn I-B-MORL)

Figure 8.3-9 depicts a possible integration concept for the MORL vehicle. The IRV system is mounted perpendicular to the MORL longitudinal axis and utilizes the same basic packaging configuration as that of the Atlas-Centaur Vehicle integration. Deployment to the emergency cooling mode or for abort and deorbit maneuvers would require external indexing of the IRV to the MORL with a track or guide system. Once this is accomplished the IRV could be pivoted about its hinge as shown by dashed lines in Figure 8.3-9 or separated from the heat exchanger, spin stabilized, and the deorbit motor ignited. This launch configuration could be a more serious radiation hazard than the separate launch and appropriate insulation and radiation shielding must be provided for crew protection. Waste heat radiators in this case are located about the external surface of the MORL power supply compartment.

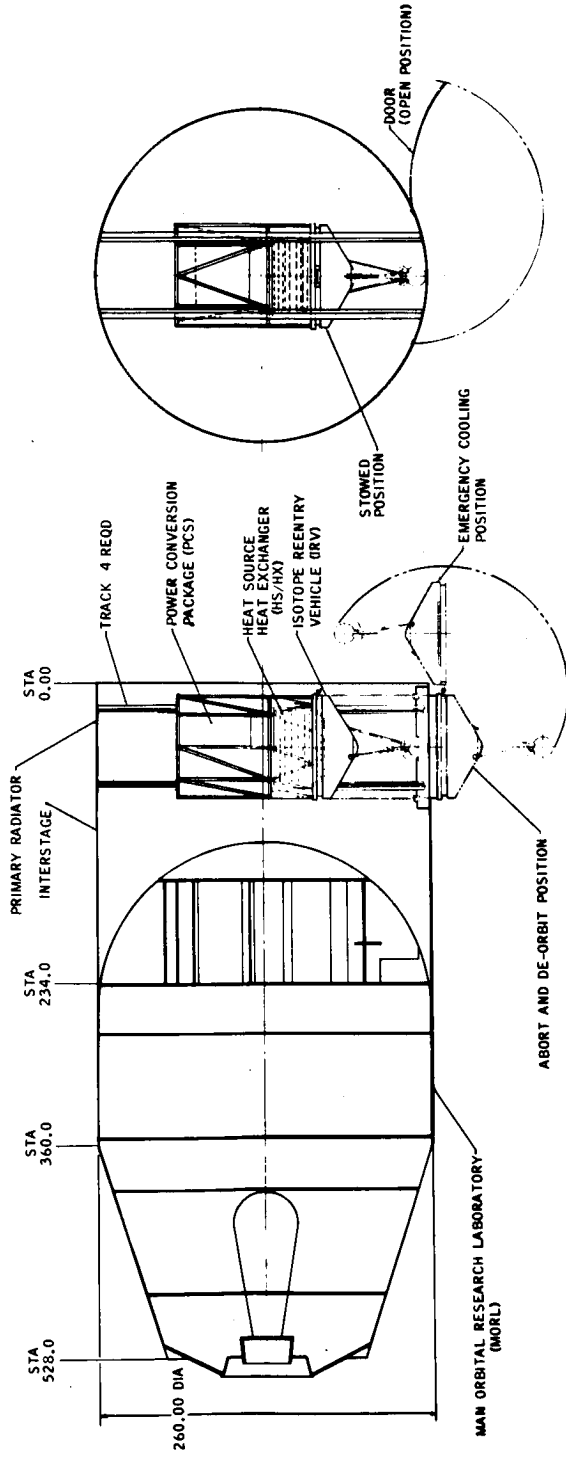


Figure 8.3-9 IRV INTEGRAL LAUNCH STUDY MORL/MIN DIAMETER VEHICLE

78-0631

APPENDIX

DYNAMICS OF THRUSTING WHILE SPINNING

A1.0 EQUATIONS OF MOTION

The body-rate equations of motion for an axially symmetric ($I_Y = I_Z = I_T$) rigid body (assuming constant inertia) are:

$$\dot{\omega}_x = \frac{M_x}{I_x} \tag{A-1}$$

$$\dot{\omega}_y = - \left[\left(\frac{I_x - I_T}{I_T} \right) \omega_x \right] \omega_z + \frac{M_y}{I_T} \tag{A-2}$$

$$\dot{\omega}_z = \left[\left(\frac{I_x - I_T}{I_T} \right) \omega_x \right] \omega_y + \frac{M_z}{I_T} \tag{A-3}$$

We consider the effect of a constant transverse moment which arises because the resultant thrust vector does not pass through the center of mass, and take the Z body axis to be that axis along which the transverse moment lies. The equations reduce to:

$$\dot{\omega}_x = 0 \tag{A-1a}$$

$$\dot{\omega}_y = - C \omega_x \omega_z \tag{A-2a}$$

$$\dot{\omega}_z = C \omega_x \omega_y + m \tag{A-3a}$$

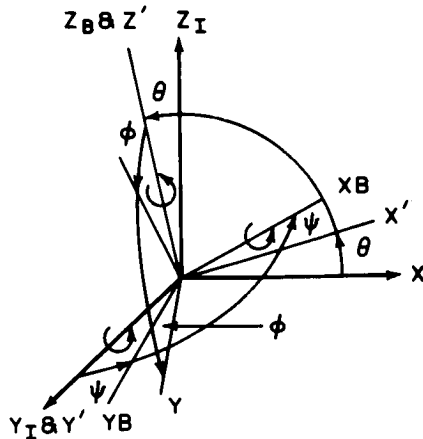
where

$$C = \left(\frac{I_x - I_T}{I_T} \right)$$

and

$$m = M_z/I_T$$

We define the angle set (θ, ψ, ϕ) which relate the body axes (x, y, z) to an inertial axis system (x_I, y_I, z_I) according to the sketch below.



Start with set (x_I, y_I, z_I)

1. θ about y_I (x', y', z')
2. ψ about z' (x_B, y_B, z_B)
3. ϕ about x_B (x, y, z)

The body rates can be expressed in terms of the angle rates as follows:

$$\omega_x = \dot{\phi} + \dot{\theta} \sin \psi$$

$$\omega_y = \dot{\theta} \cos \psi \cos \phi + \dot{\psi} \sin \phi$$

$$\omega_z = -\dot{\theta} \cos \psi \sin \phi + \dot{\psi} \cos \phi$$

which can be manipulated to yield:

$$\dot{\theta} = \frac{1}{\cos \psi} (\omega_y \cos \phi - \omega_z \sin \phi) \quad (\text{A-4})$$

$$\dot{\psi} = \omega_y \sin \phi + \omega_z \cos \phi \quad (\text{A-5})$$

$$\dot{\phi} = \omega_x - \dot{\theta} \sin \psi \quad (\text{A-6})$$

Equations (A-1), (A-2), (A-3), (A-4), (A-5), and (A-6) are an exact set of non-linear differential equations which can be integrated to describe the angular motion of a vehicle under the action of an applied torque.

Assuming that $\cos \psi = 1$ and that $\theta \sin \psi \ll \omega_x$, Equations (A-4), (A-5), and (A-6) reduce to:

$$\dot{\theta} = \omega_y \cos \phi - \omega_z \sin \phi \quad (\text{A-7})$$

$$\dot{\psi} = \omega_y \sin \phi + \omega_z \cos \phi \quad (\text{A-8})$$

$$\dot{\phi} = \omega_x \quad (\text{A-9})$$

Equations (A-1), (A-2), (A-3), (A-7), (A-8), and (A-9) are an approximate set of differential equations which remain valid as long as the angle ψ remains reasonably small and the spin-rate ω_x remains reasonably large. Note that θ and ψ describe the deviation of the body spin-axis, x , from its initial direction X_I .

A2.0 USEFUL SOLUTIONS

This section summarizes some useful closed-form solutions to the equations of the previous section for the constant spin-rate case ($M_x = 0, \omega_{x_0} \neq 0$). That is,

$$\omega_x = \text{constant} = \omega_{x_0}$$

In this case Equations (A-2) and (A-3) become linear equations with constant coefficients. Linearity permits us to consider separately the effects of the initial conditions (ω_{y_0} and ω_{z_0}) and the forcing function (m); we can then superpose the various effects.

Integration of Equation (A-9) yields

$$\phi = \omega t \quad (\omega \equiv \omega_x = \omega_{x_0})$$

The set of Equations (A-2), (A-3), (A-7), and (A-8) then become a linear set with some time varying coefficients:

$$\dot{\omega}_y = -k\omega_z \tag{A-2b}$$

$$\dot{\omega}_z = k\omega_y + m \tag{A-3b}$$

$$\dot{\theta} = \omega_y \cos \omega t - \omega_z \sin \omega t \tag{A-7b}$$

$$\dot{\psi} = \omega_y \sin \omega t + \omega_z \cos \omega t \tag{A-8b}$$

Again we can superpose the separate effects of ω_{y_0} , ω_{z_0} , θ_0 , ψ_0 , and m . In the solutions summarized below the body rate solutions are exact (assuming constant inertia) and the θ and ψ solutions are approximate valid only when Equations (A-7), (A-8), and (A-9) are valid as discussed previously.

1. Effects of ω_{y_0}

Note: $k = \omega \left(\frac{I_x}{I_y} - 1 \right)$

$$\omega_y(t) = \omega_{y_0} \cos kt \tag{A-10}$$

$$\omega_z(t) = \omega_{y_0} \sin kt \tag{A-11}$$

$$\theta(t) = \frac{\omega_{y_0}}{\omega + k} \sin(\omega + k)t \tag{A-12}$$

$$\psi(t) = \frac{\omega_{y_0}}{\omega + k} [1 - \cos(\omega + k)t] \tag{A-13}$$

2. Effects of ω_{z_0}

$$\omega_y(t) = -\omega_{z_0} \sin kt \quad (\text{A-14})$$

$$\omega_z(t) = \omega_{z_0} \cos kt \quad (\text{A-15})$$

$$\theta(t) = -\frac{\omega_{z_0}}{\omega + k} [1 - \cos(\omega + k)t] \quad (\text{A-16})$$

$$\psi(t) = \frac{\omega_{z_0}}{\omega + k} \sin(\omega + k)t \quad (\text{A-17})$$

3. Effects of m

Note: $m = M_z/I_T$

$$\omega_y(t) = -m/k [1 - \cos kt] \quad (\text{A-18})$$

$$\omega_z(t) = m/k \sin kt \quad (\text{A-19})$$

$$\theta(t) = \frac{-m}{k\omega} \sin \omega t + \frac{m}{k(\omega + k)} \sin(\omega + k)t \quad (\text{A-20})$$

$$\psi(t) = \frac{-m}{k\omega} [1 - \cos \omega t] + \frac{m}{k(\omega + k)} [1 - \cos(\omega + k)t] \quad (\text{A-21})$$

4. Combined Effects (ω_{y_0} , ω_{z_0} , θ_0 , ψ_0 , m)

$$\omega_y(t) = \omega_{y_0} \cos kt - \omega_{z_0} \sin kt - \frac{m}{k} [1 - \cos kt] \quad (\text{A-22})$$

$$\omega_z(t) = \omega_{y_0} \sin kt + \omega_{z_0} \cos kt + \frac{m}{k} \sin kt \quad (\text{A-23})$$

$$\theta(t) = \theta_0 + \frac{\omega_{y_0}}{\omega + k} \sin(\omega + k)t - \frac{\omega_{z_0}}{\omega + k} [1 - \cos(k + \omega)t] \quad (\text{A-24})$$

$$- \frac{m}{k\omega} \sin \omega t + \frac{m}{k(\omega + k)} \sin(\omega + k)t$$

$$\psi(t) = \psi_0 + \frac{\omega_{y_0}}{\omega + k} [1 - \cos(\omega + k)t] + \frac{\omega_{z_0}}{\omega + k} \sin(\omega + k)t \quad (\text{A-25})$$

$$- \frac{m}{k\omega} [1 - \cos \omega t] + \frac{m}{k(\omega + k)} [1 - \cos(\omega + k)t]$$

5. Average Values

The θ and ψ expressions above can be integrated once more to yield average value expressions. For example

$$\bar{\theta}(\tau) = \frac{1}{\tau} \int_0^{\tau} \theta(t) dt$$

is the average value of θ over τ seconds. The average values $\bar{\theta}$ and $\bar{\psi}$ are a good measure of the pointing error in the direction of ΔV due to thrusting.

$$\bar{\theta}(\tau) = \theta_0 + \frac{1}{\tau} \frac{\omega y_0}{(\omega + k)^2} [1 - \cos(\omega + k)\tau] \quad (\text{A-26})$$

$$- \frac{\omega z_0}{\omega + k} + \frac{1}{\tau} \frac{\omega z_0}{(\omega + k)^2} \sin(\omega + k)\tau$$

$$- \frac{1}{\tau} \frac{m}{k\omega^2} [1 - \cos \omega\tau] + \frac{1}{\tau} \frac{m}{k(\omega + k)^2} [1 - \cos(\omega + k)\tau] \quad (\text{A-27})$$

$$\bar{\psi}(\tau) = \psi_0 + \frac{\omega y_0}{\omega + k} - \frac{1}{\tau} \frac{\omega y_0}{(\omega + k)^2} \sin(\omega + k)\tau$$

$$+ \frac{1}{\tau} \frac{\omega z_0}{(\omega + k)^2} [1 - \cos(\omega + k)\tau] - \frac{m}{k\omega} + \frac{1}{\tau} \frac{m}{k\omega^2} \sin \omega\tau$$

$$+ \frac{m}{k(\omega + k)} - \frac{1}{\tau} \frac{m}{k(\omega + k)^2} \sin(\omega + k)\tau$$

As τ becomes large (many revolutions) the above expressions asymptotically approach:

$$\bar{\theta}_{\tau \rightarrow \infty} = \theta_0 - \frac{\omega z_0}{\omega + k} \quad (\text{A-28})$$

and

$$\bar{\psi}_{\tau \rightarrow \infty} = \psi_0 + \frac{\omega y_0}{\omega + k} - \frac{m}{\omega(\omega + k)} \quad (\text{A-29})$$

A3.0 NONDIMENSIONALIZED RESULTS

Figure A-1 summarizes the effects of a transverse moment on a spinning vehicle. Assuming that all initial conditions ($\omega_{y_0}, \omega_{z_0}, \theta_0, \psi_0$) equal zero, Equation (A-29) shows that the resulting magnitude of the long-term average deviation of the x-axis is

$$\bar{\psi} = \frac{m}{\omega(\omega + k)} = \frac{m}{\omega^2 I_x/I_T} \quad (\text{A-30})$$

Dividing ψ by the nondimensional ratio

$$\frac{m}{\omega^2} = \frac{\text{rad/sec}^2}{\text{rad/sec}^2}$$

yields

$$\frac{\bar{\psi}}{m/\omega^2} = \frac{1}{I_x/I_T} \text{ radians}$$

therefore

$$\frac{\psi}{m/\omega^2} = \frac{57.3}{I_x/I_T} \text{ degrees}$$

which is plotted in Figure A-1.

With $I_x/I_T = 1.42$, for example, the value on the curve is approximately

$$\frac{\bar{\psi}}{m/\omega^2} = 40 \text{ degrees}$$

Therefore, if $m = 1/2$ and $\omega = 2$,

$$\bar{\psi} = 5 \text{ degrees} .$$

Detailed examinations of Equation (A-27) shows that after a few revolutions the average value, $\bar{\psi}$, remains close to the value given by the asymptotic expression (A-29), except when the inertia ratio, I_x/I_T , is near unity.

The same curve could be used to indicate the effect of an initial transverse rate. Equation (A-29) shows, for this case,

$$\bar{\psi} = \frac{\omega_{y_0}}{\omega + k} = \frac{\omega_{y_0} I_T}{\omega I_x} \quad (\text{A-31})$$

Therefore,

$$\frac{\bar{\psi} \omega}{\omega_{y_0}} = \frac{57.3 I_T}{I_x} \text{ degrees}$$

which is the plotted expression.

Extending the previous example, if $I_x/I_T = 1.42$, $\omega = 2$ and $\omega_{y_0} = 0.2$,

$$\bar{\psi} = 4 \text{ degrees}$$

We return, now, to the effects of a transverse moment. Examination of Equation (A-21) shows that the maximum magnitude of ψ is given by,

$$|\bar{\psi}| = \frac{2m}{k(\omega + k)} = \left[\frac{2}{1 - I_x/I_T} \right] \bar{\psi} \text{ where } I_x/I_T < 1 \quad (\text{A-32})$$

and

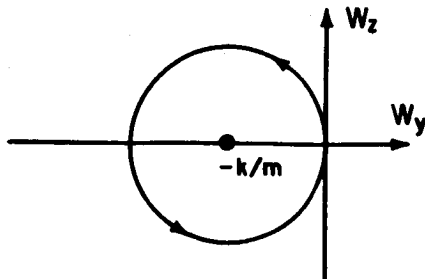
$$|\psi|_{\max} = \frac{2m}{k\omega} \left[\frac{2}{I_x/I_y - 1} \right] \bar{\psi} \text{ where } I_x/I_T > 1$$

These expressions were used to generate the ψ_{\max} curves in Figure A-1. It is important to consider these ψ_{\max} curves in addition to the ψ curve. They provide an indication of when the small angle assumption might become invalid. They also provide an indication of the ΔV magnitude loss which occurs when the cosine of the deviation angle differs from unity. The figure clearly shows the danger in having an inertia ratio I_x/I_T near unity.

A4.0 FAVORABLE BURN-TIMES

This section discusses some favorable choices for the burn-time. Assuming that the effects of transverse moments are larger than initial conditions, there are two opportunities worth considering. The first is always available; the second is available when the inertia ratio has certain special values.

Equations (A-18) and (A-19) show that due to a transverse moment, the (ω_y, ω_z) "state space" trajectory appears as shown in the sketch below, circling



about the point ($\omega_y = -m/k$, $\omega_z = 0$), and returning to the origin every time kt reaches a multiple of 2π . The quantity $k = (I_X/I_T - 1)\omega$ is the natural frequency of the transverse rate oscillation and is smaller than the spin-rate, ω . Therefore, by choosing the burn-time

$$t_b = \frac{2\pi}{k}$$

or any exact multiple of that value, the transverse rates remaining after the thrusting maneuver will be, theoretically, zero. The coning motion associated with such rates will, of course, also be zero.

The second opportunity to be considered is that of bringing the deviation angles θ and ψ to zero simultaneously with ω_y and ω_z . This is possible only when the ratio

$$\frac{1}{\frac{I_X}{I_T} - 1}$$

is an integer or a rational number (preferably a small integer). For example, suppose

$$\omega = 2 \text{ rad/sec (spin period} = \frac{2\pi}{\omega} \approx 3.14 \text{ sec)},$$

and

$$I_X/I_T = 5/3; \left(\frac{1}{\frac{I_X}{I_T} - 1} \right) = 3.$$

Then,

$$k = \left(\frac{I_X}{I_T} - 1 \right) \omega = \frac{1}{3} = \frac{2}{3} \text{ rad/sec}$$

so that the transverse oscillation period is

$$\frac{2\pi}{k} = 3\pi \approx 9.42 \text{ sec.}$$

The third frequency appearing in Equations (A-20) and (A-21) is

$$\omega + k = \omega \left(1 + \frac{I_X}{I_T} - 1 \right) = \frac{4}{3} \omega = \frac{8}{3} \text{ rad/sec.}$$

Suppose, now, the burn-time, $t_b = 9.42$ sec, is used. At this time the transverse rates, ω_y and ω_z , return to zero for the first time; the $\sin \omega t$ and $(1 - \cos \omega t)$ terms in the θ and ψ expression return to zero for the third time; and the $\sin(\omega + k)t$ and $[1 - \cos(\omega + k)t]$ terms return to zero for the fourth time. Thus,

$$\omega_y(t_b) = \omega_z(t_b) = \theta(t_b) = \psi(t_b) = 0,$$

and not only is there no coning motion, but also, the x-axis is directed along its initial direction. (Note that there is still a ΔV pointing error since ψ is not zero.)

A more physically motivated explanation of this phenomenon proceeds as follows:

1. The angular momentum vector, \bar{H} , returns to its initial position at the end of each spin period. This happens because the torque vector \bar{M}_z sweeps

out a circle in that time and $\Delta H = \int_0^{P_{SP}} \bar{M} dt = 0$.

2. Whenever the transverse rates, ω_y and ω_z , go to zero, the x-axis must point along the \bar{H} vector since

$$\bar{H} = I_X \bar{\omega}_x + I_Y \bar{\omega}_y + I_Z \bar{\omega}_z.$$

3. If 1 and 2 above can be made to happen at the same time, then the x-axis coincides with \bar{H} which coincides with \bar{H}_0 which coincides with the initial x-axis direction and the angular velocity is pure spin, ω_x .

4. The simultaneous occurrence of 1 and 2 above will happen if the two natural periods are rationally related, that is

$$\frac{P_{tr. osc.}}{P_{spin}} = \frac{m}{n}$$

where m and n are integers.

The first such occurrence is at,

$$t = |n| P_{tr. osc.} = m P_{spin}.$$

In the following table of examples of special cases, m is the number of spin cycles which must take place before these events occur for the first time.

I_X/I_T	1/2	2/3	3/4	5/4	4/3	3/2	2	3/5	5/7	9/7	7/5	10/7
m	2	3	4	4	3	2	1	5	7	7	5	7
n	-1	-1	-1	1	1	1	1	-2	-2	2	2	3

Cold Plate Design Analysis

The basic relationships for the rotational plate concept have been modified from those presented in Appendix G of the Phase IA Report as shown below.

$$M = \frac{4 F_c \ell}{27} \quad (A-33)$$

$$F_c = \frac{V_T^2 M_R}{8 h_c} \quad (A-34)$$

$$M_R = M_f + M_p \quad (A-35)$$

$$M_p = \pi/2 \ell^2 \rho_f t_f + \pi/2 \ell^2 r \rho_c \quad (A-36)$$

$$\rho_c = k \rho_f \quad (A-37)$$

$$\sigma_c = \frac{M_c r}{I} \quad (A-38)$$

$$I \approx \ell r^2 t_f \quad (A-39)$$

$$M = M_c + M_{HS} \quad (A-40)$$

Substituting (A-39) into (A-38) and (A-37) into (A-36) into (A-35) and the results and (A-40) into (A-33) gives:

$$t_f = \frac{V_T^2 (M_f + \pi/2 \ell^2 \rho_f k r) - \frac{54 h_c M_{HS}}{\ell}}{54 h_c \sigma_c r - \frac{V_T^2}{2} \pi \ell^2 \rho_f} \quad (A-41)$$

Equations (A-41) and (A-36) were programmed and parametric results were obtained as presented in Figures 7.2-3 and 7.2-4.

In the Equations (A-33) through (A-41):

M = peak bending moment

F_c = local force transmitted by the crush-up material

ℓ = heat source and cold plate diameter

V_T = terminal impact velocity

M_r = mass of the rotating components
 h_c = crush-up height
 M_f = fixed mass of the rotating components
 M_D = cold plate mass
 ρ_f = cold plate face sheet material density
 t_f = cold plate face sheet thickness
 r = cold plate half core thickness
 ρ_c = cold plate core material density
 η = proportionality factor
 σ_c = cold plate face sheet material design bending stress
 M_c = cold plate maximum bending moment
 I = cold plate cross sectional moment of inertia at point of maximum applied bending moment
 M_{HS} = bending moment capability of the heat source

REPORT DISTRIBUTION LIST FOR CONTRACT NAS3-10938

NASA Lewis Research Center
21000 Brookpark Road
Cleveland, Ohio 44135
Attention:

Lloyd I. Shure (3) Mail Stop 500-201	J. E. Dilley (1) Mail Stop 500-309
W. T. Wintucky (1) Mail Stop 500-201	P. E. Foster (1) Mail Stop 3-19
H. O. Slone (1) Mail Stop 500-201	Library (2) Mail Stop 60-3
B. Lubarsky (1) Mail Stop 500-201	Report Control Office (1) Mail Stop 5-5
T. A. Moss (1) Mail Stop 500-201	Technology Utilization Office (1) Mail Stop 3-19

NASA Lewis Research Center
Plum Brook Station
Taylor Road
Sandusky, Ohio 44870
Attention:

J. C. Nettles (1)
Mail Stop 7141-6

National Aeronautics & Space Adm.
Washington, D. C. 20546
Attention:

B. Leefer RNP (1)
T. B. Kerr RNS (1)
T. Hagler MTY (1)
H. Rothen RNP (1)

NASA Scientific & Technical Information Facility (1)
Post Office Box 5700
Bethesda, Maryland 20014
Attention:

Acquisitions Branch (SQT-34054)

NASA Ames Research Center (1)
Moffett Field, California 94035
Attention: Library

V. Peterson (1)
E. Katzen (1)
G. Goodwin (1)

NASA Manned Spacecraft Center (1)
Houston, Texas 77058
Attention: Library

NASA Marshall Space Flight Center (1)
Huntsville, Alabama 35812
Attention: Library

NASA Goddard Space Flight Center (1)
Greenbelt, Maryland 20771
Attention: Library

Air Force Systems Command (1)
Aeronautical Systems Division
Wright-Patterson Air Force Base, Ohio
45433
Attention: Library

Power Information Center (1)
University of Pennsylvania
3401 Market Street, Room 2107
Philadelphia, Pennsylvania 19104

SAMSO
Los Angeles Air Force Station
Los Angeles, California 90045
Attention: Library (1)
Maj. H. M. Butler (1)

NASA Langley Research Center (1)
Langley Station
Hampton, Virginia 23365
Attention: Library

Douglas Aircraft Company (1)
3000 Ocean Park Blvd.
Santa Monica, California 90406
Attention: Library

NASA Manned Spacecraft Center
Houston, Texas 77058
Attention:

General Electric Company (1)
Flight Propulsion Division
Cincinnati, Ohio 45215
Attention: Library

Tony Redding EP-5 (1)
E. Olling EP-4 (1)

Jet Propulsion Laboratory (1)
4800 Oak Grove Drive
Pasadena, California 91103
Attention: Library

McDonnell Douglas Corporation (1)
Missile & Space Systems Division
3000 Ocean Park Blvd.
Santa Monica, California 90406
Attention: Library

Battelle Memorial Institute (1)
505 King Avenue
Columbus, Ohio 43201
Attention: Library

General Motors Corporation (1)
Indianapolis, Indiana 46206
Attention: Library

Institute for Defense Analyses (1)
400 Army-Navy Drive
Arlington, Virginia 22202
Attention: Library

Lockheed Missiles & Space Co. (1)
P. O. Box 504
Sunnyvale, California 94088
Attention: Mr. H. Greenfield

Aerojet-General Corporation (1)
Von Karman Center
Azusa, California 91702
Attention: Library

Pratt & Whitney Aircraft (1)
400 Main Street
East Hartford, Connecticut 06108
Attention: Library

The Boeing Company (1)
Aero-Space Division
Box 3707
Seattle, Washington 98124
Attention: Library

Sunstrand Denver (1)
2480 West 70 Avenue
Denver, Colorado 80221
Attention: Library

Aerospace Corporation (1)
P. O. Box 95085
Los Angeles, California 91745
Attention: Library

Martin Marietta Corp.
P. O. Box 988
Baltimore, Maryland 21203
Attention: Mr. Barney Mead (1)
Mail Stop 836

General Electric Company (1)
Reentry Systems Department
3198 Chestnut Street
Philadelphia, Pennsylvania 19104
Attention: Mr. R. Brast

McDonnell-Douglas Corp. (1)
Lambert Field
St. Louis, Missouri 63166
Attention: Library

NASA-Langley Research Center
Langley Station
Hampton, Virginia 23365
Attention:

Mr. W. Hayes, MORL Studies Office (1)
Mr. P. J. Bobbitt, Applied Mech. Br. (1)

TRW Systems Division (1)
One Space Park
Redondo Beach, California 90278
Attention: Library

U. S. Atomic Energy Commission
Space Nuclear Systems Div.
Washington, D.C. 20545
Attention:

Dr. L. Topper (1)
Mr. R. L. Carpenter (1)
Mr. G. Newby (1)
Dr. J. A. Powers (1)

Sandia Corporation
Sandia Base
Albuquerque, New Mexico 87115
Attention: Library (1)
Mr. A. J. Clark, Dept. 9330 (1)
Mr. R. W. Hanke, Dept. 9331 (1)
Mr. J. W. McKiernan, Dept. 9331 (1)

Donald Douglas Laboratories
McDonnell-Douglas Corp.
Richland, Washington 99352
Attention: Library (1)

Bellcomm, Inc. (1)
1100 17th St. N.W.
Washington, D. C. 20036
Attention: Mr. C. Witze

Department of the Navy (1)
Naval Facilities Engineering Command
Nuclear ENGINEERING Div.
Washington, D. C. 20390
Attention: Mr. M. Starr

Atomics International
P. O. Box 309
8900 DeSoto Ave.
Canoqa Park, Calif. 91304
Attention: Mr. W. Botts (1)

USAF Aeropropulsion Lab.
Wright-Patterson AFB, Ohio 45433
Attention: Mr. G. Thompson (APIP-I) (1)

NASA Lewis Research Center
21000 Brookpark Road
Cleveland, Ohio 44135
Attention: R. N. Weltmann MS6-2 (1)

Mound Laboratory
Miamisburg, Ohio 45342
Attention: C. Henderson (1)

Navy Space Systems Activity
Air Force Unit Post Office
Los Angeles, California 90045
Attention: R. Silverman (1)

Research Library - Lowell (3)
Research Library - Wilmington (1)
Reports Distribution Center (46)

Unclassified
Security Classification

DOCUMENT CONTROL DATA - R & D

(Security classification of title, body of abstract and indexing annotation must be entered when the overall report is classified)

1. ORIGINATING ACTIVITY (Corporate author) Ayco Government Products Group Space Systems Division 201 Lowell Street Wilmington, Massachusetts 01887		2a. REPORT SECURITY CLASSIFICATION Unclassified	
		2b. GROUP	
3. REPORT TITLE Isotope Reentry Vehicle Design Study Conceptual Design -- Phase IB--Topical Report			
4. DESCRIPTIVE NOTES (Type of report and inclusive dates) Topical Report			
5. AUTHOR(S) (First name, middle initial, last name)			
6. REPORT DATE October 1968	7a. TOTAL NO. OF PAGES 302	7b. NO. OF REFS 22	
8a. CONTRACT OR GRANT NO. NAS 3-10938		8b. ORIGINATOR'S REPORT NUMBER(S) AVSSD-0193-68-CR	
b. PROJECT NO.		8c. OTHER REPORT NO(S) (Any other numbers that may be assigned this report) NASA CR-72463	
c.			
d.			
10. DISTRIBUTION STATEMENT			
11. SUPPLEMENTARY NOTES		12. SPONSORING MILITARY ACTIVITY Technical Management NASA Lewis Research Center Cleveland, Ohio	
13. ABSTRACT This document summarizes the Task IB conceptual design effort on the Isotope Reentry Vehicle (IRV) study. The major objective of the study is to develop a preliminary design of a 25 KW _t Pu 238 IRV. Major design emphasis is on system safety and developability. The IRV is configured to meet minimum practical diameter and weight limits. During Task IA various IRV, heat source, and heat-source heat exchanger concept combinations were developed and evaluated. Three IRV systems have been studied in a detailed conceptual design evaluation in Phase IB. <ol style="list-style-type: none">1. A minimum diameter circular planar Heat Source (HS) Array (with nonvented capsules)2. A minimum diameter circular planar Heat Source (HS) Array (with vented capsules)3. A minimum diameter pin cushion HS Array (with nonvented capsules) The primary objective of Task IB has been to develop candidate designs to the level required for performance comparison and then to recommend one IRV for preliminary design.			

DD FORM 1 NOV 66 1473

Unclassified
Security Classification

14. KEY WORDS	LINK A		LINK B		LINK C	
	ROLE		ROLE	WT	ROLE	WT
Isotope Reentry Vehicle Brayton Cycle Power Supplies Plutonium 238 Fuel Capsule Heat Shields Refractory Metal Structure Impact Attenuation						